



Markus Alfons Geith, M.Sc., B.Eng.

**Percutaneous Coronary Intervention:
Pre- and Intraoperative Processes,
Mechanics, and Vascular Damage**

DOCTORAL THESIS

to achieve the university degree of
Doktor der technischen Wissenschaften
submitted to

Graz University of Technology

Supervisor

Univ.-Prof. Dipl.-Ing. Dr.techn. Gerhard A. Holzapfel

Institute of Biomechanics

AFFIDAVIT

declare that I have authored this thesis independently, that I have not used other than the declared sources/resources, and that I have explicitly indicated all material which has been quoted either literally or by content from the sources used. The text document uploaded to TUGRAZonline is identical to the present doctoral thesis.

date

signature

This thesis is dedicated to my parents

—

*In loving memory
of my Father, Alfons Geith
(1943–2020)*

Preface

This cumulative doctoral thesis comprises the key results of my research performed at the Institute of Biomechanics of Graz University of Technology. Vascular biomechanics and implants as a scientific domain have fascinated me since the very first time I encountered them. The aim of the study represents an interdisciplinary framework for the improvement of the computer-aided optimization process of balloon catheters and stents. Rather little has been written about the quantification of vascular damage and the underlying mechanism induced by percutaneous coronary interventions. This thesis also aims to contribute to that gap.

I would like to thank Professor Gerhard A. Holzapfel for his supervision and for agreeing to carry out my doctorate at the Institute of Biomechanics. He did this without hesitation at a time when I felt like I had no prospect after I was suddenly without a supervisor in the middle of my first doctoral thesis in Munich. I am thankful to Professor Thomas G. Schratzenstaller for enabling me to enter the world of science and being my mentor in the first years back in Germany and beyond. My gratitude goes to Assistant Professor Gerhard Sommer for his guidance in the laboratory. I would like to thank Professor Marcus Wagner for encouraging me in common research projects as well as for many informative and delightful discussions.

This work was carried out in parallel to my avocational activity as a research assistant at King's College London. Therefore, I want to thank Associate Professor David Nordsletten and Professor Ralph Sinkus for their understanding in stressful times as well as to allow me to engineer their visions and ideas. While being part of their team, I was able to work together with excellent project partners. Thank you Daniel, Markus, and Anna-Sophie.

Many thanks to my past and present fellow researchers and colleagues, Alex, Alexander, Anna, Bettina, Birgitt, Clemens, Daniel, Gerhard, Jakob, Justyna, Kewei, Krzysztof, Laurenz, Lloyd, Malte, Manos, Michael, Misael, Osman, Selda, and Simon, for our daily exchange of ideas and thoughts, as well as the fun moments together. I very much enjoyed supervising and teaching several students in the past years and want to thank them for their assistance and commitment.

Over the past years, many people have been a source of support and inspiration. I thank my friends back in Bavaria and in countries around the world who always have been by my side, although I often had to neglect our friendship. My new-found Austrian friends helped me to explore this country and its beautiful cities, wild mountains, and stunning lakes from the ground as well as from the sky. Thank you for all adventures and unforgettable times. I want to thank my wonderful girlfriend, Carmen. Whenever I was worried and frustrated, you kept me motivated. This work would never have been finished without the unconditional love, support, and solidarity of my sister Kathrin and her family, my mother Rita, and my father, Alfons. You made it possible for me to follow this path despite all obstacles and setbacks. I am sorry that I could not always be with you in difficult times.

Abstract

After percutaneous coronary interventions (PCI), vascular narrowing or blocking continue to occur frequently. Since the extent of such complications increases with the severity of the induced damage, stents and balloon catheters must be optimized to minimize vascular injuries during PCI. The computer-aided finite element method (FEM) is a helpful tool, which is capable of calculating and visualizing harmful stresses and deformations within the arterial wall. The accuracy of FEM simulations can be increased considerably if detailed geometries and suitable constitutive models are implemented, and prevailing contact and boundary conditions taken into account.

Therefore, in the first study of this cumulative dissertation, preoperative processes, as well as the expansion process of PCI, were modeled with realistic geometries of stents, balloon catheters, and production tools with a FEM program. Induced stresses and deformations could be successively calculated with an implicit time integration method and transferred between the individual simulations. The results show that stents and balloon catheters are already exposed to significant loads during production. Furthermore, a comparison with experimental data demonstrates: if production induced residual stresses and deformations are not taken into account, results from FEM simulations can differ significantly from reality.

In the course of the second study, the material behavior of balloon catheter membranes made of polyamide 12 (PA 12) was investigated experimentally and modeled subsequently. For this purpose, special clamps have been developed which enable biaxial tensile tests on tiny membrane samples. After analyzing the experimental data, the mechanical behavior of PA 12 membranes can be described as semi-compliant, nonlinear, and viscoelastic. Above the nominal load and with increasing strain rate, the membrane material pronounces anisotropy. Mechanical data were fitted utilizing a model with a generalized polynomial-type elasticity relation together with an extension for the anisotropic response.

The third study aims to answer the question of whether the material behavior of coronary arteries changes during PCI and to what extent collagen-based damage mechanisms in the collagen structure are responsible for these alterations. For this purpose, a testing device was developed, which can simulate the multiaxial loading scenario of PCI *in vitro*. With this device, the stress-strain behavior was determined before and after the indentation of a stent strut. Besides, structural parameters of untreated and damaged samples could be quantified using second-harmonic generation microscopy. The results reveal that damage mechanisms such as tissue compression, softening, and changes in the fiber dispersion, but also the extent of injuries are directional and vary considerably with alterations in stent strut orientation, indentation pressure, and position.

Zusammenfassung

Nach perkutanen Koronarinterventionen (Engl.: *percutaneous coronary intervention* (PCI)) kommt es nach wie vor häufig zu erneuten Gefäßverengungen oder -verschlüssen. Da das Ausmaß solcher Komplikationen mit der Schwere der induzierten Schädigung steigt, müssen Stents und Ballonkatheter dahingehend optimiert werden, vaskuläre Schädigung während einer PCI gering zu halten. Dabei hilfreich ist die rechnergestützte Finite-Elemente-Methode (FEM), mit welcher schadhafte Spannungen innerhalb des Gewebes und Verformungen der arteriellen Wand berechnet und visualisiert werden können. Die Genauigkeit von FEM-Simulation lässt sich erheblich steigern, wenn detaillierte Geometrien und passende konstitutive Modelle implementiert, sowie in der Realität vorherrschende Kontakt- und Randbindungen berücksichtigt werden.

Daher wurden in der ersten Studie dieser kumulativen Dissertation preoperative Prozesse als auch der Aufdehnvorgang einer PCI mit realistischen Geometrien von Stents, Ballonkathetern und Produktionswerkzeugen in einem FEM-Programm nachmodelliert. Sukzessive konnten die induzierten Spannungen und Verformungen mit einem impliziten Zeitintegrationsverfahren berechnet und zwischen den einzelnen Simulationen übernommen werden. Die Ergebnisse belegen, dass Stents und Ballonkatheter bereits während der Produktion signifikanten Belastungen ausgesetzt sind. Der Vergleich mit experimentellen Daten zeigt: Werden die während der Produktion induzierten Eigenspannungen und Verformungen nicht berücksichtigt, können Ergebnisse aus FEM-Simulationen signifikant von der Realität abweichen.

In der zweiten Studie wurde das Materialverhalten von Polyamid 12-Ballonkathetermembranen experimentell untersucht und anschließend modelliert. Hierzu wurden spezielle Klemmen entwickelt, welche biaxiale Zugversuche von winzigen Membranproben ermöglichen. Nach Analyse der experimentellen Daten kann das Materialverhalten der Membranen als halbnachgiebig, nichtlinear und viskoelastisch beschrieben werden. Oberhalb der Nominalbelastung ist das Spannungs-Dehnungsverhalten zudem stark anisotrop. Anhand eines modifizierten polynominalen Materialmodells und einem angepassten Materialparametersatz, lässt sich die mechanische Reaktion der Membranen realistisch reproduzieren.

Die dritte Studie behandelt die Frage ob sich das Materialverhalten von Koronararterien durch PCI verändert und inwiefern Schädigungsmechanismen in der Kollagenstruktur hierfür verantwortlich sind. Dazu wurde ein Prüfstand gebaut, welcher den Lastfall einer PCI *in vitro* nachbilden kann. Mit Hilfe dieser Apparatur wurde das Spannungs-Dehnungsverhalten vor und nach dem Eindringen einer Stent-Strebe bestimmt. Multiphotonenmikroskopie konnten zudem Strukturparameter von unbehandelten und durch PCI geschädigten Proben quantifiziert werden. Die Ergebnisse zeigen, dass Schädigungsmechanismen, wie Gewebekompression, Erweichung, Änderungen in der Faserverteilung, aber auch das Verletzungsmaß richtungsabhängig sind und mit Ausrichtung der Strebe, Einpressdruck und Position stark variieren.

Contents

Preface	I
Abstract	II
Zusammenfassung	IV
Contents	IV
1 Introduction	1
1.1 Motivation and Objectives	1
1.2 Human Coronary Arteries	2
1.2.1 Distribution and function	2
1.2.2 Tissue compounds	4
1.2.3 Vascular structure	6
1.2.4 Mechanical behavior in health	8
1.3 Coronary Artery Disease	13
1.3.1 Endothelial dysfunction	13
1.3.2 Atherosclerosis and its classification	15
1.3.3 Coronary syndromes	19
1.3.4 Mechanical behavior in disease	19
1.3.5 Clinical evaluation, diagnosis, classification, and treatments	20
1.4 Percutaneous Coronary Intervention	22
1.4.1 Intra-operative procedures	23
1.4.2 Evolution of balloon catheters and stents	26
1.4.3 Manufacture and preoperative processes of catheters and stents	29
1.4.4 Computational and theoretical investigations	31
1.5 Doctoral Thesis	33
1.5.1 Organisation	33
1.5.2 Further engagements	35
2 On the Importance of Modeling Balloon Folding, Pleating, and Stent Crimping: An FE Study Comparing Experimental Inflation Tests	37
2.1 Introduction	37
2.2 Materials and Methods	41
2.2.1 Balloon catheter and stent	41
2.2.2 Preoperative processes	42
2.2.3 Inflation tests and micro-CT scans	44
2.2.4 Numerical simulations	44
2.3 Results	49
2.3.1 Folding process	49

2.3.2	Pleating process	49
2.3.3	Crimping process	52
2.3.4	Stent expansion	52
2.4	Discussion	55
3	Experimental and Mathematical Characterization of Coronary Polyamide-12 Balloon Catheter Membranes	62
3.1	Introduction	62
3.2	Materials and Methods	64
3.2.1	Coronary balloon catheter	64
3.2.2	Specimen preparation	65
3.2.3	Uniaxial extension tests	67
3.2.4	Biaxial extension tests	68
3.2.5	Material modeling	70
3.3	Results	72
3.3.1	Uniaxial mechanical response	72
3.3.2	Biaxial mechanical response	73
3.3.3	Model parameters	78
3.4	Discussion	78
3.5	Conclusion	81
4	Quantifying Stent-Induced Damage in Coronary Arteries by Investigating Mechanical and Structural Alterations	83
4.1	Introduction	83
4.2	Materials and Methods	86
4.2.1	Biomechanical principles	86
4.2.2	<i>In vitro</i> simulation of stent implantation	89
4.2.3	Structural analysis	95
4.2.4	Data analysis	97
4.3	Results	98
4.3.1	Mechanical response	98
4.3.2	Structural response	101
4.4	Discussion	105
4.4.1	Characteristics of native porcine RCA	106
4.4.2	Damage mechanisms	106
4.4.3	Impact on stented arteries	107
4.4.4	Further findings	109
4.4.5	Limitations	110
4.4.6	Future aspects	110
4.5	Conclusion	111
	References	113

1 Introduction

1.1 Motivation and Objectives

According to the latest global status report of the World Health Organization (WHO) in 2014 [1], the number of percutaneous coronary interventions (PCI) is rapidly increasing worldwide, particularly in industrialized countries such as Austria, where the number of implanted stents increased by 18% from 2009 to 2014 [2, 3]. The most challenging complications after PCI are coronary events such as in-stent restenosis and in-stent thrombosis, which still occur at rates as high as 20% despite improvements [4]. The extent of those coronary events mainly correlates with the severity of vascular injuries [5–9]. As a result, different types of stents and balloon catheters with pharmaceutical coatings have emerged to prevent in-stent-restenosis and in-stent-thrombosis. However, these drugs may postpone coronary events up to 40 months by inhibiting cell proliferation and migration [10]. With a significantly higher risk of very late in-stent-restenosis and a constant risk of in-stent-thrombosis due to delayed re-endothelialization, e.g., drug-coated stents have a similar fatality rate as uncoated stents [4, 11–14].

To improve the fatality rate of PCI, scientists and manufacturers need to develop safer stents or balloon catheters by significantly reducing the risk of vascular injuries. This may be achieved by reducing the load on the artery applied by stents and catheters. Therefore, engineers need to change geometries, materials, or both. Finite element analysis (FEA) has become an essential tool for the optimization process of stents and catheters. The accuracy of FEA highly depends on precise constitutive models. During the last years, several models emerged, aiming to describe the anisotropic and nonlinear behavior of healthy and atherosclerotic coronary arteries. However, no model is known, which considers stent-induced vascular damage. Although many models can determine the nonlinear material behavior of polymers, it is not clear which model is suitable for balloon catheter membranes. The development of constitutive models for damaged arteries and balloon catheter membranes requires a set of materials and structural parameters that needs to be obtained in experiments first. Hence, this thesis focuses partly on the quantification of stent-induced alterations of structural parameters and the identification of damage mechanisms inside coronary arteries. The gained knowledge could be used to optimize existing models. Another focus is on the characterization of the mechanical behavior of polymeric balloon catheter membranes, the quantification of respective material parameters, and the subsequent constitutive modeling. A constitutive model based on experimental data from polymers processed in membranes rather than those from the raw material may significantly improve the precision of future FEA.

The accuracy of FEA also benefits from realistic and detailed geometries. Nevertheless, it is often neglected that stents and balloon catheters endure significant loads and deformations during production, especially during preoperative processes, namely balloon folding, and pleating, as well as stent crimping. For this reason, only idealized geometries are

commonly implemented in FEA of PCI. Therefore, this thesis also covers the question of whether stresses and strains induced by preoperative processes influence the geometries and the expansion behavior of stents and balloon catheters even before PCI.

In the following, the author would like to provide a brief overview of human coronary arteries and PCI to guide the reader to the proposed research topics of this cumulative doctoral thesis and to provide the necessary knowledge for future investigations.

1.2 Human Coronary Arteries

The human heart needs to be supplied with blood to function. An undersupply of the muscular tissue of the heart, the myocardium, is called ischemia and can result in necrosis and fatal events such as infarction. The arteries responsible for the blood supply are the coronary arteries, which further divide into subbranches and, thus, perfuse the myocardium. The embryonic formation of coronary arteries includes three steps, namely vasculogenesis, angiogenesis, and arteriogenesis [15]. During vasculogenesis, endothelial cells proliferate and form a primitive vascular bed. Vascular beds of all coronary arteries are contained in the epicardial adipose tissue (EAT), which is the visceral fat deposit of the heart [16]. Angiogenesis describes the development of microvessels by endothelial proliferation. And finally, arteriogenesis denotes the remodeling of mature arteries by migrating smooth muscle cells. Coronary arteries are the first vessels that originate from the ascending aorta. Hence, blood passes coronary arteries first and reaches subsequently the aortic arch as well as the brachiocephalic, carotid, and left subclavian arteries. The coronary artery system consists of the left main coronary artery (LMCA) and the right coronary artery (RCA). Both arteries arise from the aortic sinuses of the ascending aorta in the coronary ostia. The LMCA bifurcates into the left anterior descending (LAD) and the left circumflex (LCx) branches.

1.2.1 Distribution and function

All main branches can be further divided into segments (see Figure 1.1). In addition, Table 1.1 lists the mean luminal diameters for adult men for proximal and distal segments measured by Dodge *et al.* [17]. The main branches are described in the following paragraphs.

The **LMCA** typically originates in the left posterior sinus. It travels between the pulmonary artery and the left auricle for 9.7 ± 4.3 mm [18] with a mean luminal diameter of 4.5 ± 0.5 mm [17]. The LMCA does not pronounce significant branches of its own [19], but soon bifurcates into the left anterior descending (LAD) and left circumflex (LCx) branches.

The **LAD** arises from the LMCA and travels caudally in the anterior interventricular sulcus and extends around the apex of the heart. It supplies the basal half of the ventricular septum and the anterior left ventricular free wall [20]. The LAD is divided into a proximal segment that terminates at the first septal perforator, a middle segment that leads halfway to the left

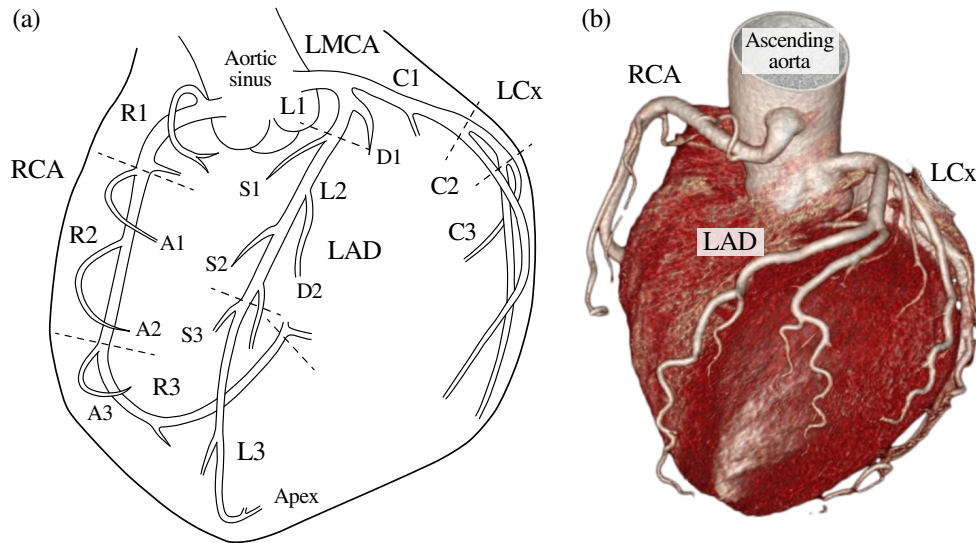


Figure 1.1 Coronary circulation: (a) simplified anterior view of the anatomy of the human coronary arteries (redrawn and modified from [17]); (b) imaging data of a human heart obtained with multidetector computed tomography (MDCT) (adapted and modified from [22] and reprinted with permission from Springer Nature). RCA = right coronary artery; LMCA = left main coronary artery; LAD = left anterior descending; LCx = left circumflex; R1–3, L1–3, C1–3 = proximal, medial, distal RCA, LAD, and LCx, respectively; A = acute marginal arteries S = septal perforator branches; D = diagonal branches.

Table 1.1 Mean luminal diameters of the proximal and distal segments of the main coronary arteries in right/left heart and co-dominance (adapted and modified from [17]).

Location	Diameter (mm)		
	right heart dominant	Co-dominant	Left heart dominant
R1	3.9 ± 0.6	3.0 ± 0.5	2.8 ± 0.5
R3	3.1 ± 0.5	2.0 ± 0.6	1.1 ± 0.4
LMCA	4.5 ± 0.5	4.4 ± 0.4	4.6 ± 0.4
L1	3.6 ± 0.5	3.6 ± 0.4	3.7 ± 0.2
L3	1.7 ± 0.5	1.8 ± 0.4	2.0 ± 0.3
C1	3.4 ± 0.5	3.4 ± 0.5	4.2 ± 0.6
C3	1.6 ± 0.6	2.5 ± 0.5	3.2 ± 0.5

ventricular apex, and a distal segment that ends at the apex [19]. In healthy human adults of mean age, the mean length of the LAD is 39 ± 23 mm [21] and the mean luminal diameter ranges between 3.6 ± 0.5 mm at its origin and tapers to 1.7 ± 0.5 mm [17].

The **LCx** bifurcates from the LMCA and follows the left atrioventricular groove around the left auricle. It has a proximal and distal segment, which is separated by the first obtuse marginal branch [19]. Generally, it perfuses the lateral wall of the left ventricle. The mean length of the LCx is 11 ± 10 mm [21], and its proximal and distal luminal diameter ranges between 3.4 ± 0.5 mm and 1.6 ± 0.6 mm [17].

The **RCA** travels between the right auricle and the infundibulum to the right section of the sulcus coronarius and the origin of the right marginal artery. It mainly supplies the anterior,

lateral, and posterior aspects of the right ventricular myocardium and the basalmost portion of the ventricular septum. The RCA has a proximal segment that terminates halfway to the acute margin, a middle segment that ends at the acute margin, and a distal segment that leads into the bifurcation of the atrial and ventricular septa [19]. The RCA shows a mean length of 56 ± 26 mm [21] and maintains a reasonably constant diameter between 3.9 ± 0.6 mm and 2.8 ± 0.5 mm [17], which makes the RCA an ideal target vessel for mechanical experiments.

As in other biological systems, coronary arteries can pronounce anomalies. These anomalies affect approximately 1% of the population [19] and constitute the second most common cause of sudden cardiac death. Coronary arteries are usually surrounded by epicardial fat. However, in 26% of all patients, myocardial bridging occurs – an anomaly pronouncing intramyocardial coronary arteries [23]. Dimensions of coronary arteries also scatter significantly as 70 to 80% of the population is right heart dominant, i.e., the RCA is more pronounced [24] and originates the posterior descending artery (PDA). Only 5 to 10% is left heart dominant, i.e., the PDA originates in the LCx, and 10 to 20% is co-dominant. Further coronary anomalies are associated with abnormal aortic origins, high take-off ostia, congenital absence of the LCMA, hypoplasia of the RCA and LCx, as well as coronary fistulas and arteriovenous malformations [19, 25]. Coronary arteries may also pronounce coronary collaterals that provide anastomotic connections, which might have a positive effect on myocardial perfusion [26, 27].

1.2.2 Tissue compounds

On the micro-scale, mature coronary arteries are biological composites consisting of endothelial cells, vascular smooth muscle cells (VSMC), fibroblasts, macrophages, and extracellular matrix (ECM) with a high content of elastin as well as different types of collagen.

Human **endothelial cells** pronounce elongated shapes with a length of 50–70 μm , a width of 10–30 μm , and a thickness of 0.1–10 μm [28]. They regulate among others the vasomotor tone, which is essential to provide appropriate tissue level perfusion and blood pressure fluctuation. These cells produce and react to locally active mediators, most importantly, nitric oxide (NO), which is released in response to mechanical stimuli. NO diffuses into the adjacent tissue and causes VSMC relaxation [29]. Known mediators are prostacyclin, angiotensin II, endothelin, and endothelium-derived hyperpolarizing factors [30]. Besides, the endothelium influences hemostasis by regulating enzymatic activities, especially of thrombin, which is important for the conversion of fibrin [31]. In addition, endothelial cells ensure other functions, namely permeability, leukocyte trafficking, angiogenesis, and innate and acquired immunity. Endothelial cells have no direct influence on the mechanical properties of an artery. For a broader overview of the phenotype of the healthy endothelium, the reader is referred to the review articles [30, 32, 33].

VSMC are fusiform cells with dimensions of 50–200 \times 5 μm in length and a width of 2–8 \times 5 μm in the resting state [34, 35]. Their primary function is to alter the diameter

of arteries by contraction or relaxation. Thus, they contribute to the regulation of the pulsatile blood flow. While VSMC hardly contributes to the passive mechanical properties of blood vessels [36–39], the active tissue response depends mostly on the VSMC contraction [38, 40, 41]. In healthy arteries, most of the VSMC are in a contractile phenotype [42]. However, they can switch to a synthetic phenotype. In this state, VSMC regulate contractile proteins (actin, myosin, etc.), proliferate, and remodel the ECM in response to specific growth factors triggered by vascular injuries.

Fibroblasts are adherent, flat, and spindle-like cells of varying size and shape. These cells are the abundant cellular constituents of connective tissues in the body and, therefore, the predominant cell type in the outer regions of the vascular wall. Fibroblasts are characterized by several complex phenotypes [43]. Thus, they produce, organize, and also degrade structural elements of the ECM, in particular fibrillar collagen. Fibroblasts also secrete growth factors and peptides, like cytokines. Furthermore, they interact with hematopoietic stem, neural, and endothelial cells as well as neuropeptides.

Macrophages are immune cells, which can change their morphology according to their function and surrounding ECM [44]. They consist of two classes: resident and blood-born infiltrating macrophages [45]. Resident macrophages are heterogeneous components of developing and mature arterial tissue. With diverse phenotypes, these cells are key regulators of healthy tissue homeostasis. They deal with waste products and produce a variety of factors that stimulate the activation, proliferation, and differentiation of other resident cell types. Thus, resident macrophages are essential for tissue repair, regeneration, and fibrosis [46]. Infiltrating macrophages have their origins from circulating monocytes, which are recruited to injured tissue.

Elastin is an insoluble and hydrophobic structural protein that is formed through cross-linking of the monomeric protein tropoelastin. Segregated by VSMC and fibroblasts, it is the predominant constituent in the ECM [47]. Coronary arteries pronounce an *in vivo* elastin content of 19% [48]. Elastin is also with 90% the largest constituent of elastic fibers [49]. These elastic fibers consist of fibrillin microfibrils and an amorphous core of elastin and pronounce relatively low stiffness. The high density of elastin allows arteries to deform and to recoil under hemodynamic loading without permanent damage and energy dissipation. Due to the elasticity of the arteries, the pulsatile blood flow gets damped during systole and pumped distal by the diastolic recoil. Thus, almost constant perfusion is reached. This vascular feature is known as the Windkessel effect.

Collagen, another structural protein, is synthesized by VSMC and fibroblasts inside arterial tissue. Its content in coronary arteries is 54% [48]. It is composed of three polypeptide chains, called α chains, in which every third amino acid is glycine – the smallest amino acid [50]. These α chains differ in their amino acid compound and their length. However, all of them are assembled in at least one triple helix that is stabilized by hydrogen bonds, water bridges, and the amino acids proline and hydroxyproline. The α chains of a triple helix are either similar or different in one or two configurations [51]. The collagen family holds 28 members numbered with Roman numerals, which are classified according to their molec-

ular assembly and pronounce 38 genetically distinct α chains [50–52]. Collagen types I, II, III, V, XI, XXIV, and XXVII are fibrillar [53] and can form hierarchic structures, starting on the amino acid level, continuing with tropocollagen molecules that form parallel fibrils which result in collagen fibers. The average thickness of fibrillar collagen in porcine coronary arteries was found to be $3.63 \pm 0.61 \mu\text{m}$, $1.29 \pm 0.47 \mu\text{m}$, and $0.93 \pm 0.36 \mu\text{m}$ for the no-load state, 30 mmHg distension, and 180 mmHg distension, respectively [54]. Collagen types IV, VIII are sheet-forming, types XV, XVIII, XIX are fibril-associated, and type VI is microfibrillar [55]. Collagen is the most abundant structural protein in the ECM, with the fibrillar types I, III, and V collagen being predominant. Due to its stiffness and strength, collagen counteracts deformations of the arterial wall due to excessive dilation and ensures stability. Vascular collagen may also influence the phenotype of VSMC [56, 57].

1.2.3 Vascular structure

Similar to all arteries, the wall of coronary arteries is composed of three concentric layers, including a luminal layer, the tunica intima, a middle layer, the tunica media, and an outer layer, the tunica adventitia [58] (see Figure 1.2(a)). Cross sections of porcine coronary walls are presented in Figures 1.2(b) and (c). The thickness ratio of the adventitia, media, and intima in adult human coronary arteries was reported to be 0.4 ± 0.03 , 0.36 ± 0.03 and 0.27 ± 0.02 , respectively [59]. The individual layers are briefly described in the following paragraphs.

The **tunica intima** is the innermost arterial layer. As in other arteries, the coronary intima serves as a barrier between the arterial wall and the lumen. It holds a single layer of endothelial cells, which elongate and align in blood flow direction [62], and faces the lumina of coronary arteries. The endothelium covers the subendothelial layer, which consists of random oriented fibrillar collagen type V, also collagen types IV, XV, and XVIII, laminin, fibronectin, and other compounds of the ECM [54, 58, 63–67]. The subendothelial layer is connected via the internal elastic lamina to the media layer. In smaller animals, the subendothelial layer is usually acellular. However, in humans or larger animals, some VSMC might also be present in the intima, which are oriented in the longitudinal direction [68–70]. While the intima of coronary arteries is very thin in young animals and human newborns [54], it is generally significantly thicker in human adults [54, 59, 71].

The mechanical behavior of healthy coronary arteries under hemodynamic loadings depends mostly on the muscular **tunica media** [69]. On the micro-scale, it is composed of multiple concentric layers of circumferential oriented VSMC reinforced by an ECM of collagen and elastic fibers. VSMC in the media (see Figure 1.2(d)) are oriented in circumferential direction [72, 73]. Fibrillar collagen, preferentially oriented in the circumferential direction, ensures stability and envelopes VSMC [49, 74]. In an unloaded configuration, collagen fibers of the coronary media are wavy, while under *in situ* deformation collagen fibers appeared to be straightened [75]. A detailed immunolocalization of predominant collagen types in healthy human coronary arteries has yet not been performed. However, a strong presence of collagen types I and III in the coronary media of rats could not be

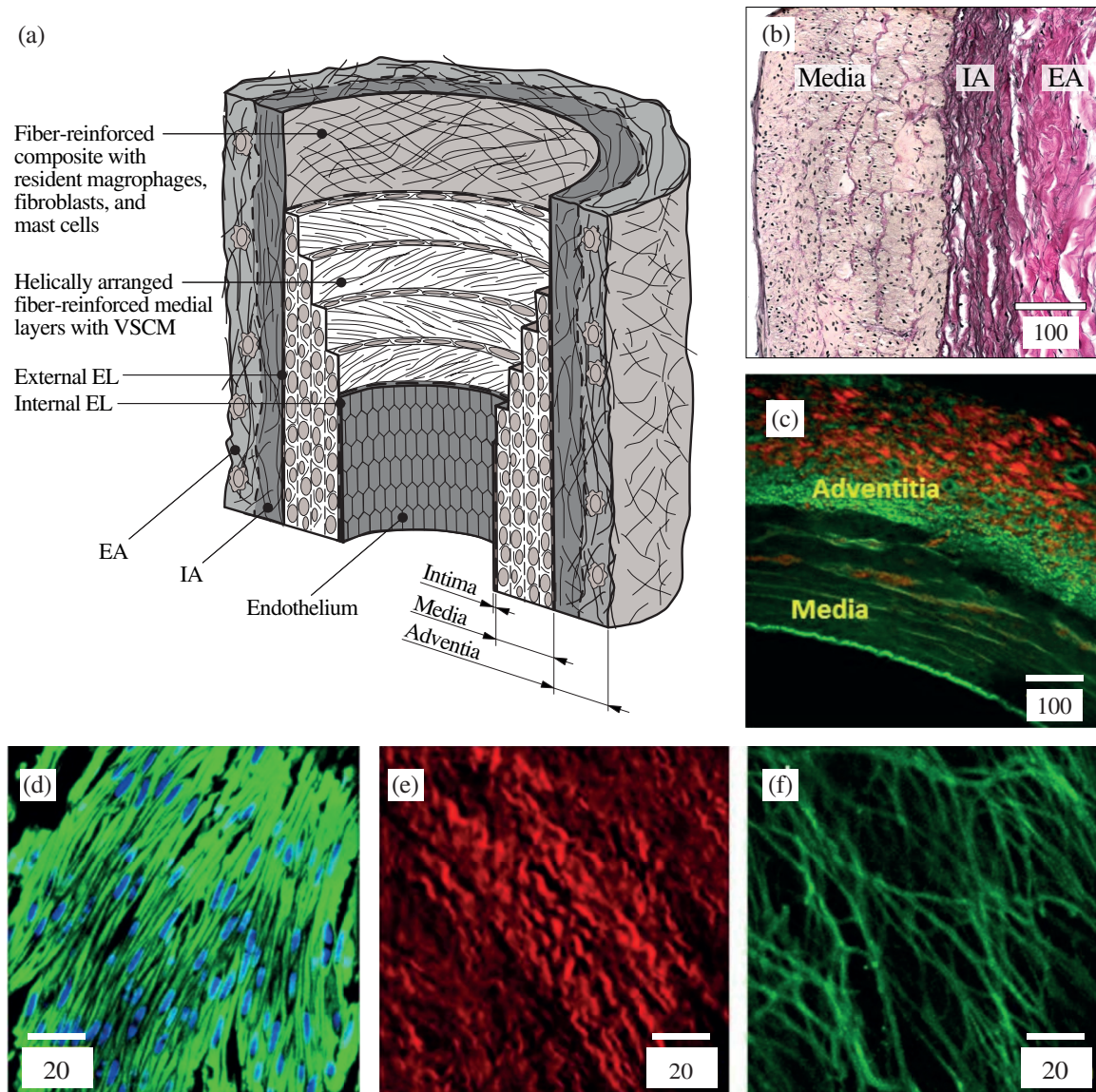


Figure 1.2 Structure and tissue compound of coronary arteries: (a) schematic of the arterial wall featuring three concentric layers, the intima, media, and adventitia. The latter has two overlapping sublayers, the inner adventitia (IA) and the exterior adventitia (EA) (redrawn and modified from [60]); (b) histological Elastica van Gieson staining showing the media, inner and exterior adventitia; (c) merged second-harmonic generation (SHG)/two-photon-excited fluorescence (TPFE) of a porcine coronary artery (red indicates collagen and green indicates elastin fibers); (d) confocal images of VSMC in the coronary media with Alexa Fluor 488 Phalloidin (Green) and DAPI staining; (e,f): SHG/TPFE images of longitudinal-circumferential sections of the inner adventitia. Figures (c)–(f) were reprinted from [61] with permission from Elsevier.

observed [76]. Collagen types IV and V were found to surround the basement membranes of VSMC in smaller arteries [67]. Rod-like elastic fibers provide the elasticity of the artery. They bond in thick continuous sheets to elastic lamella (EL), which is anchored on either side to the VSMC [77, 78]. Clark *et al.* [74] described the radial transmural arrangement of

the mentioned constituents as collagen bundles–elastin–VSMC–elastin–collagen bundles disposition. Further investigations observed that coronary media EL of narrower and more widely spaced elastic fibers form a thinner and more porous structure compared to aortas [74]. Furthermore, the EL distributes the loading evenly onto collagen fibers throughout the arterial wall [79]. The volume density of VSMC in the tissue of adult murine coronary arteries was found to be 74%, with an ECM content of 17% [80]. The collagen to elastin ratio was reported to be ~ 3.7 in porcine RCA [81].

The **tunica adventitia**, the outermost arterial layer, is divided from the media by the external elastic lamina. Its outer layers are in direct contact with the epicardial adipose tissue. It resists against overstretching and rupture under extreme loads above the physiological range. It also couples the surrounding tissue with the artery. And finally, it plays an important role in regulating the vascular tone under physiological and supraphysiological loading. The *in situ* orientation angles of collagen and elastic fibers change significantly between layers but tend to point towards the longitudinal direction of the artery [54]. In contrast to human aortas, Chen *et al.* [72, 75] reported that the coronary adventitia shows a different fiber structure in the inner adventitia than in its external counterpart, confirms the finding of own preliminary histological investigations (see Figure 1.2(b) and (c)). On the micro-scale, elastic and collagen fibers are organized in alternating packed layers with transmurally changing geometrical features (see Figures 1.2(e) and (f)). Thus, while the inner adventitia features thin collagen fibers, thick and randomly oriented collagen bundles are present in the exterior adventitia. Elastic fibers align parallel to collagen fibers with some elastin oriented in a secondary direction, organized in a reticular sublayer. In the outer adventitia, elastic fibers were hardly found. The general volume density of adventitial collagen in RCA was reported to be 34%, while the content of elastin was 22%, which results in a collagen to elastin ratio of ~ 1.5 [75]. In the coronary adventitia of rats, collagen type III was reported to be predominant [76]. The coronary adventitia is interspersed with fibroblasts and resident macrophages. The detailed collagen content of healthy human coronary arteries has yet not been investigated. Furthermore, the adventitia is grained by the vasa vasorum – small blood vessels defining the microvasculature of cells in the arterial tissue [73] – and nerve endings.

1.2.4 Mechanical behavior in health

The heart has the highest oxygen consumption of any organ in the human body. To supply the myocardium, 5% of the cardiac output needs to feed the coronary circulation [82]. The resting coronary blood flow rate is approximately $250\text{--}300\text{ ml min}^{-1}$ [83]. The cardiac cycle is divided into a myocardial contraction phase – the systole – and the refilling phase of the ventricle – the diastole. Flow occurs predominantly with $\sim 80\%$ of the cardiac demand during diastole, and falls to zero or an even reversing flow in the systole [84, 85]. The systolic arterial pressure (SAP), which ranges between $90\text{--}120\text{ mmHg}$, equals the left ventricular systolic pressure (LVSP), causing the left ventricle to compress the myocardium. Hence, the capillaries of the coronary circulation are squeezed, after which no more blood

can flow. Towards the end of the diastole, a pressure gradient between the diastolic arterial pressure (DAP) in the ascending aorta and the left ventricular end-diastolic pressure (LVEDP), the so-called coronary perfusion pressure (CPP), ensures the coronary blood flow [86]. The DAP in the ascending aorta ranges between 60–80 mmHg. The mean arterial pressure (MAP) inside human coronary arteries is approximately 100 mmHg.

As in other arteries, the coronary circulation performs active regulation of the vascular tone to maintain a balanced blood pressure distribution and flow. Thus, it was reported that an increased blood flow rate leads to an increased luminal diameter, while a decreasing flow rate results in a decreased luminal diameter [87–90]. Increased or decreased flow rates cause abnormal wall shear stresses. This stimulus triggers up- or downregulation, respectively, of the endothelial NO production and, therefore, VSMC relaxation or contraction, respectively [91]. The degree of the active coronary regulation depends on various physiological and pathological processes, in particular on fluctuating CPP and metabolism, hypoxemia, anemia, and myocardial ischemia [86]. In muscular arteries, VSMC play a key role in the active response of coronary tissue, but also in vasoconstriction and vasodilation. Tissue contraction can alter the circumferential as well as longitudinal material response due to VSMC arrangement and multi-axial vasoconstriction [92] (see Figure 1.3).

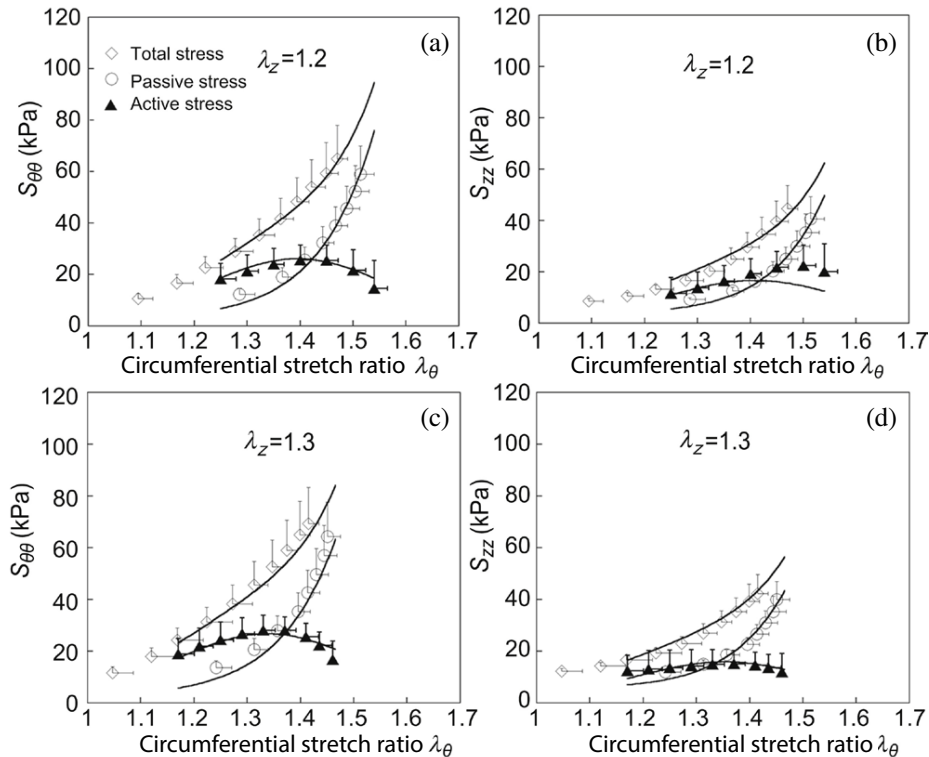


Figure 1.3 Second Piola-Kirchhoff total, passive, and active stresses of the coronary media [92]: (a) circumferential stresses at $\lambda_z = 1.2$; (b) longitudinal stresses at $\lambda_z = 1.2$; (c) circumferential stresses at $\lambda_z = 1.3$; (d) longitudinal stresses at $\lambda_z = 1.3$. Symbols present experimental measurements from distension tests, and solid curves present predicted values from theoretical investigations. Reprinted with permission from Elsevier.

Interestingly, experiments of van Loon [93], Weizsacker *et al.* [94], Brossellet and Vito [95], Schulze-Bauer *et al.* [96], and Sommer *et al.* [97] showed that the axial force, needed to physiological stretch active arterial tissue, does not change with increasing luminal pressure. However, this axial force changes significantly due to pressurization if the tissue gets stretched below or above the physiological range. Furthermore, Fridez *et al.* [98] observed that active VSMC contraction only affects the mechanical response of arterial tissue under hypertension but not under physiological conditions. VSMC seem to not influence the material properties of passive tissue [39], i.e., tissue which does not have its own contractile ability anymore but still contains VSMC [99].

Under normal physiological conditions, coronary tissue exhibits intraparietal active stress, called basal vascular tone [100]. In addition, residual tension within the vessel wall occurs mainly due to intramural and durable elastin, less due to collagen [101]. The study of Zeller and Skalak [102] exposes that collagen might be under residual compression and elastin under residual tension. The basal vascular tone, together with vascular residual stresses and the arterial blood flow-induced wall shear stresses, yield the loading scenario of a healthy coronary artery. The quantification of resulting initial longitudinal and circumferential stretches, as well as the radial compression, is essential for the experimental simulation and computational modeling of physiological boundary conditions. Humphrey *et al.* [48] introduce in their review article a theoretical approach to calculate the *in situ* longitudinal stress. The experimental study of Holzapfel *et al.* [59] quantifies the *in situ* longitudinal stretch of aged human coronary arteries with $\lambda_z = 1.044$. Liu *et al.* [103] found the longitudinal stretch for young porcine coronary arteries to be $\lambda_z = 1.3$. Recently, the group of Wang *et al.* [104] developed a new experimental approach and, thereby, observe an *in situ* longitudinal stretch of porcine LAD of $\lambda_z = 1.28$ (see Figures 1.4(a) and (b)). This value was observed on specimens that were still embedded in the native perivascular environment. The findings additionally reveal that the perivascular loading, as well as the axial tethering, significantly influence the measured longitudinal stretch. The results of Wang *et al.* [104] also include the pressure vs. outer diameter relationship (see Figure 1.4(c)) as well as the compliance-diameter response (see Figure 1.4(d)). Arterial compliance is an index for arterial elasticity and is defined by the division between the change of the luminal volume and the change of the luminal pressure ($C = \Delta V / \Delta p$). The curves in Figure 1.4(d) imply that the compliance decreases significantly with increasing luminal pressure. Nevertheless, as the walls of low pressurized arteries start to collapse, the quantification of the *in situ* circumferential stretch seems to remain an open task. Based on its high water content of approximately 80%, passive tissue of coronary is mostly considered as incompressible [105]. However, this assumption may not account for active VSMC interspersed tissue or the high-pressure domain. Hence, the quantification of radial tissue compression at certain pressure levels might be of great interest.

In general, active as well as passive coronary tissues of humans and animals pronounce a highly nonlinear stress-strain behavior under uniaxial and biaxial testing conditions [41, 59, 75, 106–110]. Beside VSMC, elastic and collagen fibers in the ECM significantly influence the material response of the tissue. Thus, the relatively low stiffness but larger

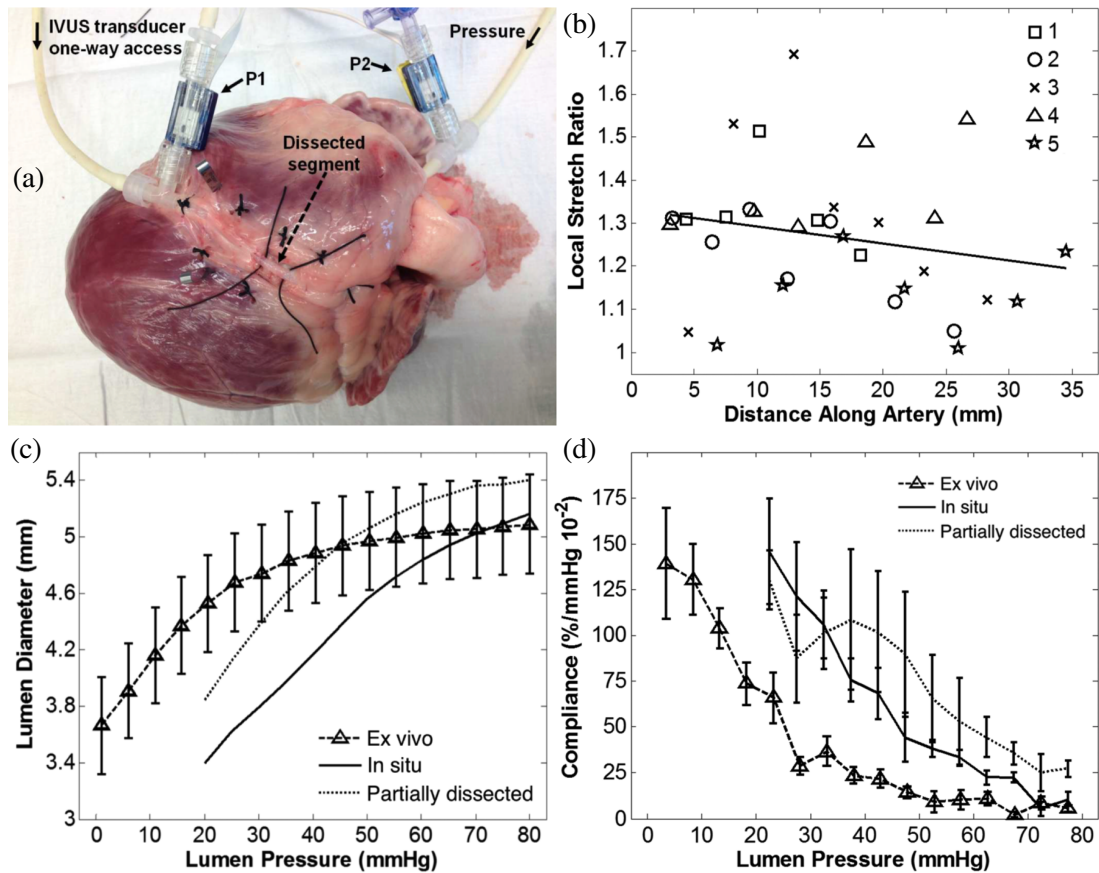


Figure 1.4 Extracts of the study from Wang *et al.* [104]: (a) portion of the experimental setup for measuring the pressure-diameter and longitudinal stretch response of coronary arteries *in situ*. Two pressure transducers, P1 and P2, are cannulated and secured between the coronary artery segment of interest. Pressure is provided by a syringe pump (not shown). An intravascular ultrasound (IVUS) transducer for luminal diameter measurement is delivered into the arterial lumen through a one-way port (not shown) and rests in the middle of the dissected segment. A series of ligatures and vascular clips are used to stop outflow from peripheral branches; (b) local longitudinal stretch ratios along the length of the LAD (sample number $n = 5$); (c) pressure-diameter response in the *ex vivo*, *in situ*, and partially dissected (without perivascular support) configuration; (d) compliance-pressure response in the *ex vivo*, *in situ*, and partially dissected configuration. Reprinted with permission from ASME.

deformability of elastic fibers promote the stability of the arterial wall at low pressure levels. Whereas the much stiffer collagen fibers remain wavy and do not resist against loading [61]. At higher pressure levels, and especially in the supraphysiological range, collagen fibers take over, straighten, and bare most of the load [54, 74, 111]. This leads to sudden stiffening in the stress-strain response. The investigation of the layer-specific material response of adult human coronary arteries reveals that the adventitia exhibit significant stiffness in the supraphysiological domain [59] (see Figures 1.5(a) and (c)). The media turned out to be the softest layers (see Figures 1.5(b) and (d)). Especially, the adventitia stiffens remarkably at high-pressure domains and fulfills the role of a protective cover that prevents the artery from overstretching and rupture.

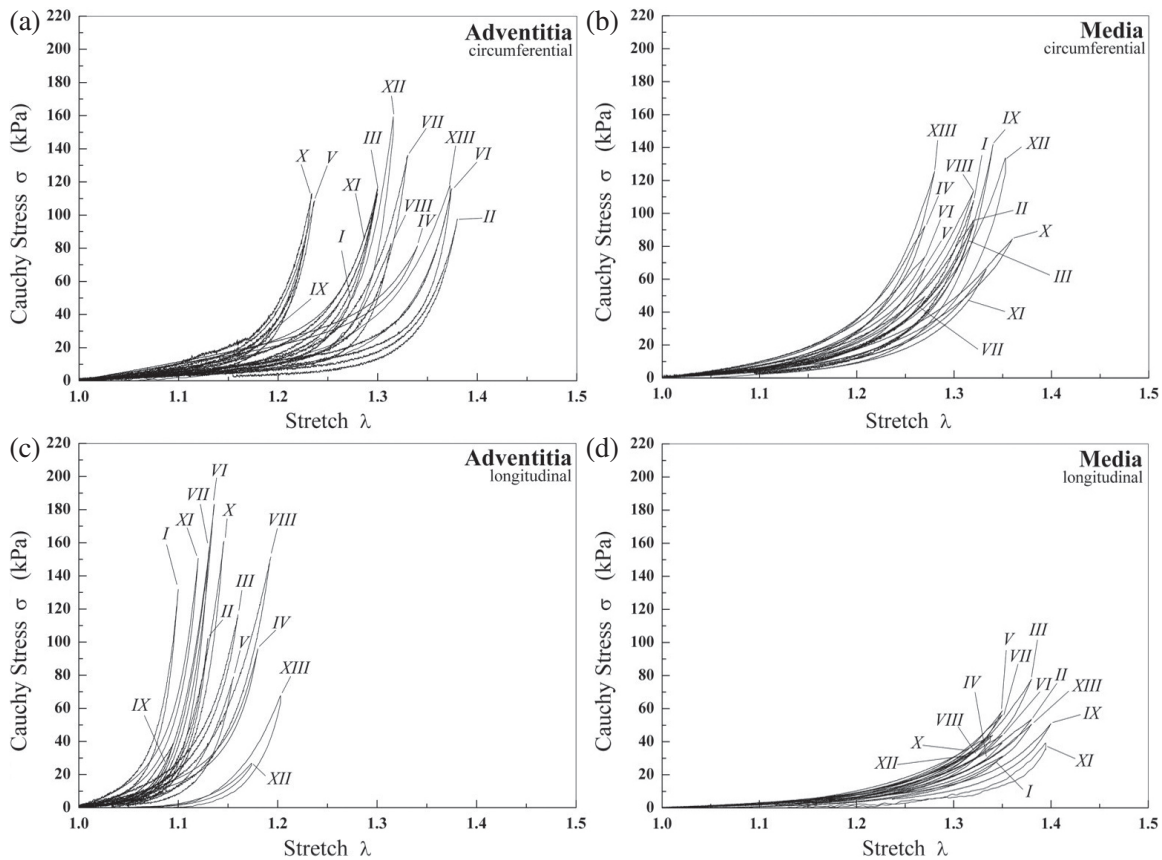


Figure 1.5 Uniaxial tensile stress-stretch response of adult coronary media samples *I-XIII* and adventitia samples *I-XIII* from Holzapfel *et al.* [59]: (a),(b) in the circumferential and (c),(d) the longitudinal direction. Reprinted with permission from Elsevier.

Coronary arteries under tension render a highly anisotropic mechanical behavior due to the directional alignment of VSMC and fibers inside the ECM. The adult human intima shows the tendency to be stiffer in the longitudinal direction [59, 112]. In the media collagen and elastic fibers tend to align in the circumferential direction, resulting in softer material response in a longitudinal direction. Huo *et al.* [41, 109] observed that VSMC contraction of the media additionally provokes a significant increase in the longitudinal stresses and a decrease in the outer diameter. Due to a counter alignment of ECM fibers, a comparatively greater longitudinal stress is induced in the adventitia [59, 72].

Materials that are both, solid and fluid-like, and pronounce a stress-strain relationship that is rate-dependent, are considered as viscoelastic materials [113]. Coronary arteries also belong to the group of materials [59, 114–117]. Viscoelasticity can be quantified by storage and loss moduli that describe the ability to store and dissipate energy [118]. Thus, under quasi-static tensile testing conditions, stress-strain curves show small hysteresis loops during cyclic loading [59] (see Figure 1.5). The viscoelasticity of porcine LAD under dynamic loading conditions was analyzed by Burton *et al.* [117]. Their results demonstrate that the storage modulus increases at higher loading frequencies. Furthermore, the storage

modulus was much higher than the loss modulus. The reason for viscoelasticity could be friction-related effects and local fluid exchanges inside the ECM.

It is important to note that the described mechanical and structural properties might change with age. These age-related changes are either of physiological nature or of pathological cause. For more information about mechanical and structural alterations in aged coronary arteries, the author refers to the review article of Chen *et al.* [61].

1.3 Coronary Artery Disease

The following is a brief overview of coronary artery disease and its underlying pathological mechanisms. Cardiovascular diseases (CVD) denote the group of disorders of the heart and blood vessels. They were the primary cause for death in 2017, resulting in an estimated 17.8 million fatalities worldwide, of which approximately three quarters were in low- and middle-income countries [119]. CVD include coronary heart, cerebrovascular, peripheral arterial, rheumatic heart, and congenital heart diseases, as well as deep vein thrombosis and pulmonary embolism. According to the American Heart Association (AHA), coronary artery diseases (CAD) held the largest share on fatalities in CVD (43.8%) in the United States in 2018, followed by stroke (16.8%), high blood pressure (9.4%), heart failure (9.0%), diseases of the arteries (3.1%), and other cardiovascular diseases (17.9%) [120]. CAD can manifest by acute and chronic coronary syndrome, myocardial infarction, silent myocardial ischemia, or sudden cardiac death [121, 122]. Typical risk factors are particularly obesity, diabetes mellitus, hyperlipidemia, hypertension, high cholesterol, homocystinuria, hyperuricemia, stress, and tobacco use [123]. The development of CAD is a complex pathological process with a not fully understood etiology. In general, CAD can be grouped into diseases with either atherosclerotic or non-atherosclerotic pathogenesis. Examples for non-atherosclerotic CAD are coronary fistula, dissection, and vasculitis [25].

1.3.1 Endothelial dysfunction

Early experiments of Minick *et al.* [126, 127] showed that the absence of endothelium provokes pathological lipid accumulation. The results also reveal more considerable intimal thickening in areas with regenerated endothelium in comparison to regions with complete endothelial denudation. Therefore, endothelial dysfunction appears to be the causative process of atherosclerosis in coronary arteries. Recently, Mundi *et al.* [125] published a review article about structures involved in endothelial dysfunction. At first, they mention **glycocalyx**, a thick layer of glycoproteins, proteoglycans, and hyaluronan (glycosaminoglycan) lining the luminal side of the endothelial monolayer. Glycocalyx enables anionic and protein molecules to access the endothelial membrane bilayer. It is screening the molecules according to their size, charge, and structure and allows water and electrolytes to pass freely [128]. Thus, the glycocalyx is important for the regulation of low-density lipoprotein (LDL) diffusion. LDL are spheroidal complexes in the blood. They transport lipids coming from the liver to cells in the extrahepatic tissue. In a healthy state, it contains 22%

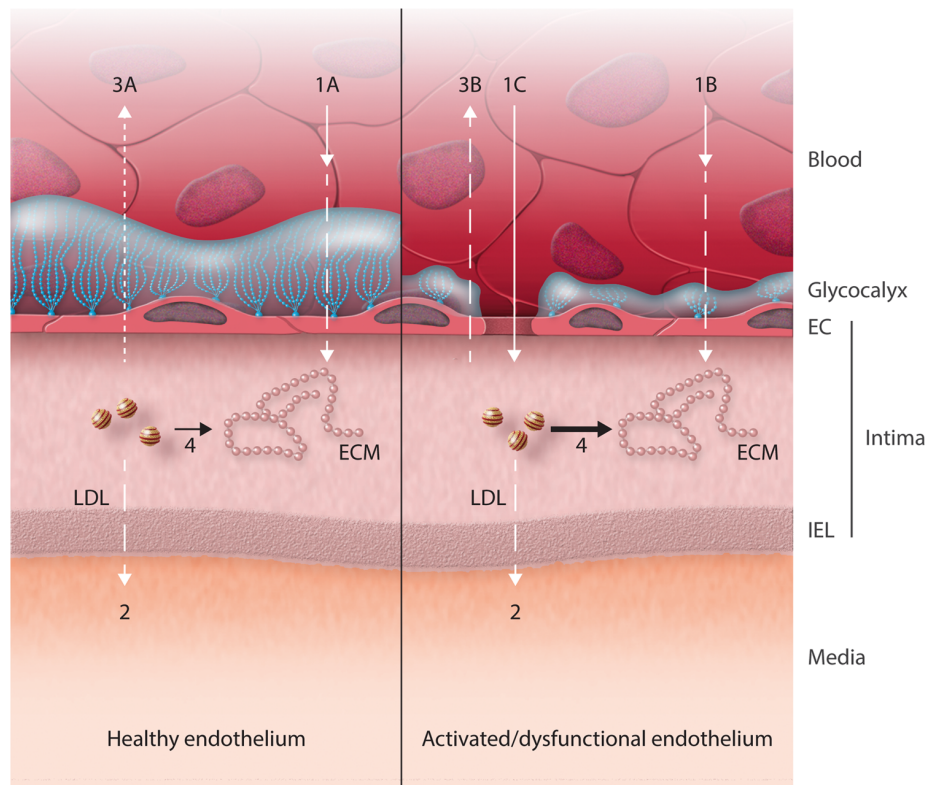


Figure 1.6 Mechanisms inside the glycocalyx layer in endothelial dysfunction (adapted from [124] and illustrated by [125]): (1A) in vessels with glycocalyx layers and endothelial cells (EC) (1B) entering low-density lipoproteins (LDL) in the arterial intima are determined by (1B) endothelial vesicles and (1C) open endothelial junctions; (2) LDL passes the internal elastic lamina (IEL); (3A),(3B) backward diffusion occurs, however, LDL can be trapped by binding to the extracellular matrix (ECM). Reprinted with permission from Oxford Academic.

of its only protein component, apolipoprotein B-100 (apoB-100), and fat molecules, to be more specific 22% phospholipids, 8% cholesterol, 42% cholesteryl esters, and 6% triglycerides [129]. Although the underlying mechanisms are still under investigation, a reduction of the glycocalyx leads to exposure of the endothelial layer and, thus, to the release of endothelial receptors, followed by accumulation of LDL [130–132] (see Figure 1.6). Studies on different animal arteries, including coronary arteries of pigeons, show that the thickness of the glycocalyx layer is significantly reduced in plaque and atherosclerotic regions [133–135]. Mundi *et al.* [125] assume that the glycocalyx reduction in these diseased regions might be the result of a discontinuous production of proteoglycans in the absence of direct exposure to laminar blood flow. Also, an excessive generation of highly reactive oxygen species (ROS), inflammatory activation of the endothelium, and the presence of oxidated LDL could be a reason [136, 137]. Furthermore, turbulent or disturbed flow leads to the shedding of proteoglycans by downregulating tissue inhibitor metalloproteinases (TIMP3) [138].

The second structural group are **caveolae**, cup-shaped pits in the plasma membrane of

the endothelium [139]. Under normal conditions, LDL complexes with diameters of 20–30 nm cannot pass endothelial junctions of 3–6 nm [125]. However, open caveolae and clathrin-coated vesicles can bind LDL via scavenger receptors [140]. Known receptors are scavenger receptor class B member 1 (SBR1) and activin receptor-like kinase 1 receptors [141]. The overall terminus for this process is endothelial transcytosis [142]. A pathological configuration induced by the common risk factors of CAD is characterized by a hyperactive endothelial transcytosis. The general mechanism known in the literature for this process is the silencing of the protein caveolin-1 (Cav-1), the major component of the caveolae plasma membrane, and an increased endothelial vascular cell adhesion molecule (VCAM)-1 expression. Low-density lipoprotein receptor (LDLR) and SBR1 can also cause an increased endothelial transcytosis, which underlines the importance of LDL and cholesterol presence for an increased endothelial permeability [143].

The third structure involved is **cell–cell junctions** of the endothelial cells, more specific tight junctions (TJ), adherens junctions (AJ), and gap junctions (GJ). These junctions are composed of membrane proteins, bonded to the cytoskeleton, and controlled via an extensive signaling network [144]. For a better illustration see Figure 1.7. According to Alberts *et al.* [145], the different junction types can be described as follows: TJ are pathways between the apical and basolateral domains of the endothelium that regulate the diffusion of membrane proteins and lipids. They also seal neighboring cells together. Each of their sealing strands is composed of several transmembrane adhesion proteins, especially claudins, occludins, and zonula occludens. AJ form adhesion belts, which encircle the interacting endothelial cells. In every endothelial cell, actin filaments, oriented parallel to the plasma membrane, lie next to the adhesion belt. These actin filaments are attached to the membrane through the anchor proteins catenins, vinculin, and α -actinin. Thus, they hold cells together and bind them to the ECM. And finally, GJ are direct plasmatic connections assembled from connexins, a family of 21 proteins in humans [146]. So-called connexons (Cx), pore-forming complexes of six connexins, develop hexagonally arranged compounds. These Cx can diffuse laterally and dock to another connexion from a neighboring cell and, thus, forming intercellular channels for the transport of ions and small water-soluble molecules. Therefore, GJ are important in the mediation of electrical and chemical coupling of cells. The enzyme lipoprotein lipase (LPL) can hydrolyze circulating triglyceride-rich lipoproteins into remnants that might affect the proteins of AT and JT significantly and, thus, increase the endothelial permeability [147]. It was reported, that in advanced atherosclerosis, TJ open and enable plasma molecules and LDL to pass [148]. Furthermore, hypercholesterolemia and the presence of pro-inflammatory cytokines can lead to destabilization of GJ channels due to altered connexins Cx37, Cx40, Cx43, and assumably Cx45 expression [146, 149–152].

1.3.2 Atherosclerosis and its classification

In healthy coronary arteries, the endothelium, as natural barrier, regulates the LDL uptake (see Figure 1.8(a)). In disease, LDL freely pass the dysfunctional endothelium, deposit in

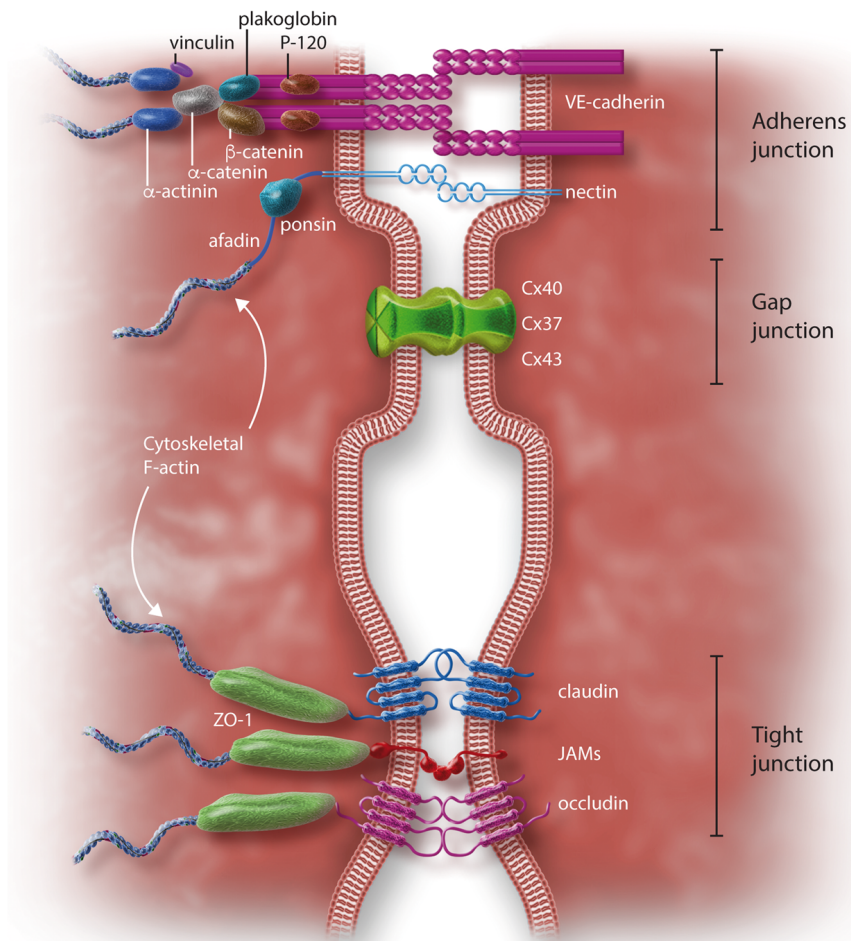


Figure 1.7 Proteins involved and mechanisms of the endothelial junctions summarized by Mundi *et al.* [125]: adherens junctions (AJ) are composed of cadherin-catenin and nectin-afadin complexes. Vascular endothelial (VE) cadherin binds to β -catenin, plakoglobin, and p120. β -Catenin and plakoglobin again bind to α -catenin, a filamentous (F) actin-binding protein, the primary link between the AJ and the actin cytoskeleton. α -Catenin can bind vinculin and α -actinin, stabilizing the anchorage to F-actin microfilaments. When α -catenin is stretched (upon tension on the junctions), a latent vinculin binding site becomes available and initiates a second interaction of the cadherin-catenin complex with the F-actin cytoskeleton. Nectin links to afadin, which in turn establish bonds with ponsin, connecting nectin to the F-actin cytoskeleton; Tight junctions (TJ) are complexes of occludin, claudin, junctional adhesion molecules (JAM), and intracellular components, such as ZO-1; Gap junctions (GJ) are in general composed by the connexins Cx37, Cx40, and Cx43. Reprinted with permission from Oxford Academic.

the intimal layer, undergo oxidation, and transforms into oxidized LDL (ox-LDL). Oxidation is a chemical chain reaction of loss of electrons that is usually inhibited by naturally occurring antioxidant agents [153]. The process is regulated by several metabolic products, endothelial cells, VSMC, monocytes, macrophages, etc., and is believed to take place in the absence of endogenous antioxidants and under oxidative stress (overproduction of free highly reactive radicals, i.e., ROS). Ox-LDL induces endothelial cells to express inflammatory mediators and adhesion molecules [154]. Blood-borne monocytes attach to the

individual endothelial cells, diffuse through the endothelial junctions, and immigrate into the subendothelial layer [155] (see Figure 1.8(b)). Once monocytes become resident to the subendothelial layer, they differentiate into macrophages affected by macrophage-colony stimulating factors [156, 157]. These macrophages express cell surface receptors, or to be more specific, scavenger receptors (reviewed in [158]), which attract unmodified LDL as well as ox-LDL. These lipids accumulate within the cytoplasm of macrophages [159]. Now, as the oxidation of LDL amplifies itself, a chain reaction starts and more and more lipids get accumulated. This moment is the birth of so-called lipid-laden macrophages or foam cells. These foam cells secrete cell recruiting proteins, namely cytokines [160, 160], which again attract cycling leukocytes such as lymphocytes, mast cells, and T cells [122]. Thus, plaque, also called atheroma, starts to develop (see Figure 1.8(c)). Furthermore, cytokines recruit VSMC in the intima as well as the atheroma. These VSMC are from a synthetic phenotype and produce collagen, proteoglycans, and elastin. This neo-ECM forms a fibrous cap around the atheroma [161]. Platelet-derived growth factors (PDGF), which are stored primarily by platelets but also other cells, including endothelium and VSMC, cause VSMC to proliferate inside the atheroma [162]. Eventually, a lipid pool grows within the intima, which is promoted by the apoptosis of foam cells and necrosis at the edge of the core [163] (see Figure 1.8(d)). Finally, lipid and cell debris accumulate to a lipid-rich pool [122].

In the progression of the lesion, calcification is also an important mechanism. Here, an initial process is micro-calcification, potentially initiated by mineralization-competent matrix vesicles (MV) secreted by VSMC [165, 166]. MV are small membrane-bound bodies nucleating the mineral hydroxyapatite that crystallizes. Micro-calcifications originate from the deeper regions of the lipid core, extend into the surrounding collagenous matrix, and finally form calcified sheets or plates [167]. Calcification can also occur as a spotty pattern in more extensive and diffuse atherosclerosis [168, 169]. These spotty calcifications are assumed to intensify stresses in the circumferential direction and to cause plaque rupture [170–172]. Smaller calcium deposits continue to form and grow to extensive calcifications. As a hallmark of atherosclerosis, these investigations are still of high interest. The topic was recently reviewed by Shioi and Ikari [173] and by Shi *et al.* [174].

A well-established classification scheme for atherosclerotic lesions based on pathological studies was developed by Stary *et al.* [175–177] and recommended by the AHA Committee on Vascular Lesions. In their review, Virmani *et al.* [178] focused on vulnerable plaques, i.e., plaque susceptible to rupture [179]. Accordingly, they modified the classification scheme of the AHA by considering events like erosion, rupture, thinning of the fibrous cap, and development of pro coagulation and thrombotic environment. After reviewing the new data, an updated classification scheme was adopted by the AHA [180, 181]. The updated classification scheme includes eight types of atherosclerotic lesion numbered with Roman numerals. According to the summary of Akyildiz *et al.* [182], the severity of atherosclerosis describes a range starting with early lesions of small accumulations of foam cells (type I), multiple foam cells (type II), and by the formation of pre-atheroma (type III). Inside the pre-atheroma, extracellular lipids are already present in the intima,

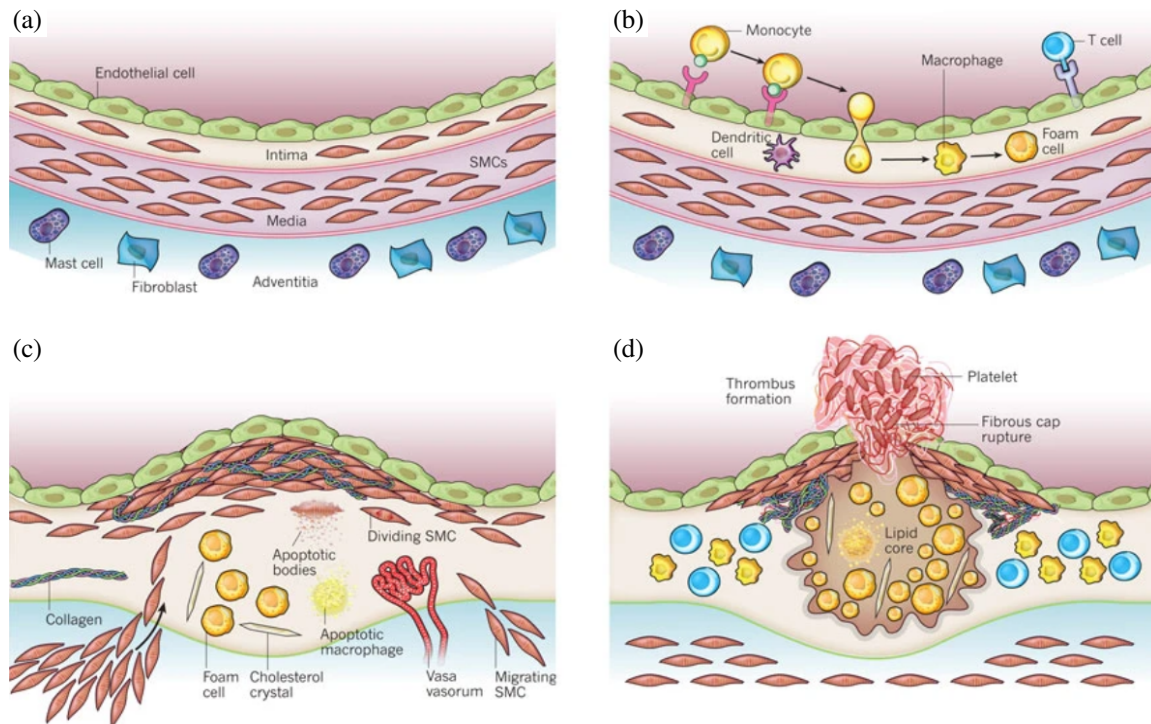


Figure 1.8 Pathogenesis of atherosclerosis [164]: (a) In a healthy coronary artery, the intima is lined by a monolayer of endothelial cells, which cover the subendothelial layer. On the micro-level, the media contains VSMC embedded in an ECM of collagen and elastin. In the adventitia, resident macrophages, fibroblasts, and mast cells are present; (b) early atherosclerosis include the adhesion of blood-cycling leukocytes to the endothelium, leukocyte migration, and maturation of monocytes into macrophages with sequential uptake of oxidized LDL, yielding foam cell formation; (c) an atheroma starts to develop due to intimal VSMC migration and proliferation as well as ECM synthesis. Extracellular lipids from apoptotic cells accumulate, forming a necrotic core. Advanced lesions contain cholesterol crystals; (d) a lipid core with a fibrous cap has developed. After rupture, blood coagulation components come into contact with tissue factors, and a thrombus starts to form. Reprinted with permission from Nature.

located between migrated VSMC. The migrated VSMC cause additionally intimal hyperplasia with decreasing arterial lumen. However, in the stage of pre-atheroma formation, the media and the adventitia remain unaffected in the development of early lesions. The first clinical important lesion (type IV) comprises atheroma formation by the presence of a lipid core. These lesions might already cause significant narrowing of the arterial lumen, i.e., stenosis formation. They are usually not visible to conventional imaging and screening techniques and remain clinically silent [181]. Fibro-atheroma lesions (type V) increasingly pronounce fibrous tissue, while ruptured lesions (type VI) include surface defects or intra-plaque bleeding. In calcified lesions (type VII), the intima contains extensive calcifications with lipid depositions. And finally, in fibrotic lesions (type VIII), no more lipid core is present, but large amounts of fibrous tissue.

1.3.3 Coronary syndromes

Angina pectoris or simply ‘angina’ is a type of thoracic or retrosternal pain, which may radiate to the left of both arms, jaws, or back [183]. In general, angina results from under-supply of the myocardium, either through obstructive stabilized plaque, also known as stenosis, by plaque rupture, or by a combination of both. **Chronic coronary syndrome (CCS)** is a new terminus for patients with stable angina. CCS is, by definition ‘stable’ if angina episodes last for more than three to six months [184, 185]. The cause for CCS is a progressive growth of atheroma.

Atheromas may rupture due to vasospasm-induced or hemodynamic shear stresses, circumferential stress concentrations in the plaque cap – in particular at the plaque shoulders – or smaller transmural pressures in the stenosis [186–190]. During rupture, receptor-driven platelets attach onto the exposed subendothelial layer followed by further recruitment, activation, and stabilization of additional platelets [191–194]. Finally, a superimposed thrombus develops (see Figure 1.8(d)), which may critically reduce the blood flow on-site or in distal arteries after separation. This sudden event is called unstable angina or **acute coronary syndrome (ACS)**. ACS with total coronary occlusion may cause reduced contractility of the myocardium within seconds [195] followed by myocardial cell death or ST-elevation myocardial infarction (STEMI). ‘ST’ in STEMI denotes the ST segment of sinus rhythm. Non-occluding thrombi may result in non-ST-elevation myocardial infarction (NSTEMI).

1.3.4 Mechanical behavior in disease

While the investigation of the atherosclerotic pathogenesis in coronary arteries and resulting structural changes has been the focus of numerous biological motivated studies, the characterization of the mechanical behavior of sclerotic coronary arteries still ventures into uncharted terrain. In general, atherosclerosis involves two mechanisms of vascular alterations, which are essential for the mechanical behavior of diseased coronary arteries – namely arterial thickening and mechanical stiffening [196]. However, in experimental investigations, it is difficult to distinguish whether the mechanical behavior is based on age- or atherosclerosis-based alterations. Hence, the following will provide a short overview of the main mechanisms of both cases.

Through an early investigation in 1985 published by Velican and Velican [197], it was found that aged-based coronary intimal thickening refers to several arterial processes triggered by physiological and pathological stimuli. Their results also confirm their previous findings [198, 199], which state that intimal thickening is sex- and position-dependent. Furthermore, the mean intimal thickenings in 932 subjects were found to be three times as much as the ones in the media [197]. Age-dependent thickening of coronary arteries was also observed in the comprehensive study of Ozolanta *et al.* [200]. They documented that the mean wall thickness, as well as the outer diameter gradually increases with age. These results are consistent with the findings of Holzapfel *et al.* [59], who detected significant intimal thickening in aged coronary arteries. However, it was also reported that the wall-

thickening process is non-uniform in proximal and distal parts of human LAD and LCx [200]. And, finally, Ozolanta *et al.* [200] observed a decreasing vascular deformability in the circumferential direction and, therefore, an increase of wall rigidity at a higher age.

Mechanical properties of coronary arteries can be quantified *in vitro* with uni- or multi-axial rheology, tensile, and expansion tests. Jankowska *et al.* classified atherosclerotic tissue into three stages, i.e., (i) thickening of the artery, (ii) visible plaque, and (iii) large plaque [201]. After performing uniaxial tensile testing, the mechanical response exposes pathological changes, in particular severe stiffening of the vascular wall. The highest values of the stiffness coefficients were obtained for tissues of stage (iii). In addition, their experimental data show that tissue of diseased coronary arteries continues to pronounce anisotropic behavior in every stage.

In vitro experimental data of aged and atherosclerotic human coronary arteries are hardly available, as these arteries are difficult to test due to tiny sample sizes. Therefore, several studies focused on *in vivo* approaches. Minimally invasive intravascular ultrasound (IVUS) is a standard low-sensitivity imaging technique to visualize cross-sections of coronary walls. With the help of intravascular ultrasound catheters and the echogenicity of acoustic waves, this technique can provide dimensions of healthy and atherosclerotic parts of arteries in real-time [202]. For some time, a combination of IVUS and elastography is used to produce elastograms at different intraluminal pressures. Elastography allows the determination of local strains by quasi-statically or dynamically deforming tissue and measuring displacements between the reference and deformed configuration [203]. Using IVUS elastography, different strain values between fibrous, fibro-fatty, and fatty plaques could be detected [204]. In 2002, Korte *et al.* [205] reported significant lower strain values in calcified tissue in comparison to healthy tissue. In general, higher shear strains were found in diseased tissue with maximum amplitudes at the plaque shoulders [190, 206]. Furthermore, heterogeneous plaque morphology was associated with higher shear strains and thicker lipid pools, while fibrous plaques resulted in lower strains. For a representative example of IVUS derived displacement fields see Figure 1.9. The echograms show fibrous plaque from 4 to 7 o'clock, while the rest of the cross-section is fibrofatty plaque.

1.3.5 Clinical evaluation, diagnosis, classification, and treatments

Before the actual diagnosis test, patient evaluation starts with a pre-test. In general, this pre-test includes a patient interview, also known as anamnesis, that clarifies the underlying health conditions, prior test results, risk factors, characteristics of angina, possible organizational and operative procedures, and potential risks [122]. Furthermore, the patient is assigned to CAD probability categories according to country-specific guidelines, e.g., the Diamond and Forrester Chest Pain Prediction Rule, the Goldman Reilley criteria, the Morise Score, Thrombolysis in Myocardial Infarction (TIMI) risk score, or lately the 2012 ACCF/AHA guideline [207–211]. This step is followed by a physical examination, including the observation of symptoms, resting electrocardiography (ECG), and the quantification of pulse, oximetry, blood pressure, as well as biomarkers (troponin, sodium,

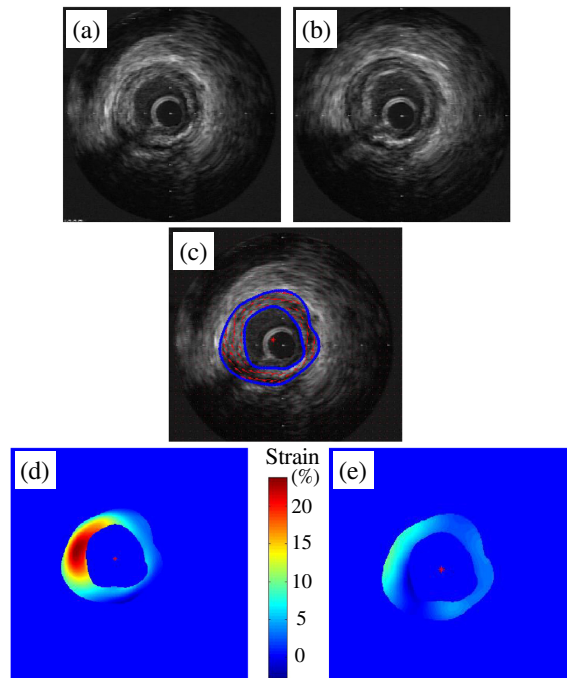


Figure 1.9 Intravascular ultrasound investigation of a diseased LAD [190]: image (a) shows the LAD site at diastole and (b) at systole; (c) displacement field between the segmented lumen boundary and media-adventitia interface (blue curves); (d) radial strain inside the arterial wall; (e) circumferential strain. Reprinted with permission from Elsevier.

creatinine, etc.).

Based on the pre-test, clinicians choose diagnostic tests for further examinations. However, they must decide whether non-invasive (not entering the body) or invasive diagnostic tests (cutting and entering the body) should be performed. Following the 2012 ACCF/AHA guidelines, patients at low pre-test risk should undergo non-invasive testing [211, 212]. At intermediate risk, patients could also be tested with non-invasive methods combined with treatments adapted to symptoms and risk factors. Finally, at high risk, non-invasive tests are usually bypassed and invasive tests preferred. The first group of non-invasive tests includes anatomical investigations such as coronary computed tomography angiography (CCTA), as well as coronary artery calcium (CAC) scoring. The second group comprises functional investigations like exercise ECG, stress echocardiography, positron emission tomography (PET), single-photon emission computed tomography (SPECT), as well as cardiac magnetic resonance (CMR) imaging [213]. In invasive tests, catheter-based X-ray coronary angiography, in short, ‘invasive coronary angiography’ (ICA) has established as a standard diagnostic test. It is the most utilized method to assess CAD and considered as gold-standard. ICA can be combined with IVUS as well as fraction flow reserve (FFR), and more recently with optical coherence tomography (OCT) imaging. As ICA and PCI are usually performed within one clinical session one after another, both procedures will be described in more detail in *Section 1.4*.

The choice of the ideal treatment of the tested patient depends on the diagnosis, but also on costs, availability, as well as skills of the clinician. Treatments for CAD are subdivided into the categories of medical therapy and revascularization. Typical medical therapies include the administration of drugs, like antiplatelets (mostly acetylsalicylic acid (ASA) and clopidogrel), statins (mostly atorvastatin, fluvastatin, lovastatin, pravastatin, and simvastatin), beta-blockers (bisoprolol and metoprolol), as well as ACE inhibitors and angiotensin II antagonists [214, 215]. However, medical therapies also involve the treatment of secondary conditions as diabetes and hypertension [212]. Revascularization includes two main techniques, namely, PCI and coronary artery bypass graft (CABG) surgery. PCI describes a minimally invasive surgical technique that aims to restore the original diameter of a stenotic or blocked coronary artery. For this purpose, a balloon catheter is deployed and inflated at the narrowed part of the affected artery, and, if necessary, a stent implanted. Other PCI-based approaches include high-pressure and super-high pressure non-compliant, cutting/scoring/cryoplasty, atherectomy, excimer lasers, and lately intravascular lithotripsy (IVL) balloon catheters [216, 217]. CABG is an extensive surgical technique that denotes the bypassing of diseased coronary arteries with grafted arteries or veins.

In the case of finding an ideal treatment for CAD, decision-making is a complex and often over-straining process with severe consequences for patients. While medical therapy seems to be the cornerstone for CCS, specific guidelines can help to assess the need for revascularization. An international widely used and by the AHA recommended grading system for the complexity of CAD is based on the SYNTAX I, II, and III trials [218–220]. After the examination of the clinical picture, this grading system aims to define a SYNTAX score, which is based on the complexity of the prevailing CAD. Despite this decision-making aid, there is a controversial discussion about whether and when PCI should be preferred over CABG. Katritsis *et al.* recently summarized in their review article factors for the correct choice between PCI and CABG [221]. Hence, CABG should be favored for multiple vessel disease (especially for three-vessel disease), left ventricular dysfunction, left main coronary artery disease, chronic total occlusion of major vessels, and diffuse diseases. However, PCI shows better outcomes for one- or two-vessel disease as well as for patients in advanced age, with preserved left ventricular function, suitable anatomy, and comorbidities. A detailed overview of recent trials and outcomes is given in references [221–223].

1.4 Percutaneous Coronary Intervention

PCI, formerly known as balloon angioplasty or percutaneous transluminal coronary angioplasty (PTCA) with stenting, remains the prevailing technique for revascularization in the USA. According to the 2020 update of the Heart Disease and Stroke Statistics of the AHA, 480,000 PCI and 371,000 CABG surgeries were counted in 2014 [224]. In Austria, 2,559 PCI per million people were carried out in 2014 [225] and 2,777 PCI per million people in 2017 [226], which represents a significant increase of 8.87%. In 1977, Grüntzig performed the first PTCA on an awake patient by dilating a stenotic LAD with a balloon catheter

[227]. To overcome vascular recoil and restenosis formation, a structure was needed that can provide intravascular support. Therefore, for the first time, a self-expanding, stainless steel wire mesh was implanted in a human coronary artery by Sigwart *et al.* [228] in 1986. These implantable wire-meshes or strut-structures became simply known as ‘stents’, as similar structures for other medical applications were already denoted as such. In 1987, the first balloon-expandable stent with FDA-approval, the Palmaz-Schatz[®] stent, was launched [229]. Since then, PCI with stenting developed through much progress in the catheter, stent, and manufacturing technologies. However, the general working principle of classic PCI remains the same.

1.4.1 Intra-operative procedures

When ICA reveals disease pattern that confirms the need for immediate minimally invasive revascularization, ICA and PCI are usually performed sequentially, as both techniques are catheter-based. Before every standard ICA and PCI, the patient receives situation-dependent medication. Typical drugs are dual antiplatelet therapy with aspirin, clopidogrel, prasugrel, or ticagrelor, to prevent thrombosis. In addition, hydration can be ensured with isotonic saline infusions. As the last step before PCI, the patient must be checked by an anesthesiologist for former contrast medium allergy, chronic kidney disease, and diabetes [230]. Inside the cardiac catheterization laboratory, the patient lies on an adjustable table. For radiological imaging during ICA and PCI, the region of interest is most commonly centered inside a C-arm system. A C-arm system is made of an X-ray source and detector attached to a gimbal-mounted C-shaped frame and provides real-time X-ray imaging. Orbital and angular movements of the C-arm system enable both 2D and 3D images [231]. Monoplane devices provide one image, while biplane devices can manage to display two spatial planes in real-time simultaneously. Thus, the biplane technology might reduce complications, radiation exposure, and procedure time [232].

The initial step of primary ICA and PCI with stenting is the puncture of either the femoral, radial or brachial artery. At first, adequate conscious sedation of the patient and a local anesthetic of the skin and the subcutaneous tissue at the puncture site must be ensured. For puncture, different techniques and needle systems are known [233]. In general, front wall puncture is performed by piercing a cannulation or micropuncture needle into the anterior wall of the artery until a pulsating blood flow starts to leak. After needle placement, angiography of the femoral artery can be performed to check for correct puncture and possible calcification. Here, contrast agents might be injected with a syringe. Contrast agents are iodine and barium based solutions, which enhance the contrast between lumen and tissue. Next, a guidewire with an atraumatic j-shaped tip is inserted, followed by the removal of the needle. Guidewires are small-caliber (0.25–0.50 mm) steerable wires with radio-opaque coating. After the needle is removed, a vascular introducer set is pushed along the guidewire into the artery. An introducer set contains a sheath and a tapered dilator. The internal dilator aims to guide the sheath through the entry into the artery. After the dilator and the guidewire are removed, the port of the sheath gets flushed with a

physiologic saline solution and sealed. The port diameter is usually given in French (1 F or 1 Fr = 0.333 mm) and ranges between 4–7 Fr for ICA and 5–9 Fr for PTA [233].

The ideal transluminal route for ICA and PCI is a controversial discussed matter. Recently, several studies consider the transbrachial/radial (TB/TR) approach as superior with respect to mortality risk, hospital stay, patient comfort, and complications such as bleeding, hematoma formation, and ecchymosis [234–238]. Furthermore, TB/TR might be an attractive alternative in the presence of femoral stenosis, aortic dissection, and aortic aneurysms. However, TB/TR is technically challenging and very difficult to perform in patients with abnormal radial artery anatomy, small radial artery, or tortuous subclavian artery. Techniques, such as ultrasound- or infrared light-guided punctures, may facilitate TB/TR. Traditionally, the transfemoral (TF) approach has been preferred due to better accessibility and use of large size catheters.

The objective of ICA is the complete visual depiction of all coronary arteries, including the collateral circulation, i.e., bypasses and veins, and gets usually combined with cardiac ventriculography. ICA starts with the insertion of a diagnostic catheter in the size of 4–6 Fr and a length of 100–125 cm [233]. Diagnostic catheters are pipes with a non-thrombogenic, lubricious outer and inner layer. The inner layer sheaths a guidewire. The front end has an atraumatic tip and is available in different shapes depending on the target artery (left-/right judkins/amplatz, pigtail, cobra, hockey stick etc.) [239]. At the back end, a strain relief support, a wire port, and a grip are mounted. The latter allows the clinician to turn and steer the catheter inside the lumen. Once it is guided through the transluminal route and intubated into the respective coronary ostium, the diagnostic catheter is freed from its guidewire and flushed with saline solution. With a 2- or 4-way manifold, which is attached to the wire port, the diagnostic catheter can be connected to a syringe with a contrast agent and a manometer for arterial pressure monitoring. By analyzing the arterial pressure, the clinician can already deduce the type and severity of the underlying disease. However, the exact location of stenoses and thrombi can only be determined by injecting contrast agents. Finally, after the satisfactory completion of a coronary angiogram, the diagnostic catheter is removed.

When the clinician decides to proceed with revascularization performed with PCI and stent placement, a guiding catheter, together with a coronary guidewire, is inserted. Guiding catheters like diagnostic catheters have lubricious and non-thrombogenic inner and outer layers, but additionally, a middle layer made of stainless-steel mesh. The size of the guiding catheter strongly depends on the selected stent and balloon catheter and ranges between 4–9 Fr [233]. After the intubation of the guiding catheter into the coronary ostium, the guidewire is removed. This is the moment either pre-dilatation of the diseased site with a balloon catheter or direct stent implantation is performed. For pre-dilatation, a slightly smaller balloon catheter without stent is positioned at the center of the stenosis via the guiding catheter and a special coronary guidewire and subsequently inflated.

At the distal end of these catheters, a folded cylindrical balloon is attached. The proximal and distal ends of this balloon are usually labeled with X-ray markers. For stent

implantation, a stent is crimped onto the center of the balloon membrane. Two types of balloon catheters dominate the market, namely over-the-wire (OTW) and rapid exchange balloon catheters. OTW catheters are 145–155 cm long, and have two lumens, one for the guidewire and another for balloon pressurization [233]. Furthermore, these catheters have an inflation and wire port. The main advantage is a fast exchange of the guidewire. However, additional personnel is needed as the guidewires for this catheter type are usually very long (300 cm). Rapid-exchange (Rx) catheters, with a length of 150–180 cm, are the standard catheters for PCI [240]. These Rx catheters have only one continuous lumen since the wire lumen does not go through the entire catheter but only 17–40 cm at the distal end of the catheter. Thus short guidewires can be used, and sudden balloon catheter exchanges are more straightforward. Balloon membranes of both systems are available in diameters of 2–5.5 mm and in lengths of 10–40 mm. The diameter of the stent must be chosen according to the luminal diameter of the healthy part of the artery. Standard coronary stents are available for arterial diameters of 2–5.5 mm and in lengths of 8–25 mm [241]. Stents in 4.5 and 5.5 mm sizes are ideal for large vessels, such as RCA, LDA, LCx. Stent sizes of 2.0 mm are suitable for extra-small branches and tight lesions. In an optimal PCI, the stent should cover the entire length of the stenosis but must not block bifurcations.

Once placed in the center of the stenosis, the balloon catheter gets pressurized with an inflation device and expanded together with the stent. Depending on the brand and the balloon catheter size, nominal pressures of 5–15 bar are common. With increasing pressurization, the tapers of the balloon catheter start to expand. This causes the outer segments of the stent to deform first. This effect is called ‘dogboning’. When reaching the nominal pressure for the first time, the balloon pressure might decay initially due to the semi-compliant mechanical behavior of the balloon material [239]. Therefore, the clinician has to reinflate the balloon as long as the pressure stabilizes. At a certain pressure, further central stent segments, as well as the folded balloon membrane, suddenly expand and eventually touch the arterial wall. In an optimal PCI, the stent is fully expanded if all struts are in contact with the arterial wall. If the stent is not ideally expanded, over-pressurization is sometimes necessary. It is also common practice to post-dilate the stent with a second, less compliant balloon catheter that is slightly shorter as the stent [242]. With these special balloon catheters, individual stent segments that are not fully expanded can be reshaped. This step reduces the risk of stent malapposition, i.e., the lack of contact between stent struts and the arterial wall, and thrombus formation [243]. As soon as the balloon catheter is inflated, the diameter of the stent slightly decreases due to elastic recoil.

After the stent implantation, the balloon catheter, the guidewire, the guiding catheter, and the sheath are removed. There are two options to close the arterial access site: manual compression or insertion of a vascular closing device. According to several studies, modern closure devices can reduce post-operative complications like bleeding and hematoma [244–246].

1.4.2 Evolution of balloon catheters and stents

After few years of successful treatment, the use of **PCI with uncoated balloons** marked the beginning of a race between cardiology and a new enemy: The reduction of the renewed lumen of more than 50% after PCI, better known as ‘restenosis’. Restenosis is associated with PCI-induced vascular damage and correlates with the severity of the injury [5–9]. The pathogenesis of restenosis is a continual process, starting with the overstretching of the arterial wall. Excessive overstretching causes stresses and strains in the supraphysiological range. Supraphysiological loadings lead to barotrauma, laminar dissection, and subsequent recoil of the arterial wall [247]. Large-scale endothelial denudation and injuries in the intima and media lead to sudden inflammatory reactions, VSMC proliferation as well as rapid intimal migration, excessive ECM deposition, and, eventually, to neointimal hyperplasia [248–251]. The underlying biochemical mechanisms coincide with those of initial atherosclerosis but are significantly accelerated by a mechanical stimulus of greater magnitude. Thus, PCI with balloon angioplasty show very high restenosis rates of 32–55% [252, 253].

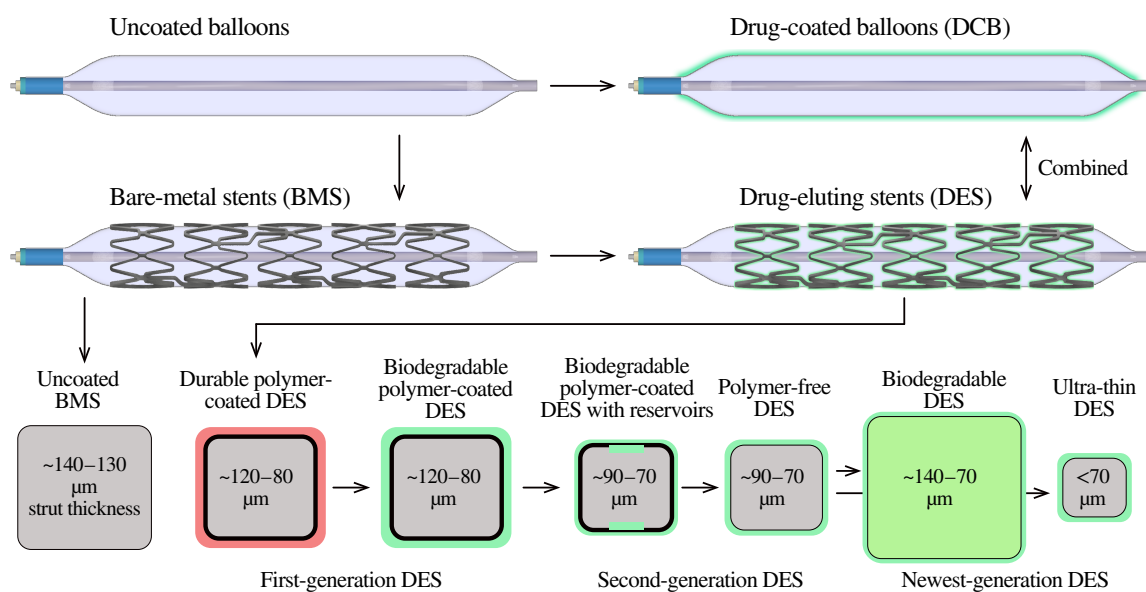


Figure 1.10 Evolution of percutaneous coronary intervention (PCI) from treatments with uncoated and drug-coated balloons (DCB) to bare-metal stent (BMS) and drug-eluting stent placements.

First PCI with stent placement incorporated non-coated stainless steel implants, so-called **bare-metal stents (BMS)** (see Figure 1.10) to prevent recoil and dissection. The use of BMS improved the restenosis rate to 17–41% [254, 255]. However, the problem of restenosis formation inside BMS, now denoted as ‘in-stent restenosis’ (ISR), remained. It was observed that ISR lead to focal lesions in 42% of all analyzed restenosis patients, in 21% lesions were found along the entire stent, in 5% the artery was occluded, and in 30% lesions developed outside the stent. During the first two month, cell proliferation and afterward accumulations of ECM contributes most to ISR formation [256]. ISR growth finds

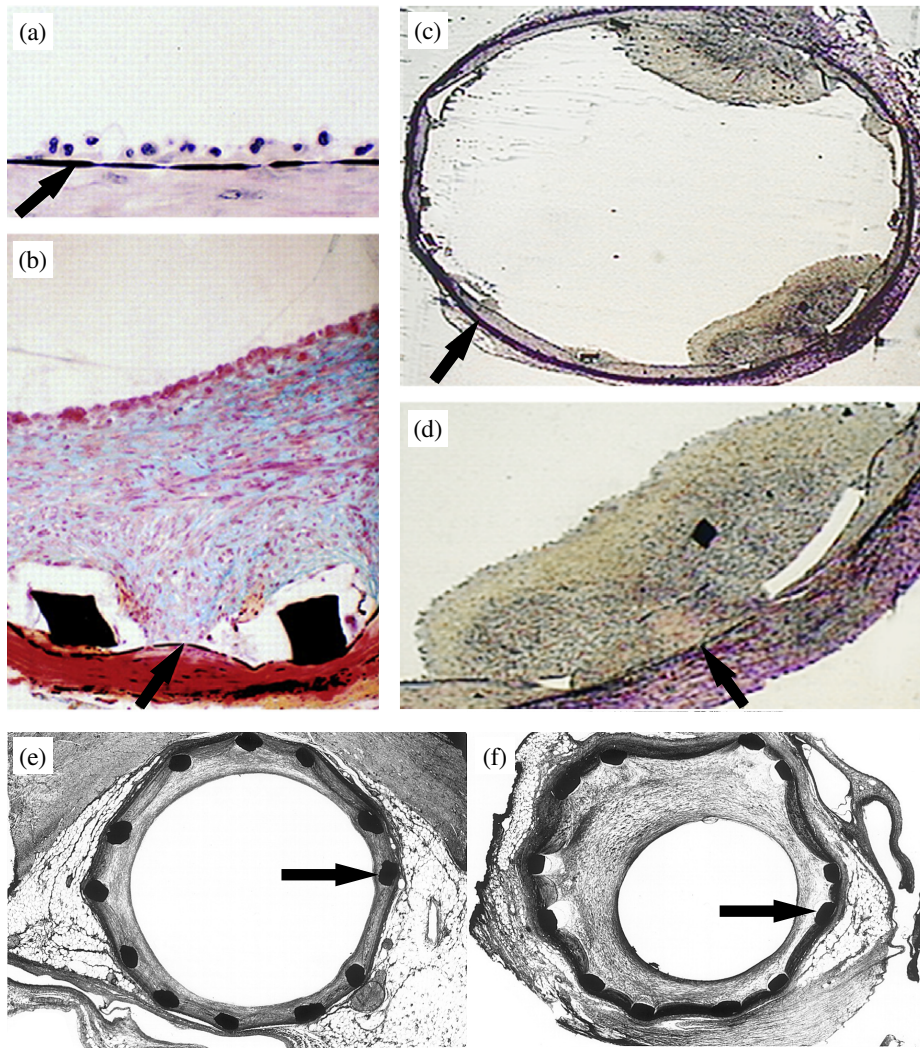


Figure 1.11 Pathological response after PCI illustrated with histological sections: (a) three days after PCI, first mononuclear cells start to attach to the internal elastic lamina (black arrow); (b) two weeks after PCI, robust neointimal hyperplasia separates the lumen from the internal elastic lamina (black arrow); (c) acute and subacute thrombi attached to the internal elastic lamina (black arrow) can be observed; (d) detailed view of a thrombus. (a)–(d) are reprinted from [247] with permission from Elsevier. The implantation of a Palmaz-Schatz stent (struts marked by black arrows) into porcine coronary arteries lead to (e) slight neointimal response if antiproliferating drugs were applied, and (f) to severe neointimal hyperplasia and ISR formation [261]. (e),(f) are reprinted with permission from AHA.

its peak after approximately six months, stabilizes after one year, and may even regress [247, 257, 258]. In addition to ISR, acute in-stent thrombosis (IST) due to fibrin, platelet, and leukocyte aggregation may develop during the first two weeks of BMS implantation [259, 260]. Figures 1.11(a)–(d) illustrate early and advanced stages of ISR and IST.

As a further evolution step, stents became drug delivery systems to impede cell proliferation and inflammation after PCI. **First generation drug-eluting stents (DES)** usually have

a polymer coating and carry pharmacologic anti-proliferative and/or anti-inflammatory agents on their surface. Depending on the agent, these drugs are either very rapidly or very slowly released to the vascular wall [262]. First-generation DES use sirolimus and paclitaxel to prevent VSMC proliferation [263]. Sirolimus deactivates the protein mTOR, which leads to the prevention of the progression of the G₁ phase of the cell cycle [264]. Paclitaxel interrupts the VSMC cycle by stabilizing microtubules, highly dynamic cellular polymers, and thereby interfere mitosis [265]. Both drugs are lipophilic, which guarantees rapid cellular uptake. With the launch of DES, the ISR rate was successfully reduced to 10% [266, 267]. Figures 1.11(e)–(f) demonstrate the impact of DES on neointimal hyperplasia. However, sirolimus and paclitaxel also retard endothelial regeneration up to 40 months after DES implantation, resulting in an increased risk of early as well as very late IST [10, 268].

For **second-generation DES** a lot of effort was put into the manufacture of chromium-based stents, but also into the improvement of polymer platforms and stent geometries. New materials enabled thinner struts with approximately 80 µm, which has been associated with a significant reduction of ISR [269, 270]. Struts with textured surfaces, reservoirs or cavities for extended drug release also brought meaningful improvements [271]. To overcome inflammatory reactions, polymer-free or bioabsorbable polymer DES were launched to the market. Polymer-free stents avoid the risk of injuries caused by polymer fragments during and after PCI. Having no or degrading polymers on stents also improves the healing process and reduces the duration of dual antiplatelet therapy [272]. In addition, zotarolimus, a derivative of sirolimus, and everolimus, a further mTOR inhibitor, replaced previous drugs. The occurrence of earlier (<6 months) and later (<1 year) IST could be reduced in comparison to BMS and the first-generation DES [273–275]. However, a very comprehensive study with more than 9000 subjects reveals that patients with second-generation DES have a significantly higher risk of very late (> 1 year) ISR and IST. According to this study by Bønaa *et al.* [4] (see Figure 1.12), there is no significant effect on the rates of death or spontaneous myocardial infarction as well as in the quality of life for patients receiving BMS or first-/second-generation DES, which was approved by the results of further groups [11, 12, 276].

Rigid metal stents, permanently eliminate physiologic vasomotion in the stented arterial segment and induce a continuous mechanical stimulus for ISR and IST [277]. To overcome this problem, new approaches are being pursued with **biodegradable stents** (BDS) made out of biopolymers or magnesium. While the idea seems to be clinically feasible, this new approach is still not very well established. The primary issue for biopolymeric BDS are bulky designs. For example, large stent struts cause flow disruption, limited distensibility, and slow degradation rates. Further issues concern inorganic degradation substances and material-related inflammatory responses [278–280]. Up until now, BES, when compared to second-generation DES, show no significant improved clinical outcome [281–283]. Nevertheless, it can be assumed that due to new manufacturing methods and improved materials, BDS will become the stents of choice in the future. In the meanwhile, a meaningful approach for reducing ISR and IST are BMS or DES with ultra-thin

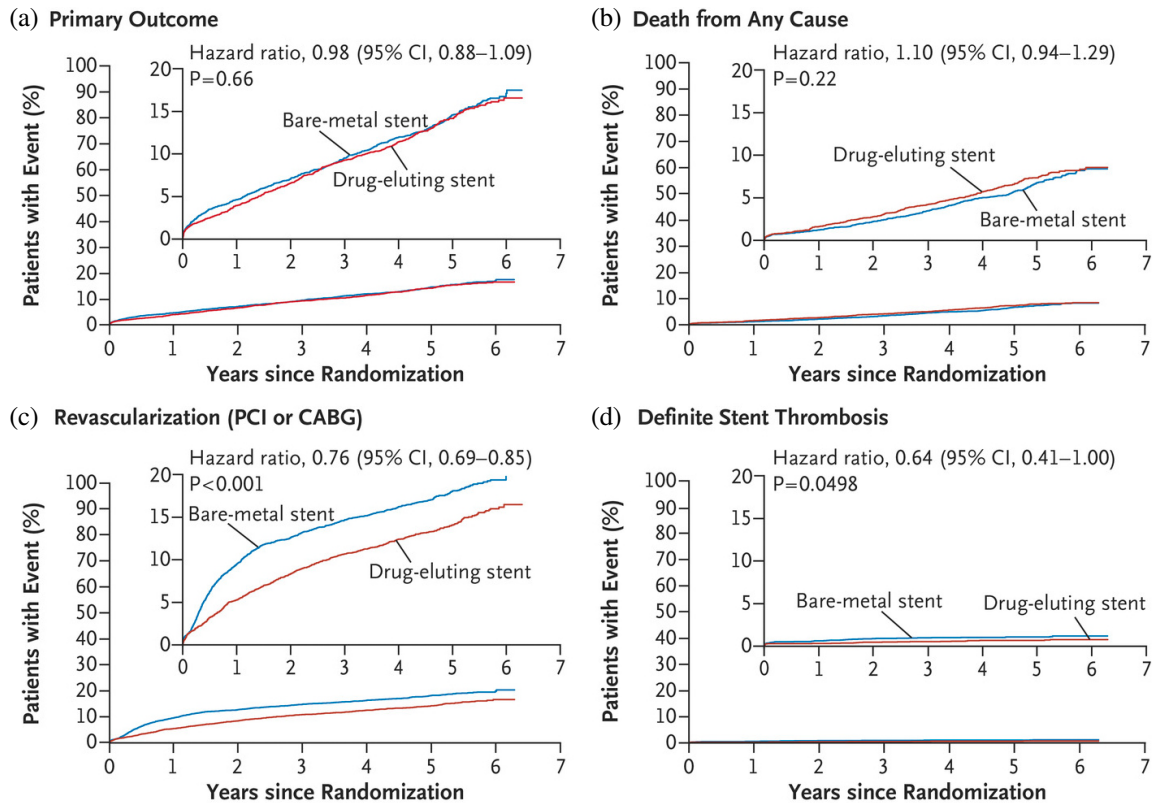


Figure 1.12 Clinical outcomes from 9013 patients comparing bare-metal stents (BMS) and second generation drug-eluting stents (DES) [4]. The diagrams show Kaplan-Meier curves for patients with (a) any coronary events, (b) fatal outcomes, (c) revascularization after PCI, and (d) with in-stent thrombosis (IST). CI = confidence interval. Reprinted with permission from Elsevier.

struts. While strut thicknesses of early-generation BMS or DES were $\sim 140\text{--}130\ \mu\text{m}$ and in newer-generations $\sim 140\text{--}80\ \mu\text{m}$, strut thicknesses of $<70\ \mu\text{m}$ have been achieved with ultra-thin stents [284–286]. With ultra-thin struts, only small lesions are created, and little endothelium is removed or covered. An increased number of stent struts also ensures a reduction in harmful stress peaks inside the tissue. However, there is a lack of robust long-term studies for ultra-thin stents as well as for BDS. In a recent review article of Jeger *et al.* [287] the latest development in PCI was discussed – the treatment with drug-coated balloons (DCB). In combination with DES placement, DCB has been established as a technique, which guarantees a homogeneous and fast transfer of antiproliferative drugs into the vessel wall. In addition, Jeger *et al.* [287] consider PCI without stenting and DCB only as a potential and robust treatment of CAD.

1.4.3 Manufacture and preoperative processes of catheters and stents

Balloon catheter membranes and stents are ideally the only components of the whole stent-delivery system that are in direct contact with the arterial wall during PCI. From a technical

point of view, inflation mechanisms are of high interest for the improvement of the clinical outcome. The mechanical behavior of balloon catheter membranes and stents, as well as their interplay, however, depend strongly on the factors material, manufacturing, and preoperative processes. These factors are briefly examined in the following paragraphs.

Membranes of coronary balloon catheters are commonly made from polyethylene (PE), polytetrafluoroethylene (PTFE), polyurethane (PUR), or polyamides (PA). Such synthetics are hydrophobic, chemically resistant, and, thanks to their high strength, enable the production of balloon membranes with very thin walls (20–30 μm). Furthermore, these materials ensure a semi-compliant material character, i.e., a limited increase of the diameter past the nominal pressure. The geometry of balloon catheter membranes consists of a long cylindrical part and two tapered shoulders. This typical shape pronounces during the manufacturing procedure of balloon-forming, a specific blow-molding technique. The main production steps, in detail described by Sauerteig and Giese [288], Garramone [289], and Fu *et al.* [290], can be summarized as follows: during extrusion, the dried granular raw material is fed into a screw-driven and heated extruder. With a shaping dye, the molten mass is extruded into tubes. While necking, chilled and cropped tubes get stretched into parisons with necked ends. And, finally, in the actual balloon forming process, the parison is inserted into a hollow glass mold and heated up to the specific glass-transition temperature while being pressurized. After the balloon-forming, the membrane is welded onto the shaft of the balloon catheter. From a mechanical point of view, the assembled balloon catheter now passes two more important procedures, which are from now on referred to as ‘preoperative processes’: in the folding process, three or more wings of the balloon are formed with curved folding blades, and during the pleating process, the balloon is wrapped around the catheter. The number of wings depends on the diameter of the balloon and the folding technique.

Balloon-expandable coronary stents are available in a wide variety of different materials. In early times, nondegradable stents were made of 316 stainless steel. Nowadays, 316 stainless steel is still used for BMS. However, the shift to cobalt-chromium and platinum-chromium alloys is nearly completed [271]. These alloys have provided better radiopacity, but above all, a higher strength, and thus, enable thinner stent struts. For fully degradable stents, magnesium, poly-L-lactide acid (PLLA), and polycaprolactone (PCL) is used. While the design of the first stents showed coil-/spiral-like or woven structures, modern stents feature sequential rings with cells [271]. Here, a distinction is made between closed-cell and open-cell design. Closed-cell stents have small cell areas between struts, whereas open-cell stents have larger gaps with bridge elements [291]. Traditional manufacturing processes for metallic stents include etching, micro-electro discharge machining (EDM), electroforming, and die-casting. However, the standard technique for metal stents is laser cutting, in which a 2D pattern is cut into a tube that turns around its longitudinal axis. However, the laser beam causes thermal damage, i.e., unwanted hardening effects, which make further thermal post-processing necessary. In addition, laser-produced stents have struts with a prism-like cross-section. This cross-section results from the laser beam, which is always focused on the longitudinal axis of the tube. Thus, during the cutting

process, the struts are tapered towards the tube center. New promising techniques for the production of metal and polymer stents such as stereolithography, selective laser sintering, fused deposition modeling, and electrospinning may overcome these problems [292]. With most of these 3D-printing techniques, complex multi-directional structures can be manufactured, including fluid dynamically optimized struts and cavities for extended drug release. Stents might also be adapted to the patient's arterial anatomy in this way. After the stent is manufactured, it needs to be crimped on the balloon catheter. In this third preoperative procedure, a smaller outer diameter can be reached to access small lumina of guiding catheter and arteries. In addition, crimping ensures a tight fit between the stent and the balloon membrane and, thus, holds the stent in position until it is expanded.

During the last years, several mechanical tests emerged, intending to observe the material properties as well as the inflation mechanisms of stents ready for PCI. Those tests include bend and torsion testing of whole stents, but also tensile testing of stent struts. Some of these tests are even mandatory for the market launch of new stents and, therefore, precisely defined in technical standards (see, e.g., ASTM F2394, F2477, F2606, F2516, and F3067). Similar standards exist for the accreditation of balloon catheters (see, e.g., ISO 10555-4). However, none of these standardized tests or research studies describe the experimental observation of the stress-strain behavior of balloon membranes under multiaxial loading. Motivated by the lack of experimental data, the study described in *Chapter 3* was carried out.

1.4.4 Computational and theoretical investigations

For manufacturers and scientists, computational investigations have been for years a useful tool for the optimization of balloon catheter and stent prototypes. However, most research efforts in this field have been pursued in the investigation of the intra-operative process of PCI, i.e., the balloon driven inflation of a stent inside a stenotic vessel. With FEA, relevant information can be gathered, such as local strain-stress distributions, inflation mechanisms, longitudinal extension/shortening, dogboning, compliance, and recoil of catheters and stents as well as balloon-stent-artery interactions, and even atherosclerotic growth. For representative literature, see, e.g., the references [293–299]. The increasing computing power provides the opportunity to implement and analyze even complex and detailed geometries without simplification. Thus, in several studies, geometries of balloon catheters membranes are often not considered at all [300–305] or modeled as simplified structures. These simplifications include rigid cylindrical shells with displacement controlled deformation [306–309], pressurized hyperelastic cylindrical shells [310, 311] or curved shells with open ends [294]. Detailed membrane geometries might be derived from imaging data, e.g., through micro-CT scans [294], and also by applying mathematical transformation techniques [312–315]. However, it is entirely unknown how preoperative processes, mentioned in *Section 1.4.3*, affect the inflation behavior of stents and balloon catheters. The magnitude of the effect of work hardening due to balloon folding and pleating, as well as stent crimping, has not yet been observed. To close this knowledge gap, the study

in Chapter 2 was carried out. Besides FEA, further computational investigations such as computational fluid dynamics (CFD) and fluid-structure interaction (FSI) have been applied to investigate and solve PCI-related problems. For a broader overview of state-of-the-art research works in these fields, the reader is referred to reference [66]. In the first preliminary efforts of this doctorate, the author tried to combine FEA with FSI to analyze the membrane diameter vs. flow rate of the expansion medium during PCI. These results are depicted in Figure 1.13 and show that balloon expansion in PCI simulations can be initiated by proximally injected expansion medium.

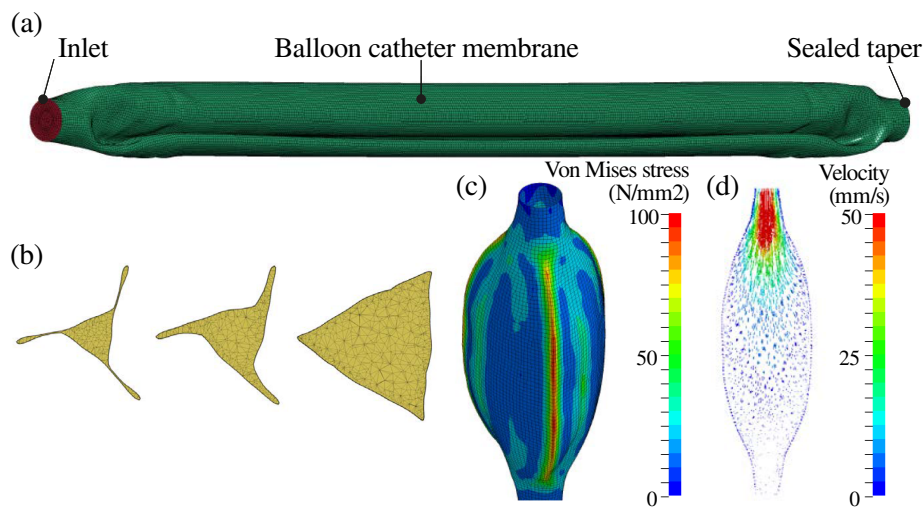


Figure 1.13 Fluid-structure interaction (FSI) of an expanding balloon catheter membrane [316]: (a) modeled and mesh balloon catheter membrane with inlet for the injection of the expansion medium; (b) cross-section of the membrane showing the adaptive remeshing of the fluid mesh during expansion; (c) von Mises stress distribution during expansion; (d) velocity pattern of the injecting expansion medium.

During the last years, computational investigations have benefited from the rapid development of more precise constitutive models for stents, arterial layers, plaque, and blood. Recent overviews, e.g., about suitable models for healthy and diseased coronary arteries has been provided in review articles by Chen and Kassab [61], Holzapfel and Ogden [317], as well as Charpenter *et al.* [66]. Latter also provides a collection of fluid models for blood. For reproducing the material behavior of metallic stents, elasto-plastic models with isotropic and kinematic hardening are frequently used [318]. For years, a wide variety of such models are implemented in commercial FEA programs (see, e.g., the references [319, 320]). Several microstructure-based constitutive models have been developed to mimic the nonlinear stress-strain behavior of passive coronary arterial tissue in health and disease [61]. These microstructural models can be divided into two groups with dissenting assumptions for cells and ground substance. The first ones assume a fluid-like ECM in which a composite of elastin and collagen is embedded [92, 321–326]. The second ones consider the arterial wall as a fiber-reinforced composite, of which the non-collagenous or non-fibrous ECM is a load-bearing solid [60, 327–329]. No matter from which group, every microstructural model relies on material and structural parameters. While material

parameters must be quantified with uni- or multiaxial tensile tests, structural parameters can be obtained by imaging analysis, e.g., fluorescence, second-harmonic generation (SHG), and diffusion tensor imaging. The determination of material and structural parameters of healthy and diseased arteries, including those of coronary arteries, has already been carried out several times (see *Sections 1.2.4* and *1.3.4*). Nonetheless, it is not known whether and how these parameters alter due to the indentations of stent struts. Hence, for the investigation of stent-induced damage mechanisms, the study described in *Chapter 4* was initiated.

Surprisingly, the implementation of precise material models for balloon catheter membranes is widely neglected. And this although the loading scenario during PCI is not only influenced by the stent and the arterial wall, but primarily by the balloon catheter. Thus, almost all state-of-the-art FEA of PCI only consider simple isotropic constitutive models for balloon membranes that are based on material parameters provided by the manufacturers of the raw materials [313, 315, 330, 331]. However, when processed, polymers usually render anisotropic material behavior [332]. Only Gasser and Holzapfel [333] presented a phenomenological approach in which they mimic the anisotropic material response of balloon membranes by fitting structural parameters according to the peculiar inflation characteristic of the analyzed balloon catheter. Nevertheless, no experimental data of multiaxial tensile tests of balloon catheter membranes for parameter estimation of phenomenological or microstructure-based models are yet available in the literature. Thus, in *Chapter 3*, a material model for coronary balloon catheter membranes together with a full set of constitute parameters is presented.

1.5 Doctoral Thesis

1.5.1 Organisation

The dissertation is a compilation of three scientific peer-reviewed articles which cover experimental and computational methods to deliver a comprehensive framework for the optimization of future finite element analyses as well as material models of balloon catheters, stents, and coronary arteries. Furthermore, this cumulative doctoral thesis provides first insights into mechanisms of stent-induced vascular damage.

As part of this research, new novel multi-axial, multi-sensorial test rigs were designed, built, and commissioned. Furthermore, protocols for sample preparation, storage, as well as testing, were developed. And finally, new methods for tissue imaging and numerical analysis have been developed and established. All key results have been published in the following journal papers:

1. **M.A. Geith, K. Swidergal, B. Hochholdinger, T.G. Schratzenstaller, M. Wagner, and G.A. Holzapfel,**

On the Importance of Modeling Balloon Folding, Pleating, and Stent Crimping: a FE Study Comparing Experimental Inflation Tests, International Journal for Numer-

ical Methods in Biomedical Engineering, 35:e3249, 2019.

The first research paper studies the influence of residual stresses and strains of pre-operative processes on the accuracy of implicit FEA of expanding stents. Therefore, implicit FEA of the balloon folding, pleating and stent crimping were carried out and the resulting residual stresses incorporated in the simulation of an expanding stent. All results were verified with images from micro-CT scans and stent inflation tests. The study demonstrates that the incorporation of residual stresses and strains and the use of the implicit solver improved the accuracy of finite element analyses of expanding stents. In addition, the FEA reveals that balloon catheter membranes and stents are exposed to significant stresses during preoperative processes, which may cause severe damage prior to the actual implantation.

2. **M.A. Geith, J.D. Eckmann, D.Ch. Haspinger, E. Agrafiotis, D. Maier, P. Szabo, G. Sommer, T.G. Schratzenstaller, and G.A. Holzapfel,**

Experimental and Mathematical Characterization of Anisotropic Polyamide 12 Balloon Catheter Membranes, PLoS ONE, in press.

The second research paper focuses on the material properties of balloon catheter membranes. An experimental methodology is proposed that enables uniaxial and biaxial extension tests of commercial coronary balloon catheter membranes under quasi-static and dynamic testing conditions. The tested membranes can be characterized as a semi- or non-compliant, nonlinear, and viscoelastic material with pronounced anisotropy above the nominal loading. A modified polynomial model was introduced with a compact set of constitutive model parameters for future FEA of expanding balloon catheters.

3. **M.A. Geith, L. Nothdurfter, M. Heiml, E. Agrafiotis, M. Gruber, G. Sommer, T.G. Schratzenstaller, and G.A Holzapfel,**

Quantifying Stent-Induced Damage in Coronary Arteries by Investigating Mechanical and Structural Alterations, Acta Biomaterialia, in press.

The final study reports new methods for the quantification of vascular damage due to stenting. First, the multiaxial loading scenario of stent implantation was simulated *in vitro* by indenting a strut into a physiologically loaded porcine coronary artery. Secondly, the material response of the coronary artery to the strut indentation was measured. And finally, three-dimensional surface and second-harmonic generation scans were performed to investigate changes in the collagen fiber dispersion and lesion extend. For the first time, we were able to correlate experimental with imaging data and to define stent-induced damage mechanisms. In addition, recommendations of the improvements for constitutive damage models of coronary arteries for future FEA were made.

1.5.2 Further engagements

The author contributed to the following publication:

- **E. Agrafiotis, M.A. Geith, M.A. Golkani, G. Sommer, V. Hergesell, S. Spiliopoulos, G.A. Holzapfel:**
Real-time Controlling of Arterial Compliance for Mock Circulatory Systems, ASAIO Journal, submitted.

During his doctorate, the author successfully filed one patent application as one of the concept designers and principal inventors:

- **M.A. Geith, E. Agrafiotis, M. Gruber, Spiliopoulos, G. Sommer, V. Hergesell, O.E. Dapunt, and G.A. Holzapfel:**
Cardiac simulation device EP 19 17 9022, European Patent Office, 2019.

Another patent is currently in the filing process.

- **M.A. Geith, D.A. Nordsletten, R. Sinkus, and G.A. Holzapfel:**
MRI-compatible device for dynamic multiaxial deformation and elastography test under real-time force sensing.

Additionally, the following conference contributions, in the form of talks and papers, are part of this thesis:

- Conference talk and paper
L. Wiesent, M.A. Geith, M. Wagner: *Simulation of fluid-structure interaction between injection medium and balloon catheter using ICFD*, 11th European LS-DYNA Conference, Salzburg, Austria, May 9–11, 2017.
- Conference talk
M.A. Geith, G. Sommer, T.G. Schratzenstaller, and G.A. Holzapfel: *First approaches in quantifying acute vascular damage due to stenting*, The 23rd Congress of the ESB, Sevilla, Spain, July 2–5, 2017.
- Conference talk and paper
M.A. Geith, G. Sommer, T.G. Schratzenstaller, and G.A. Holzapfel: *Biomechanical and structural quantification of vascular damage: a unique investigation of stent implantation*, ARTERY 2017, Pisa, Italy, October 12–14, 2017.
- Conference talk
M.A. Geith, K. Swidergal, T.G. Schratzenstaller, G.A. Holzapfel, and M. Wagner: *Numerical analysis of stent delivery systems during pre- and intraoperative processes*, 15th German LS-DYNA Forum, Bamberg, Germany, October 15–17, 2018.

Furthermore, the author contributed as a concept designer and principal author to following project proposals from which the doctorate was partly funded:

- **Project OptiStent AZ VIII.2-F1116.RE/17/3**, Bavarian State Ministry for Education, Culture, Science and Arts.
- **Research Fellowship Project PIZ-225-18**, Bavarian Research Foundation.
- **Stand-Alone Project P 32713**, Austrian Science Fund, Fonds zur Förderung der wissenschaftlichen Forschung (FWF).

2 On the Importance of Modeling Balloon Folding, Pleating, and Stent Crimping: An FE Study Comparing Experimental Inflation Tests

Abstract. FE-based studies of preoperative processes such as folding, pleating, and stent crimping with a comparison to experimental inflation tests are not yet available. Therefore, a novel workflow is presented in which residual stresses of balloon folding and pleating as well as stent crimping, and the geometries of all contact partners were ultimately implemented in a FE code to simulate stent expansion by using an implicit solver. The numerical results demonstrate that the incorporation of residual stresses and strains experienced during the production step significantly increased the accuracy of the subsequent simulations, especially of the stent expansion model. During the preoperative processes, stresses inside the membrane and the stent material also reached a rather high level. Hence, there can be no presumption that balloon catheters or stents are undamaged before the actual surgery. The implementation of the realistic geometry, in particular the balloon tapers, and the blades of the process devices improved the simulation of the expansion mechanisms, such as dogboning, concave bending or overexpansion of stent cells. This study shows that implicit solvers are able to precisely simulate the mentioned preoperative processes and the stent expansion procedure without a preceding manipulation of the simulation time or physical mass.

2.1 Introduction

The number of coronary stent implantations (CSI) rises rapidly, particularly in industrialized countries such as Austria, where the number of implanted stents increased by 21 % between 2012 and 2017 [334]. The most challenging complication after CSI is the adverse event of restenosis, which occurs at rates as high as 20 % for bare metal (BMS) and drug-eluting stents (DES) despite improvements [4]. To reduce the severity of neointimal hyperplasia due to excessive cell proliferation and migration after the use of BMS [335], researchers around the world are undertaking great efforts to apply cell growth inhibiting drugs onto the stent surface, e.g., sirolimus [336] and paclitaxel [267]. This resulted in the first generation of DES, which initially showed good results in lowering the rate of early restenosis from 30 % [337, 338] to about 10 % [266, 339–341]. However, first clinical long-term outcomes revealed that patients having the first generation DES implanted tend to have a higher risk of late vascular events (> 3 weeks, < 1 year) compared to patients with BMS. The reason is a delayed endothelialization of the stent struts what entails the danger of late in-stent thrombosis [342, 343] and incomplete embedding that again causes malapposition [344].

In order to regulate and to extend the delivery of drugs after the stent is implanted, it is currently common to apply polymers to the stent surface as a carrier for pharmaceutical

substances. Such stents represent the second generation of DES. Some of these polymers seem to be ineligible because of possible inflammatory responses [345, 346]. Lately, clinical studies have confirmed that even the newer generation of DES are not superior to BMS and show equal fatality rates [4, 12, 273]. The study of Timmins *et al.* [347] proves that increasing arterial wall stress leads to a more severe neointimal response in the form of cell migration and proliferation. Therefore, to reduce the fatality rate of BMS as well as DES for CSI, scientists and manufacturers need to develop safer stents by significantly lowering the risk of vascular injuries. This goal may be achieved by reducing the load on the artery applied by the stent and the balloon catheter. Therefore, engineers need to change the stent/balloon geometry, their material, or both.

Stents for CSI are usually expanded by the inflation of a non-compliant balloon catheter. For minimally invasive and endovascular treatments balloon catheters consist mainly of a blow-molded, cylindrical balloon with short tapers at both ends, which are adhered to a catheter. Stents and balloon catheters pass through three important preoperative processes before they are – purely mechanically – ready to be implanted as a unit: (i) in the folding process, three wings of the balloon are formed with curved folding blades; (ii) during the pleating process, the balloon is wrapped around the catheter creating a distorted star-shaped balloon cross-section; (iii) in the crimping process, the stent is plastically deformed by reducing its diameter and it is pressed onto the pleated balloon. The load acting on the balloon and stent during the folding, pleating and crimping processes cannot be measured. The movement of the displacement-controlled blades of all these processes is based on empirical values only. The authors assume that wrong process parameters can adversely increase initial residual stresses inside the balloon catheter and the stent before CSI. The change in the residual stresses could negatively influence typical expansion mechanisms and the final geometry of the implanted stent. This circumstance could result in severe damage to the balloon catheter, the stent, and, of course, the arterial wall. Due to this fact, it seems even more critical for the optimization process of balloon catheters and stents to know and to consider initial residual stresses and strains experienced during the preoperative processes.

Finite element analysis (FEA) has become an effective tool not only to investigate the expansion behavior of balloon catheters and stents. FEA can save valuable development time and costs by replacing or reducing extensive material tests and ethically questionable animal experiments. FEA can also provide information about whether the strength of the stent is sufficient to withstand the stresses during a CSI.

Especially the expansion behavior of a stent depends decisively on the balloon catheter type, i.e., its geometry, the applied folding and pleating technique, and its operating pressure. In first FEA, pressure was applied to the luminal surface of the stent to expand it [300–305]. These early studies demonstrated already the great potential of FEA in analyzing the stresses and strains of an expanding stent. However, it is becoming more apparent that it is essential to integrate an important contact partner of the stent, the balloon catheter, into up-to-date FEA. Therefore, during the last two decades, FEA have been performed

with balloon catheter models showing an increasing level of geometrical detail. The first refinement step includes FEA with simple rigid cylindrical shells [306–309]. By increasing the diameter of these cylindrical models, a displacement-controlled expansion of the stent could be simulated.

On the contrary, using a simple cylinder for stent expansion during the FEA does not allow to mimic a realistic contact pressure distribution between stent and balloon. Ju *et al.* [310] and Kiouisis *et al.* [311] overcame this problem by pressurizing the luminal surface of elastic cylinders with a hyperelastic material model, which constitutes the second refinement step. Nevertheless, the influence of the unsymmetrical star-like shape of a folded balloon on the expansion process of the stent cannot be investigated with such models. It is documented that the unsymmetrical folding of the balloon catheter has a more considerable influence on the expansion behavior of a stent than the mechanism of the stent itself [348]. By implementing a hyperelastic balloon model consisting of a folded model with open ends and star-shaped cross sections, De Beule *et al.* [294] initiated the third refinement step.

Open balloon models may not be used to study the influence of tapers at both ends of a balloon catheter on stent expansions. Without the tapers, hyperelastic balloon models lack a design-based resistance to an unimpeded expansion of the balloon ends. Therefore, the fourth refinement stage characterizes modern FEA of stent implantations in which folded balloon models with tapers are implemented. In order to gain the detailed geometry of a folded balloon model, different approaches have been pursued which include (i) the modeling of the balloon membrane in an already pleated and folded state by using computer-aided design (CAD) methods or by the application of mathematical transformation techniques [312–315], (ii) the extraction of the balloon geometry using data from 3D micro-computed tomography (micro-CT) scans [349] and (iii) the application of pressure to the outer surface of the membrane to deflate the balloon [330, 331]. However, to the authors' knowledge, no study has yet considered the modeling and simulation of the folding and pleating processes mentioned above by implementing the one-to-one blade geometry of a multi-head tool in order to recreate a realistically folded balloon model. This further refinement step is necessary because the possibility that balloon membranes are exposed to high stresses during these preoperative processes cannot be excluded. High stresses can lead to plastic strains or even damage to the membrane material, which can significantly influence the expansion mechanism of the balloon catheter and, therefore, also of the stent.

A few other groups such as Wu *et al.* [350] and Li *et al.* [351] reach a broader perspective on known issues of stent optimization through the additional consideration of the crimping process in their FEA. For both, the expansion and the crimping process, they use radially expandable rigid cylinders to vary the diameter of the stent. Schiavone *et al.* [352] simulated the crimping procedure following the iris principal, where twelve rigid blades of a multi-head tool press the stent on a linear elastic isotropic balloon model. The results show that the tested stent is already exposed to a significant amount of stress during crimping, and thence substantiated the assumption that damage to stents may arise even before their implantation. This matches with the results from Möller *et al.* [353] which reported about

significant residual stresses in crimped stents after using the X-ray diffraction method. It is also essential to consider an investigation of balloon catheters during the crimping process. Rondeau *et al.* [354] demonstrated in their study that balloon membranes show alterations on their surface like streaks and even abrasion after stents were crimped on them.

CSI is a quasi-static procedure. Nevertheless, almost all mentioned research groups used explicit solvers for the FEA of CSI. On the one hand, convergence problems due to non-linearities, large deformations, sliding contact, and coarse meshes are usually prevented. On the other hand, the explicit time integration method allows only small time steps which can culminate in several days of computational time [355]. A drastic reduction of the FEA simulation time of CSI from several seconds to fractions of a second and a mass scaling are popular but possibly mistrustful countermeasures. Although the method of mass scaling [356] allows larger time steps, it can lead to an additional falsification of the results in CSI simulations in which large deformations and dynamic effects are expected. Despite increased computational costs and high demands on the mesh quality, contact definition and boundary conditions, the implicit time integration method allows larger time steps without adding nonphysical mass or changing the quasi-static character of the CSI simulation. Bukala *et al.* [315] have been the first group to demonstrate the benefits of an implicit solver by analyzing the crimping and stent expansion process. However, no FEA-based studies are known in which all preoperative processes (folding, pleating, and stent crimping) were simulated neither with an implicit nor an explicit solver.

For this reason, this study aims to show how existing FEA simulations of CSI can be supplemented by considering the folding, pleating, and crimping procedures and by using an implicit solver. Therefore, FEA of the three preoperative processes were performed following an optimized computer-aided engineering (CAE) process workflow: starting with designing the geometries of a balloon catheter and a stent, going through discretizing the 3D-models with a pre-processor, continuing with simulating the processes with an FEA program using the highly precise implicit time integration method and ending with the evaluation of the results in a post-processor. Finally, initial residual stresses and all generated geometries were used in a final simulation of an expanding stent to investigate the influence of the preoperative processes. The results of the FEA were verified with images from micro-CT scans and with an inflation test documented with a high-speed camera. And finally, the FEA using the new method was compared with simulations following (more) classical approaches known from the literature. Along with the new approach devised by Geith *et al.* [357], the authors of this study mainly focus on the quantification of vascular damage due to CSI by analyzing biomechanical and structural changes of coronary arteries to define a more precise damage and growth model for coronary arteries. The present study suggests important preliminary steps for subsequent numerical analyses.

2.2 Materials and Methods

2.2.1 Balloon catheter and stent

For this study, the over-the-wire balloon catheter Baroonda stent delivery system (SDS, 08BO-3520A, Bavaria Medizin Technologie GmbH, Wessling, Germany) with a tri-folded and non-compliant balloon membrane made from the thermoplastic Grilamid L25 (EMS-Chemie AG, Domat/Ems, Switzerland) was used (Figure 2.1). Once the operating pressure of $p = 1.0$ MPa for the Baroonda is applied and the membrane is fully inflated, the original state of the balloon cannot be restored and the catheter needs to be disposed. As mentioned, balloon catheters for coronary stents are usually blow-molded. Therefore, it can be assumed that the polymer chains of the Grilamid L25 align in the circumferential direction of the balloon and thus strongly anisotropic material properties prevail. Because of the lack of experimental data in the literature, only material parameters of unprocessed, isotropic Grilamid were available to the authors. In addition, a stent made of 316 LVM stainless steel (ThyssenKrupp Steel Europe, Duisburg, Germany), stress-relieved stainless steel, with closed cells, based on the prototype ESPRIT V1 design, was investigated (Figure 2.2). The ESPRIT V1 design was developed during a separate preliminary study. Table 2.1 presents the essential material parameters for Grilamid L25 and 316LVM.

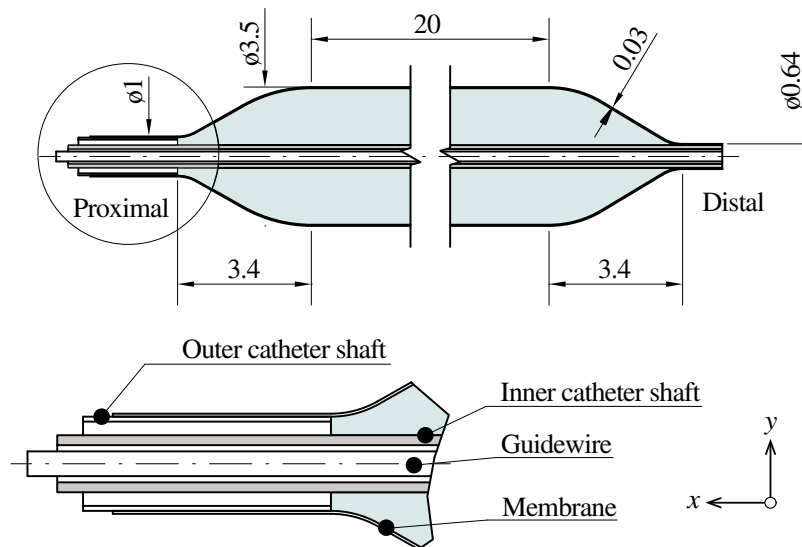


Figure 2.1 Baroonda SDS balloon catheter: while the distal end of the membrane is fused to the inner catheter shaft, the proximal end, connected to the outer catheter shaft, is free to slide along its longitudinal axis. All dimensions are in mm and taken from own measurements.

The distal taper of the balloon membrane is connected to the inner catheter shaft, which exits the balloon at the proximal end. The proximal taper is connected to the outer catheter shaft, which can slide freely to a certain degree along its longitudinal axis in the global x -direction, see Figure 2.2. Thus, the balloon catheter can compensate elongations during the preoperative processes and the stent expansion. Based on the dimensions measured with

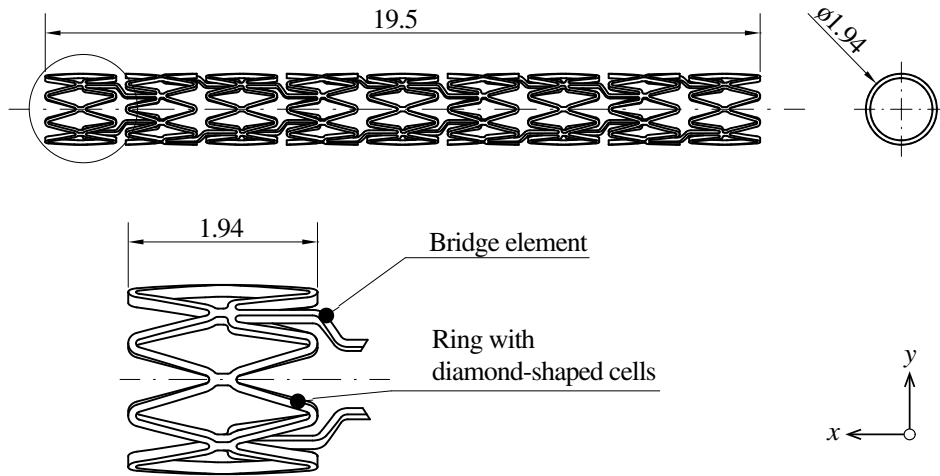


Figure 2.2 Half-section of the ESPRIT V1 stent before the preoperative processes: the stent has nine rings along its longitudinal axis with respectively eight diamond-shaped cells. The rings are connected to each other with two bridge elements. The structure of the stent was designed as symmetrical as possible to reduce twists and asymmetrical expansion/elongation. All dimensions are in mm and taken from own measurements.

Table 2.1 Material properties of the raw materials for the Baroonda SDS balloon catheter (Grilamid L25, unprocessed, isotropic – PA 12) and the ESPRIT stent (316LVM – 1.4441) provided by the manufactures.

		Grilamid L25 (raw material)	316 LVM
Density ρ	[ton/mm ³]	1.010E-09	7.850E-09
Young's modulus E	[MPa]	1100	2.100E+05
Yield point $R_{p0.2}$	[MPa]	–	332
Tensile strength R_m	[MPa]	45	671
Poisson's ratio ν		0.40	0.29

the light microscope VHX-2000 (Keyence, Osaka, Japan), a 3D design of the unfolded and untreated balloon catheter was created with Autodesk Inventor 2018 (Autodesk, San Rafael, USA). Figures 2.1 and 2.2 show all necessary dimensions of the Baroonda SDS balloon catheter and the ESPRIT V1 stent. Using a 2D template, which was wrapped around a cylinder and extruding with the 'emboss' feature in Inventor, an exact 3D model of the stent could be created. Finally, the ESPRIT V1 stent was manufactured by MeKo Laser Material Processing GmbH (Sarstedt, Germany) by laser cutting, annealing, and electropolishing. The finished ESPRIT V1 stent has a total stent length of 19.5 mm, an outer diameter of 1.94 mm, a strut width of about 80 μm and a depth of 120 μm .

2.2.2 Preoperative processes

To ensure that stents and arteries are not getting overstretched during CSI, balloon membranes are made from rather non-compliant materials. Therefore, the balloon membrane

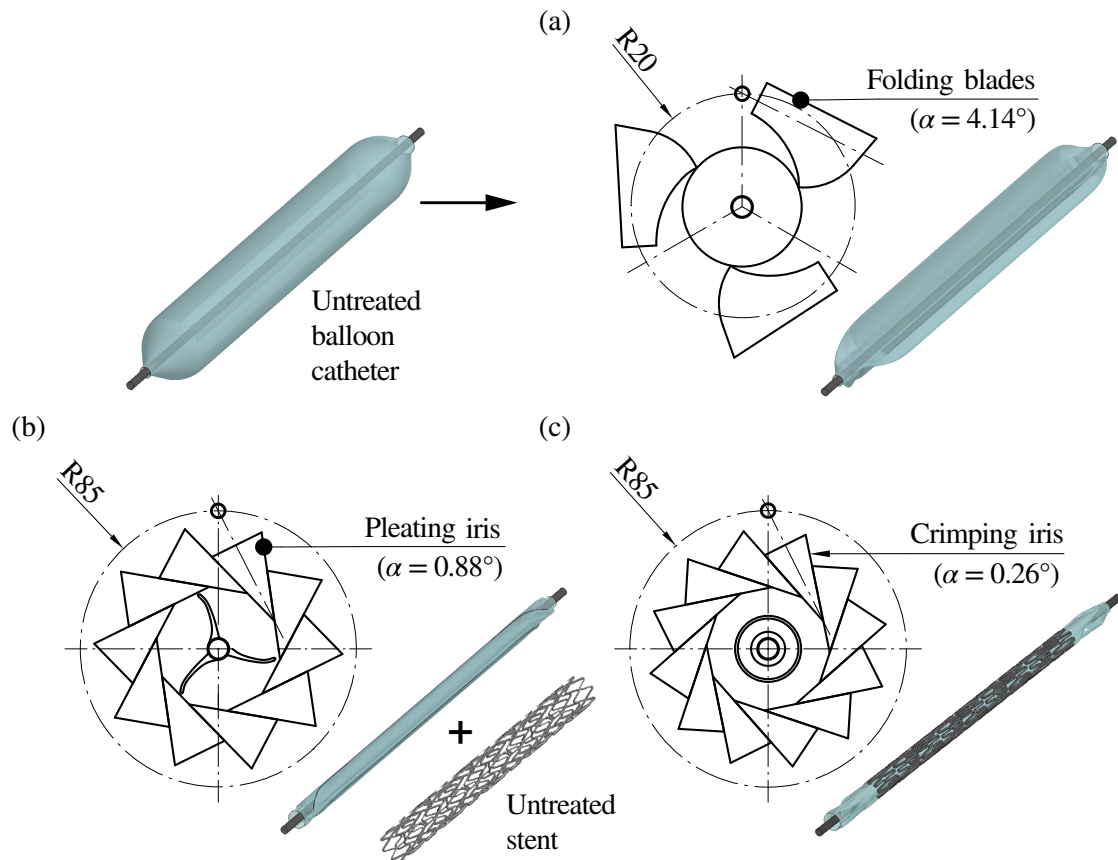


Figure 2.3 Overview of the three preoperative processes: (a) in the folding process, the untreated balloon catheter is pressed into a star-like shape with three wings; (b) during pleating, the wings are folded over and pressed against the inner catheter shaft; (c) in the crimping process, the stent is crimped onto the folded balloon catheter. The blades rotate with the displacement angle α around the pivot axes which are parallel to the longitudinal direction of the balloon/stent.

has to be folded and pleated to reduce its diameter until it is small enough to crimp a stent onto it. During the folding process (Figure 2.3(a)), the balloon catheter is pressurized with 0.1 MPa while three blades press the cylindrical membrane into the characteristic star shape with three slightly slanted wings within a process time of 2 s. This creates a preferred folding direction of the wings. As soon as the star shape is formed, a vacuum of 0.1 MPa is drawn to prevent a springback. The second process, the so-called pleating (Figure 2.3(b)), serves to press the balloon wings onto the catheter. Ten blades are arranged in the shape of an iris. By rotating the blades, the diameter of the iris can be reduced in 2 s. The pleating and folding process was performed with a customized multi-head tool (MSI, Flagstaff, USA) by the manufacturer of the balloon catheter. After the three wings are pressed around the catheter tube, a vacuum is again generated.

During the crimping process (Figure 2.3(c)), the pleated balloon catheter is placed together with the stent inside the crimper, which features 12 blades. By reducing the iris diameter, the stent is plastically deformed and pressed onto the pleated balloon. After a process time

of 2 s, the stent is compressed to its smallest diameter. Once the iris opens again and crimp pressure is reduced, the stent recoils to its final diameter. For the crimping procedure, a fully functional and automated prototype was used. After a sterilization procedure, the balloon catheter with the stent is ready for CSI.

2.2.3 Inflation tests and micro-CT scans

To validate the numerical results of the present work, water was pumped into the balloon catheter to expand the stent. For the nominal diameter of 3.5 mm, an internal pressure of $p = 1.0$ MPa was deployed within $t \sim 2$ s with the commercial pump BasixCOMPAK (Merit Medical, South Jordan, USA) with a handwheel. The inflation finished after another 2 s. In parallel, the pressure was measured at the adapter of the balloon catheter with the sensor XMLP600PP13FQ3 (Telemecanique, Rueil-Malmaison, France). The pressure curve usually varies greatly with every trial and shows plateaus and sudden increases, as presented in Figure 2.4. This is due to the manually operated pump, air pockets inside the catheter shaft, the viscous flow of the contrast medium solution, and the abrupt volume expansion when a certain pressure is reached and the stent bursts open. During the inflation test, the balloon catheter was filmed with the high-speed camera HCC-1000 (VDS Vosskühler, Osnabrück, Germany) to measure the diameter of the stent at its ends and in its center. In addition, to analyze its cross-section, the Baroonda SDS balloon catheter was scanned with the x-ray microtomography scanner (micro-CT) GEv—tome—xs (General Electric, Boston, USA).

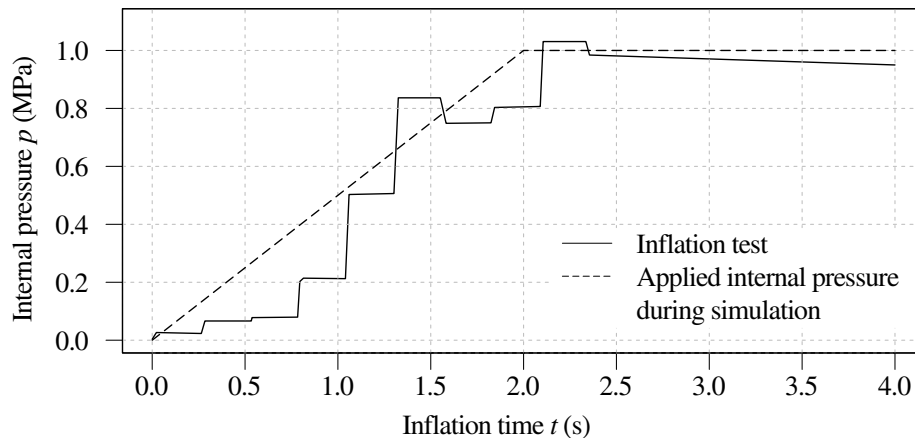


Figure 2.4 Internal pressure p of the balloon catheter expanding the stent vs time t during an inflation test: while the realistic pressure curve shows rapid increases followed by plateaus, a linear pressure increase of 2 s was assumed for the FEA of CSI.

2.2.4 Numerical simulations

For the FEA, the mid-surface of the 3D-CAD model of the Baroonda SDS balloon membrane was extracted and discretized with the pre-processor ANSA v18.1.0 (BETA CAE

Systems, Farmington Hills, USA) by means of 97 820 fully integrated quadrilateral shell elements with a shell thickness of 0.03 mm. A mesh with elements distributed in rows along the longitudinal axis and a very fine taper-meshing showed positive effects on the computations. The mesh was refined until no significant changes – i.e., more than 1% of the maximum stress was obtained. A further criterion for the mesh sensitivity of the balloon membrane was to find the ideal correlation between the number of shell elements along the smallest appearing radii and the computational time. 200 elements in the circumferential direction showed to be sufficient. The ESPRIT V1 stent was meshed with 119 680 fully integrated hexahedral elements. Here, three elements along the strut width and four through the thickness fulfilled the criteria for the mesh sensitivity. While the straight strut segments contained a coarse mesh, the connecting, bridge, and curved segments featured a symmetrical and fine element mesh. Only the contact surfaces of the blades of the folding, pleating and crimping tools were implemented, as presented in Figure 2.5, and discretized with a coarse mesh. The folding blades' geometry is very complex due to their curved surfaces. The use of their correct dimensions is essential for realistic numerical results. Therefore, the blades were photographed frontally with a scale and their contours retraced with Autodesk Inventor 2018. FEA simulations of the three preoperative processes and

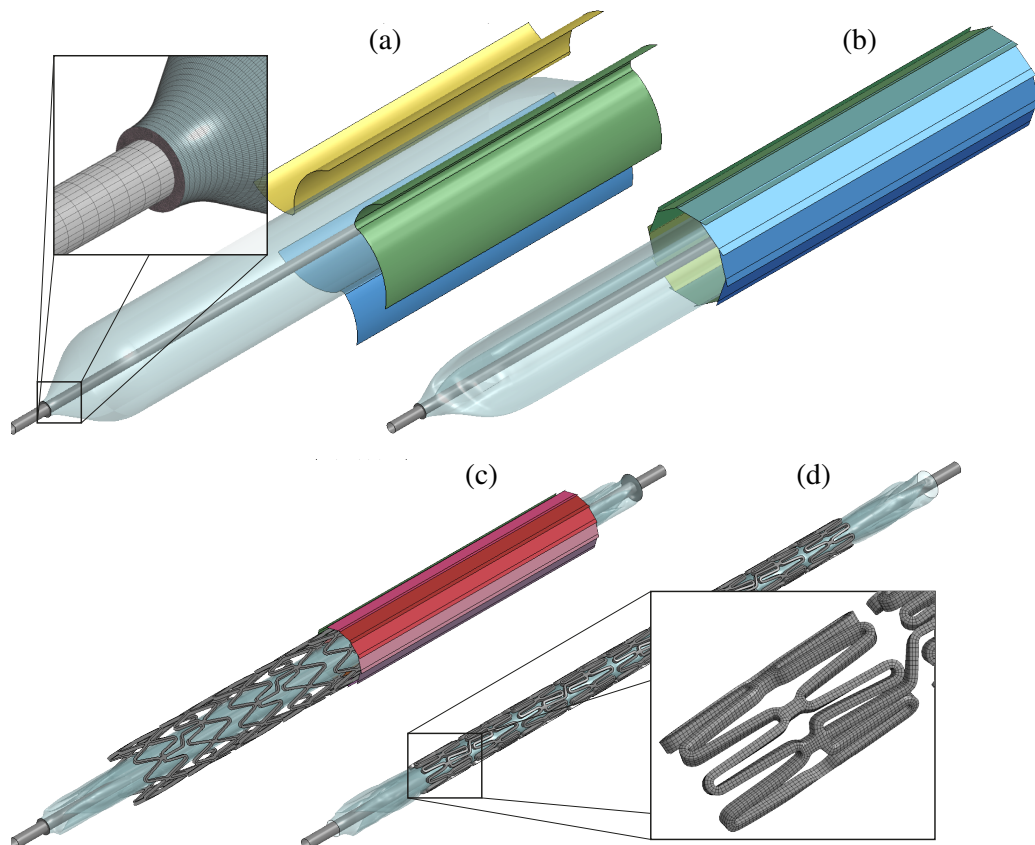


Figure 2.5 Reduced geometries for the FEA: of the (a) folding, (b) pleating, (c) crimping, and (d) expansion process. For better visualization, only one half of the blades of the devices is visible.

the stent deployment procedure were performed with LS-DYNA (LSTC, Livermore, USA) with the implicit double precision version R10.1.0 for shared memory parallel processing. For the simulation times of the preoperative processes, the actual times of the respective work process were measured and adopted. The simulation time for the FEA of the CSI was adjusted according to the pressure ramp presented in Figure 2.4. Stresses and strains of the balloon membrane and the stent during the last time step of each simulation were transferred into the subsequent FEA. The stent and the balloon materials were based on a piecewise linear isotropic plasticity formulation in MAT24 [319] for the 316 LVM steel and MAT89 [319] for the Grilamid L25 polymer. The flow behavior of these models is defined by the von Mises flow rule [358].

$$\Phi = \frac{1}{2}s_{ij}s_{ij} - \frac{\sigma_y^2}{3} \leq 0, \quad (2.1)$$

where s_{ij} are the deviatoric stress components and σ_y is the yield stress which is defined as

$$\sigma_y = c(\sigma_0 + f_h(\epsilon_{\text{eff}})). \quad (2.2)$$

The parameter c accounts for strain rate effects and scales the quasi-static yield stress, σ_0 is the initial yield strength and f_h is a function of the effective plastic strain ϵ_{eff} . For both material models, stress versus strain curves provided by the material manufacturers are implemented. In MAT24, the transition from the elastic to the plastic domain is characterized by the current yield stress. On the contrary, the material model MAT89 assumes the material to have yielded if the gradient of the user-defined stress versus strain curve is smaller as the gradient defined by the Young's modulus E . This method is well suited to approximately mimic the nonlinear behavior of polymers. However, the authors are aware that this model is not suitable to simulate the anisotropic material response of the blow-molded balloon membrane. It can be expected that the alignment of the polymer chains in the circumferential direction allows the membrane to endure twice as much stress as in the longitudinal direction. To enable higher stresses within the ultimate tensile strength, the stress versus strain curves were extrapolated. Failure criteria to simulate the fatigue life of the balloon membrane were not defined due to the lack of data from biaxial tensile tests. Instead, the stress/strain curve in the plastic range was adjusted so that the inflation behavior of the balloon coincides as accurately as possible with the observations of the inflation tests. The inner and outer catheter shaft and the blades of all devices were defined as rigid. The blades were placed in a way, that only a small gap of 0.01 mm between the balloon membrane and the stent was present. An artery model was not included, as this study mainly focuses on the influence of the preoperative processes on the simulation of the inflating balloon catheter and the expanding stent. For information about a constitutive model for wall mechanics of healthy and diseased arteries, we refer to, e.g., Holzapfel *et al.* [329] with more references in there.

The nonlinear equilibrium equations are solved using the dynamic-implicit Newmark- β integration scheme [315, 358]. Firstly, because of the expected accuracy and secondly to

account for the support situation of the system. In general, the equation system is solved for the time step $n + 1$ as

$$\mathbf{M}\mathbf{a}_{n+1} + \mathbf{D}\mathbf{v}_{n+1} + \mathbf{t}(\mathbf{u}_{n+1}) = \mathbf{f}(\mathbf{u}_{n+1}), \quad (2.3)$$

where \mathbf{u} is the nodal displacement vector, \mathbf{v} denotes the velocity vector, and \mathbf{a} is the acceleration vector. Discretizing the weak form of the differential equation system yields the mass matrix \mathbf{M} , the vector of the internal reaction forces \mathbf{t} and the external forces \mathbf{f} . The damping matrix \mathbf{D} can be set up in several ways, e.g., with constant or Rayleigh-damping.

The Newmark- β scheme introduces the following difference quotients

$$\mathbf{u}_{n+1} = \mathbf{u}_n + \mathbf{v}_n \Delta t + \left[\left(\frac{1}{2} - \beta \right) \mathbf{a}_n + \beta \mathbf{a}_{n+1} \right] \Delta t^2, \quad (2.4)$$

$$\mathbf{v}_{n+1} = \mathbf{v}_n + [(1 - \gamma) \mathbf{a}_n + \gamma \mathbf{a}_{n+1}] \Delta t, \quad (2.5)$$

which leads to an implicit difference equation in time. The parameters have been set to $\beta = 0.38$ and $\gamma = 0.6$, which introduces a certain amount of numerical damping. Due to the nonlinearity in the internal and external force vectors, a BFGS quasi-Newton solution algorithm was applied [358, 359].

LS-DYNA allows controlling convergence of the solution by scaling the values for the convergence criteria with ε_d , ε_e , ε_r , ε_a , which are the displacement, the energy, the residual, and the absolute tolerance, respectively [360, 361]. After several runs, different criteria strategies were chosen. For folding and pleating, it was identified that efficient calculations could be performed if the displacement tolerance ε_d was loosened and set to

$$\varepsilon_d = \|\Delta x_k\| / u_{\max} = 0.01, \quad (2.6)$$

where $\|\Delta x_k\|$ is the norm of the incremental displacement, and u_{\max} is the maximum attained displacement in any iteration k . To solve the more difficult problems of the stent crimping and the deployment process, ε_d and ε_e were disabled by putting them to large numbers. The residual tolerance ε_r was lowered to

$$\varepsilon_r = \|F_k\| / \|F_0\| = 0.01, \quad (2.7)$$

in which $\|F_k\|$ stands for the norm of the residual force, and $\|F_0\|$ for the first residual vector for the implicit step j . In parallel, the absolute tolerance was set to $\varepsilon_a = -10$. In LS-DYNA, the negative value states that

$$\|F_k\| < |\varepsilon_a|. \quad (2.8)$$

Contact treatment in implicit simulations of CSI is highly demanding. For this reason, penalty-based, predefined segment-to-segment, automatic contacts based on the Mortar method [360–362] were applied within LS-DYNA. Although the friction model of Mortar

contacts is based on the isotropic standard Coulomb law with a constant frictional coefficient only, it features options to overcome convergence problems and to increase the robustness and accuracy of implicit analyses. With large deformations of the balloon membrane, the normal vectors of the segments change permanently and thus also the contact parameters such as contact forces and segment velocity. This can cause convergence problems during implicit calculations if the balloon membrane and its contact partner – the blades and the stent – have different element sizes. With the Mortar method, an intermediate layer of contact elements is considered in which the node of each Mortar element is either a projection of a slave node or of a master node itself. In contrast to node-to-segment contacts, the calculation of the contact nodal forces is performed in this intermediate layer and follows the principle of virtual work. For the mathematical framework, the reader is referred to the work of Puso and Laursen [362]. As a result, energy-consistent contact stresses are calculated, which usually reduces convergence issues. The Mortar contacts were defined by part-to-part sets in which the rigid elements of the blades and shafts were generally chosen as master surfaces.

In the contact definition between the stent and the balloon membrane, the stent was classified as master and the much softer membrane as slave. In addition, single surface contacts for the stent and the balloon membrane had to be implemented. In all simulations, the outer nodes of the balloon membrane were attached to the rigid shafts via a node set and a constraint-condition.

The rotary motion of every blade was defined by a pivot axis – represented by a vector – an angle α , and the process time mentioned above as presented in Figure 2.3. The respective axis of rotation was characterized by a unit vector \mathbf{e} parallel to the longitudinal direction with its origin in a pivot point characterized by the position vector \mathbf{p} . The endpoint \mathbf{r} of \mathbf{e} can then be expressed in matrix form as

$$[\mathbf{r}] = [\mathbf{p}] + [\mathbf{e}] = \begin{bmatrix} 0 \\ \cos\left(\frac{2\pi}{n}i\right)R \\ \sin\left(\frac{2\pi}{n}i\right)R \end{bmatrix} + \begin{bmatrix} 1 \\ 0 \\ 0 \end{bmatrix}, \quad (2.9)$$

where n stands for the total amount of blades of the respective process tool, i represents the number of the specific blade, and R is the radius from the tool center to the pitch circle of the pivot points.

In the folding and pleating processes, a ring of nodes of the membrane center was constrained in its longitudinal direction x . To enable elongation of the balloon catheter as close as possible to the motion inside the folding and pleating devices, both shafts were allowed to move and rotate along the x -axis. Similar boundary conditions were used for the crimping process. The rotary motion of the balloon membrane was constrained around the x -axis to support the wrapping mechanism of the wings. In a real stent expansion, both shafts allow certain movement along and around x . However, the authors decided to fully constrain the rotational degrees of freedom in x for both balloon ends. As a result,

the angular momentum of the inflating wings of the balloon membrane and the expanding stent can be thoroughly analyzed.

For expanding the stent, the pressure on the inner surface of the balloon membrane was constantly increased to 1 MPa within 2 s according to the graph shown in Figure 2.4.

2.3 Results

2.3.1 Folding process

The computational time for the folding process was 2 h and 37 min on an Intel Core i7-6700k CPU, 4.00 GHz, 32 GB (Intel Corporation, Santa Clara, USA) with a simulation time of 1 s and by using four cores. For the folding and the other processes, an automatic time step scaling with a maximum time step of 0.02 s was selected. The resulting star-like cross section had a maximum diameter of $d = 1.77$ mm.

As can be seen in Figure 2.6(a), the balloon membrane experiences a significant deformation. Along the outer folding edges, extensive bruises could be detected with an over-estimation in the von Mises stress distribution of more than 100 MPa. Despite the freely movable tapers, considerable buckling was obtained. During the procedure, the balloon lengthened by 0.5 mm. On the proximal side, the outer shaft rotated by 18.39° and on the distal side, the inner shaft rotated by 19.43° around the x -axis. This resulted in a twist of 1.04° between the proximal and distal ends. Due to the different diameters of the outer and inner shafts and thus, a different shape of the proximal and distal tapers, an asymmetrical stress/strain field along the balloon membrane was determined. At the proximal end, i.e., at the taper of the outer catheter shaft, significantly higher stresses were present. This is a result of the larger diameter of the distal end. Furthermore, in order to create the wings of the typical star shape, less membrane material needs to be deformed in order to obtain the same folding geometry.

2.3.2 Pleating process

From a numerical point of view, the most expensive task with a computational time of 14 h and 27 min and a simulation time of 2 s was the pleating process. The geometries of all three wings show good agreement with the micro-CT scans as presented in the comparison of Figure 2.7(a). Large deformations of the balloon membrane required temporary small time steps.

During the proceeding compression of the three wings, inflection points appear along the folding edges in the outer areas of the tapers causing high-stress singularities with an over-estimation of about 140 MPa, as shown in Figure 2.6(b). These inflection points are also present on actual balloon catheters. Figure 2.7(b) displays a direct comparison. The positions of these inflection points moved from the big to the small balloon diameter until the process was finished. This seems to cause streaks on the surface, which can be again seen

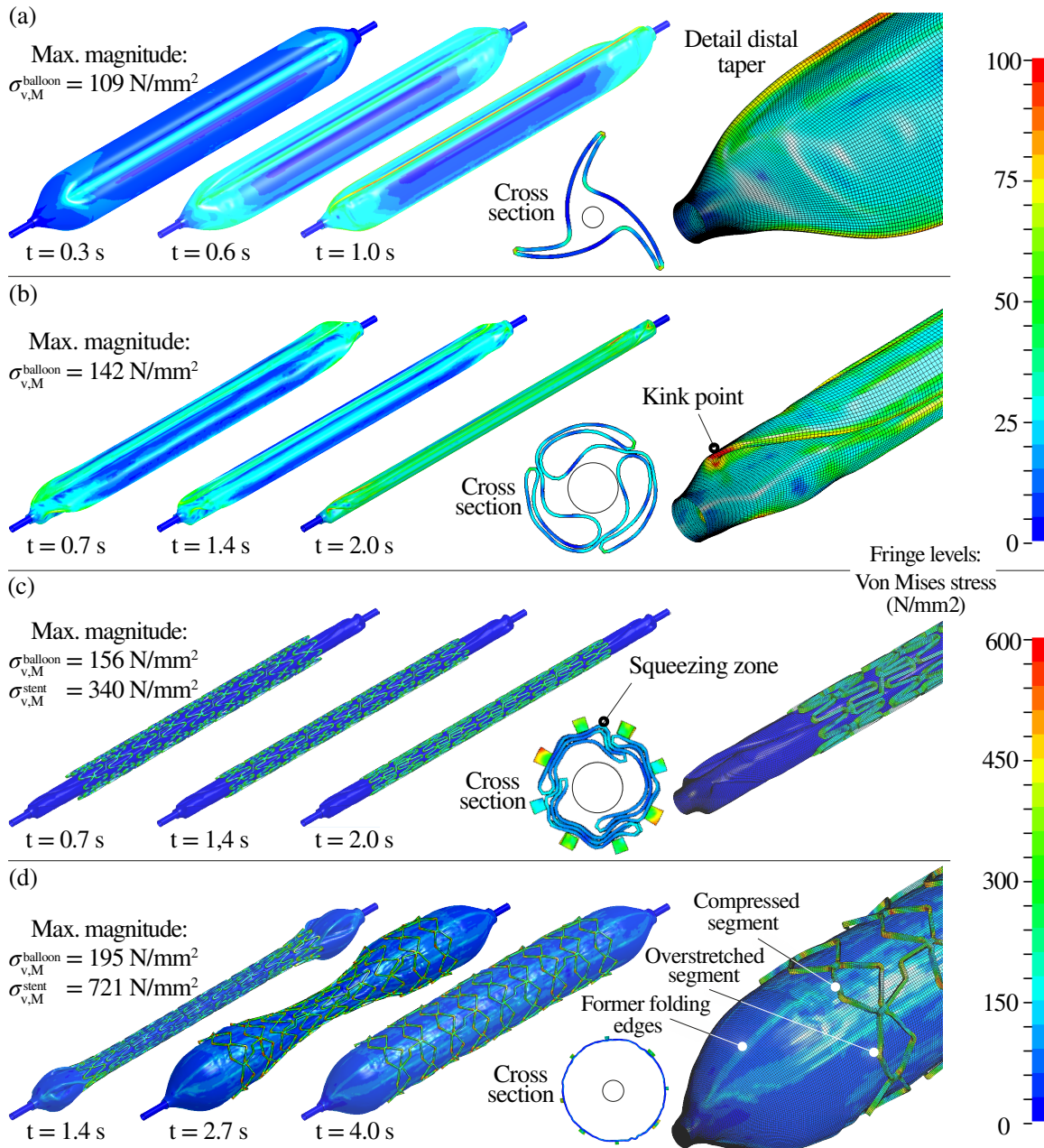


Figure 2.6 Distribution of the von Mises stress $\sigma_{v,M}$ for the Baroonda SDS balloon catheter and the Esprit VI stent during (a)–(c) the preoperative processes and (d) the stent expansion. The collection shows three isometric general views of the balloon and the stent after one- and two-thirds of the simulation time and the final result. Furthermore, an out-of-scale sectional view taken from the center and a detailed view from the distal taper are presented. For better visualisation, the blades of the respective devices of the preoperative processes are hidden. (a) During the folding process, stress peaks occur at the outer wing edges of the balloon membrane. (b) During the pleating process, the membrane gets heavily stressed, especially in kink points around the taper areas. (c) In the crimping process, the membrane is additionally pressed into the gaps between the stent struts. (d) Finally, during the expansion process, the floating stent segments, which lie between the membrane wings, get overstretched.

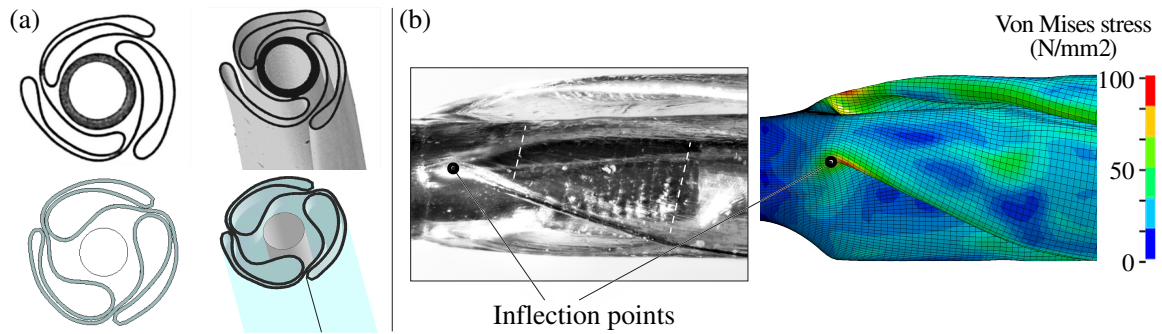


Figure 2.7 Comparison of the geometry of the folded and pleated Baroonda SDS balloon catheter: (a) taken from micro-CT scans (top) and from the simulation (bottom); (b) inflection points can be detected in the light microscope images of the folded and pleated balloon and in the FEA. The positions of the inflection points change during pleating and move from the big to the small diameter of the tapers. This process causes streaks on the tapers (visible in the zone between the dashed lines).

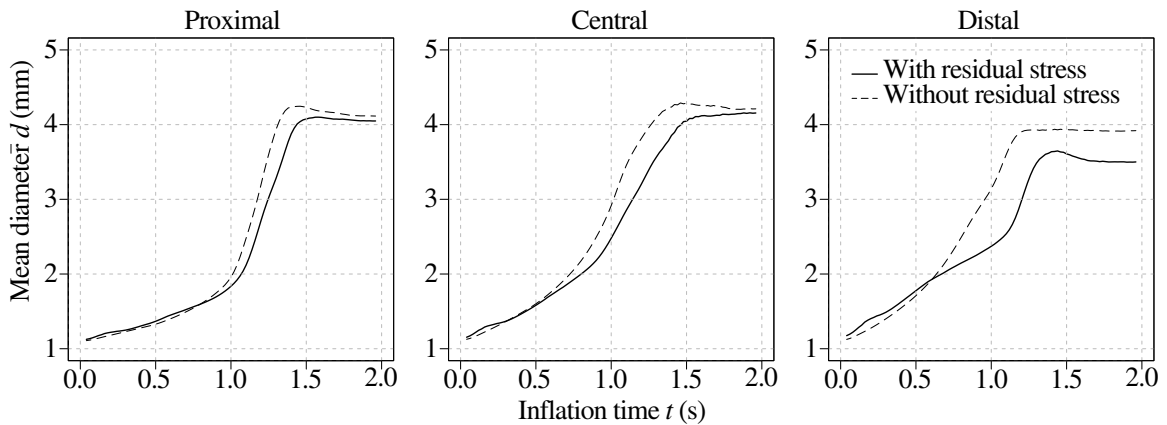


Figure 2.8 Simulation results showing the mean proximal, central, and distal diameter \bar{d} of the Baroonda SDS balloon catheter during its inflation over time t of 2 s after incorporating or ignoring initial residual stresses. By ignoring residual stresses, it can be detected that all three sections of the balloon membrane expand faster and to a bigger end diameter.

in the microscopic image of Figure 2.7(b).

After finishing the simulation of the pleating process, it was verified that both tapers differed slightly in their shape due to the different shaft diameters. The final diameter d of the central cross section was 0.55 mm. The balloon catheter lengthened again by 0.14 mm, which resulted in a final length of the blank, folded, and pleated membrane of 27.16 mm. Also, a twist around the longitudinal direction of the proximal end of 58.72° and the distal end of 60.66° could be observed, which results in a twist of 2.94° during pleating and a final twist of 3.98° after the folding and pleating process.

Figure 2.8 shows the inflation behavior of the balloon catheter by incorporating or ignoring initial residual stresses. Here it should be mentioned, that – apart from the implementation of the residual stresses – both simulation models were identical. To identify the differences

in the expansion behavior, three diameters from the proximal, central, and distal sections of the balloon membrane were measured, from which each results from coordinates of three nodes lying on the tips of the folding edges of the wings. Afterward, the mean diameter \bar{d} for every section was calculated. A comparison of the mean diameters indicates that in all three segments, the expansion of the membrane without initial residual stresses proceeded faster. Furthermore, differences in the final balloon diameters could be detected. The membrane without initial residual stresses continued to expand further, especially in the distal section.

2.3.3 Crimping process

The simulation of the last preoperative process – the crimping – with a computational time of 9 h and 4 min and a simulation time of 2 s, was the second most expensive task – not including the FEA of the CSI. A high number of predefined contacts – a total of 15 contact segment-to-segment pairs and two single surface contacts – certainly had a strong influence on the computational effort.

Again, the stress in the balloon membrane increased to a maximum magnitude of 156 MPa. Parts of the membrane are squeezed into the gaps between stent struts, as presented in Figure 2.6(c). A clear pattern of indenting stent struts was evident on the outer surface of the membrane. Furthermore, the balloon elongated by 0.016 mm and the stent by 0.1 mm. Due to the dodecagonal geometry of the crimping iris, segments of the stent get pressed into the corners formed by the blades, which resulted in a non-circular cross-section of the crimped stent. In Addition, the respective stent cells showed different compression ratios depending on their position. During crimping, the starting diameter of the untreated stent of $d = 1.94$ mm got reduced to its smallest diameter of $d = 1.20$ mm before it recoiled to its implantation diameter of $d = 1.28$ mm.

2.3.4 Stent expansion

This last simulation was characterized by a computational time of 10 h and 28 min and a simulation time of 4 s (Figure 2.6(d)). At about 1.3 s the balloon and the stent started to show the typical dogboning effect (Figure 2.6(d) and Figures 2.9(a) and (b)) in which the structurally weaker ends expand first. Towards the end of the simulation time, the stent rings expanded step by step from outside to inside. At the same time, the stent cells reached a maximum angle of 29.70° with respect to the longitudinal axis. Also, a slight tendency of the distal end to expand faster than the proximal end is recognizable in both the experimental and FEA images of the Figures 2.9(a) and (b).

Due to dogboning and the resulting steep angle between the affected stent cells and the longitudinal axis, stent segments are bent outwards (Figure 2.9(a)). It is also noticeable that the cells, which are located at the folding edges, get overstretched by the lever of the expanding wings and thus show larger deformations and higher stress peaks (Figure 2.6(d)). Thus, a maximum stress of 721 MPa in one of the overstretched cells was achieved. Dur-

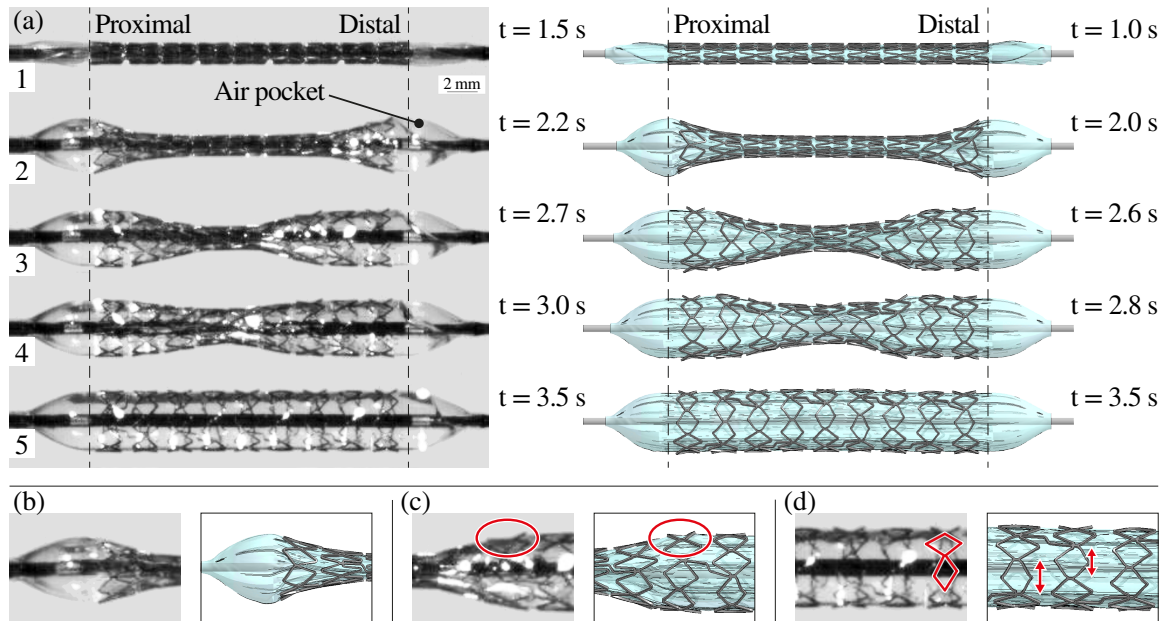


Figure 2.9 Expansive behavior of the SDS: (a) overall, a very good agreement in the expansion behavior between the results of the experimental inflation test and the simulation can be observed. As can clearly be seen the stent first shortens and then slightly elongates. Furthermore, the presented finite element method shows that typical expansion mechanisms, such as (b) dogboning, (c) concave bending of single cells, and (d) overexpansion of cells located at the folding edges, can be simulated.

ing the expansion process, the stent first shortened from 19.6 mm to 18.0 mm at $t = 2.2$ s before it elongated again to 18.5 mm at $t = 3.0$ s. Due to the expansion mechanism of the balloon wings, the proximal end of the stent rotated 84.72° around the longitudinal axis and the distal end 93.05° . This results in a total twist of 8.33° .

Furthermore, two simulations – incorporating and ignoring residual stresses due to the pre-operative processes - were performed to investigate the influence of previously experienced deformations of the balloon and the stent. As presented in Figure 2.10, the balloon and stent models incorporating residual stress expand faster and to a bigger diameter – although the latter applies only marginally.

Figure 2.11 presents the relationship between the outer diameter d of the distal stent end and the time t for the inflation test (I) and the FEA using the modeling method presented in this study (II) and classic approaches with the pure balloon geometry – which is taken from micro-CT data or created due to the use of mathematical algorithm – without residual stresses (III) and implementing a displacement-controlled expanding cylinder (IV) and a folded cylinder without tapers (V). Only the inflation test and the FEA using the presented method show a good agreement. Especially, if one considers that the expansion behavior of the balloon membrane depends on external influences such as the size of the air pockets inside the catheter, the viscosity of the expansion fluid, and the abrupt opening of the stent at a certain pressure. In the beginning, the proximal and distal stent diameter changes almost linearly, and suddenly it increases exponentially at a pressure of 0.62 MPa until it

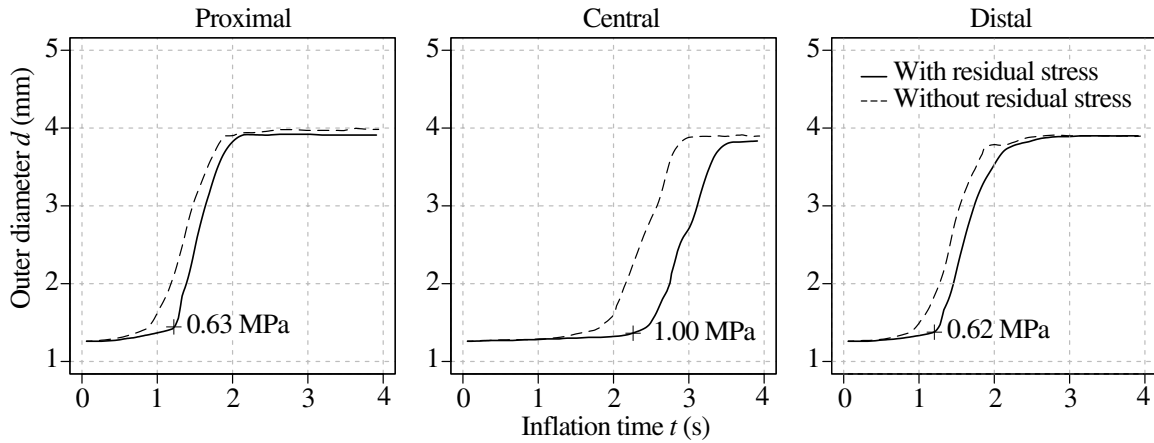


Figure 2.10 Simulation results showing the proximal, central, and distal diameter d of the Esprit V1 stent during its expansion after incorporating or ignoring initial residual stresses. By ignoring residual stresses it can be detected that all three sections of the stent expand faster and in the proximal and central section also to a bigger final diameter. The burst point, i.e., the beginning of the exponential increase of the diameter, is reached at a pressure of ~ 0.60 MPa for the proximal and distal ends.

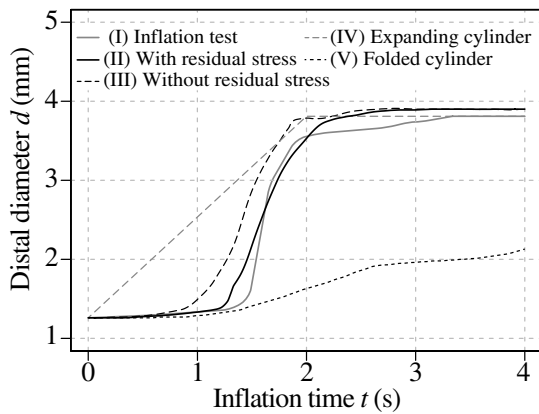


Figure 2.11 Distal stent diameter d against inflation time t of the experimental inflation tests (I) and of the FEA using the presented method incorporating initial residual stresses (II) and ignoring them (III) as well as of the FEA implementing an expanding cylinder (IV) and a folded cylinder (V) for the balloon model.

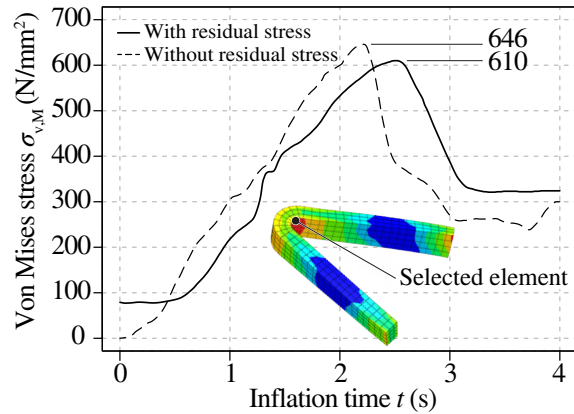


Figure 2.12 Von Mises stress $\sigma_{v,M}$ vs inflation time t for the selected finite element incorporating and ignoring initial residual stresses due to the preoperative processes. The element is randomly taken from a stent cell located at the last ring of the distal stent end.

reaches its final size. On the contrary, the displacement-controlled expanding cylinder is characterized by an expectedly linear expansion. Without the influence of faster expanding balloon tapers, the folded cylinder model expands slower and never reaches the final diameter within the simulation time.

When comparing the von Mises stress $\sigma_{v,M}$ against the time t of the simulations with and without incorporating residual stresses, differences occur again, as shown in Figure 2.12. The maximum magnitude of the von Mises stress distribution in a curved segment of the

outer ring of the distal stent end reached 610 MPa in the FEA with residual stresses and 646 MPa without residual stresses. Hence, the latter value almost exceeds the ultimate tensile strength of 671 MPa, which would incorrectly characterize the corresponding strut as a potential failure area.

2.4 Discussion

This study presents a successful workflow for more accurate FEA of SDS and stent during CSI. The expansion behavior of the SDS, i.e., the Baroonda SDS balloon catheter with its shafts and the ESPRIT V1 stent, showed in the simulation model a very satisfying agreement with the experimental results. Three factors contributed to this: (i) implementing detailed geometries of the balloon membrane and the stent without simplifying them, (ii) incorporating initial residual stresses and strains experienced during folding, pleating, and crimping, and (iii) using an implicit solver for the quasi-static problem of a CSI.

To implement the detailed geometry of the stent and the balloon, and their contact partners, the blades of the multi-head tools of the preoperative processes was indispensable for a successful FEA. The production of a crimpable balloon catheter is a complex process in which the balloon membrane is pressed into the characteristic slanted star shape. In order to obtain a realistic cross-section of the balloon, the implementation of the correct geometry of the folding blades was of great significance. The length and folding radii of the balloon wings depend on the folding blades. Also the correct arrangement of the pleating and crimping blades according to the iris principle may influence the simulation results. Both, the balloon membrane and the stent were pressed into the corners of the iris, creating a polygonal cross-section. The methods known from the literature in regard to modeling the balloon geometry with the help of numerical, CAD, or imaging techniques [294, 312–315, 330, 331, 349], and using a simple shrinking cylinder for crimping [350, 351] instead of a pleating and a crimping iris seem not to be ideal for creating a realistic model for the FEA of the stent expansion.

Furthermore, a realistic geometry of the balloon membrane influenced the simulation of certain expansion mechanism of the stent. Since the tapers start to inflate first, they appear to be responsible for the opening impulse of the stent. At a certain pressure, the balloon wings in the area of the taper open explosively and thus push against the outer stent rings. The shortening of the balloon supported this mechanism. Figure 2.11 even indicates that a balloon without tapers is not able to start the stent expansion, even if the same inner pressure is applied. In addition, the tapers prevented the stent from showing abnormal dogboning and overexpansion. An indicator of this is the slightly bulgy shape that the balloon adopted during its expansion. Figure 2.8 proves that the maximum diameter is reached in the center of the balloon. This behavior cannot be precisely captured by using balloon catheter models without tapers, as known from the study of De Beule *et al.* [294]. As the results of this study demonstrate, both balloon and stent also twisted during the preoperative processes. A consistent strut width along the entire stent also favors pronounced

dogboning. Individual cells can bend concavely (Figure 2.9(c)), which can cause stress peaks in the arterial wall and, therefore, severe vascular injuries. The authors believe that this effect could be prevented if excessive dog boning is counteracted by the reinforcement of the outer stent rings.

Furthermore, it has been shown that especially the tapers of the balloon are exposed to high stresses. Thus, the balloon membrane could already be significantly weakened during folding and pleating in addition to the damage described by Rondeau *et al.* [354] caused by crimping. Balloon tapers could typify the weak point of an SDS, which is why special attention must be paid to them during the early stage of development. However, the maxima in the von Mises stress distribution of the balloon membrane during the preoperative processes are an overestimation as they exceed the ultimate tensile strength. This is partly due to stress singularities, which occur at the folding edges and the inflection points. On the other hand, no failure criteria were defined in the material model, and the material curves were simply fitted to the experimental data. Therefore, to show the correctness of this finding, a new material model for the balloon membrane should be implemented as a future refinement step. This model must be able to mimic the anisotropic material response as well as the fatigue life of the membrane. The modeling approach must be based on data from biaxial tensile tests.

The use of a folded and pleated balloon model for the FEA of the stent expansion is crucial for the observation of expansion mechanisms of the whole SDS. As illustrated in Figure 2.9(a), the cells of every ring did not open symmetrically. The reason for this mechanism is the partial lack of contact between some stent cells and the balloon membrane. This is particularly the case when the specific stent cell is located next to the folding edge of a balloon wing. When opening the wings, the cell loses contact with the membrane. Due to the lack of friction, this cell gets now overstretched. Elsewhere along the circumferential direction, friction prevents overstretching of cells. As a result, on the one hand, stent cells are exposed to different loads and experience nonuniform strains in the circumferential direction. Perhaps this can be prevented by developing new folding techniques, which generate balloons with symmetrical cross-sections. On the other hand, the extent of stent cell deformation directly affects the shortening and elongation behavior of every individual stent ring, and consequently of the whole stent in the longitudinal direction. Thus, the shear stresses induced in the arterial wall may also be influenced indirectly by the geometry of the implemented balloon and the stent models. This unsymmetrical cell mechanism cannot be detected in FEA studies, in which simple cylindrical balloon models have been implemented [306–311]. Therefore, the present approach seems to be superior.

The authors also advise against using only a quarter or half of the stent geometry, even if the stent is perfectly symmetrical along its longitudinal axis. Necessary degrees of freedom would be erroneously constrained. The FEA of the stent expansion disclosed that the stent end twist towards each other due to the influence of the different diameters of the balloon ends. Of course, the effect of this twist and all expansion mechanisms depend on the specific balloon and stent types. However, the authors are not aware of a balloon or a stent

which feature an symmetrical geometry.

There is no question that a detailed geometry of an SDS can also be obtained from image data of micro-CT scans. This could be shown by Mortier *et al.* [349] and by the scans presented in Figure 2.7. However, the micro-CT method has some disadvantages, which is why the methodology of the present study is preferable. Firstly, micro-CT scans are usually associated with high costs. This includes high acquisition or operating costs and also the license costs for the image processing software. Second, the processing of the image data is very time-consuming. Thus, the scan of the SDS and the stent used in this study may take several hours. After that, the images must be preprocessed and segmented before the geometry can be cleaned, idealized, and meshed. Third, scans of balloon catheters and stents are often associated with a high number of disruptive image artifacts. The reason for this is the contrast ratio between the balloon membrane and the metallic stent. In addition, artifacts are induced by the X-ray marker attached to the catheter.

Evidence of residual stresses and strains which stents experience during preoperative processes (balloon folding, pleating, and stent crimping) was already shown by Möller *et al.* [353]. Now, this study demonstrates that initial residual stresses and strains have a significant impact on the results of FEA of CSI. The Expansion mechanism, the final geometry, and the stress distribution of the inflating SDS can be affected and, therefore, influence the optimization process of stents and balloon catheters. As presented in Figures 2.8 and 2.10, the balloon and the stent inflate faster and even overexpand to an unrealistic diameter if residual stresses are not implemented. This contradicts the non-compliant nature of the membrane of the Baroonda balloon catheter. Also, the time interval between the full expansion of the stent ends, and the central segments was smaller without residual stresses. This affected the extent of the dogbone and of the opening of the cells. As mentioned above, Figure 2.12 demonstrates that residual stresses prevented the stent from overexpansion. The stresses in the respective stent-strut do not exceed the ultimate tensile strength. In this case, it seems that there is no need for further optimizations of the strut geometry, in contrast to the case when residual stresses are not considered. Therefore, the consideration of residual stresses and strains can significantly influence the factors time and costs during the optimization process of a stent. In addition, If a model of an artery is implemented in the FEA, the resulting changes in the kinematic energy of the expanding stent and the contact pressure between the stent and the arterial wall can falsify the resulting stress distribution inside the biological tissue. Figure 2.13 summarizes and underlines again the benefits of the presented method in comparison with the above-mentioned refinement steps in the balloon catheter and stent modeling.

Initial residual stresses also influenced the stress distribution of the balloon and the stent during the expansion of the SDS, as illustrated in Figure 2.12. It is noticeable that the implementation of the residual stresses resulted in lower stress magnitudes, but a higher stress concentration appears when the final stent diameter was reached. This supports the hypothesis of Schiavone *et al.* [352] which states that residual stresses may contribute to the flexibility of a stent during its deployment. Therefore, it can be assumed that a realistic

	(I) Displacement controlled rigid cylinder ^{26,27,28,29}	(II) Unfolded elastic cylinder ^{30,31}	(III) Folded cylinder without tapers ³³	(IV) Modeled balloon without residual stresses ^{34,35,36,37,38,39,40}	(V) Folded, pleated, and crimped model
Time-saving	Marginal modeling effort	Low modeling effort	Medium effort to model the balloon cross-section	Complex MRI data, deflation mechanism or algorithm	Multiple simulations needed
Pressure-dependent inflation behavior	—	Unrealistically high pressure is needed	Overexpansion of the balloon ends	Realistic reaction to pressurization	Realistic reaction to pressurization
Realistic expansion mechanism	—	—	Only realistic for the central segments	Shows dogboning / concave bending	Shows dogboning / concave bending /
Influence of inflating balloon wings	—	—	—	Shows unsymmetric stent cell expansion	Shows unsymmetric stent cell expansion
Influence of taper geometry	—	—	—	Realistic expansion of the balloon ends	Realistic expansion of the balloon ends
Influence of residual stresses / strains	—	—	—	—	Realistic pressure / diameter ratio

Figure 2.13 Comparison of all modeling approaches for balloon catheters from the literature: (I) displacement controlled rigid cylinder as balloon model [306–309]; (II) unfolded elastic cylinder [310, 311]; (III) folded cylinder without tapers [294]; (IV) balloon model without residual stresses with a geometry gained from MRI data, by applying modeling algorithms, or by pressurizing the outer surface of the balloon [305, 312–315, 330, 349]; (V) folded, pleated, and crimped model – present approach. The refinement level is clearly increasing from the left to the right.

geometry obtained from micro-CT data or by mathematical algorithms is not sufficient to realistically simulate the stress/strain field of an SDS during the expansion phase.

The implicit solver used for all performed simulations turned out to be very robust. Only minor modifications on the convergence criteria had to be undertaken. The authors believe that by eliminating dynamic inertia effects induced by mass scaling during explicit time integration, the accuracy of the simulations is increased. As implicit analyses have no inherent limit on increments of the calculations, larger time steps can be performed. This significantly decreases the computational time of all performed FEA. Furthermore, realistic process times could be simulated. These findings coincide with those of Bukala *et al.* [315]. Figure 2.14 shows the advantages and drawbacks of the implicit solver in comparison with the explicit method. For solving the quasi-static problem of a CSI in FEA, the implicit solvers seem to offer more benefits

Explicit solver	Implicit solver
<ul style="list-style-type: none"> ▲ Ideal for large deformations, sliding contacts, and coarse meshes 	<ul style="list-style-type: none"> ▲ No dynamic inertia effects (mass scaling) ▲ Large time steps possible ▲ Realistic simulation time
<ul style="list-style-type: none"> ▼ Small time steps only ▼ Unrealistic simulation time ▼ Dynamic inertia effects (mass scaling) 	<ul style="list-style-type: none"> ▼ High demands on element, material, and contact quality ▼ Case-specific convergence criteria

Figure 2.14 Comparison between explicit and implicit solvers. For solving the quasi-static problem of a CSI in FEA, the implicit solvers seem to offer more benefits.

Although the suggested method seems to be sophisticated, small time steps need to be chosen to enforce equilibrium for some problems. This included the intensive deformation of the balloon membrane during the folding process and the recoiling of the stent after crimping. The chosen parameters for the convergence criteria may not function for every problem. Here, different strategies must be deliberate and tested in a few trial iterations. Finally, special care must be taken in the contact treatment to establish contact between all parts during the initial time step.

Only if basically all relevant factors of CSI are considered, i.e., the blood flow and the catheter injection medium, more precise material models, detailed geometries, and residual stresses and strains of all pre-/inter- and postoperative processes of the balloon membrane and the stent, a realistic load case for the artery can be simulated. This is the key for successful optimization processes of stents and other vascular implants such as stent grafts and transcatheter aortic valve implants. Therefore, and to continue the improvement of the presented method, the authors consider additional aspects for future studies. Balloon catheters usually tend to expand from their proximal to their distal end. Responsible for

this is the fluid, which is injected into the catheter. It breaks through the cavities of the balloon membrane, which are separated by the stent segments. By adding more fluid the internal pressure increases, the cavities get connected, and the stent rings expand step by step. This procedure could be simulated using the method of fluid-structure interaction or by expanding the balloon catheter via the discrete element method. With such a model, a more realistic pressure/time behavior may be achieved. Own preliminary studies were already presented by Wiesent *et al.* [316].

Furthermore, an anisotropic material model of the balloon membrane with failure criteria needs to be implemented. Balloons of catheters are manufactured by blow molding. It is very likely the case that due to the production process, the polymer chains are orientated in the circumferential direction. In the future thermomechanical effects should also be investigated, since the blades of the folding and pleating devices are heated to prevent the recoiling of the balloon membrane. Even though this is beyond the scope of the present study, in future investigations, the most important contact partner of a stent should be implemented – the artery. Therefore, a precise damage and growth model for the specific target vessel, based on experimental data, is needed.

In conclusion, the importance of preoperative processes of SDS and stents – balloon folding, pleating, and stent crimping – on the FEA of stent expansion models have been analyzed. The results demonstrate that the incorporation of initial residual stresses experienced during the previous production step significantly increased the accuracy of subsequent simulations and especially of the FEA of the stent expansion. During the preoperative processes, stresses inside the membrane and stent material also reached a severe level. Therefore, it can not be excluded that an SDS or stents are already damaged before the actual surgery. The implementation of the realistic geometry of an SDS, in particularly the balloon tapers, and of blades of the process devices improved the simulation of important expansion mechanism, like dogboning and concave bending or overexpansion of stent cells. Furthermore, this study showed that up-to-date implicit solvers are able to precisely analyze all mentioned quasi-static processes without the manipulation of the simulation time or the physical mass. Finally, the authors recommend to optimize the preoperative processes in a way that the resulting balloons catheters feature symmetrical cross-sections, and that stents show reduced dogboning and limited concave cell bending.

Acknowledgment

This study was funded by the Bavarian Research Foundation within the project ‘PIZ-225-18’. The authors express their gratitude to Fabian Koch and to Ulrich Weber, who performed preliminary FEA using an explicit solver. A special thank goes to Birgit Striegl from the Regensburg Center of Biomedical Engineering of the Regensburg University of Applied Sciences for performing all micro-CT scans and to Siegfried Schrammel as well as Friedrich Muehlenberg for the technical support in the experimental setups for the inflation tests. Furthermore, the authors are grateful for the free samples of the tested balloon

catheter delivered by Bavaria Medizin Technologie GmbH.

3 Experimental and Mathematical Characterization of Coronary Polyamide-12 Balloon Catheter Membranes

Abstract. The experimental quantification and modeling of the multi-axial mechanical response of polymer membranes of coronary balloon catheters have not yet been carried out. Due to the lack of insights, it is not shown whether isotropic material models can describe the material response of balloon catheter membranes expanded with nominal or higher, supra-nominal pressures. Therefore, for the first time, specimens of commercial polyamide-12 balloon catheter membranes were investigated during uniaxial and biaxial loading scenarios. Furthermore, the influence of kinematic effects on the material response was observed by comparing results from quasi-static and dynamic biaxial extension tests. Novel clamping techniques are described, which allow to test even tiny specimens taken from the balloon membranes. The results of this study reveal the semi-compliant, non-linear, and viscoelastic character of polyamide-12 balloon catheter membranes. Above nominal pressure, the membranes show a pronounced anisotropic mechanical behavior with a stiffer response in the circumferential direction. The anisotropic feature intensifies with an increasing strain-rate. A modified polynomial model was applied to represent the realistic mechanical response of the balloon catheter membranes during dynamic biaxial extension tests. This study also includes a compact set of constitutive model parameters for the use of the proposed model in future finite element analyses to perform more accurate simulations of expanding balloon catheters.

3.1 Introduction

Finite element analysis (FEA) has become a powerful tool for the optimization process of coronary balloon catheters and stents. FEA enables the prediction of the stress/strain response of stents and balloon catheters, and the constituents of the coronary artery to static and dynamic loading. Nevertheless, almost all state-of-the-art FEA of expanding balloon catheter and stent included standard isotropic material models for balloon membranes, in which the mathematical formulation and the material parameters were based on data of unprocessed polymers [313, 315, 330, 331, 363, 364]. One exception is presented by Gasser and Holzapfel [333] where a versatile theory of fiber-reinforced materials is used according to [60] in order to mimic the anisotropic material response of angioplasty balloon membranes. However, in their study, the material and structural parameters of the balloon membrane model were not quantified by experimental data but fitted according to the respective inflation characteristic of the analyzed balloon catheter.

Membranes of coronary balloon catheters are mostly produced from polymers like polyethylene (PE), polytetrafluoroethylene (PTFE), polyurethane (PUR), or polyamides (PA). Many groups are known which investigated the morphology and the associated anisotropic material behavior of extrusion-casted films of such polymers by performing uni- or biax-

ial extension tests, differential scanning calorimetry (DSC), Fourier transform infrared (FTIR) spectroscopy, small-angle X-ray scattering (SAXS), and wide-angle X-ray diffraction (WAXD) [365–368]. However, there is no openly available literature dealing with the study of the multiaxial mechanical properties of processed polymers of balloon catheter membranes.

Balloon catheter membranes with their typical cylindrical shape and two tapers are produced by the manufacturing technique of balloon-forming, a specific blow-molding technique. The standard procedure was described in detail by Sauerteig and Giese [288], Garramone [289], and Fu *et al.* [290]. The main production steps, schematically presented in Figure 3.1(a), can be summarized as follows: (i) during extrusion, the dried granular raw material is fed into a screw-driven and heated extruder with a shaping dye and then it is extruded into tubes; (ii) while necking, chilled and cropped tubes get stretched into parisons with necked ends; (iii) in the actual balloon forming process, the parison is inserted into a hollow glass mold and heated up to the specific glass-transition temperature T_g while being pressurized. The authors assume that the morphology of balloon catheter membranes

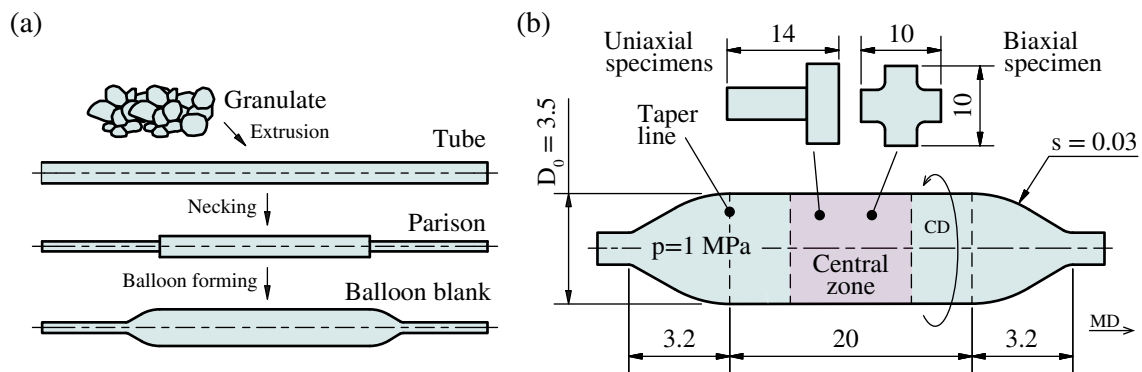


Figure 3.1 Manufacturing cycle and geometry of the Baroonda SDS balloon catheter: (a) schematic production cycle of balloon catheter blanks; (b) illustration of the blank of the Baroonda SDS balloon catheter after blow molding. In the present study, specimens for uniaxial extension, quasi-static and dynamic biaxial testing were taken from the central zone. For location-depending biaxial testing, specimens were also extracted next to the taper lines. All dimensions are in mm and taken from Geith *et al.* [363]. MD: machine direction; CD: circumferential direction; D_0 : outer diameter at the unpressurized state; s : thickness of the membrane; p : nominal pressure.

changes several times during each of these production steps. Thus, Aggarwal *et al.* [366] found that the molecular chains of the molten polymer align in flow/machine direction (MD) inside the extruder. However, as soon as the polymer leaves the extruder it cools down and needle-like crystallites start to form. These crystallites proliferate perpendicular to the molecular chains and, therefore, to MD. In the flowing matrix, the crystallites rotate and align parallel to MD, which leads to molecular chains in the crystalline areas pointing perpendicular to MD [365]. With necking most manufactures artificially increase the degree of crystallinity of the ends of the parison, while the central part which is going to be molded into the balloon should remain unchanged. By pressurizing and heating the pari-

son to T_g during the balloon-forming process, still amorphous molecular chains are free to flow and additionally stretch in circumferential direction (CD) [369]. This can cause an excessive softening of the blank's membrane in MD. To compensate this effect after the forming pressure is reached and to shape the tapers of the balloon membrane, the blank is additionally stretched in MD during several drawing steps. Thus, the crystallinity of membrane increases. Due to the complexity of the production process, it is plausible that the material response of the final membrane differs from the ones of the raw material through the deliberate reorientation of the crystalline regions and the molecular chains of the polymer. However, it has not yet been investigated whether the manufactured membranes show an isotropic or an anisotropic material behavior.

A polymer that is established in the manufacture of coronary balloon catheter membranes is the semicrystalline polyamide-12 (PA 12). The material behavior of the heated PA 12 during the balloon forming process was experimentally and numerically analyzed by Menary and Armstrong [370] and Fu *et al.* [290]. However, to the authors' knowledge, no study is published which documents the mechanical behavior of finished balloon catheter membranes made of PA 12 or other polymers under uni- or biaxial extension and under realistic testing conditions. Due to the lack of mechanically derived experimental data, the influence of the balloon forming process on the material behavior of PA 12 is not known. The authors suppose, that future FEA of balloon catheter and stent expansion could be significantly improved, by using a suitable material model for polymers with experimentally verified constitutive parameters for PA 12 balloon membranes.

Thus, this study presents a detailed description of the material characteristics of a standard commercial PA 12 balloon catheter for main coronary arteries and proposes a simple micro-structurally motivated constitutive model which is able to mimic the pronounced anisotropic material response observed in the performed experiments. The outcomes finally deliver the essential ingredients for the implementation of realistic balloon catheter material models in FEA. For this purpose, various uni- and biaxial extension tests with quasi-static and dynamic loading scenarios were performed on specimens of a state-of-the-art balloon catheter for coronary interventions. The study also describes how to prepare tiny strip-type as well as cross-shaped specimens and novel clamping techniques for uniaxial- and biaxial tests. Moreover, Cauchy stresses and stretches were computed to analyze the multiaxial viscoelastic features of the PA 12 membranes. Finally, material parameters were identified by fitting the proposed constitutive model to the data set of biaxial extension tests.

3.2 Materials and Methods

3.2.1 Coronary balloon catheter

As in the previous study published by the authors [363], membranes of the Baroonda stent delivery system (SDS, 08BO-3520A, Bavaria Medizin Technologie, Wessling, Germany) were used for all present investigations (see Figure 3.1(b)). The balloon membrane of

the Baroonda SDS was fabricated from PA 12, also known as 'Nylon 12' or under the trademark 'Grilamid', featuring a density of $\rho = 1010 \text{ kg/m}^3$ and a Poisson's ratio of $\nu = 0.40$. According to the manufacturer, the balloon membrane shows a semi-compliant character, i.e., a limited increase of the diameter past the nominal pressure. The *in vivo* nominal pressure of the Baroonda SDS is $p = 1 \text{ MPa}$. The cylindrical part of the balloon blank has a length of 20 mm and an outer diameter at the unpressurized state of $D_0 = 3.5 \text{ mm}$. The thickness of the membrane is $s = 30 \pm 1 \mu\text{m}$.

3.2.2 Specimen preparation

For both, uni- and biaxial testing, the tapers of the balloon blanks had to be removed with a scalpel. Afterward, the cylindrical parts of the balloon blanks were pushed over forceps to slice the membrane along MD. The specimen preparation for uni- and biaxial testing differs and can be described as follows: (i) To perform uniaxial extension tests, two samples were excised from the central zone of three membranes, as depicted in Figure 3.1(b) – one with its long side parallel to MD and the other with its long side parallel to CD. These rectangular specimens had dimensions of $10 \times 4 \text{ mm}$. The long side of the specimens pointed either in MD or in CD of the balloon blank. At the center of every specimen two fine lines with a distance of approximately 2.5 mm between each other were added as markers for subsequent video-extensometer (VE) measurements (Figure 3.2(a)).

To prevent slipping between the specimens and the clamps of the extension testing device, $8 \times 4 \text{ mm}$ pieces of strong double-sided adhesive tape Doppelband Extrem (45531, UHU, Baden, Germany) had to be attached to $20 \times 10 \text{ mm}$ pieces of sandpaper Super Easy Cut P120 (65459, SCHULLER Eh'klar, Austria) (Figure 3.2(b)). Finally, the bottom surface of each end of the membrane specimens was attached to a piece of sandpaper via previously-applied adhesive tape, and the sandpaper was folded in half to press its upper part with adhesive tape onto the surface of the membrane (Figure 3.2(c)). (ii) For biaxial testing, specimens with a simple cross shape were found to be the best option after performing several preliminary tests on the tiny balloon membranes. First, square cuts were again taken from the central zone of the balloon membranes (see Fig 3.1(b)), which were then cropped into a cross shape. The cross had a dimension of $10 \times 10 \text{ mm}$ with a flank width of 4 mm (Figure 3.3(a)).

To prevent crack formation at the cross edges, a curved transition with a radius of 0.5 mm had to be fabricated by using a biopsy punch Integra™ Miltex® (3331AA, Integra, Plainsboro, NJ, USA). The center of the cross was marked with four small dots for VE measurements. Due to the small specimen size, a special clamping system had to be designed and manufactured (Figures 3.3(b) and (c)). It consists of an upper and a lower clamp, a pin, and a countersunk bolt on each cross side, and a centered support platform. All parts were made of aluminum to minimize the influence of the weight on the measurement results. As a first step, fine double-sided adhesive tape 3M Scotch (6651263, 3M, Saint Paul, MN, USA) had to be placed on the support platform to prevent the specimen from slipping. Next, the cross-shaped specimen was attached to the top surface of the support platform.

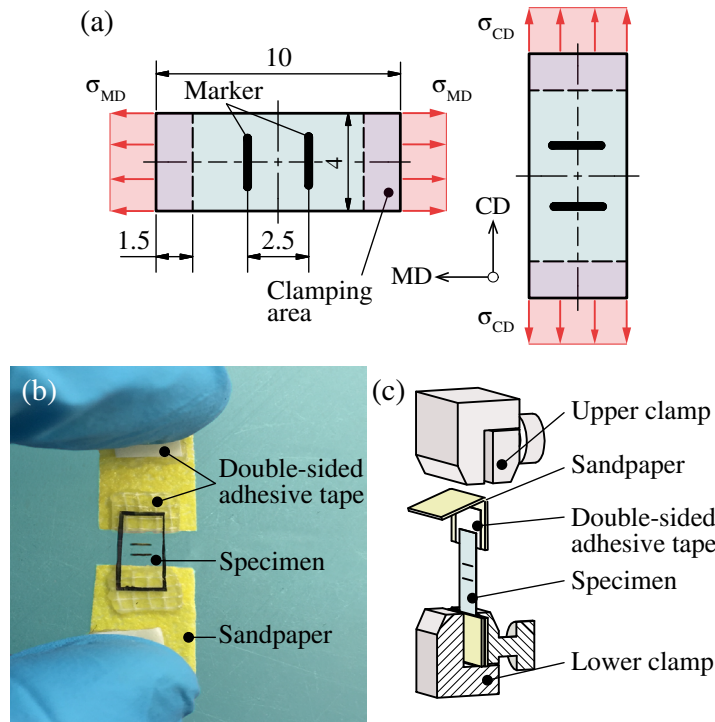


Figure 3.2 Specimen preparation for uniaxial extension testing: (a) sketch of a rectangular specimens for uniaxial extension tests cut from the balloon membrane in MD or CD; (b) photograph of a specimen with double-sided adhesive tape and sandpaper before testing; (c) two thin markers were added for stretch measurement. Schematic sketch of the clamping method. The rectangular strips were attached to sandpaper with adhesive tape to obtain the required friction between the specimen and the clamps of the uniaxial testing device. All dimensions are in mm. MD: machine direction; CD: circumferential direction; σ_{MD} : Cauchy stress in MD; σ_{CD} : Cauchy stress in CD.

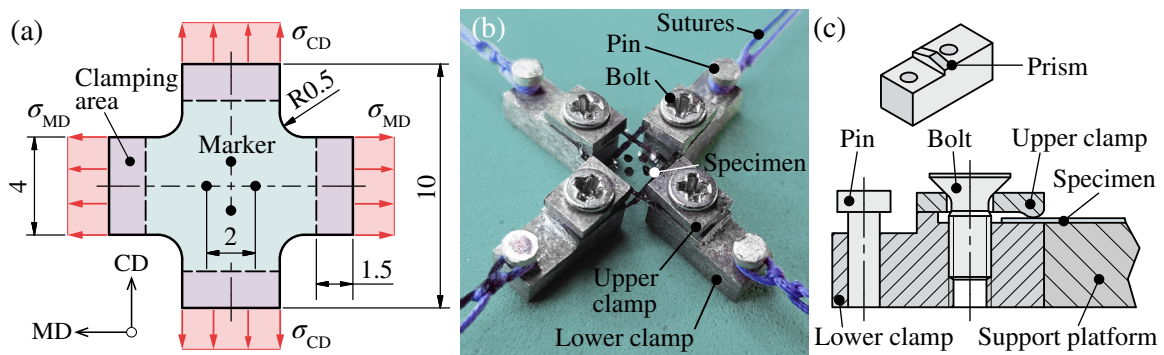


Figure 3.3 Specimen preparation for biaxial extension testing: (a) sketch of the cross shape of a specimen for biaxial extension testing; (b) photograph of the cross-like specimen mounted in the clamping system and surgical sutures; (c) cross-section of one unit of the clamping system and isometric view of the lower clamp with its prismatic surface. With thin double-sided adhesive tape, the specimens were placed on the support platform, which helps to place all upper and lower clamps symmetrically. All dimensions are in mm. MD: machine direction; CD: circumferential direction; σ_{MD} : Cauchy stress in MD; σ_{CD} : Cauchy stress in CD.

Here it is important that the inner surface of the membrane faces to the support platform to keep the curling membrane flat. After pushing the lower clamps into the cavities of the platform, the upper clamps were assembled with the countersunk bolts. The top side of the lower clamps is shaped like a prism. Therefore, the back of the upper and lower clamps only touch each other at the peak of that prism. When tightening the bolts, both – upper and lower clamps – align themselves, which exerts a homogeneous clamping pressure along every flank of the cross-shaped specimen. Due to the special shape of the clamps, no sandpaper was needed. Finally, the support platform with the adhesive tape was removed and a thick surgical suture could be tied to every pin for the attachment of the clamping system to the biaxial extension testing device. Both, the specimen geometry and the clamping system were designed to reduce the boundary effects with the aim to obtain a relatively large homogeneous deformation and stress field in the center of the specimen, where the deformations are tracked.

3.2.3 Uniaxial extension tests

Preliminary mechanical experiments were performed by using the uniaxial extension testing device μ -strain (ME 30-1, Messphysik Materials Testing, Fürstenfeld, Austria) in combination with the 20 N load cell Xforce HP (Zwick Roell, Ulm, Germany) with an accuracy of 0.02 % [371]. Every specimen got submerged for 15 min in 37 °C warm decalcified water to overcome hygroscopic and thermal changes inside the PA 12. These effects are well known from the literature [372, 373], and might occur during a several minutes lasting coronary intervention. With the results from the VE ME 46-350 (Messphysik Materials Testing, Fürstenfeld, Austria) with a resolution of $\pm 0.15 \mu\text{m}$ and a sample rate of $f_s = 20 \text{ Hz}$, the specimen stretches λ_{MD} and λ_{CD} were calculated according to

$$\lambda_{\text{MD}} = \frac{l_{\text{MD}}}{L_{0,\text{MD}}} \quad \text{and} \quad \lambda_{\text{CD}} = \frac{l_{\text{CD}}}{L_{0,\text{CD}}}, \quad (3.1)$$

where l_{MD} and l_{CD} are the current deformed lengths and $L_{0,\text{MD}}$ and $L_{0,\text{CD}}$ are the reference lengths of the specimen with its long side pointing to MD or CD, respectively. The lengths $L_{0,\text{MD}}$ and $L_{0,\text{CD}}$ were measured after the specimen was attached to the device and preloaded with 0.01 N. Before the actual experiment, the specimen was preconditioned. Therefore, several loading and unloading cycles with a testing speed of $v_{\text{test}} = 1 \text{ mm/min}$ were performed to a stretch of $\lambda = 1.02$. After a maximum of four preconditioning cycles, no more softening was recognized and the stress-stretch behavior of the membrane could be reproduced.

The question of whether preconditioning should be performed prior uni- or biaxial extension testing is controversial. During the preconditioning phase the specimen exhibits a softening effect until the results become reproducible. In fact, most manufacturers expand their balloon catheters several times with the *in vivo* nominal pressure after production to check their functionality. Thus, the authors assume, that the balloon membrane is in a preconditioned state prior to implantation.

For further proceedings, three specimens were stretched with a quasi-static testing velocity of 1 mm/min until rupture. Under the assumption of incompressibility, Cauchy stresses σ_{MD} and σ_{CD} were calculated as

$$\sigma_{\text{MD}} = \frac{f_{\text{MD}}}{W_{\text{CD}}T} \lambda_{\text{MD}}, \quad \sigma_{\text{CD}} = \frac{f_{\text{CD}}}{W_{\text{MD}}T} \lambda_{\text{CD}}, \quad (3.2)$$

with f_{MD} and f_{CD} denoting the current forces, $W_{\text{MD}} = W_{\text{CD}} = 4 \text{ mm}$ and $T = 0.03 \text{ mm}$ are the mean specimen width and the thickness in the reference state, respectively.

3.2.4 Biaxial extension tests

To determine the multiaxial mechanical response of balloon catheter membranes under typical deformations during coronary interventions, planar biaxial extension tests were carried out. For the tests, a customized biaxial extension testing device described by Sommer *et al.* [374] with four linear stages, the 50 N load cells U9C (HBM, Darmstadt, Germany) with an accuracy of 0.2 % and a position-controlled testing protocol could be used. The stretch measurement was performed with the software Laser Speckle Extensometer (Version 2.23.3.0, Messphysik Materials Testing, Fuerstenfeld, Austria) with a resolution of $\pm 0.15 \mu\text{m}$ and a sample rate of $f_s = 20 \text{ Hz}$. Before starting the tests, all specimens were submerged for 15 min in 37 °C warm decalcified water. Every side of the cross-shaped specimen was attached to the respective linear stage of the testing rig via the mentioned clamping system and thick surgical sutures. Every suture was placed collinear to the center axis of the respective load cell. The specimen was preloaded in MD and CD to lift the specimen, sutures, and the clamps up to the level of the center lines of the four load cells. Afterward, the VE camera had to be focused onto the specimen and calibrated to enable stretch measurements. Preloading forces of only 0.02 N were vanishingly small in comparison to the maximum forces measured in the proposed study. Therefore, and since stretch measurements were only possible if the specimen was within the focal of the camera, all preloading forces were neglected and set to zero before starting the experiment. In order to observe a possible anisotropic character of the processed PA 12 and to account for its viscoelastic features as well as the location-dependent mechanical behavior of the balloon membrane, three test scenarios were executed as follows:

(i) **Quasi-static biaxial testing.** Three specimens were stretched with a testing velocity of $v_{\text{test}} = 1 \text{ mm/min}$ and underwent a systematic sequence of stretch ratios $(\lambda_{\text{MD}} - 1) : (\lambda_{\text{CD}} - 1) = \{1 : 1, 1 : 0.75, 0.75 : 1, 1 : 0.5, 0.5 : 1\}$ in MD and CD. Furthermore, the equibiaxial stretch-protocol with an increasing stretch in $\Delta\lambda = 0.02$ steps, starting at $\lambda = 1.02$ was performed on three additional specimens. This biaxial testing approach was proven to provide the basic set of material parameters for a subsequent modeling of the in-plane anisotropy [374].

(ii) **Dynamic biaxial testing.** To investigate the viscoelastic features of PA 12 under dynamic loading, the tests of (i) had to be repeated with a testing velocity of $v_{\text{test}} =$

10 mm/min. In addition, equibiaxial tests on three specimens were performed with the stretch increasing until failure, i.e., the specimens slipped out of the clamps or cracks started to form. An approximation of the actual inflation speed v_{app} can be derived as

$$v_{\text{app}} = \frac{\Delta U}{\Delta t} = \frac{\pi(D_{\text{max}} - D_0)}{t - t_0}, \quad (3.3)$$

where $D_0 = 3.5$ mm is the diameter of a fully unfolded but yet not stretched balloon catheter membrane at $t_0 = 2.95$ s in Fig 3.4. The diameter D_0 equals to the outer diameter of the tested membrane blanks (see Fig 3.1(b)). The maximum diameter of the stretched membrane at nominal pressure at $t = 3.33$ s is denoted by D_{max} . The diameter D_{max} of the fully expanded Baroonda SDS balloon catheter can be determined by analyzing the data of the stent inflation tests known from Geith *et al.* [363] and presented in Figure 3.4. By measuring the outer diameter of the stent in the fully expanded state under the nominal pressure and by subtracting the stent strut height of $h = 0.12$ mm, the maximum outer diameter is $D_{\text{max}} = 3.57$ mm. This leads to an inflation speed of $v_{\text{app}} = 34.72$ mm/min and a corresponding stretch of $\lambda_{\text{app,CD}} = D_{\text{max}}/D_0 = 1.02$ in CD. Despite the fact that $v_{\text{test}} \ll v_{\text{app}}$, a further increase in the testing velocity leads to not reproducible results due to errors in the VE measurements.

(iii) **Location-dependent biaxial testing.** One can hypothesize that the preferred orientations of the crystallites and the molecular chains in the taper region differ from the ones in the center of the membrane. To prove this hypothesis, further quasi-static biaxial tests similar to (i) were carried out with specimens that were extracted next to the taper lines of the balloon catheter membrane, as shown in Figure 3.1(b). The data were compared with the results from tests with centered specimens. Only one specimen could be taken from every blank due to the short length of the balloon catheter membrane in MD. The authors do not expect different test results for samples taken at different locations along the circumference and, therefore, assume a homogeneous material response along CD.

Because of the limited amount of donated balloon membrane blanks, all biaxial tests – static/dynamic equibiaxial stretch tests, static/dynamic stretch ratio sequences, dynamic equibiaxial rupture tests, and location-dependent tests – were only repeated two times. This results in 18 specimens for biaxial testing and additionally six specimens for uniaxial testing. Only tests in which the specimens did not tear at the clamp edges or were pulled out of the clamps were rated as successful. In total 16 biaxial tests and four uniaxial tests failed, which gives a total number of 44 specimens.

Cauchy stresses in MD and CD were computed as

$$\sigma_{\text{MD}} = \frac{f_{1,\text{MD}} + f_{2,\text{MD}}}{2W_{\text{CD}}T} \lambda_{\text{MD}}, \quad \sigma_{\text{CD}} = \frac{f_{1,\text{CD}} + f_{2,\text{CD}}}{2W_{\text{MD}}T} \lambda_{\text{CD}}, \quad (3.4)$$

in which $f_{1,\text{MD}}$, $f_{2,\text{MD}}$, and $f_{1,\text{CD}}$, $f_{2,\text{CD}}$ represent the measured reaction forces and $\lambda_{\text{MD}} = x_{\text{MD}}/X_{\text{MD}}$, $\lambda_{\text{CD}} = x_{\text{CD}}/X_{\text{CD}}$ the membrane stretches in MD and CD, respectively, calcu-

lated with the marker distances in the actual, loaded (x_{MD} , x_{CD}) and the reference (X_{MD} , X_{CD}) states. Due to the specimen size, the detection of shear components was neglected and the overall mechanical response of the PA 12 membranes was assumed to be incompressible.

3.2.5 Material modeling

The PA 12 balloon catheter membrane was modeled as a fiber-reinforced incompressible rubber-like hyperelastic material in which an isotropic matrix material, the amorphous domain, is reinforced by two families of extensible fibers, aligned due to crystallization, rendering the balloon catheter material anisotropic. It is assumed that all fibers of the two fiber families are perfectly aligned, continuously distributed throughout the material and can therefore be described by the two direction vectors \mathbf{M} and \mathbf{M}' in the reference configuration. Hence, the continuum theory of fiber-reinforced materials is the constitutive theory of choice. Briefly, in continuum mechanics a material point \mathbf{X} of a body in the reference configuration is transformed to a position $\mathbf{x} = \chi(\mathbf{X})$ in the deformed configuration by means of the bijective map χ . In addition, the deformation gradient $\mathbf{F} = \partial\chi(\mathbf{X})/\partial\mathbf{X}$ is introduced, as well as the left Cauchy-Green tensor $\mathbf{b} = \mathbf{F}\mathbf{F}^T$ and the right Cauchy-Green tensor $\mathbf{C} = \mathbf{F}^T\mathbf{F}$. For hyperelastic materials the material response can be quantified in terms of a strain-energy function Ψ , i.e., the recoverable energy stored in the material as it deforms. Hence, the generalized polynomial-type elasticity relations first published by Rivlin and Saunders [375] with a polynomial extension for the anisotropic part were applied. The related strain-energy function Ψ for the fiber-reinforced incompressible material takes on the form

$$\Psi = -\frac{\hat{p}}{2}(I_3 - 1) + \widehat{\Psi}(I_1, I_2, I_4, I_6), \quad (3.5)$$

where the strain-energy function Ψ is defined for the incompressibility constraint $I_3 = \det\mathbf{C} \equiv 1$, \hat{p} is an indeterminate Lagrange multiplier, and the second term is defined as

$$\widehat{\Psi}(I_1, I_2, I_4, I_6) = c_{10}(I_1 - 3) + c_{02}(I_2 - 3)^2 + c_{11}(I_1 - 3)(I_2 - 3) + k_1 \sum_{i=4,6} (I_i - 1)^2, \quad (3.6)$$

with c_{10} , c_{02} , c_{11} and k_1 are material parameters, and I_1 , I_2 , I_4 and I_6 are four invariants defined by

$$I_1 = \text{tr}\mathbf{C}, \quad I_2 = \frac{1}{2} [(\text{tr}\mathbf{C})^2 - \text{tr}(\mathbf{C}^2)], \quad I_4 = \mathbf{C} : \mathbf{M} \otimes \mathbf{M}, \quad I_6 = \mathbf{C} : \mathbf{M}' \otimes \mathbf{M}'. \quad (3.7)$$

The two invariants I_4 and I_6 denote the square of the fiber stretches in the fiber directions \mathbf{M} and \mathbf{M}' , respectively [376]. Thus, the term in Ψ associated with the invariants I_4 and I_6 accounts for the nonlinear stiffening of the fibers with increasing fiber stretch. Both fiber families are modeled as equally strong and are assumed to be symmetric with respect to CD. Hence, the fiber directions $[\mathbf{M}] = [\cos \alpha, \sin \alpha, 0]^T$ and $[\mathbf{M}'] = [\cos \alpha, -\sin \alpha, 0]^T$ are defined by the angle α measured with respect to CD. The constitutive equation for the

Cauchy stress tensor $\boldsymbol{\sigma}$ is obtained as

$$\boldsymbol{\sigma} = -\hat{p}\mathbf{I} + (\hat{\psi}_1 + I_1\hat{\psi}_2)\mathbf{b} - \hat{\psi}_2\mathbf{b}^2 + \hat{\psi}_4\mathbf{m} \otimes \mathbf{m} + \hat{\psi}_6\mathbf{m}' \otimes \mathbf{m}', \quad (3.8)$$

where $\mathbf{m} = \mathbf{FM}$ and $\mathbf{m}' = \mathbf{FM}'$ denote the two direction vectors in the current configuration. For notational simplicity we have introduced the abbreviation $\hat{\psi}_i = 2\partial\hat{\Psi}/\partial I_i$, $i = 1, 2, 4, 6$.

For biaxial extension (neglecting shear) the deformation gradient, the left and right Cauchy-Green tensors can be expressed in terms of principal stretches. In the matrix form this reads $[\mathbf{F}] = \text{diag}[\lambda_{\text{MD}}, \lambda_{\text{CD}}, \lambda_z]$ and $[\mathbf{b}] = \text{diag}[\lambda_{\text{MD}}^2, \lambda_{\text{CD}}^2, \lambda_z^2] = [\mathbf{C}]$, where λ_z denotes the stretch orthogonal to the plane spanned by MD and CD. By means of the thin membrane assumption ($\sigma_{zz} = 0$), and by considering the incompressibility constraint ($\det\mathbf{C} \equiv 1$), the only non-zero components of Cauchy stress tensor $\boldsymbol{\sigma}$ are the normal stresses in MD and CD, which read

$$\sigma_{\text{MD}} = -\hat{p} + (\hat{\psi}_1 + I_1\hat{\psi}_2)\lambda_{\text{MD}}^2 - \hat{\psi}_2\lambda_{\text{MD}}^4 + (\hat{\psi}_4 + \hat{\psi}_6)\lambda_{\text{MD}}^2 \cos^2 \alpha, \quad (3.9)$$

$$\sigma_{\text{CD}} = -\hat{p} + (\hat{\psi}_1 + I_1\hat{\psi}_2)\lambda_{\text{CD}}^2 - \hat{\psi}_2\lambda_{\text{CD}}^4 + (\hat{\psi}_4 + \hat{\psi}_6)\lambda_{\text{CD}}^2 \sin^2 \alpha, \quad (3.10)$$

with

$$\hat{p} = (\hat{\psi}_1 + I_1\hat{\psi}_2)(\lambda_{\text{MD}}\lambda_{\text{CD}})^{-2} - \hat{\psi}_2(\lambda_{\text{MD}}\lambda_{\text{CD}})^{-4}. \quad (3.11)$$

The estimation of the material parameters c_{10} , c_{02} , c_{11} , k_1 and α was achieved by applying the least-squares method for the nonlinear objective function, which is

$$\phi = \{c_{10}, c_{02}, c_{11}, k_1, \alpha\} = \underset{\phi}{\text{argmin}} \chi^2(\phi), \quad (3.12)$$

where the objective function is defined as

$$\chi^2(\phi) = \sum_{ij \in \zeta} \frac{\sum_{n=1}^{N_{ij}^{\text{exp}}} (\sigma_{ij}^n - \bar{\sigma}_{ij}^n)^2}{\max(\bar{\sigma}_{ij}^n)}, \quad (3.13)$$

with $\zeta \in [\text{MD}, \text{CD}]$ are the experimental modes and N_{ij}^{exp} denotes as the number of of experimental data points for both directions. The analytical results of the stress are denoted by σ_{ij} and the experimental results by $\bar{\sigma}_{ij}$. The normalization is performed in order to weight the data from the two experimental modes equally. With the intention to cover a wide deformation range, three more dynamic equibiaxial extension tests until failure were performed. For the nonlinear data fitting, MATLAB R2019a (The MathWorks, Natick, USA) with the `lsqnonlin` function was used to estimate the material parameters (c_{10} , c_{02} , c_{11} , k_1 , and α) by minimizing the least-squares differences between the computational and the experimental data. The quality of the estimation was evaluated by calculating

the correlation coefficients R_{MD}^2 and R_{CD}^2 for both directions according to

$$R_{ij}^2 = \frac{\sum_{n=1}^{N_{ij}^{\text{exp}}} [(\sigma_{ij}^n - \sigma_{ij}^{\text{mean}}) (\bar{\sigma}_{ij}^n - \bar{\sigma}_{ij}^{\text{mean}})]}{\sqrt{\sum_{n=1}^{N_{ij}^{\text{exp}}} (\sigma_{ij}^n - \sigma_{ij}^{\text{mean}})^2} \sqrt{\sum_{n=1}^{N_{ij}^{\text{exp}}} (\bar{\sigma}_{ij}^n - \bar{\sigma}_{ij}^{\text{mean}})^2}} \quad \text{for } ij \in \{\text{MD}, \text{CD}\}, \quad (3.14)$$

where $R_{ij}^2 \in [0, 1]$ ($R_{ij}^2 = 1$ indicates a perfect estimation of the model parameter), and $\sigma_{ij}^{\text{mean}}$, $\bar{\sigma}_{ij}^{\text{mean}}$ are mean stresses, while σ_{ij}^n , $\bar{\sigma}_{ij}^n$ are the stresses at any data point predicted by the model and calculated from the experimental data, respectively. The root-mean-square error (RMSE) was calculated by

$$\text{RMSE} = \frac{\sqrt{\frac{\chi^2(\phi)}{\sum_{ij \in \xi} N_{ij}^{\text{exp}} - q}}}{\sum_{ij \in \xi} \bar{\sigma}_{ij}^{\text{mean}}}, \quad (3.15)$$

in which q is the number of parameters in ϕ , compare with Holzapfel *et al.* [115] and Schulze-Bauer *et al.* [96].

Robustness of the parameter estimation was ensured by using: (i) a variety of different loading conditions (i.e., stretch ratios) to make sure that the hyperelastic material model is able to predict correct stress values under all conditions of interest; and (ii) different roots for the initial guesses of the fitting procedure. A minimum of six minimization cycles ensured that best-fit parameters are independent of the initial guesses. Hence, the authors focus here more on the robustness of the entire model prediction than on the individual parameters. Nevertheless, physical relevance of the parameters has to be ensured, e.g., by restricting the search space [377].

Although the authors assume that PA 12 is highly viscoelastic, a respective model feature has not been implemented. Similar to many FEA based studies who describe the maximum stresses in stents and catheters during expansion [313, 315, 330, 331, 363, 364], only the loading curve is of interest to the authors to be able to investigate the maximum stresses in vascular tissue in future work.

3.3 Results

3.3.1 Uniaxial mechanical response

A representative Cauchy stress-stretch response of the PA 12 balloon membrane during preliminary uniaxial rupture tests is presented in Figure 3.5. The tests reveal a nonlinear and anisotropic stress-stretch response of PA 12 in MD and CD. The membrane shows a pronounced stiffer response for small and large stretches in CD. In MD, the specimens are very ductile, especially at minimal and very large stretches, while an increase in the stiffness is detectable at medium stretches. The median of the Cauchy stress in MD at

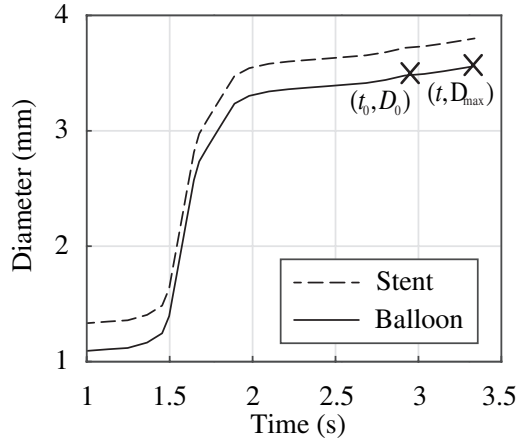


Figure 3.4 Stent and balloon diameter vs. inflation time. The dashed curve of the stent inflation tests was adapted from Geith *et al.* [363]. t_0 : time at which the balloon reaches its initial diameter; t : time at which the balloon reaches its final diameter at nominal pressure; D_0 : initial balloon diameter; D_{\max} : diameter at nominal pressure.

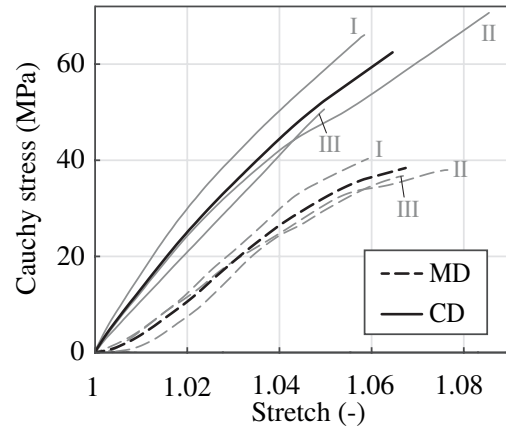


Figure 3.5 Uniaxial Cauchy stress-stretch relationship in MD and CD. The diagram shows the results of respectively three specimens (I, II, III). The bold solid and bold dashed curves represent the corresponding median curves.

$\lambda = 1.02$ was computed to be $\tilde{\sigma}_{\text{MD}} = 8.4$ MPa, which is 40.2% of the corresponding Cauchy stress at the equal stretch $\lambda_{\text{app,CD}}$ at nominal pressure in CD with $\tilde{\sigma}_{\text{CD}}(\lambda_{\text{app,CD}}) = 20.9$ MPa. The median of the ultimate tensile stress at rupture in MD was calculated to be $\tilde{\sigma}_{\text{MD,max}} = 32.0$ MPa, which is 61.4% of the ultimate tensile stress in CD with $\tilde{\sigma}_{\text{CD,max}} = 52.1$ MPa. The corresponding ultimate tensile stretches were determined to be $\tilde{\lambda}_{\text{MD,max}} = 1.0675$ and $\tilde{\lambda}_{\text{CD,max}} = 1.0645$.

3.3.2 Biaxial mechanical response

The graphs in Figure 3.6 present the characteristic equibiaxial relaxation behavior (Cauchy stress vs. time) of the PA 12 membranes under quasi-static ($v_{\text{test}} = 1$ mm/min) and dynamic loading ($v_{\text{test}} = 10$ mm/min). Similar graphs for both, MD and CD, indicate an isotropic material response. Upon closer inspection of the graph during the first seconds, it shows a nonlinear increase over time followed by an immediate drop and a gradual decrease of the Cauchy stresses of approximately 25% after the linear stages of the testing device stopped when the stretch of $\lambda = 1.02 \hat{=} \lambda_{\text{app,CD}}$ was reached and held in position for $t = 200$ s. This is a clear evidence of the viscoelastic nature of PA 12. In comparison, the results of the dynamic equibiaxial relaxation tests illustrated in Figure 3.6 indicate a faster material response, however, without any strain-rate depending stiffening. No significant differences in the maximum Cauchy stresses and the Cauchy stresses in the relaxed state were found between quasi-static and dynamic testing. Nevertheless, the subsequent drop of the Cauchy stresses happened faster during dynamic testing.

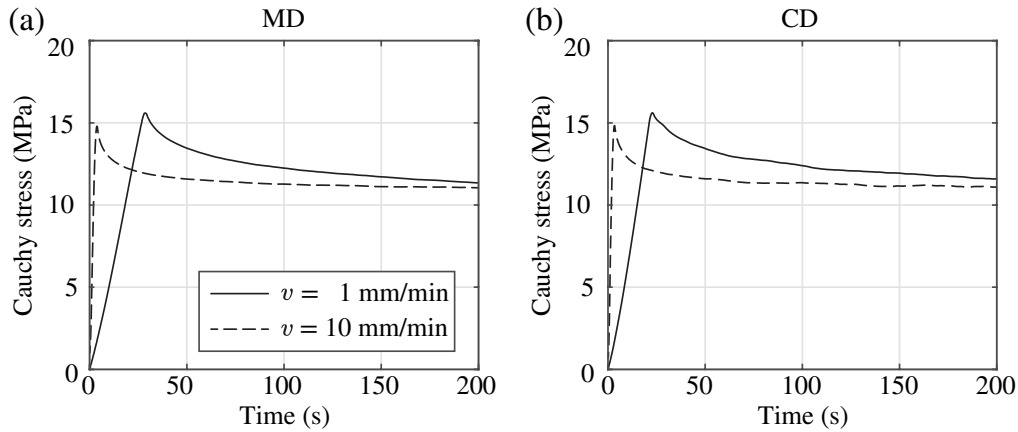


Figure 3.6 Representative quasi-static (dashed curve) and dynamic (solid curve) equibiaxial relaxation behavior: normal Cauchy stress in (a) MD and (b) CD under a stretch of $\lambda = 1.02$ as a function of time.

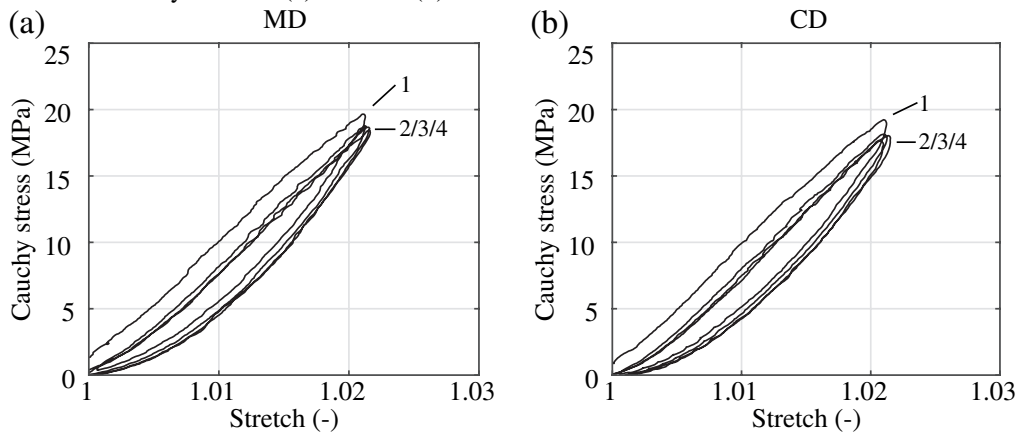


Figure 3.7 Representative quasi-static preconditioning behavior: (a) in MD and (b) in CD at a stretch of $\lambda = 1.02$ and under a testing velocity of $v = 1$ mm/min. Due to softening, cycle 1 induced a small offset and shifted cycles 2–4 to the right.

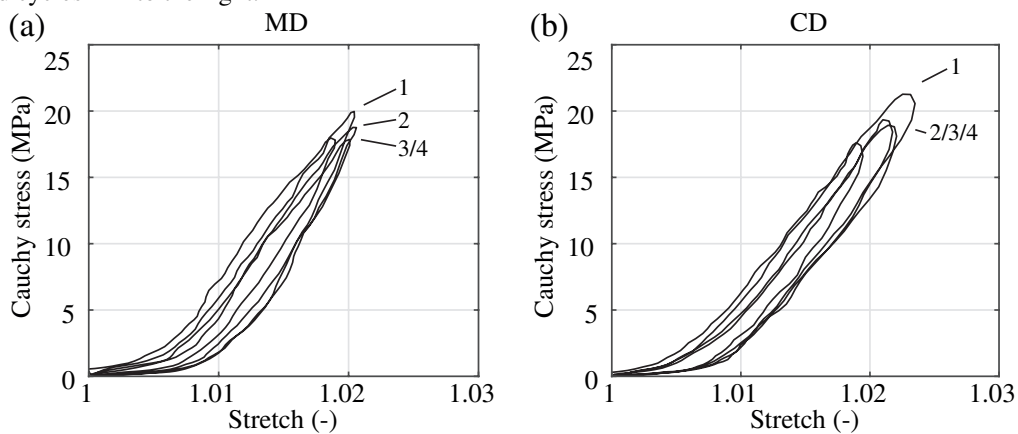


Figure 3.8 Representative dynamic preconditioning behavior: (a) in MD and (b) in CD at a stretch of $\lambda = 1.02$ and under a testing velocity of $v = 10$ mm/min. Due to softening, cycle 1 induced a small offset and shifted cycles 2–4 to the right.

In the preconditioning, where the specimens were equibiaxially deformed under quasi-static and dynamic conditions with a small stretch of only $\lambda = 1.02 \hat{=} \lambda_{\text{app,CD}}$, the membranes show no significant difference in the material behavior, see Figures 3.7 and 3.8. The illustrated stress-stretch relationship is almost identical apart from a more compliant initial material response during dynamic preconditioning. It appears that kinetic effects and the predominant direction of the polymer chains have hardly any influence on biaxially deformed PA 12 balloon catheter membranes under nominal pressure. This is in contradiction to the measurement data from preliminary uniaxial tests, where the data in Figure 3.5 suggest a distinctive anisotropic material characteristic even in a low stretch range ($\lambda \leq 1.02$). In both, the quasi-static and dynamic testing, the PA 12 membranes show no more softening after the third loading and unloading cycle in both direction (Figures 3.7 and 3.8). However, the first preconditioning cycle induced an offset and, therefore, shifted the following curves to the right. This offset was small during dynamic preconditioning. After the fourth preconditioning cycle, the current marker distance at force zero was defined as the reference marker distance, denoting $\lambda = 1$, for all subsequent measurement cycles.

The graphs in Figures 3.9 and 3.10 enable a comparison of quasi-statically and dynamically loaded PA 12 membranes under different equibiaxial stretch levels ranging from smaller stretches $\lambda = 1.02$, to medium ($\lambda = 1.04$) and larger stretches ($\lambda = 1.06$). While the material response of all specimens of both test modes is of an isotropic nature for smaller stretches only, the data reveal an increasingly significant anisotropic characteristic as soon as the stretches exceed $\lambda = 1.02$. The maximal Cauchy stresses are also higher in the dynamically loaded specimens. Another indicator for the viscoelastic material behavior of PA 12 is the presence of forming hysteresis loops between the loading and unloading during preconditioning and equibiaxial measurement cycles. While the hysteresis loops are rather small after small stretches, they show a much more pronounced shape after medium ($\lambda = 1.04$) and larger stretches ($\lambda = 1.06$). However, the development of the hysteresis loops with increasing stretches is equal for quasi-statically and dynamically tested PA 12 membranes. Noticeable is only the slightly curved peaks of the graphs in Figure 3.10 in comparison to the sharp peaks in Figure 3.9. This is based on the inertia of the material response during fast loading changes, which can be attributed to the viscoelasticity of the material or to the time delay of the VE. One may assume that the loading curves in Figures 3.9 and 3.10 should be collinear. However, this is not true for smaller stretches in the quasi-static tests and for the whole stretch range in the dynamic tests. The authors suppose that micro-damage or rearrangement of the molecular chains occurred during every equibiaxial loading cycle, which are more pronounced during dynamical testing.

A representative comparison of the Cauchy stress-stretch relationship of specimens taken from different locations of the cylindrical part of the balloon catheter membrane is shown in Figure 3.11. No significant deviation of the graphs in the respective directions had been found. It can, therefore, be assumed that PA 12 shows a homogeneous material behavior along the cylindrical part in MD of the balloon catheter membrane.

The material responses of three specimens until failure and their medians in MD and CD

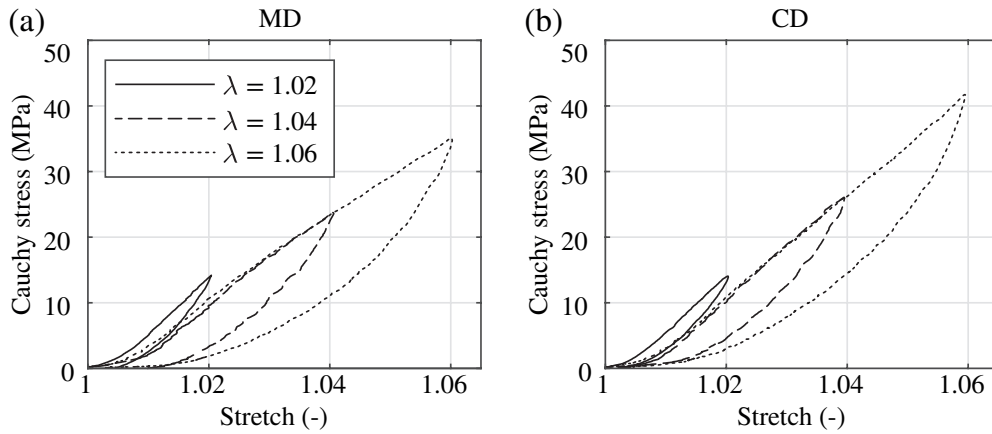


Figure 3.9 Representative quasi-static equibiaxial Cauchy stress-stretch behavior: (a) in MD and (b) in CD under various stretch levels ranging from 1.02 to rupture in 0.02 stretch increments and a testing velocity of $v = 1$ mm/min.

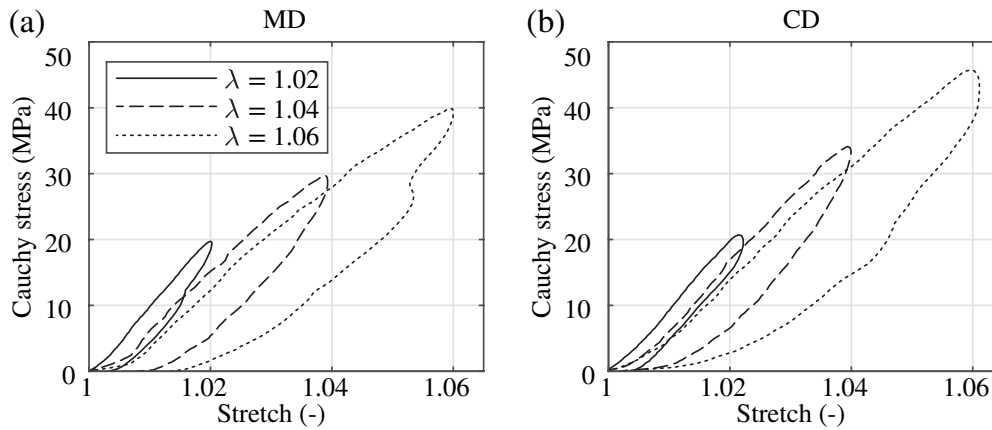


Figure 3.10 Representative dynamic equibiaxial Cauchy stress-stretch behavior: (a) in MD and (b) in CD under various stretch levels ranging from 1.02 to rupture in 0.02 stretch increments and a testing velocity of $v = 10$ mm/min.

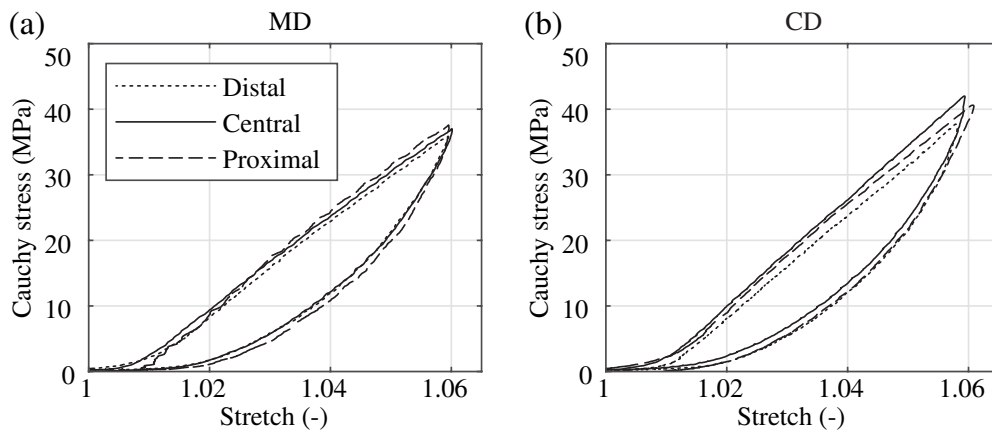


Figure 3.11 Representative comparison of the Cauchy stress-stretch behavior of the distal, central, and proximal parts of PA 12 balloon catheter membranes: (a) in MD and (b) in CD under a stretch of $\lambda = 1.04$ and a testing velocity of $v = 1$ mm/min.

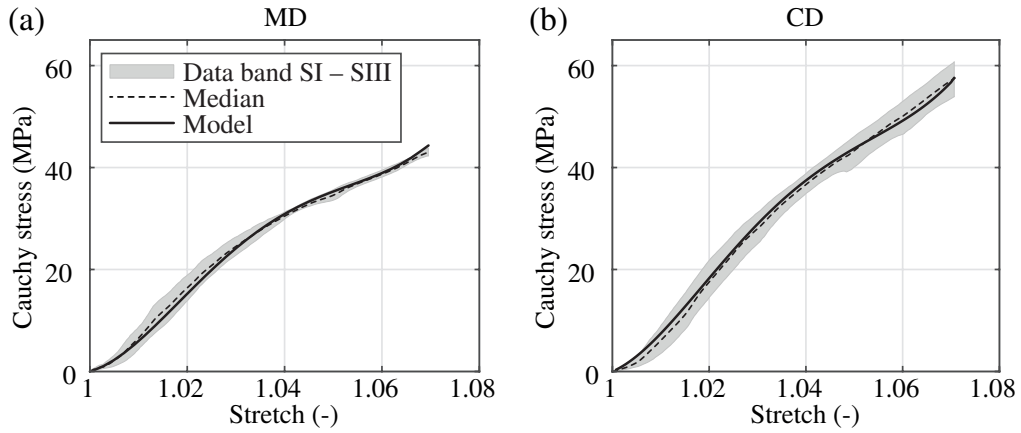


Figure 3.12 Cauchy stress-stretch behavior until failure and material model response: (a) in MD and (b) in CD under a testing velocity of $v = 10$ mm/min. All values of the tested Specimens SI–SIII are within the gray data band.

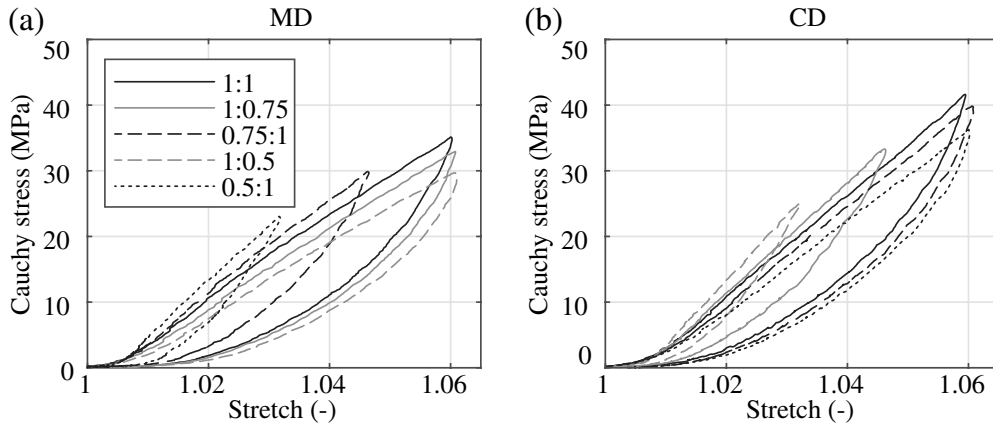


Figure 3.13 Representative quasi-static biaxial Cauchy stress-stretch behavior for different stretch ratios: (a) in MD and (b) in CD with a testing velocity of $v = 1$ mm/min. Stretch ratios $\lambda_{MD} : \lambda_{CD} = \{1 : 1, 1 : 0.75, 0.75 : 1, 1 : 0.5, 0.5 : 1\}$.

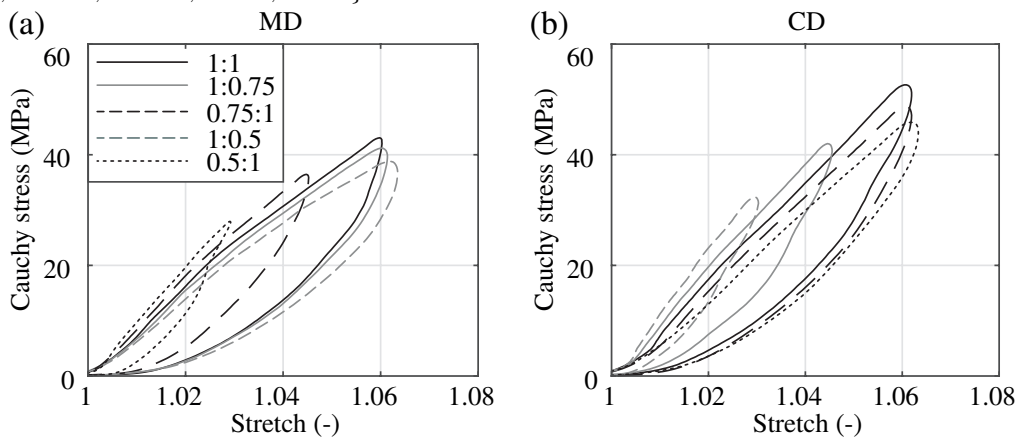


Figure 3.14 Representative dynamic biaxial Cauchy stress-stretch behavior for different stretch ratios: (a) in MD and (b) in CD with a testing velocity of $v = 10$ mm/min. Stretch ratios $\lambda_{MD} : \lambda_{CD} = \{1 : 1, 1 : 0.75, 0.75 : 1, 1 : 0.5, 0.5 : 1\}$.

are illustrated in Figure 3.12. Again, as during cyclic loading, the material shows an isotropic response until a stretch of $\lambda \leq 1.02$ is reached and then manifests a distinctive anisotropic characteristic. The median of the normal Cauchy stress at nominal pressure under $\lambda = 1.02 \hat{=} \lambda_{\text{app,CD}}$ was computed to be $\tilde{\sigma}_{\text{MD}} = 16.7$ MPa in MD, which is 92.3 % of the corresponding Cauchy stress $\tilde{\sigma}_{\text{CD}}(\lambda_{\text{app}}) = 18.1$ MPa in CD. At $\lambda = 1.04$ the difference increases ($\tilde{\sigma}_{\text{MD}} = 30.4$ MPa, $\tilde{\sigma}_{\text{CD}} = 36.9$ MPa, pct = 82.4 %), becomes more significant at $\lambda = 1.06$ ($\tilde{\sigma}_{\text{MD}} = 38.7$ MPa, $\tilde{\sigma}_{\text{CD}} = 50.1$ MPa, pct = 77.3 %), and finally peaks at failure ($\tilde{\sigma}_{\text{MD,fail}} = 44.5$ MPa, $\tilde{\sigma}_{\text{CD,fail}} = 58.2$ MPa, pct = 76.5 %). The corresponding median of the failure stretch $\tilde{\lambda}_{\text{fail}} \sim 1.07$ is 3.5 times higher than the stretch under nominal pressure $\lambda_{\text{app}} = 1.02$.

Nevertheless, all graphs generated from experimental data in Figures 3.9, 3.10 and 3.12 feature a short exponential increase in the Cauchy stresses under small stretches. At around $\lambda \sim 1.02$ and after a further inflection point at $\lambda \sim 1.04$ the graphs are polynomial; nearly linear until failure. Thus, the balloon membranes show the typical stress vs. stretch progression for polyamides known from the literature [378–380].

3.3.3 Model parameters

The graphs in Figure 3.12 illustrate the comparison between the model fit and the experimental data. The proposed model was able to give a very satisfying representation of the dynamic equibiaxial behavior for the whole stretch range ending at a stretch of $\lambda \sim 1.07$. The model parameters and the associated median and the deviations between the fit and the experimental data of all three test specimens *SI–SIII* are shared in Table 3.1. For fu-

Table 3.1 **Constitutive model parameters, squared Pearson’s coefficients R_{CD} , R_{MD} , and the root-mean-square error RSME for the proposed model (3.5).** All results were obtained by fitting the hyperelastic strain-energy function to the median of the experimental equibiaxial data of the tested PA 12 balloon catheter membranes.

	Constitutive parameters					R_{CD}^2 (–)	R_{MD}^2 (–)	RMSE (–)
	c_{10} (MPa)	c_{02} (MPa)	c_{11} (MPa)	k_1 (MPa)	α (°)			
Median	–1 791	28 736	–36 242	2 770	44.77	0.9995	0.9992	0.02

ture advanced modeling approaches, e.g., the mathematical description of the viscoelastic features, the authors want to share a representative biaxial tensile response of the PA 12 balloon catheter membrane at different stretch ratios between MD and CD under quasi-static and dynamic loading represented in Figures 3.13 and 3.14, respectively.

3.4 Discussion

Balloon catheter membranes significantly influence the expansion behavior of stents. Despite the well-known fact that the molecular chains of extruded polymers exhibit a preferred

direction, current studies [313, 315, 330, 331, 363, 364] focusing on the optimization of stent designs and stent delivery systems by the help of the FEA, using almost exclusively isotropic material models for balloon catheter membranes. This work shows, however, that the decision to use an isotropic or anisotropic material model must be carefully considered.

This statement is based on the key finding of this work, in which the material behavior of the PA 12 balloon catheter membrane shows a stiffer response to loading in CD, as illustrated in Figures 3.9, 3.10, 3.13, and 3.14. The stiffer response might be the result of the predominant orientation of molecular chains in CD in extruded and stretched polymers, as described in several studies [365–367]. By examining the results from uniaxial extension tests depicted in Figure 3.5, this effect is even noticeable within the whole loading range. On the contrary, the stress-stretch relationship of specimens under small equibiaxial stretches is almost identical but starts to differ at stretches λ above 1.02.

The authors assume that the biaxial mechanical response of PA 12 under small stretches is highly influenced by the coupling between the polymer chains ('Poisson effect'). Stretches arising in CD will certainly be accompanied by stretches in MD. The influence of this effect probably decreases with higher stretches and an anisotropic material behavior emerges. On average, the specimens showed a slightly softer behavior in uniaxial than in biaxial extension. This conforms with the expectation that the 'Poisson Effect' would favor a stiffer reaction in biaxial extension. Compared to other tested polymers [381, 382] and injection molded PA 12 [372], the processed balloon catheter membranes reveal a very stiff response even at small stretches. This is an indicator of the semi-compliant characteristic of the Baroonda SDS membrane which was achieved through a tailored balloon-forming process.

The induced stresses in the PA 12 membranes were found to be higher during dynamic equibiaxial testing above nominal pressure. The increase in the maximum stresses due to a higher strain-rate conforms with the findings of McFerran *et al.* [372]. In the relaxation tests, the difference between the maximum stresses and the stresses after 200 s did not increase with a higher testing speed. The effect of strain-rate dependence only pronounces at larger stretches. Thus, no significant influence of the strain-rate between quasi-static and dynamic testing modes at small stretches could be detected.

Furthermore, a characteristic of the viscoelastic nature of balloon-molded PA 12 membranes was observed. The results from quasi-static and dynamic relaxation tests reflect the typical time-dependency of the strain-recovery inside initially loaded polymers if compared with Meyer *et al.* [382]. A further indicator for the typical viscoelastic polymer-like response is the pronounced hysteresis in the equibiaxial tests. The differences in the loading and unloading curves become more significant in the dynamic testing mode. The authors assume that the viscoelastic response of PA 12 is again associated with the rearrangement of molecular chains in the amorphous regions, as described for polypropylene by Coulon *et al.* [383].

Preconditioning of PA 12 balloon catheter specimens should be taken into account for ex-

tension tests as the balloon catheters usually get pressurized several times after manufacturing to test its functionality. However, only a minor effect of the cyclic loading during preconditioning on the mechanical response at small stretches was found. The difference between the first and the last preconditioning cycle seems to be the result of early stretches based on viscoplastic effects. The viscoplasticity of polymers at small stretches can usually be explained with rearrangement mechanisms in the amorphous regions and micro-damage mechanisms. Similar to the tests of Meyer *et al.* [382], the first loading cycle in CD and MD of the quasi-static and dynamic preconditioning shows a large initial hysteresis loop. The hysteresis loops of the following loading cycles become smaller and the maximum stresses slightly drop.

No differences in the stress-stretch behavior along the cylindrical part of the Baroonda SDS membrane was found. Biaxial extension tests with specimens taken from the distal, central, and proximal part of the membrane show similar results.

The presented clamping system of the VE-based biaxial extension tests was found to be suitable for small specimens with a cross shape. By choosing to manufacture the clamps from aluminum and the small dimensions of the clamps, the influence of the clamps on the measurement results could be reduced to a negligible amount. Due to the novel design of the clamps, a homogeneous clamping pressure distribution along every flank of the specimens can be assured. Besides, the support platform guaranteed the symmetrical arrangement of all four clamps. The sample design also leaves enough space to place four markers for VE-measurements. Furthermore, biaxial testing better represents the multi-axial loading case during percutaneous coronary intervention than uniaxial testing. Thus, biaxial testing provides an adequate setting for the proposed modeling approach.

As mentioned above, standard PA 12 balloon catheter membranes show an almost isotropic behavior at small stretches when biaxially loaded. Small stretches occur within the balloon pressure range between zero to nominal pressure of the Baroonda SDS balloon catheter. In this case it would be reasonable to use an isotropic material model that can numerically describe the material response to small stretches based on the experimental data of this work. If the balloon catheter gets pressurized above the nominal pressure, the anisotropic character of the membrane clearly emerges. In this case, the authors suggest to continue with the modeling approach presented in this study. Inspired by the work of Rivlin and Saunders [375], the modified version of the polynomial model used shows overall a very satisfying fit of the loading curve of dynamic tested PA 12 membranes. Note, however, that the proposed material model is a purely elastic model, and hence it does not account for material damage. Manufacturers and scientists have to deliberate how accurate FEA results need to be in simulations with balloon catheters pressurized above the nominal pressure to meaningfully contribute to the optimization process of balloon catheters and stents with respect to computational expenses. It should be noted that the internal balloon pressure most likely exceeds the nominal pressure several times during the coronary treatment. The reason for this could be the geometry or material properties of the vital part of the artery, the stenosis, or the stent, and accidents or unwary performance.

Even though all presented methods appear to be robust to quantify the stretches of PA 12 balloon catheter membranes and to model them accordingly, this study has some limitations. The presented model, and the constitutive parameters, account only for the biaxial material behavior of standard PA 12 balloon catheter membranes for main coronary interventions, i.e., for balloon catheters with a thickness of approximately 30 μm . Although almost all manufacturing processes of balloon catheter membranes are standardized, varying the manufacturing parameters can influence the morphology of PA 12 and, therefore, its mechanical response. In contrast to biaxial testing, where the sample is in direct contact with the rigid clamp, the elastic adhesive tape and the sandpaper may contribute to the measured material response. It is possible that the adhesive tape and the sandpaper slightly falsify the measured material response. For the biaxial testing modes, the influence of shear stresses was not observed due to the small size of the specimens. Thus, with the used VE-based method, it can only be assumed that the stress-stretch distribution in the field of interest is homogeneous and shear deformation have no major influence on the normal stresses. Furthermore, the realistic strain-rate could not be fully achieved with the present biaxial extension testing device. Due to the limited amount of donated balloon catheter blanks and the extent of preliminary testing, the number of the final test series is small. Further biaxial extension tests might be necessary to substantiate the statistical validity of the findings and to observe the influence of shear stresses on the results. In addition, the modeling approach in this study does not incorporate the observed viscoelastic nature of PA 12; incorporation of a viscoelastic model for this type of anisotropic material at finite strains can be achieved [115]. To the authors' opinion, vascular injuries, and possible damage to the balloon or the stent occur mainly during the expansion phase of the implantation. Therefore, only the modeling of the dynamic loading behavior was of interest. However, the complex mathematical description of the strain-dependency and the hysteresis formation of the balloon membranes should be the matter of further studies.

3.5 Conclusion

In conclusion, the cylindrical part of the PA 12 membranes of the Baroonda SDS balloon catheter for main coronary arteries can be characterized as homogeneous, semi-compliant, and viscoelastic, which shows a nonlinear isotropic material response at nominal balloon pressure when being loaded biaxially. However, above the nominal pressure, anisotropy, and strain-rate dependency of the material behavior emerges significantly with increasing stresses.

To the authors' knowledge, this study presents the first set of experimental data of the mechanical response of standard PA 12 balloon catheter membranes for main coronary arteries. In uni- and biaxial extension tests, a stretch-driven protocol was used to simulate the loading scenarios of balloon catheter membranes expanding with an inner pressure ranging from zero to the supra-nominal level. Furthermore, novel methods are described to carry out quasi-static and dynamic extension tests on tiny planar specimens taken from balloon catheter membranes for the first time. The study provides a modeling approach,

which uses a generalized polynomial-type elasticity relation together with a polynomial extension for the anisotropic part. This model can reproduce the biaxial behavior of the tested PA 12 membranes very well.

Thus, the authors assume that even a FEA simulating the expansion of PA 12 balloon catheter membranes with nominal pressure – e.g., the authors' previous work [363] – may benefit by implementing the proposed model. The isotropic material response of the balloon catheter in such a FEA would finally be based on experimental data from extension tests performed on actual PA 12 membranes. However, it cannot be excluded that the stresses inside the balloon membrane reach a supra-nominal level, e.g., due to incorrect handling of the catheter or due to unfavorable contact situations with stents or stenoses. Therefore, for FEA, in which the consequences of an over-expanded membrane on the balloon catheter, stent, and the artery due to supra-nominal pressurization are of interest, the authors advise the use of the proposed material model. Furthermore, experimental data, specifying the material response of PA 12 membranes at different stretch ratios, and rates are provided in this article. Based on these data, the proposed model could be improved by incorporating the viscoelastic features of the tested PA 12 membranes.

Data Accessibility

The experimental data collected in the biaxial extension tests presented in the Figs 6–10, 13, 14, the Cauchy stress-stretch relation until failure of the median and all single samples depicted in Fig 12 can be downloaded from:

<https://doi.org/10.6084/m9.figshare.12116715.v1>.

Acknowledgments

The authors are grateful for balloon catheter blanks donated by Bavaria Medizin Technology GmbH. Furthermore, the authors thank Lloyd Kimble for his valuable insights in the field of polymer processing and helpful discussions.

4 Quantifying Stent-Induced Damage in Coronary Arteries by Investigating Mechanical and Structural Alterations

Abstract. Vascular damage develops with diverging severity during and after percutaneous coronary intervention with stent placement and is the prevailing stimulus for in-stent restenosis. Previous work has failed to link mechanical data obtained in a realistic *in vivo* or *in vitro* environment with data collected during imaging processes. We investigated whether specimens of porcine right coronary arteries soften when indented with a stent strut shaped structure, and if the softening results from damage mechanisms inside the fibrillar collagen structure. To simulate the multiaxial loading scenario of a stented coronary artery, we developed the testing device ‘LAESIO’ that can measure differences in the stress-stretch behavior of the arterial wall before and after the indentation of a strut-like stamp. The testing protocol was optimized according to preliminary experiments, more specifically equilibrium and relaxation tests. After chemical fixation of the specimens and subsequent tissue clearing, we performed three-dimensional surface and second-harmonic generation scans on the deformed specimens. We analyzed and correlated the mechanical response with structural parameters of high-affected tissue located next to the stamp indentation and low-affected tissue beyond the injured area. The results reveal that damage mechanisms, like tissue compression as well as softening, fiber dispersion, and the lesion extent, are direction-dependent, and the severity of them is linked to the strut orientation, indentation pressure, and position. The findings highlight the need for further investigations by applying the proposed methods to human coronary arteries. Additional data and insights might help to incorporate the observed damage mechanisms into material models for finite element analyses to perform more accurate simulations of stent-implantation.

4.1 Introduction

Despite the great efforts of scientists and manufacturers in recent years, in-stent restenosis (ISR) remains the most frequent and critical post-surgical event of percutaneous coronary intervention (PCI) cardiologists have to face [4, 11]. During and after PCI with stent placement, the coronary artery is exposed to a triaxial loading scenario in the supraphysiological range, i.e., above the hemodynamic loading. The expanding stent causes an increase in the diameter of the artery to an abnormally high value, i.e., the tissue gets stretched in the longitudinal and the circumferential directions. This mechanical stimulus and supraphysiological loadings provoke pathological processes in the form of cell migration and proliferation, resulting in neointimal thickening [347]. It is shown that the extent of ISR correlates with the severity of the stent-induced injury [5–9, 384].

However, even newest generations of so-called drug-eluting stents (DES) show similar fatality rates to uncoated bare-metal stents (BMS) in the long-term (> 5 years) of about 15–20 % [4, 11–14]. To lower the fatality rate of BMS and DES, scientists and manufacturers

need to develop safer stents by significantly lowering the risk of vascular damage caused by PCI. Stent induced vascular damage must be differentiated from age-related, atherosclerotic and non-atherosclerotic damage. The actual moment stent-induced vascular damage becomes clinically relevant is difficult to determine. It must be assumed that vascular damage and subsequent neointimal hyperplasia start to develop as soon as the artery is exposed to supraphysiological loading. The mechanical, as well as structural alterations may become more severe and even irreversible with an increasing mechanical stimulus.

To prevent excessive vascular damage, the load applied on the artery must be reduced by optimizing the geometry or the material of the stent and the stent delivery system. Finite element analysis (FEA) has become a promising tool to fulfill this mission. Modern FEA is able to precisely simulate the interaction between all components of an expanding stent-delivery system. For representative literature, the reader is referred to the articles of Geith *et al.* [363], Wiesent *et al.* [364], and He *et al.* [385] have shown. In addition, progressive constitutive models for vascular tissue are meant to describe the behavior of healthy or diseased arteries in a physiological or pathological state [116, 329], but under the assumption that mechanical and structural properties remain constant. The equations of the latest constitutive models often contain structure tensors in which experimentally validated structural parameters of different arterial layers are implemented. However, as soon as such a model is considered within a FEA, a significant limitation is added: so far, vascular damage, defined by stent-induced mechanical and structural alterations, has not yet been considered in any constitutive model.

Only a few studies are known which try to quantify the vascular damage inside arteries after PCI. Schwartz *et al.* [5] implanted stents in porcine arteries, prepared and analyzed histological sections with light microscopes, and evaluated the lesions with a stent injury score. Thus, Schwartz *et al.* [5] created a revolutionary tool allowing damage classification by the degree of injury more than 25 years ago. However, the assessment of the respective stent injury score is highly subjective and based on empirical data. Adapting the mentioned stent injury score, Schwartz *et al.* [386] and Swier *et al.* [387] aimed to correlate the severity of the injury with the neointimal thickening. Nevertheless, the results presented in these studies cannot be correlated with the indentation pressure and the orientation of a stent strut, as well as the mechanical response of the tissue.

Pathological alterations inside of coronary tissues are only detectable if one compares the properties of an arterial wall before and after the iatrogenic event of PCI. To date, altered properties of coronary arteries can be quantified in three ways:

- (i) One can observe biomechanical alterations caused by atherosclerotic and non-atherosclerotic cardiovascular events, such as inflammation, endothelial denudation, in-stent restenosis and in-stent thrombosis, angiogenesis, vasospasm, and dissection, which is the focus of several biologically-oriented research efforts, *cf.* [388–393].
- (ii) Mechanical alterations of the arterial wall can be determined by measuring the stress-stretch response of the tissue. Here, during standard tensile tests, specimens are stretched

in one or two orthogonal directions, and their stress-stretch relationship is measured. The *in vitro* mechanical response of healthy and diseased arteries in a passive or active state to physiological and supraphysiological biaxial loadings have been substantially analyzed, as Chen and Kassab [61] summarized in their review article. However, experimental setups for conventional uni- and biaxial tensile tests are ineligible to simulate the triaxial loading scenario of PCI. A precise *in situ* measurement of the indentation pressure, which interacts between the stent strut and the artery, is technically not feasible due to the tiny dimensions of the stents and the poor accessibility. Therefore, an experimental setup is needed to mimic the loading scenario of a stented artery under *in vitro* conditions and to enable the measurement of the prevailing stress-stretch relationship of the artery in parallel. However, to this point, it seems that no study has been published, which describes experiments with such a setup.

(iii) One can investigate structural changes inside of arterial tissues, which helps to explain the mechanical response. Technologies such as fluorescence microscopy with DAPI staining or antibody labeling and modern, high-quality multi-photon microscopy in combination with specific tissue clearing methods allow deep tissue imaging. Thus, a display of all constituents such as collagen, elastin, and vascular smooth muscle cells is feasible. Since the mechanical behavior of vascular tissue is highly dependent on fibrillar collagen type I, [115] *q.v.*, in particular, second-harmonic generation (SHG) imaging has become an important tool for the investigation of structure-related alterations in the extracellular matrix [54, 329, 394–397]. By analyzing the imaging data of SHG scans, constant values for structural parameters were obtained and incorporated into a constitutive model in order to capture the physiological and pathological mechanisms of healthy and diseased arterial tissues more precisely [329, 396]. However, to this day, structural parameters for injured tissue of stented arteries could not be provided. Nevertheless, we assume that most of these structural parameters, as well as the mechanical properties of the arterial tissue, will change due to PCI. Furthermore, it is very likely that the structural parameters of stented tissues vary with increasing indentation pressure exerted by the stent, and depend on the orientation of the stent struts, and also alter with increasing distance to the lesion.

For the proof of this hypothesis, new experimental and imaging methods are presented in this pilot study, which aim to observe the influence of PCI on the mechanical properties and morphology of porcine right coronary arteries (RCA). First, we explain the theoretical background to describe the *in situ* loading scenario of PCI and to impart the meaning of the structural parameters introduced by Holzapfel *et al.* [329]. Subsequently, a new experimental setup together with a specially designed testing protocol is presented to simulate the *in situ* loading scenario and to carry out stress-stretch measurements in real-time. This study also introduces an imaging strategy, including adapted procedures for optical tissue clearing as well as three-dimensional (3D)-surface and SHG scans. Finally, mechanical and structural data are presented, correlated, as well as key and further findings are interpreted.

4.2 Materials and Methods

4.2.1 Biomechanical principles

In situ loading scenario

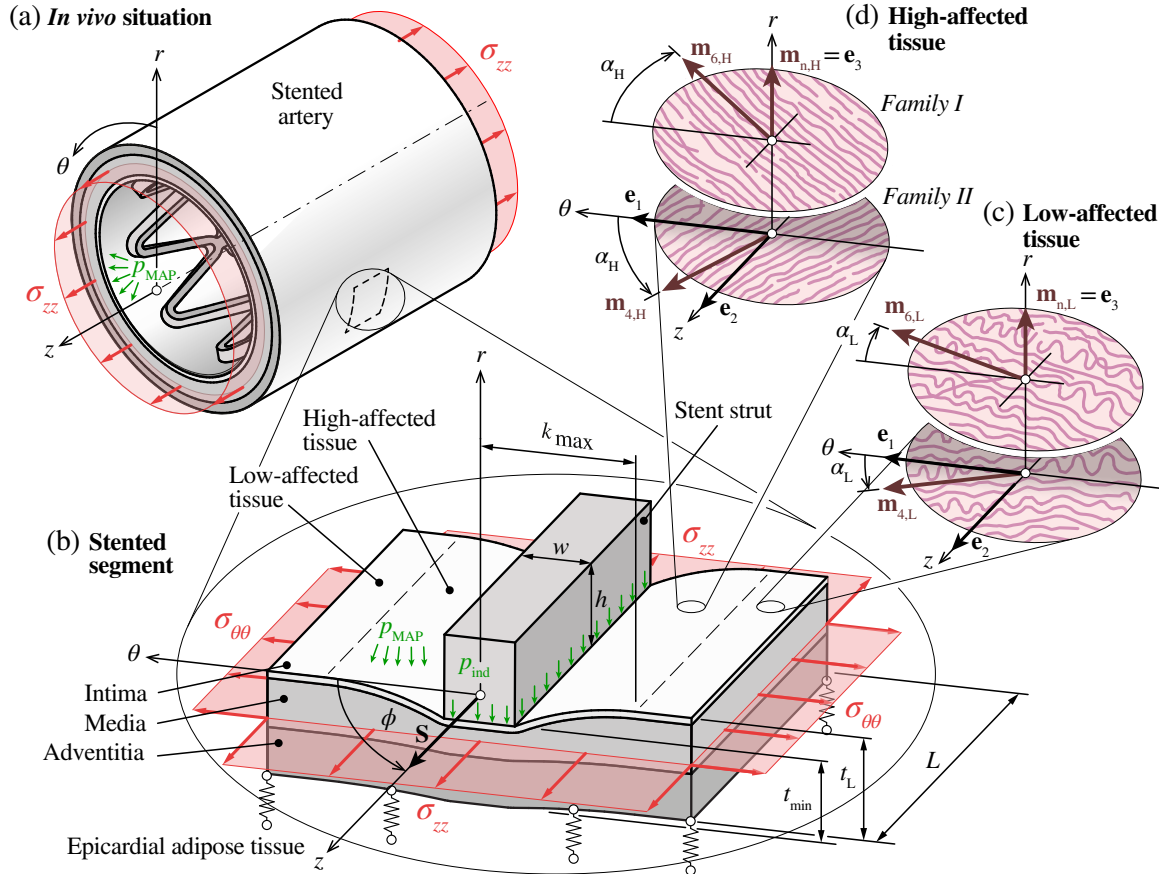


Figure 4.1 Schematic illustration of the *in situ* loading scenario and fiber directions of a stented coronary artery: (a) cross-section of the arterial wall labeled by a cylindrical coordinate system with two axes in the z - and r -direction and a third one in the θ -direction; (b) planar and square segment of a stented artery with a damaged area surrounding the stent strut within the distance $k \in [0, k_{\max}]$, with a transformed rectangular Cartesian coordinate system. Here, the strut orientation angle is $\phi = 90^\circ$. The springs symbolize the epicardial adipose tissue; (c) symmetric mean fiber directions $\mathbf{m}_{4,L}$ and $\mathbf{m}_{6,L}$ of the two fiber families of the low-affected tissue in the stented configuration, each making an angle α_L with the θ -direction and \mathbf{e}_1 , whereas $\mathbf{m}_{n,L}$ denotes the unit out-of-plane vector; (d) symmetric mean fiber directions $\mathbf{m}_{4,H}$ and $\mathbf{m}_{6,H}$ of the high-affected tissue in the stented configuration next to the stent strut, with the angle α_H and the unit out-of-plane vector $\mathbf{m}_{n,H}$; $\mathbf{e}_1, \mathbf{e}_2, \mathbf{e}_3$: unit basis vectors; k_{\max} : distance between the low-affected tissue and the strut; indentation; L : segment side length; w : strut width; h : strut height; t_L : arterial wall thickness of the low-affected tissue; t_{\min} : minimal compressed wall thickness; p_{MAP} : mean arterial pressure; $\sigma_{zz}, \sigma_{\theta\theta}$: Stresses in the z - and θ -direction; ϕ : strut orientation angle.

In the following, we consider a planar and square segment from a homogeneous wall of a coronary artery, shown schematically in Figure 4.1(a) and (b). Coronary arteries con-

sist of three layers, intima, media, and adventitia, which are separated by transition layers around the membrana elastica interna and externa. In the following, the circumferential, longitudinal, and radial directions are denoted as θ , z , and r , respectively. The physiological, i.e., hemodynamical or *in situ* loading of coronary arteries is a result of the interplay between the blood pressure, intraparietal active stresses, and the residual stresses inside the arterial tissue. For the sake of simplicity, only a static loading scenario was assumed in this study. Therefore, the dynamically changing blood pressure was replaced by a constant mean arterial pressure (MAP) $p_{\text{MAP}} \approx 100 \text{ mm Hg} \approx 13.3 \text{ kPa}$. The physiological values for stresses inside the tissue in the θ - and z -direction can be approximated by using Laplace's equation. Hence, corresponding physiological Laplace mean stresses in the z - and θ -direction in an untreated, i.e., not stented artery are according to

$$\sigma_{zz}^{\text{MAP}} = \frac{p_{\text{MAP}}L}{4\pi T} \quad \text{and} \quad \sigma_{\theta\theta}^{\text{MAP}} = \frac{p_{\text{MAP}}L}{2\pi T}, \quad (4.1)$$

where L is the side length of the tissue segment and T is the thickness of the arterial wall in the reference configuration, i.e., under physiological load. As Humphrey *et al.* [48] concluded in their review article, the projected pressure p_{MAP} alone may not sufficient to maintain a physiological stretch as the loading in the z -direction may remain constant for different pressures. Before further studies are carried out, we recommend that this problem should be investigated experimentally on porcine and/or human coronary arteries and the derivation of the stresses reconsidered according to prior and recent approaches [48, 75, 104, 377].

If a stent strut of width w and height h indents with an indentation pressure p_{ind} , a lesion develops. The compression along the elevation profile of the cross-section of the lesion can be expressed as the nonlinear function

$$\lambda_r(k) = \frac{t(k)}{T}, \quad (4.2)$$

where t is the compressed wall thickness in the stented-configuration at the distance k to the center of the strut indentation. The compression finds its smallest magnitude λ_r^{min} directly under the stent at $k = 0$ and $t = t_{\text{min}}$, then the compression increases nonlinearly with an increasing k and reaches its maximum λ_r^{max} at k_{max} and $t = t_{\text{L}}$, whereby the subscript L stands for 'low-affected tissue'. Subsequently, we denote tissue beyond k_{max} as 'low-affected', since the arterial wall gets only stretched in the θ - and z -direction by the expanding stent, and the radial compression λ_r is not directly influenced by any stent strut. Therefore, the compression never becomes zero in the low-affected area, but can be assumed as constant. Whereas within k_{max} , the tissue is denoted as 'high-affected', as the nearby stent strut causes an additional decrease of λ_r .

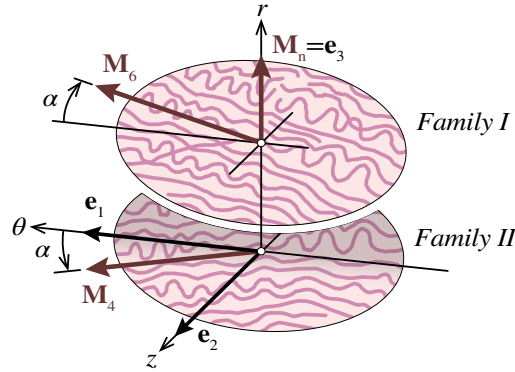


Figure 4.2 Physiological, i.e., *in vivo* fiber direction of an untreated artery in the reference configuration. The unit vectors \mathbf{M}_4 and \mathbf{M}_6 of the two fiber families are located in the $(\mathbf{e}_1, \mathbf{e}_2)$ -plane, α is the mean angle between \mathbf{M}_4 , \mathbf{M}_6 and \mathbf{e}_1 , whereas \mathbf{M}_n is the unit out-of-plane vector given by $\mathbf{e}_1 \times \mathbf{e}_2$. Adapted and modified from [329].

Structural alterations

In this stage of our investigations we focus on the contribution of the load-bearing fibrillar collagen structures of the medial and adventitial layer only as the intima of young pigs is assumed to not contribute to the mechanical properties [54]. Following the modeling approach of Holzapfel *et al.* [329], a rectangular Cartesian coordinate system is introduced, in which \mathbf{e}_1 , \mathbf{e}_2 , and \mathbf{e}_3 are the three (unit) basis vectors pointing in the θ -, z -, and r -direction, respectively (see Figure 4.2). The content of collagen fibril bundles enveloping SMC is rather low in the media of coronary arteries [80] and mainly oriented in the θ -direction [72, 75]. According to [61], the adventitia can be divided into an inner adventitia (IA) and an exterior adventitia (EA). In the IA, the density of collagen bundles gets higher, and the fibers tend to align with the z -direction. The collagen content peaks in the EA with a rather high degree of fiber dispersion. The mean fiber directions \mathbf{M}_4 and \mathbf{M}_6 for both symmetric fiber families of an untreated artery are located in the $(\mathbf{e}_1, \mathbf{e}_2)$ -plane. In this reference configuration, both mean fiber directions can be described through

$$\mathbf{M}_4 = \cos \alpha \mathbf{e}_1 + \sin \alpha \mathbf{e}_2 \quad \text{and} \quad \mathbf{M}_6 = \cos \alpha \mathbf{e}_1 - \sin \alpha \mathbf{e}_2, \quad (4.3)$$

where $\alpha \in [-90^\circ, 90^\circ]$ is the mean fiber angle between the mean fiber directions \mathbf{M}_4 and \mathbf{M}_6 and the unit vector \mathbf{e}_1 (see Figure 4.1(c)). For the mathematical quantification of the fiber dispersion, Holzapfel *et al.* [329] introduced further the generalized structure tensors \mathbf{H}_4 and \mathbf{H}_6 as

$$\mathbf{H}_i = A\mathbf{I} + B\mathbf{M}_i \otimes \mathbf{M}_i + (1 - 3A - B)\mathbf{M}_n \otimes \mathbf{M}_n, \quad i = 4, 6, \quad (4.4)$$

where \mathbf{M}_n is a unit out-of-plane vector given by $\mathbf{e}_1 \times \mathbf{e}_2$, \mathbf{I} is the identity tensor, and A and B are parameters according to

$$A = 2\kappa_{\text{op}}\kappa_{\text{ip}} \quad \text{and} \quad B = 2\kappa_{\text{op}}(1 - 2\kappa_{\text{ip}}), \quad (4.5)$$

which are composed by the two scalar quantities κ_{ip} and κ_{op} as

$$\begin{aligned}\kappa_{ip} &= \frac{1}{2} - \frac{I_1(a)}{2I_0(a)}, \\ \kappa_{op} &= \frac{1}{2} - \frac{1}{8b} + \frac{1}{4} \sqrt{\frac{2}{\pi b}} \frac{\exp(-2b)}{\operatorname{erf}(\sqrt{2b})},\end{aligned}\tag{4.6}$$

where $\operatorname{erf}(\bullet)$ is the error function of (\bullet) , a and b are concentration parameters, and I_0 and I_1 are the modified Bessel functions of the first kind of order 0 and 1, respectively. If κ_{ip} increase and κ_{op} decrease, the degree of the in- and out-of-plane dispersion becomes greater. In [329], the structural parameters are denoted by α , κ_{op} , and κ_{ip} , which can be determined by SHG analysis, see, e.g., reference [396].

After PCI, the orientation of the respective stent strut is defined by the vector \mathbf{S} through

$$\mathbf{S} = \cos \phi \mathbf{e}_1 + \sin \phi \mathbf{e}_2,\tag{4.7}$$

where the stent orientation angle $\phi \in [-90^\circ, 90^\circ]$ is the angle between \mathbf{e}_1 and \mathbf{S} in the (θ, z) -plane, see Figure 4.1(b). In the stented configuration, two cases must be considered:

- (i) The low-affected tissue is located beyond a distance to the stent strut greater than k_{\max} , as presented in Figure 4.1(c). Therefore, $\mathbf{M}_4, \mathbf{M}_6, \mathbf{M}_n, \alpha$ become $\mathbf{m}_{4,L}, \mathbf{m}_{6,L}, \mathbf{m}_{n,L}, \alpha_L$.
- (ii) The high-affected tissue is located next to the stent within $k < k_{\max}$, as depicted in Figure 4.1(d). Thus, the reference configuration transforms into $\mathbf{m}_{4,H}, \mathbf{m}_{6,H}, \mathbf{m}_{n,H}, \alpha_H$.

We assume and aim to show with this study that the structural parameters α , κ_{ip} , κ_{op} of the low-affected tissue depend mainly on the indentation pressure p_{ind} . In the high-affected tissue, the structural parameters are expected to depend additionally on the stent strut orientation angle ϕ . Finally, they are assumed to be dependent on the position, which means that they alter with the compression $\lambda_r(k)$. Either way, alterations of the structural parameters would influence the structure tensors \mathbf{H}_4 and \mathbf{H}_6 and, therefore, the material response of the stented tissue of coronary arteries.

4.2.2 *In vitro* simulation of stent implantation

Experimental setup LAESIO

For the simulation of the loading scenario of a stented coronary artery, we developed the LAESIO (Latin for *lesion*) testing device. As schematically depicted in Figure 4.3(a), it consists of two main units: the biaxial extension unit (BIAX), which aims to simulate physiological stretching of the planar specimen in the z - and θ -direction, and the triple-axis unit (TAU) which simulates the indentation pressure p_{ind} between the stent strut and the arterial wall.

The BIAX setup is an arrangement of four linear stages LTM 60F-50-HSM (Owis, Staufen

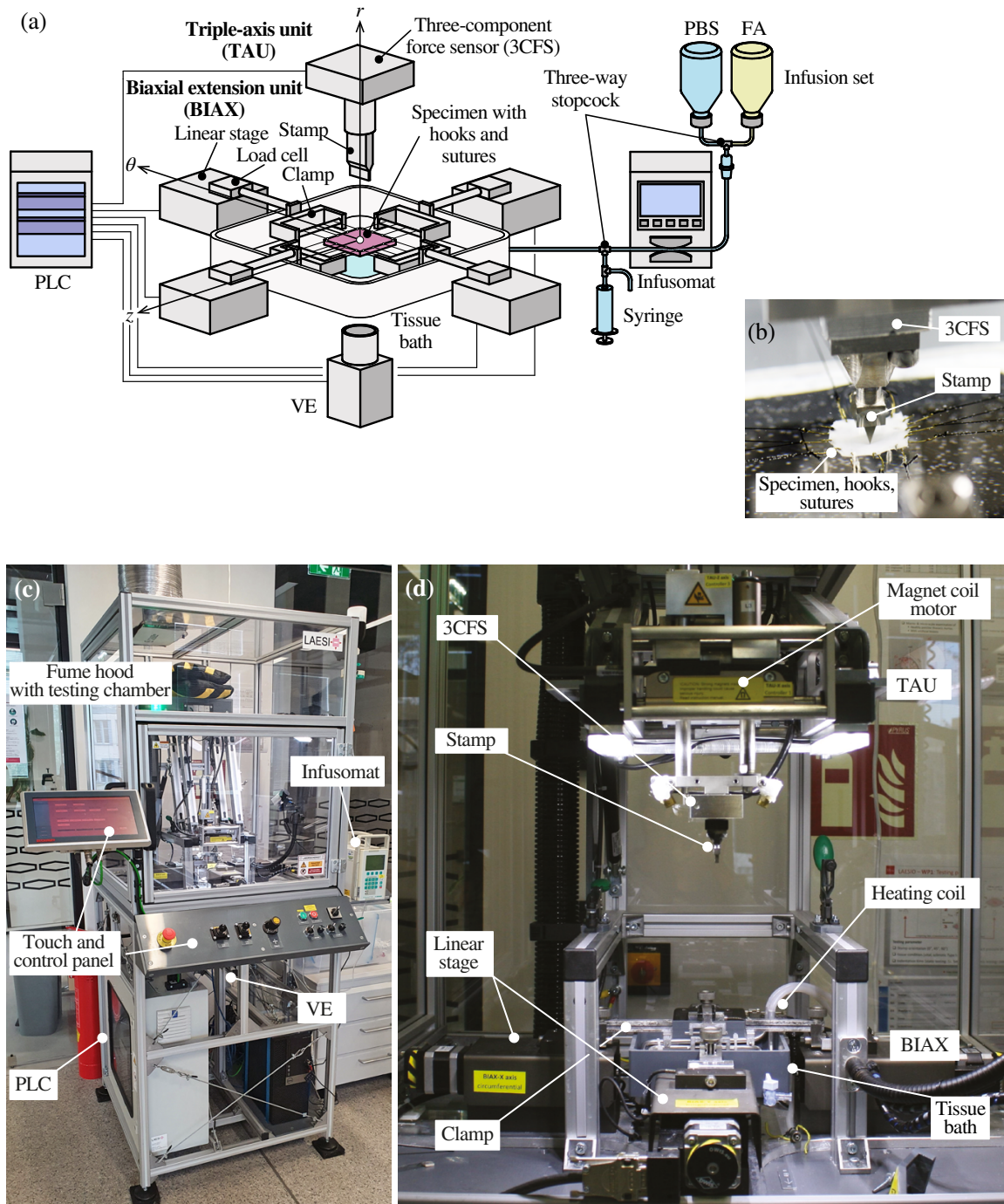


Figure 4.3 Testing rig (LAESIO): (a) schematic illustration of the main components; (b) specimen of a porcine coronary artery during stent strut indentation; (c) exterior view of the encapsulated testing rig with the testing chamber, fume hood, touch and control panel, programmable logic controller (PLC), video extensometer (VE), and infusomat; (d) interior view of the LAESIO testing chamber with the components of the illuminated triple-axis unit (TAU), and the biaxial extension unit (BIAX), the bath, and the heating coil underneath; PBS: phosphate-buffered saline; FA: formaldehyde.

im Breisgau, Germany), two in the θ - and two in the z -direction, which can be controlled independently. The linear stages hold load cells KD40s (ME-Messsysteme, Henningsdorf, Germany) with a max. capacity of ± 5 N and an accuracy of 0.1%. These load cells are connected via extensions to clamps to which the specimens are attached using surgical sutures and hooks. The specimen and the clamps are submerged in a tissue bath. The fluid inside can be heated to 37°C with a coil, which is operated by the heating immersion circulator series ED (Julabo, Seelbach, Germany). To counteract evaporation during long-term tests, the infusion pump infusomat fmS (BBraun Melsungen, Melsungen, Germany) is connected to the bath. It keeps the fluid level above the specimen by injecting ideally 19 ml/h. For chemical fixing specimens under load, the phosphate-buffered saline (PBS) can be exchanged with formaldehyde (FA) solutions. A system consisting of an infusion set, two three-way stopcocks, and two bottles enables a fast exchange between PBS and FA. A syringe allows the user to drain the bath before exchanging the fluid or after testing. To monitor the tissues' true stress-stretch behavior, the four load cells measure the reaction forces of the arterial tissue, while a video extensometer (VE) underneath the bath tracks markers on the stained and illuminated adventitia. For 2D stretch measurements, the software Laser Speckle Extensometer 2.23.3.0 (Messphysik Materials Testing, Fürstenfeld, Austria) with a resolution of ± 0.15 μm and a sample rate of 20 Hz was used.

The TAU can be freely placed above the BIAX and the specimen. It is equipped with a straight stamp with its cross-section being identical to a square stent strut with a standard strut width of $w = 0.08$ mm of modern stents [398]. Artificial lesions are generated by indenting the strut into the arterial wall (see Figure 4.3(b)). When the strut touches the specimen, the three-component force sensor (3CFS) K3D40 (ME Messsysteme) with a max. capacity of ± 2 N and an accuracy of 0.05% and is connected to the strut, and it measures the reaction forces in all three directions. The position of the strut can be altered by three magnet coil motors of the product series PS01-23 (NTI AG LinMot & MagSpring, Spreitenbach, Switzerland). The stent strut in each direction is monitored by an absolute linear encoder MS01-1/D-SSI (LinMot) with an accuracy of ± 0.001 mm.

The ideal choice of the strut shape is controversial. At this point, it must be noted that we decided to not consider the effect of curved strut segments or struts with round cross-sections in this early stage of our investigations. We used a straight strut segment with a total length l of 3 mm, which is shorter than the side length L of the specimen. This strut shape has the disadvantage that the strut ends induce stress singularities into the tissue of the floating specimen. However, preliminary tests on porcine aortas [357], and the obtained results, show that the compression underneath the strut is almost homogeneous along l . Therefore, we consider the following simplification for the calculation of the maximum strut indentation force F_{ind} , i.e.,

$$F_{\text{ind}} = p_{\text{ind}}wl. \quad (4.8)$$

The advantage of a shorter strut is that it is possible to investigate the tissue's response next to the strut, and, therefore, if the tissue structure contains transition zones for fiber orientation and dispersion. Thus, the proposed strut design was beneficial for the first

findings and insights during this early stage of our investigations but should be carefully reconsidered in future studies.

All actuators of the LAESIO testing device are controlled, and all sensors are monitored by the programmable logic controller (PLC) CX5130 (Beckhoff Automation, Verl, Germany). With the touch panel CP3911-0000 (Beckhoff Automation) and a control panel, the user was given the ability to change the testing protocol and parameters in real-time. For coding the machine software, SELMOmodeler (SELMO, Dobl, Austria) was used. The BIAx and TAU are encapsulated inside a sealed cabin with a fume hood to protect the user from direct contact with carcinogenic FA vapor (see Figure 4.3(c)). A more detailed view of the interior of LAESIO is presented in Figure 4.3(d).

Specimen preparation and storage

Two whole hearts of five-month-old domestic pigs were obtained from a local slaughterhouse. The RCA was used for our investigations because we found that more samples can be taken than from the main branches of the left coronary artery. Within a post-mortem interval of one hour, the RCA was carefully excised from the coronary ostium to the bifurcation of the right marginal artery and cut into tubes. To preserve all tubes in the long-term, snap-freezing was performed. Therefore, every tube was put into a beaker filled with 2-methyl-butane, which was cooled in liquid nitrogen for 60 s, and subsequently stored inside a freezer at -80°C . Slow and gradual cryopreservation may be more appropriate in future studies because snap-freezing could affect the mechanical properties of the arteries [399–401]. Before testing, each tube was slowly thawed, freed from 2-methyl-butane residue in 37°C warm PBS, and cut open along the z -axis. The z -side length had to be adapted to the circumference which resulted in a mean side length of $\bar{z} = 8.54 \pm 0.85$ mm and a mean thickness of $\bar{T} = 0.93 \pm 0.11$ mm of the specimens (see Table 4.1). Finally, hooks with eyelets were pierced through the arterial wall on each side of the specimen and connected with surgical sutures, as presented in Sommer *et al.* [402]. In addition, markers were applied to the adventitia with tissue ink black 3408-3 (BioGnost, Zagreb, Croatia). Despite the recommendations of Eilaghi *et al.* [403] to attach five hooks per specimen edge, only four hooks could be placed due to limited space.

Preconditioning

Before testing, every side of the specimens was attached to the respective linear stage of the LAESIO testing device via the mentioned clamps and surgical sutures. The specimen was equally preloaded in the z - and θ -direction with $f_{\min} = 0.01$ N to lift the specimen to the level of the center lines of the four load cells. Before testing, the particular specimen was submerged in 37°C PBS (pH 7.4) and subsequently preconditioned. For preconditioning, every specimen was biaxially loaded with five cycles within the assumed physiological range, i.e., within the average hemodynamic loading at MAP. The absolute values of the tensile forces at MAP for the z - and θ -direction can be calculated according to

$$f_z^{\text{MAP}} = \sigma_{zz}^{\text{MAP}} A_z \quad \text{and} \quad f_{\theta}^{\text{MAP}} = \sigma_{\theta\theta}^{\text{MAP}} A_{\theta}, \quad (4.9)$$

Table 4.1 Tested specimens harvested from right coronary arteries of two porcine hearts as well as specimen information and strut indentation parameters.

Test scenario	Sample no.	Heart no.	Sample information		Indentation parameters		
			L_0 (mm)	T_0 (mm)	ϕ ($^\circ$)	$F_{\text{ind}}/p_{\text{ind}}$ (N/MPa)	
A	S I	1	9.0	0.81	-	-	
	S II	2	8.0	0.93	-	-	
B	S III	1	9.0	0.88	-	-	
	S IV	2	8.5	0.98	-	-	
C	S V	1	8.0	0.85	90	1.0/4.1	
	S VI	2	9.0	1.03	90	1.0/4.1	
	S VII	1	8.0	0.93	90	2.0/8.3	
	S VIII	2	8.0	1.05	90	2.0/8.3	
	S IX	1	9.5	1.09	0	1.0/4.1	
	S X	2	8.0	0.72	0	1.0/4.1	
	S XI	1	8.0	0.84	0	2.0/8.3	
	S XII	2	7.5	0.93	0	2.0/8.3	
	<i>Control</i>	S XIII	1	8.0	0.72	-	-
	Median	-	-	8.0	0.93	-	-
[Q1;Q3]	-	-	[8;9]	[0.84;0.98]	-	-	
Mean	-	-	8.4	0.90	-	-	
SD	-	-	0.6	0.12	-	-	

L_0 : side length of the unloaded specimen; T_0 : thickness of the unloaded specimen; ϕ : strut orientation angle with respect to θ ; p_{ind} : indentation pressure.

where $A_z = A_\theta$ is the out-of-plane cross-section of the specimen defined by the (r, θ) - and the (r, z) -plane, respectively. Substitution of Eq. (4.1) into Eq. (4.9) gives

$$f_z^{\text{MAP}} = \frac{p_{\text{MAP}} L_0^2}{4\pi} \quad \text{and} \quad f_\theta^{\text{MAP}} = \frac{p_{\text{MAP}} L_0^2}{2\pi}, \quad (4.10)$$

where L was here replaced with L_0 , which is the side length of the unloaded specimen. To measure L of the respective physiologically loaded specimen was technically not feasible. A fully automated force-controlled protocol ensured a linear loading and unloading behavior with a testing speed of $v_{\text{BIAX}} = 1$ mm/min and with tensile forces within the physiological range $f_z \in [f_{\text{min}}, f_z^{\text{MAP}}]$ and $f_\theta \in [f_{\text{min}}, f_\theta^{\text{MAP}}]$. The force versus time curves have the shape of a triangular function with a constant ratio of $f_z^{\text{MAP}} : f_\theta^{\text{MAP}}$ between both axis. The results of this study show that three preconditioning cycles are adequate for porcine RCA specimens (see Section 4.3.1).

Preliminary tests

In order to investigate the mechanical response of coronary arteries to constant physiological (*in situ*) and supraphysiological (iatrogenic) loadings caused by PCI over a specific time, two preliminary tests were designed and executed as follows.

(A) *Equilibrium Tests*: The *in vitro* mechanical response of the RCA tissue to physiolog-

ical loadings can alter over time due to biochemical, thermodynamical, and mechanical processes inside the arterial tissue, e.g., vasoactivity [377] *q.v.*, thawing, and preloading. Thus, this preliminary test was performed on specimens S I and S II using a stretch-controlled protocol in order to determine the waiting time before the mechanical response becomes reproducible and when the specimen is ready for further testing. Five measurement series had to be carried out with a testing speed of $v_{\text{BIAX}} = 1 \text{ mm/min}$, where every series stands for a sequence of five loading and unloading cycles. During every loading cycle, the testing device has stretched the specimens with a linearly increasing and subsequently decreasing stretch within the mentioned physiological range. The maximum stretch was reached when the load cells recognized forces greater than or equal to f_{θ}^{MAP} and f_z^{MAP} . In parallel, the force-stretch response of the tissue was recorded. The first series started at $t = 0 \text{ min}$ and the last one at $t = 180 \text{ min}$, with resting intervals of 30 min in between. Finally, the ideal equilibrium time t_{equ} was derived, which defines the interval between the experiment start and the moment where the stress-stretch response of the specimen became reproducible.

(B) *Relaxation Tests:* Quasi-static relaxation tests were carried out with a force-controlled protocol to determine the time range between the moment a stent is fully expanded and recoiled inside the artery and the moment the viscoelastic tissue has adapted to the new loading scenario. Two specimens, S III and S IV, from two different RCA were stretched by the BIAX with a testing speed of $v_{\text{BIAX}} = 1 \text{ mm/min}$ until the tensile forces at MAP f_z^{MAP} and f_{θ}^{MAP} were reached. Afterwards, the linear stages stopped and kept their position. Finally, the strut of the TAU was subsequently indented with an indentation speed of $v_{\text{ind}} = 1 \text{ mm/min}$ until an indentation force of $F_{\text{ind}} = 2 \text{ N}$ was reached, which equals the maximum loading capacity of the 3CFS. The indentation force was kept constant, and the relaxation time t_{relax} measured after no change in the resulting tensile forces f_z and f_{θ} could be registered anymore.

Indentation tests

The proposed quasi-static indentation tests enable the documentation of alterations in the mechanical response of the RCA after they underwent supraphysiological loadings during stent implantation. Thus, after the mentioned equilibrium time t_{equ} (see Figure 4.4(a)) followed by the preconditioning process (see Figure 4.4(b)), the measurement series I with five additional loading and unloading cycles was performed (see Figure 4.4(c)). Every specimen was subsequently loaded and f_z^{MAP} and f_{θ}^{MAP} kept constant. Finally, the strut was indented with a constant F_{ind} and with $v_{\text{ind}} = 1 \text{ mm/min}$ (see Figure 4.4(d)). After the creep time, t_{relax} expired, the strut was removed, and measurement series II carried out equally to series I. Finally, the stress-stretch responses of both measurement series were compared to determine the damage mechanism due to the strut indentation. As listed in Table 4.1, we varied two test parameters. The first parameter is the indentation force $F_{\text{ind}} = \{1, 2\} \text{ N}$ resulting in an indentation pressure of $p_{\text{ind}} = \{4.14, 8.30\} \text{ MPa}$. The second parameter is the stent strut orientation angle $\phi = \{0, 90\}^\circ$, in which the strut points in the θ -direction are at $\phi = 0^\circ$ and in the z -direction at $\phi = 90^\circ$. Although that stent struts are mostly oriented

transversely to the z - and θ -direction (compare with Figure 4.1(a)), we decided to perform the indentation tests with the strut oriented parallel to the two main directions. Thus, in this first approach, we could investigate the influence of the strut indentation on the normal stress components without artificially induced transversal shear. The indentation tests were repeated on the specimens from the pig heart 2. In addition, two measurement series without strut indentation in between were performed on the control specimen S XIII.

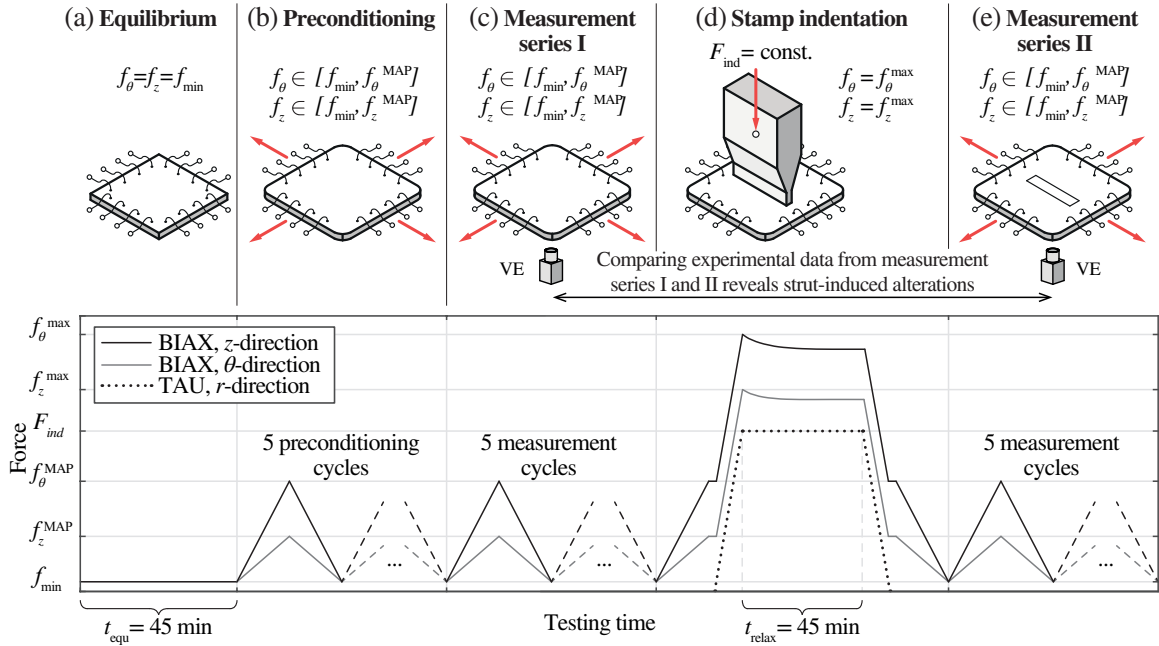


Figure 4.4 Testing protocol of the proposed indentation tests in comparison with the force-time behavior: (a) equilibrium of the mechanical response can be reached by biaxially loading the specimen continuously with a minimum force f_{\min} and waiting for t_{equ} minutes; (b) the specimen must be preconditioned with $n = 5$ loading cycles with the physiological forces f_{θ}, f_z ; (c) the first measurement cycle on the vital tissue is performed with $n = 5$ loading cycles; (d) the strut is indented with a constant indentation pressure p_{ind} (defined by the strut surface $A_{\text{strut}} = wl$ and the indentation force F_{ind}) for t_{relax} minutes; (e) the second measurement cycle on the high-affected tissue is performed. VE = video extensometer.

4.2.3 Structural analysis

Optical clearing

By finishing the measurement series II of Section 4.2.2, the strut was indented again, according to Figure 4.4(d). The PBS inside the bath was replaced with a solution of 4% FA to chemically fix under load. the tissue under force-controlled loading during a fixation time of $t_{\text{fix}} = 6$ h. Then, up to four specimens were stored at once inside the biopsy cassettes M508-Micromesh (Simport Scientific, Saint-Mathieu-de-Beloeil, Canada) with four compartments and kept in 4% FA at room temperature. In every compartment, the specimen was embedded between two biopsy foam pads M476 (Simport Scientific) to prevent

buckling.

An optical tissue clearing procedure described by Schriebl *et al.* [395] was utilized to increase the penetration depth during subsequent multi-photon microscopy without destroying the tissue. First, the biopsy cassettes with the specimens were exposed to ethanol solutions with concentrations of 50, 70, 95 and twice to 100% in steps lasting 45 min. Afterwards, the biopsy cassettes were submerged in 1:1 ethanol:benzyl alcohol, benzyl benzoate (BABB) solution for 4 h followed by an exposure to pure BABB of at least 12 h. Finally, each specimen was placed on a standard microscope slide between a washer, which formed a basin filled with BABB. The size of the washer was chosen in a way that its height was greater than the whole specimen. The washer with the specimen inside was sealed with a coverslip and nail polish to protect the microscope lens.

Nonlinear optical imaging

To show if it is feasible to quantify structural alterations in stented coronary arteries, 3D-surface and SHG scans were carried out on the specimens S V, VII, IX, XI, and XII of pig heart 1, which were all chemically fixed in a loaded configuration. All scans were performed on a multi-photon SP8MP upright microscope (Leica Microsystems, Mannheim, Germany) at the Core Facility Bioimaging of the Biomedical Center, Ludwig-Maximilians-Universität München. An HC IRAPO L 25x/1.00W motCORR water immersion lens with a working distance of 2.6 mm was used. To observe potential alterations of the structural parameters κ_{op} , κ_{ip} , and α of the artificially damaged and the control specimens on the micro-level and to define the geometrical extent of the lesion by defining k_{max} and $\lambda_r(k)$, two imaging processes were carried out:

(A) *3D-surface Scanning*: The detection of elevation profiles of all lesions was achieved by performing 3D-surface scans on the specimens with the intima facing up in the r -direction (see Figure 4.5). Confocal images were recorded in the reflection mode with an internal conventional photomultiplier tube by using solid-state laser excitation at 0.488 μm . The image pixel size was set to 0.5 μm .

(B) *Second-harmonic Generation Imaging*: SHG analyses of the fibrillar collagen structure were carried out with pulsed InSight DS+ laser (Spectra Physics, Mountain View, USA) and an excitation wavelength of 0.88 μm . An AT 420/40 emission filter with a BS 488LPXR beam splitter was equipped to observe the collagen structure of the media and the adventitia layer. The intima was expected to be detached and removed during specimen preparation. Images were recorded with an external, non-descanned hybrid photodetector (HyD) in an 8-bit mode with an image pixel size of 0.1 μm , and frame accumulation of $n = 3$. For SHG scanning, specimens were physically quartered with the sections going through the center of the lesion, pointing in the θ - and z -direction, as indicated by the blue and green planes in Figure 4.5.

In the following, the (θ, z) -plane is denoted by ‘in-plane’ and the (r, θ) - and (r, z) -plane are called ‘out-of-plane’. A single-row mosaic of the in-plane image stacks had to be scanned with the first stack centered at point $P_L(0, k_{max}, t_L)$ located in the low-affected tissue. It

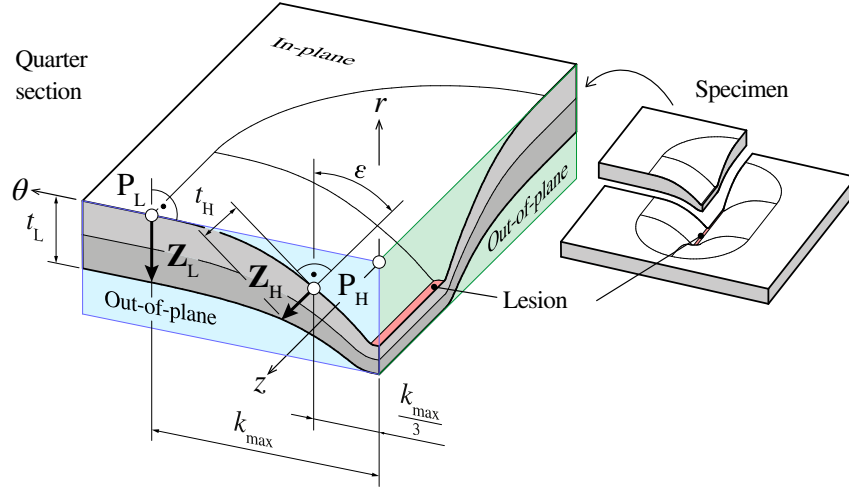


Figure 4.5 Sketch showing a quarter section of a specimen with a lesion pointing in the z -direction. Out-of-plane scans were taken in the (r, θ) - and (r, z) -planes and in-plane (θ, z) image stacks around the points P_L and P_H . The normal vectors of the image stacks were parallel to the vectors \mathbf{Z}_L and \mathbf{Z}_H , whereas \mathbf{Z}_H is perpendicular to the tangent laying on the intima in P_H making the angle ϵ with r . k_{\max} : distance between the low-affected tissue and the strut indentation; t_L : wall thickness at P_L ; t_H : wall thickness at P_H .

was not possible to obtain any information about the fiber dispersion from the tissue directly in the strut indentation due to severe compression and signal artefacts. Therefore, the location of the center of the last stack $P_H(0, k_{\max}/3, t_H)$ of the mosaic was chosen in a way that the images do not include the strut indentation itself. The distance between every image of the stacks was $5 \mu\text{m}$. Furthermore, out-of-plane scans had to be provided within the same range as the mosaic scan, with the normal vectors of the images being parallel to the long side of the lesion.

4.2.4 Data analysis

Mechanical data

In all testing scenarios, Cauchy stresses in the z - and θ -direction were computed from mechanical data as follows:

$$\sigma_{zz} = \frac{f_{z,1} + f_{z,2}}{2L_0T_0} \lambda_z \quad \text{and} \quad \sigma_{\theta\theta} = \frac{f_{\theta,1} + f_{\theta,2}}{2L_0T_0} \lambda_\theta, \quad (4.11)$$

where $f_{z,1}$, $f_{z,2}$, $f_{\theta,1}$, $f_{\theta,2}$ represent the measured reaction forces at every load cell and $\lambda_z = x_z/X_z$ and $\lambda_\theta = x_\theta/X_\theta$ the stretches in the z - and θ -direction, calculated with the marker distances from the reference (X_z, X_θ) and the deformed configuration (x_z, x_θ) . We assume negligible shear deformations due to the orthotropic natural structure of healthy coronary arteries [59].

Structural data

The 3D-surface scans were visualized with LAS X Life Science (Leica Microsystems). By virtually slicing the 3D-surface scans normal to the long side of the lesions, out-of-plane cross-sections of the lesion and the surrounding tissue were generated. With the help of these cross-sections, the values for t in the points P_H and P_L were measured. All SHG scans had to be preprocessed in Fiji (<http://fiji.sc/Fiji>, Ashburn, VA, USA). The normal vectors of the stacks in both points are denoted by \mathbf{Z}_L and \mathbf{Z}_H . While \mathbf{Z}_L is normal to the (θ, z) -plane, the high-affected tissue tends to bend due to the strut indentation. Therefore, all SHG images of the in-plane stack and the out-of-plane scans had to be rearranged to \mathbf{Z}_H and tilted with the angle ϵ around an axis going through P_H and being parallel to the z -direction (see Figure 4.5). This was achieved by using the `reslice` and `transform` commands in Fiji.

The structural parameters κ_{op} , κ_{ip} , α for native, low-affected, and high-affected tissues were obtained by following the workflow described by Schriebl *et al.* [395]. Briefly, the fiber directions for the media and adventitia were extracted from every in-plane SHG-image of the stacks and the out-of-plane images via a Fourier-based image analysis method with wedge filtering [394]. From the angular data set, the mean fiber angle was obtained with respect to θ . According to Eq. (4.6), the in-plane dispersion quantity κ_{ip} of the media and adventitia was calculated. Due to the small thickness of the specimens, only one value of κ_{op} for both layers could be derived. All structural parameters were obtained and subsequently compared using MATLAB R2019a (The MathWorks, Natick, USA). Finally, the compression in the low- and high-affected tissue was calculated according to Eq. (4.2), i.e.,

$$\lambda_{r,L} = \frac{t_L}{T_0} \quad \text{and} \quad \lambda_{r,H} = \frac{t_H}{T_0}, \quad (4.12)$$

where t_L and t_H is the wall thickness in the low- and high-affected area, respectively. The wall thickness of the unloaded specimen T_0 had to be used since it was technical not feasible to measure the respective thickness T of the physiologically loaded specimen.

4.3 Results

4.3.1 Mechanical response

The curves in Figure 4.6(a) show a representative preconditioning behavior of the RCA tissue loaded biaxially within the physiological range. In the z - and θ -direction, the non-linear stress-stretch relationship reveals no visible softening between the first and the third loading and unloading cycles. Thus, porcine RCA display almost exclusively elastic behavior within the physiological range. For specimen S I, mean stresses of $\sigma_{zz}^{\text{MAP}} = 18.6$ kPa, $\sigma_{\theta\theta}^{\text{MAP}} = 38.1$ kPa, and stretches of $\lambda_z^{\text{MAP}} = 1.14$, $\lambda_\theta^{\text{MAP}} = 1.22$, and for S II $\sigma_{zz}^{\text{MAP}} = 18.5$ kPa, $\sigma_{\theta\theta}^{\text{MAP}} = 39.4$ kPa, and $\lambda_z^{\text{MAP}} = 1.14$, $\lambda_\theta^{\text{MAP}} = 1.25$ were obtained. Both graphs in Figure 4.6 show that the hystereses are not pronounced, which is a sign of marginal

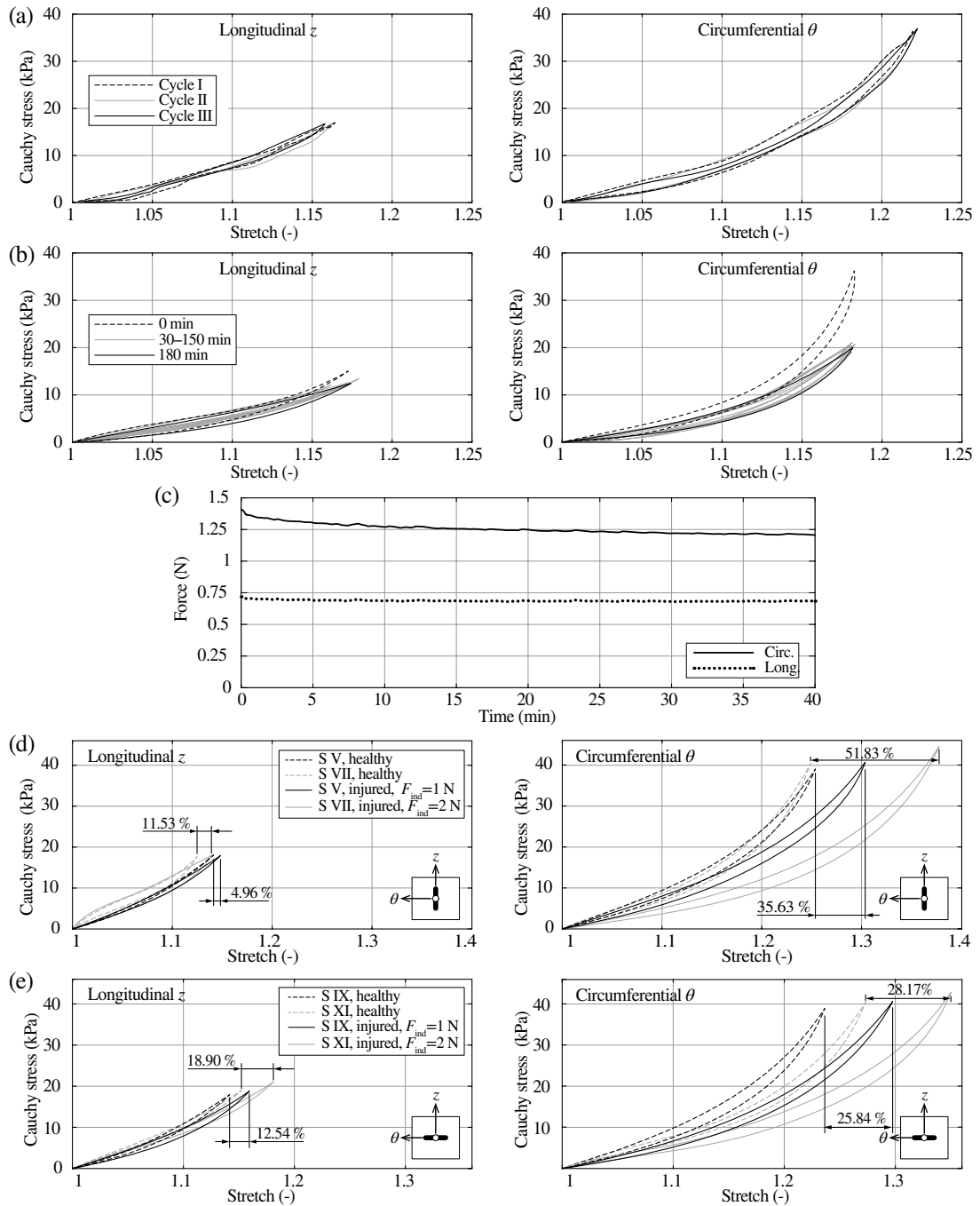


Figure 4.6 Mechanical results taken from all three test scenarios: (a) representative preconditioning behavior of the RCA tissue of specimen S I depicted as the Cauchy stress-stretch relationship during the first three physiological loading cycles; (b) representative material behavior of specimen S II reaching an equilibrium state after 30 min; (c) representative relaxation behavior, i.e., force vs. time relationship of specimen S III loaded with an indentation force of $F_{ind} = 2$ N.; (d) comparison of the Cauchy stress-stretch behavior of specimens S V ($F_{ind} = 1$ N) and S VII ($F_{ind} = 2$ N) before and after strut indentation and with the long side of the strut pointing in the z -direction; (e) comparison of the Cauchy stress-stretch behavior of specimens S IX ($F_{ind} = 2$ N) and S XI ($F_{ind} = 2$ N) before and after strut indentation and with the strut pointing in the θ -direction. Every curve in (b), (d) and (e) represents the mean of five loading, and unloading cycles.

viscoelasticity under physiological loading and the given testing rate.

Representative results of the equilibrium tests of S II are shown in Figure 4.6(b). Especially in the θ -direction, a significant drop of the Cauchy stress can be recognized after 30 min. Therefore, to secure an equilibrium of the mechanical response of the tissue, the equilibrium time was set to $t_{\text{equ}} = 45$ min for all subsequent indentation tests.

In addition, the curves in Figure 4.6(c) present a representative relaxation behavior of the RCA during relaxation tests. When reaching the indentation force of $F_{\text{ind}} = 2$ N, the biaxial response of the specimen peaked at $f_z^{\text{max}} = 0.71$ N, $f_{\theta}^{\text{max}} = 1.40$ N for S III and $f_z^{\text{max}} = 0.95$ N, $f_{\theta}^{\text{max}} = 1.41$ N for S IV, which results in supraphysiological Cauchy stresses of $\sigma_{zz}^{\text{max}} = 101.0$ kPa, $\sigma_{\theta\theta}^{\text{max}} = 203.7$ kPa and $\sigma_{zz}^{\text{max}} = 117.3$ kPa, $\sigma_{\theta\theta}^{\text{max}} = 171.8$ kPa, respectively. While keeping the indentation force constant, the forces in the θ - and z -direction dropped immediately, followed by a gradual decrease of approximately 14 and 4%, respectively. After about 30 min, almost no further decrease of the reaction forces was found. Based on these findings and by adding an extra buffer time, the timer for the strut indentation in the indentation tests was set to $t_{\text{relax}} = 45$ min.

The representative Cauchy stress-stretch relationship of measurement series I of specimens S V, and S VII depicted in Figure 4.6(d) exposes a very heterogeneous material response of vital porcine RCA tissue in both directions. Nevertheless, by comparing the data from measurement series I and II, i.e., data from healthy and injured tissue, softening can be detected after the strut indentation. If the strut points toward z , a longitudinal softening of $\Delta\lambda_z = 0.007$ (gain: 5.0%) after indenting with $F_{\text{ind}} = 1$ N and $\Delta\lambda_z = 0.014$ (gain: 11.5%) when indenting with $F_{\text{ind}} = 2$ N, and a circumferential softening of $\Delta\lambda_{\theta} = 0.056$ (gain: 35.6%) after indenting with $F_{\text{ind}} = 1$ N and $\Delta\lambda_{\theta} = 0.129$ (gain: 51.8%) when indenting with $F_{\text{ind}} = 2$ N was measured.

If the strut points toward θ , a longitudinal softening of $\Delta\lambda_z = 0.017$ (gain: 12.5%) after indenting with $F_{\text{ind}} = 1$ N and $\Delta\lambda_z = 0.027$ (gain: 18.9%) when indenting with $F_{\text{ind}} = 2$ N, and a circumferential softening of $\Delta\lambda_{\theta} = 0.057$ (gain: 25.8%) after indenting with $F_{\text{ind}} = 1$ N and $\Delta\lambda_{\theta} = 0.720$ (gain: 28.2%) when indenting with $F_{\text{ind}} = 2$ N was measured. This reveals a trend, which implies that in particular the circumferential softening increases remarkably with higher indentation pressures if the strut points toward z . If the strut is turned toward θ , the softening in the longitudinal direction seems to increase with the indentation pressure, while the increase of the circumferential softening is not as severe. An equal trend could be derived from the data of the specimens of pig heart 2. The test with the control specimen S XIII without strut indentation showed no difference in the material response. The Cauchy stresses and stretches ranged in intervals of $\sigma_{zz}^{\text{max}} \in [16.5, 19.7]$ kPa, $\sigma_{\theta\theta}^{\text{max}} \in [40.6, 41.3]$ kPa, $\lambda_z^{\text{max}} \in [1.12, 1.18]$, $\lambda_{\theta}^{\text{max}} \in [1.21, 1.30]$ when indenting with $F_{\text{ind}} = 1$ N, and in $\sigma_{zz}^{\text{max}} \in [17.8, 21.0]$ kPa, $\sigma_{\theta\theta}^{\text{max}} \in [42.8, 45.1]$ kPa, $\lambda_z^{\text{max}} \in [1.14, 1.18]$, $\lambda_{\theta}^{\text{max}} \in [1.28, 1.38]$ when indenting with $F_{\text{ind}} = 2$ N.

4.3.2 Structural response

Elevation profiles of lesions generated with varying strut orientations and indentation pressures are presented in Figure 4.7. In all four samples, the tissue bulges at the end of the indentation, while the compression in the area of interest, i.e., the center of the lesion and along the strut, is rather homogeneous. Every specimen got compressed more with increasing indentation pressure. However, differences in the extent and shape of the lesion can be detected between specimens with a strut orientation angle of $\phi = 0^\circ$ and 90° . Thus, the values for $k_{\max} = \{1.25, 1.00\}$ mm generated with $F_{\text{ind}} = \{1, 2\}$ N and $\phi = 90^\circ$ were rather high, while the compression under the strut was, with $\lambda_r^{\text{min}} = \{0.11, 0.09\}$, mostly moderate (see Figure 4.7(a) and (b)). The sidewalls of the lesions protruded slightly with a small angle. The opposite can be observed when the strut is oriented in the θ -direction with $\phi = 0^\circ$ (see Figure 4.7(c) and (d)). The extent of the lesion is, with $k_{\max} = \{0.65, 0.60\}$ mm, smaller, the compression under the strut, with $\lambda_r^{\text{min}} = \{0.09, 0.07\}$, more severe, and the lesion exhibited steeper sidewalls next to the indentation. However, k_{\max} seems to decrease with increasing force in both cases (see Figure 4.7(a) with (b), and (c) with (d)).

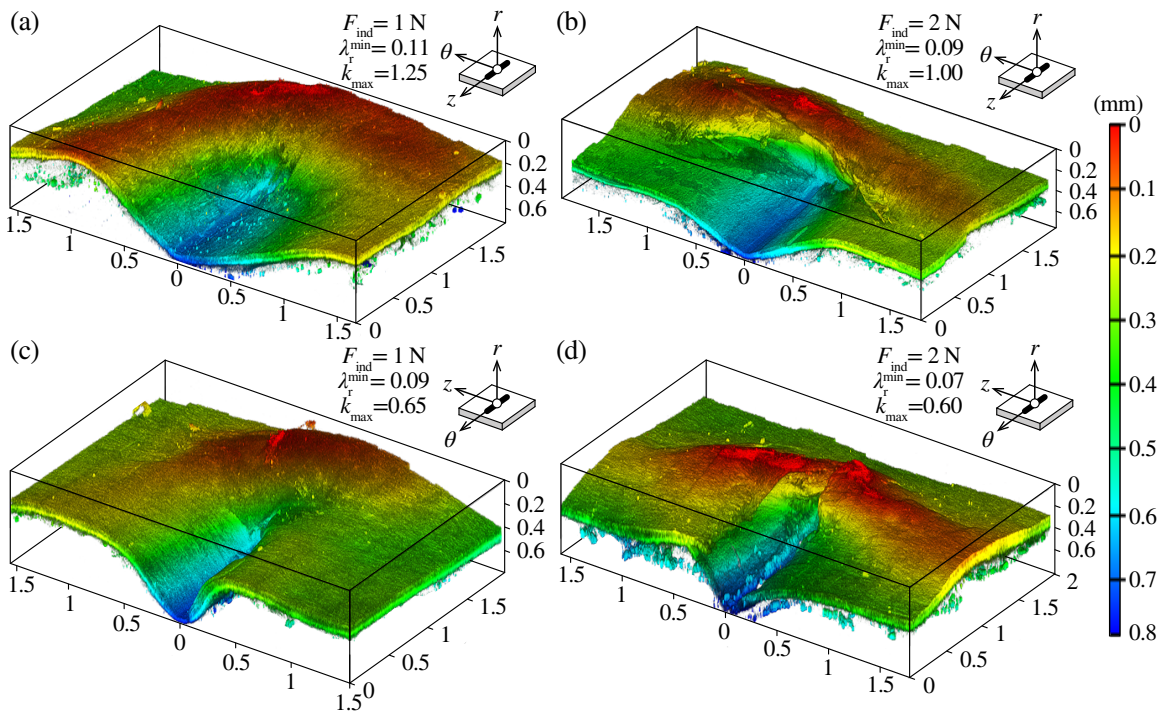


Figure 4.7 Half isometric 3D-surface scans of injured porcine RCA specimens: (a),(b) show scans of specimens S V and S VII generated with an indentation force of $F_{\text{ind}} = \{1, 2\}$ N, respectively, and the lesion points in the z -direction; (c),(d) show scans of specimens S IX and S XI generated with $F_{\text{ind}} = \{1, 2\}$ N, and the lesion points in the θ -direction. All dimensions are in millimeter; λ_r^{min} : compression in the center of the lesion; k_{\max} : distance between the low-affected tissue and the strut indentation.

Detailed out-of-plane sections of the control specimen S XIII taken in the normal directions to the (r, z) - and (r, θ) -plane, are presented in Figures 4.8(a) and (b). Two layers are clearly

distinguishable, the media and the adventitia, whereas the intima was not visible, and, therefore, considered as part of the media. In both sections, the adventitia is clearly divided into its sub-layers, the IA and EA, which take up two-thirds of the wall thickness. The quality of the signal is best with both out-of-plane sections in the EA, where thick and randomly dispersed bundles of wavy collagen fibers are present. However, in Figures 4.8(a) and (b), the signal quality differs for the media and the IA. Thus, the fine collagen structure can be better obtained in the media if an out-of-plane section is generated parallel to the fibers in the (r, θ) -plane (see Figure 4.8(b)), while most of the thicker fiber bundles of the IA can be better distinguished in out-of-plane sections in the (r, z) -plane (see Figure 4.8(a)).

Cross-sections of the left sides of the lesions of specimens S IX and S XI generated with $F_{\text{ind}} = 2\text{ N}$ are depicted in Figures 4.8(c) and (d). Again, the signal quality for the layers differs in both images. However, the angles of the sidewalls of the lesions are rather small if the strut is turned to the z -direction (see Figures 4.8(c)), but the lesion is twice as wide in comparison to specimen S XI where the strut was oriented in the θ -direction (see Figure 4.8(d)). When comparing both sections, the media and the whole adventitia in Figure 4.8(c) are getting gradually thinner over the entire lesion, while in Figure 4.8(d) the two layers get only significantly compressed next to the lesion. Although the media, IA, and EA retain the reference ratio of their thicknesses even in the deepest point of the lesion if the strut points toward z , the media and IA get almost completely thinned out if the strut is oriented in the θ -direction. In both cases, the fibers in the adventitia lose their waviness and align toward the lesion, as can be seen more clearly in Figure 4.8(c). In addition, the fiber density increases next to the lesion, especially in the indentation, and gaps are hardly noticeable. It is remarkable that no visible fiber ruptures were detected, not even at the strut ends. Fibers next to the indentation are pushed aside, reoriented, and formed a ‘boat-like’ structure (see Figure 4.8(e)). In the deepest point of the indentation, a consistently strong but blurred signal is dominating. Individual fibers and their orientation can no longer be determined.

Detailed in-plane sections of all layers and the respective intensity plot of the control specimen S XIII under physiological loading in the reference configuration are depicted in Figure 4.9(a). The intensity plot illustrates the collagen fiber orientation and dispersion throughout the entire wall of a porcine RCA. A fiber angle of 0° implies perfect orientation in the θ -direction, while $\pm 90^\circ$ corresponds to perfect z -orientation. Dark red spots intensify angles with preferred fiber orientations, whereas dark blue spots relate to zero fiber density. The media layer starts with a short transition layer (TL), namely the membrana elastica interna, with random orientation, followed immediately by a central part with fibers which tend to point toward θ with little dispersion. The media and IA are separated by another TL, the membrana elastica externa. In the IA, the fibers gradually undergo an orientation change and align with the thick and wavy fiber bundles of the EA, which are more oriented in the z -direction. The images in Figure 4.9(b) show in-plane sections and intensity plots derived from low-affected tissues at P_L and high-affected tissues at P_H from specimens S VII and S XI. It is striking that both tissues at P_L and P_H have been compressed more severely when the strut points to z , which coincides with the re-

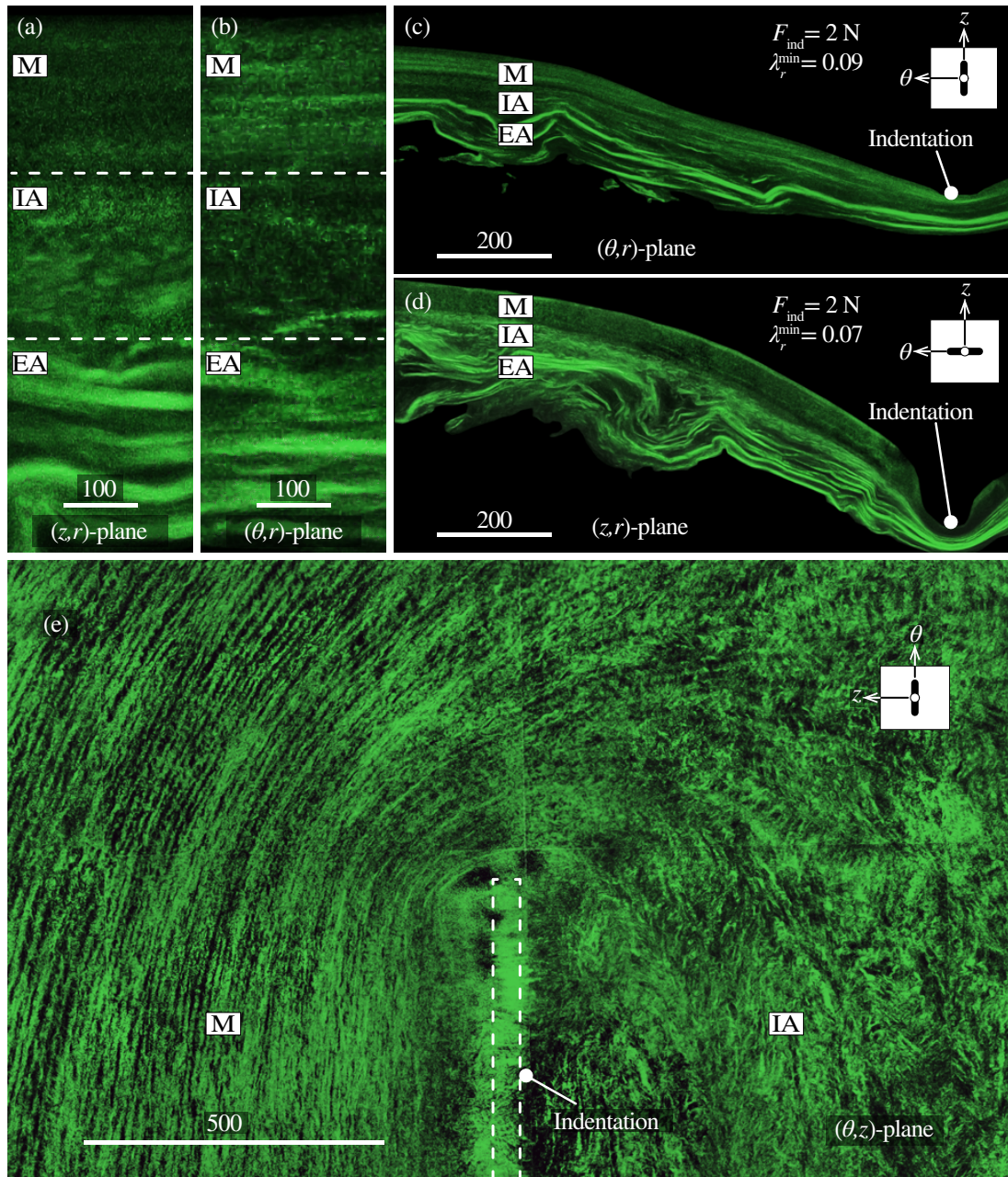


Figure 4.8 Collection of SHG-images of porcine RCA tissue in the deformed configuration: (a), (b) are detailed out-of-plane sections of native tissue of specimen S XIII under physiological loading taken from the (r,z) - and (r,θ) -plane, respectively. Only the media (M), the inner adventitia (IA), and the exterior adventitia (EA) are distinguishable; (c), (d) are out-of-plane images showing cross-sections of the lesions of specimens S VII and S XI in the (r,z) - and (r,θ) -plane generated with an indentation force of $F_{\text{ind}} = 2 \text{ N}$, with the strut pointing in the z - and θ -direction, respectively; (e) in-plane section of S IX in the (θ,z) -plane reveals the tendency of collagen fibers to take on a 'boat-shape' surrounding close to the indentation of the strut. The image plane was slightly tilted around θ so that the media can be seen on the left side and the IA on the right side. All dimensions are in mm.

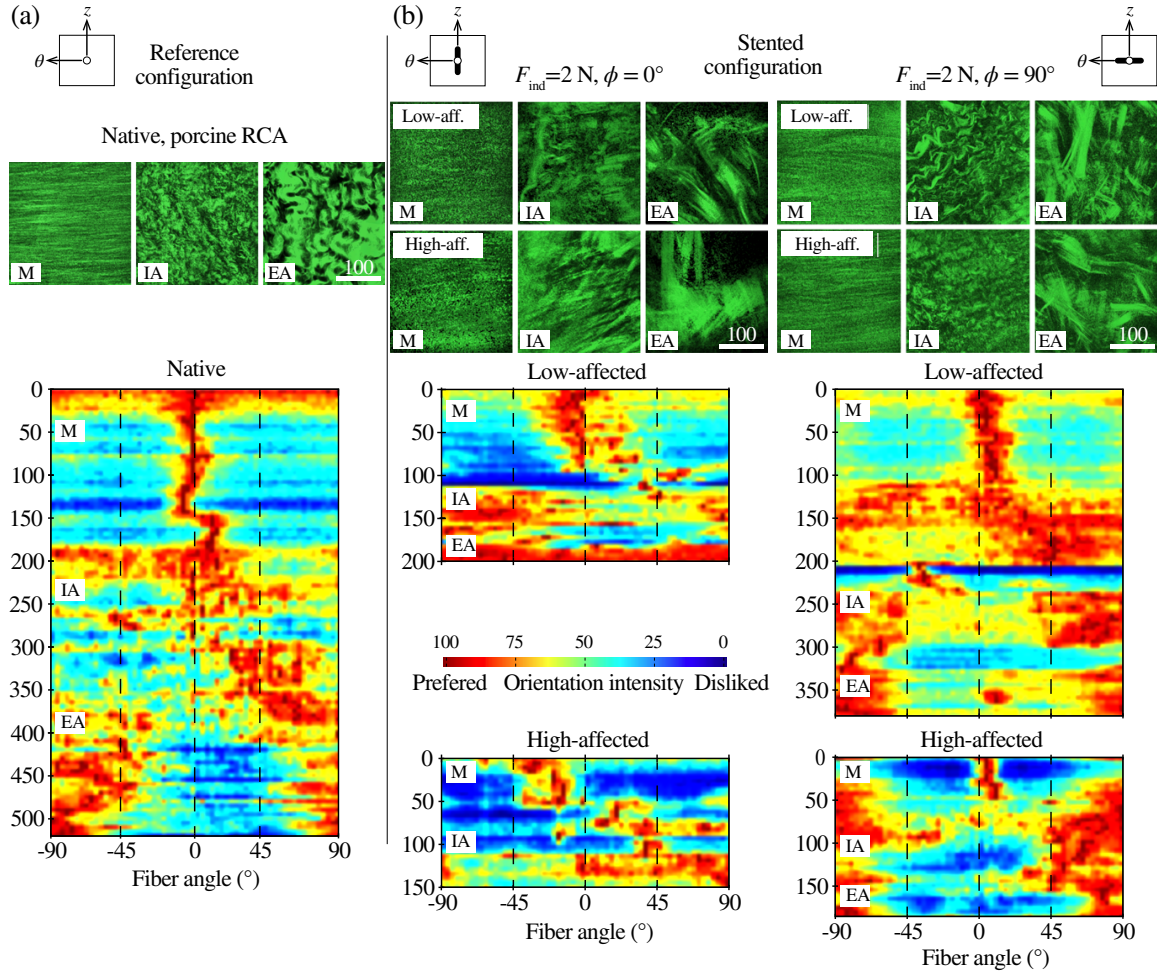


Figure 4.9 Collection of in-plane SHG-images and intensity plots of the media (M), inner adventitia (IA), and exterior adventitia (EA) of porcine RCA tissue: (a) native, porcine RCA tissue of specimen S XIII in the reference configuration; (b) low-affected (at P_L in $k = k_{max}$) and high-affected (at P_H in $k = k_{max}/3$) tissue of specimens S VII and S XI in the deformed configuration treated with an indentation force of $F_{ind} = 2\text{ N}$, and the strut points in the z - and θ -direction, respectively. All dimensions are in μm . In the intensity plots, the abscissas refer to the fiber angle, where 0° and $\pm 90^\circ$ denote for the z - and θ -direction, respectively. The preferred fiber directions are intensified with red areas and blue areas correspond to a low fiber density. $\phi =$ strut orientation angle; $k \in [0, k_{max}] =$ distance to lesion; $P_L =$ point in the zone of low-affected tissue at distance k_{max} (see Figure 4.5); $P_H =$ point in the zone of high-affected tissue next to the lesion.

sults in Figures 4.7(a) and 4.8(c). A closer observation of the mean values of the structural parameters α , κ_{ip} , κ_{op} in Table 4.2 gives rise to the first supposition about structural alterations and prevailing mechanisms due to strut indentation. Thus, in the specimens S V, and S VII, in which the strut indented with its long side pointing toward z , the mean fiber angle α becomes smaller if the indentation pressure increases. In comparison, α increases with a higher indentation pressure, if the strut is oriented in the θ -direction. This mechanism operates exactly the other way around in the adventitia. The in-plane dispersion quantity κ_{ip} was found to be smaller in the media than in the adventitia, which is consistent with

the findings for human aortas [396]. However, κ_{ip} increases if the strut indents with a higher indentation pressure, and it is oriented in the z -direction. Again, in the adventitia, this mechanism seems to operate the other way around. If the strut orientation is in the θ -direction, κ_{ip} seems to increase only at a higher indentation pressure. The out-of-plane dispersion quantity κ_{op} did not change due to indentation.

Table 4.2 Mean values of the structural parameters α , κ_{ip} , and κ_{op} obtained from SHG images of the media and adventitia layers of the native specimen S XII in the reference configuration, and the injured specimens S V, VII, IX, XI in the stented configuration correlated with the indentation parameters, the resulting tissue softening, and compression.

Sample no.	Con.	Indentation parameters		Softening		Compression			Layer	Structural parameters		
		F_{ind}/p_{ind} (N/MPa)	ϕ ($^{\circ}$)	$\Delta\lambda_z/\Delta\lambda_{\theta}$ (%)	k_{max} (mm)	T_0 (mm)	t (mm)	$\lambda_{r,i}$ (-)		α ($^{\circ}$)	κ_{ip} (-)	κ_{op} (-)
S V	LA	1.0/4.1	90	4.96/35.63	1.25	0.85	0.31	0.36	M	6	0.033	0.47
	A								49	0.130		
	M								9	0.071		
S VII	LA	2.0/8.3	90	11.53/51.83	1.00	0.97	0.20	0.20	M	14	0.104	0.49
	A								55	0.245		
	M								27	0.156		
S IX	LA	1.0/4.1	0	12.54/25.84	0.65	0.66	0.22	0.33	M	2	0.027	0.47
	A								63	0.123		
	M								1	0.020		
S XI	LA	2.0/8.3	0	18.90/28.17	0.60	0.94	0.38	0.41	M	3	0.103	0.40
	A								69	0.151		
	M								2	0.163		
S XII	Ref.	-	-	-	-	0.82	0.52	0.63	M	6	0.071	0.46
	A								56	0.172		

LA/HA: low/high affected; F_{ind} : indentation force; p_{ind} : indentation pressure; ϕ : strut orientation angle with respect to θ ; $\Delta\lambda_z/\Delta\lambda_{\theta}$: softening gain; k_{max} : distance between the low-affected tissue and the strut indentation; T_0 : thickness of the unloaded specimen; t : thickness of the specimen at point P_L and P_H, respectively; $\lambda_{r,i}$: compression of the low- or high-affected tissue with $i = L, H$; α : angle between the mean fiber direction and the θ -direction; κ_{ip} , κ_{op} : in- and out-of-plane dispersion quantities.

4.4 Discussion

In this pilot study, we quantified vascular damage by defining damage mechanisms inside the tissue by investigating mechanical and structural alterations. We have outlined that tissue of porcine coronary arteries softens when indented by a stamp which is shaped as a stent strut, but the severity is directional and changes with position, strut orientation, and indentation pressure. It turns out that all of these mechanical phenomena are influenced by changes in the fibrillar collagen structure. We confirmed our hypothesis whereby the structural parameters α , κ_{op} , κ_{ip} introduced in reference [329] differ between native and injured tissues. The presented *in vitro* experimental methods combined with an advanced imaging strategy were highly efficacious for the quantification of strut-triggered mechan-

ical and structural alterations in porcine coronary arteries. We have demonstrated that the proposed experimental testing rig LAESIO has the potential to simulate the *in situ* loading scenario during PCI in an *in vitro* environment. Morphological analysis including tissue clearing and 3D-surface, as well as SHG scanning could be applied to deformed specimens. The determination of structural parameters for native, low-affected, and high-affected tissues following the approach proposed in [329, 394–396], and their subsequent comparison turned out to be a potential tool to quantify changes in the fiber dispersion in the layers of coronary arteries. To our knowledge, this is the first study that provides information on how the mechanical behavior and structural parameters of porcine coronary arteries change due to an indenting stent strut. Despite a small number of tested specimens, we are able to identify key drivers for specific damage mechanisms after analyzing the experimental and imaging data.

4.4.1 Characteristics of native porcine RCA

After analyzing the results from experimental preconditioning and relaxation tests (compare with Figures 4.6(a) and (b)), tissues of porcine RCA under physiological loading can be described as an anisotropic, nonlinear, and marginal viscoelastic material, which agrees with findings in the literature, see, e.g., [61]. Consistent with Wang *et al.* [404], the scanned media layers of untreated coronary arteries (Figures 4.8(a),(b) and 4.9(a)) contained a fine collagen structure with a high degree of fiber orientation in the θ -direction, with a small degree of dispersion indicated by rather small values for κ_{ip} (see Table 4.2). The results show that the adventitia can be subdivided into the sublayers IA and EA, which confirms the findings documented in [72, 75]. The thicker fibers in the IA tend to align more in the θ -direction, while the wavy fiber bundles of the EA point mostly toward the z -direction. The degree of dispersion in the adventitia is significantly higher as in the media, as shown by larger values for κ_{ip} .

4.4.2 Damage mechanisms

With the help of the proposed experimental indentation tests damage mechanisms such as tissue compression and softening, differences in the collagen fiber dispersion and lesion formation could be identified. These damage mechanisms depend significantly on (i) the contact pressure between the coronary artery and the indenting stent strut, (ii) the strut orientation, and (iii) the position, i.e., the distance between a point of interest inside the tissue and the center of the strut indentation.

Influence of indentation pressure

Higher indentation pressures seem to primarily increase the severity of damage mechanisms. Thus, higher pressures led to more softening in the z - and θ -direction of all tested specimens, which could be a potential indicator for vascular damage. However, the percentage gain in the stretch due to softening was higher in the θ -direction in all tests (see

Figures 4.6(d) and (e)). Furthermore, an indentation with a higher pressure led to a greater radial compression λ_r of the tissue directly below the strut (see Figures 4.7(a) and (b)). Again, λ_r was more severe in the θ -direction. On the contrary, the distance k_{\max} seemed to shrink at a higher indentation pressure.

Influence of strut orientation

Our findings demonstrate the importance of the strut orientation angle ϕ for the directional development of damage mechanisms. The out-of-plane section in Figure 4.8(c) uncovers that a strut, which is oriented in the z -direction, cannot push fibers to the side since they are aligned perpendicular to the long side of the strut. The affected fibers of the media and the IA resist against the indentation and get straightened and significantly compressed. This results in a severe softening of the tissue in the θ -direction (see Figure 4.6(d)). This trend coincides with our findings from preliminary tests with porcine descending aortas [357]. The degree of fiber dispersion, however, decreases with a higher indentation pressure, as shown by the smaller values for κ_{ip} (see Table 4.2). Both fiber families seem to align as the mean fiber angle α gets smaller. On the contrary, if oriented in the θ -direction, the strut potentially squeezes through the collagen fibers of the media and IA as long as the strut orientation aligns with the orientation of the fibers. This might be the reason why the strut was able to indent deeper into the tissue. In addition, fewer fibers are affected by the indentation, causing less severe softening in the θ -direction, but slightly more severe softening in the z -direction (see Figure 4.6(d)), as the gap splits and, therefore, widens the tissue. The degree of fiber dispersion, however, is increasing, as κ_{ip} increases. In addition, both fiber families seem to split up more as α increases at higher indentation pressures.

Influence of position

If the strut is oriented in the z -direction, the degree of dispersion in the high-affected tissue increases, as shown by higher values for κ_{ip} . Even if the fibers get compressed, we assume them to get squeezed into each other in the r -direction and, due to the increased fiber density, pushed toward the strut ends, which leads to a greater dispersion; thus, also α increases. If the strut was oriented in the θ -direction, κ_{ip} and α decrease in the high-affected tissue. We assume that this is caused by the local compression of the fibers in the θ -direction. Through the increasing fiber density, the fibers have to align and the dispersion decreases.

4.4.3 Impact on stented arteries

To summarize these key findings, we transfer them to the scenario of a straight element of a stent strut that indents into the tissue of a porcine coronary artery, as depicted in Figure 4.1(b). For a better understanding, we interpret the findings by consulting Figure 4.10 together with Table 4.3. We now consider two cases of stent strut indentation, both with an indentation pressure in the suprphysiological range:

Case (A) – strut points toward z ($\phi = 90^\circ$): A large number of collagen fibers in the

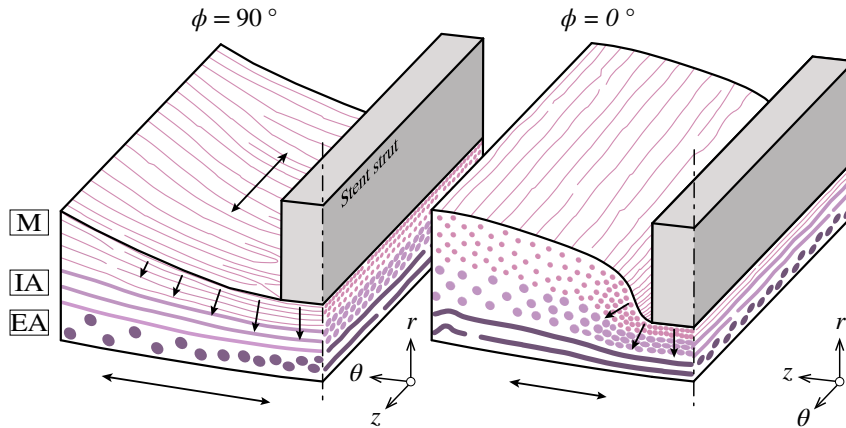


Figure 4.10 Schematic sections of the fibrillar collagen structure of the media (M), inner adventitia (IA), and exterior adventitia (EA) as well as the development of the damage mechanism at increasing indentation pressure inside coronary arteries for the strut orientation angles $\phi = \{0^\circ, 90^\circ\}$.

Table 4.3 Development of damage mechanisms at increasing indentation pressure p_{ind} for low- and high-affected tissues influenced by the stent strut orientation angle ϕ .

		$\phi = 90^\circ$	$\phi = 0^\circ$
Tissue compression	λ_r^{min}		>
	$\lambda_{r,L}$		=
	$\lambda_{r,H}$		<
Tissue softening	$\Delta\lambda_z$		<
	$\Delta\lambda_\theta$		>
Fiber dispersion	α^{media}	Increase	Decrease
	$\alpha^{\text{adventitia}}$	Decrease	Increase
	$\kappa_{\text{ip}}^{\text{media}}$	Increase	Decrease
	$\kappa_{\text{ip}}^{\text{adventitia}}$	Decrease	Increase
	κ_{op}		=
Lesion extent	k_{max}		>

λ_r^{min} : compression directly under the strut; $\lambda_{r,L}$: compression of the low-affected tissue; $\lambda_{r,H}$: compression of the high-affected tissue.

media and IA get compressed along the entire strut length, but both layers keep their thickness ratio. In the EA, mainly fibers are affected, which are located directly under the strut. In addition, a flat but broad lesion starts to form. These broad lesions may provoke extensive cell proliferation and, therefore, pronounced in-stent restenoses. The fiber density increases inside the tissue, and the volume of the extra-cellular matrix shrinks next to the strut and beyond, as the indentation pressure is distributed over a large area. Thus, the tissue stretches which results in softening in the z - and in particular in the θ -direction. We assume that the fibers in the media and IA get pushed into each other. Due to the increasing density, they give way to the neighboring fibers and cause an increase in the degree of the fiber dispersion and the mean fiber angle. A few affected fibers in the adventitia align along

the strut due to stretching, i.e., the fiber dispersion decreases together with the mean fiber angle as the compression in the θ -direction is only moderate.

Case (B) – strut points toward θ ($\phi = 0^\circ$): In comparison to *case (A)*, the collagen fibers in the media and IA get compressed more and mainly in the immediate vicinity of the strut. The thick fiber bundles of the EA have to bear most of the load. The lesion is deeper, and its sidewalls are steep. This may cause only local restricted cell proliferation. Nevertheless, these narrow lesions located perpendicular to the flow direction could increase the risk of thrombus formation. The softening is now more severe in the z -direction since most of the fibers of the EA are affected. The softening in the θ -direction is smaller if compared with *case (A)* as only a few fibers of the media and the IA get stretched under and next to the stent strut. The degree of the fiber dispersion in the adventitia increases as fibers get squeezed into each other, but decreases in the media as fibers align parallel to the stent strut. In both cases, the fibers directly under the stent strut might get severely squeezed or even destroyed, as individual fibers under the strut were not visible in our SHG images (see Figure 4.8(e)).

4.4.4 Further findings

The preconditioning behavior reveals that only three loading cycles are enough to reproduce the material behavior in the assumed physiological range. The stress-stretch relationship matches with the results of Wang *et al.* [404]. We found that a waiting time of 45 mins is adequate to reach a biochemical, thermodynamical, and mechanical equilibrium for porcine coronary arteries prior to tensile tests (see Figure 4.6(b)). Only then it can be guaranteed that experimental data are reproducible. The activities of vital SMC in the tissue might be decisive for this phenomenon. We suppose that the waiting time is influenced by sample preparation and storage techniques. Humphrey [377] *q.v.* mentioned that this equilibrium also depends on the imposed mechanical loads. Finally, we defined a relaxation time of at least 30 mins for the tissue of porcine RCA to overcome viscoelastic processes and creep if a strut indents with $p_{\text{ind}} = 8.30$ MPa (compare with Figure 4.6(c)). This rather long relaxation time is a sign of a very high amount of viscous material in the RCA tissue and might be caused by a high content of SMC in the medial layer [80].

LAESIO, the proposed testing device, was found to be suitable to realistically simulate the loading scenario of stented coronary arteries and to chemically fix the specimen under load. The testing protocol demonstrated to be robust and straightforward to perform.

The combination of 3D-surface as well as a set of in- and out-of-plane SHG scans enabled the determination of the lesion extent and the fibrillar collagen structure. The method proposed by Schriebl *et al.* [394, 395] could be adapted for analyzing alterations of the mean fiber angle and the fiber dispersion in low- and high-affected tissues of the medial and adventitial layers. The subsequent computer-assisted image preprocessing made it possible to derive structural parameters from deformed and injured tissue.

4.4.5 Limitations

In the biaxial extension tests, dynamic effects caused by the blood pressure and the rapid expansion of the stent were not considered and instead a static loading scenario was assumed (see Figure 4.1(a)). Furthermore, we only investigated vascular injuries caused by straight stent struts. In the future, different stamp designs with curved struts should be added to the study. As it is technically not feasible to measure the indentation pressure of a stent strut *in situ*, the extremum of the loading range was taken as a first reference from the FEA investigation of a Palmaz-Schatz stent [405]. The boundary conditions between the epicardial adipose tissue and the adventitia were ignored during testing to enable stretch measurements. The number of samples in the subsequent tests should be significantly increased since tissues of coronary arteries tend to be heterogeneous and also seem to differ from pig to pig. Sample preparation, indentation tests, chemical fixation, tissue clearing, and the imaging process turned out to be very time consuming. Thus, a fixed and cleared specimen is ready after approx. 24 h. Imaging takes up to 6 h. While performing SHG scans, we were confronted with poor signal quality in the media of some specimens, even after tuning the wave length and the resolution. Imaging issues caused by a weaker SHG signal in the media layer of coronary arteries have already been mentioned by Zoumi *et al.* [54]. Fluorescence microscopy with antibody labeling of certain collagen types might enhance the signal quality.

4.4.6 Future aspects

At this stage, it is challenging to formulate recommendations for the improvement of constitutive damage models, to simulate the presented damage mechanism with the finite element method. Within a continuum framework, an expansion of the model proposed in [329] seems to be feasible. Additional parameter sets need to be incorporated in such a model, which allow to fit the numerical results to an experimentally obtained function that describes the stress-stretch relationship in dependency of the radial compression λ_r . For this purpose, whole specimens of healthy and diseased tissues have to be compressed homogeneously with defined varying pressures and the stress-stretch response in the z - and θ -direction subsequently measured. Nevertheless, with this study we have shown that the material response and the injury development of stented coronary arteries seem to be influenced by the load-, direction-, and position-dependent damage mechanisms inside the tissue. Thus, the collagen structure adapts to the load, compresses, and fibers reorientate (see Figure 4.8(e)), while the severity of the damage decreases with increasing distance to the stent strut. Therefore, a discrete modeling approach might be preferable to describe the dominant damage mechanism more accurately. Due to the lack of experimental data and for deeper insights into these pathological events, the proposed study should be pursued. Further experiments, including tests with healthy and diseased human tissues with extended test series including a wider variety of indentation pressures and strut orientation angles have to be carried out. By analyzing empirical data, Swier *et al.* [387] successfully linked the injury score of Schwartz *et al.* [5, 384] with the degree of neointimal growth.

We suppose that the same injury score could be used to classify artificially created vascular injuries of the proposed experiments. In this way, cell growth could be correlated with mechanical and imaging data. Additionally, the contributions of other constituents to vascular damage formation such as elastin and proteoglycans should be investigated at the nano, micro, and macrolevels. Finally, the observation of stent-triggered alterations of the contractile or synthetic phenotype of endothelial cells, fibroblasts, and vascular smooth muscle cells as well as apoptosis and cell proliferation in active tissue is an important task to assign if the induced vascular damage is irreversible.

4.5 Conclusion

The main finding of this study is that PCI-triggered damage mechanisms such as tissue compression and softening, and changes in collagen fiber dispersion contribute to the formation of vascular damage. We demonstrated that the development of these damage mechanisms and the extent of lesions are directional, and the severity is linked to strut orientations, the indentation pressure, and the position. No fiber ruptures were discovered during our tests. To our knowledge, we have presented the first approach that links multiaxial mechanical data of high-affected tissue with structural parameters obtained from three-dimensional scans of the collagen structure. The testing device LAESIO has shown to be suitable to simulate PCI *in vitro* and to quantify mechanical alterations. Our testing protocol was adapted to the findings of equilibrium and relaxation tests. Imaging methods like 3D-surface and SHG scans could be performed on deformed specimens.

This research should be considered as a foundation for further studies, which focus on the examination of vascular damage – the most potent stimulus for in-stent restenosis development. More data would be necessary to strengthen the statistical power of these findings and to develop more accurate damage models for the use in FEA to contribute further to the optimization process of stents.

Declaration of Interests

The authors declare that they have no known competing financial interests or personal relationships that could have appeared to influence the work reported in this paper.

Acknowledgment

We want to show our gratitude to S. Diezel from the Core Facility Bioimaging at the Biomedical Center, Ludwig-Maximilians-Universität München, for assisting the SHG-imaging process, A. Pukaluk and S. Sherifova from the Institute of Biomechanics, Graz University of Technology, for their advises in the image analysis, and the members of the Regensburg Center of Biomedical Engineering for their helpful support, in particular F. Erzinger and F. Muehlenberg for assistance during the setup process of the first version of

the testing rig.

This research was funded by the Bavarian State Ministry for Education, Culture, Science, and Arts within the project ‘OptiStent’ (AZ VIII.2-F1116.RE/17/3 and PIZ-225-18). Personnel funds, consumables, and imaging costs were subsidiary financed from the project ‘LAESIO’ (P 32713) of the Austrian Science Fund (FWF). Technical equipment was partly financed by the Regensburg Center of Biomedical Engineering (RCBE) and by private parties.

References

- [1] World Health Organization. Global status report on noncommunicable diseases.
- [2] R. Griebler, J. Anzenberger, and A. Eisenmann. *Herz-Kreislauf-Erkrankungen in Österreich: Angina Pectoris, Myokardinfarkt, ischämischer Schlaganfall, periphere arterielle Verschlusskrankheit; Epidemiologie und Prävention*. Bundesministerium für Gesundheit, Wien, 2014.
- [3] V. Mühlberger, L. Kaltenbach, and H. Ulmer. Cardiac catheterization, coronary angiography (CA) and PCI in Austria during the Year 2014. *J Cardiol*, 2014.
- [4] K.H. Bønaa, J. Mannsverk, R. Wiseth, L. Aaberge, Y. Myreng, O. Nygård, D.W. Nilsen, N.-E. Kløw, M. Uchto, T. Trovik, B. Bendz, S. Stavnes, R. Bjørnerheim, A.-I. Larsen, M. Slette, T. Steigen, O.J. Jakobsen, Ø. Bleie, E. Fossum, T.A. Hanssen, Ø. Dahl-Eriksen, I. Njølstad, K. Rasmussen, T. Wils-gaard, J.E. Nordrehaug, and NORSTENT Investigators. Drug-eluting or bare-metal stents for coronary artery disease. *N Engl J Med*, 375(13):1242–1252, 2016.
- [5] R.S. Schwartz, K.C. Huber, J.G. Murphy, W.D. Edwards, A.R. Camrud, R.E. Vlietstra, and D.R. Holmes. Restenosis and the proportional neointimal response to coronary artery injury: Results in a porcine model. *J Am Coll Cardiol*, 19(2):267–274, 1992.
- [6] R. Kornowski, M.K. Hong, F.O. Tio, O. Bramwell, H. Wu, and M.B. Leon. In-stent restenosis: Contributions of inflammatory responses and arterial injury to neointimal hyperplasia. *Am J Cardiol*, 31(1):224–230, 1998.
- [7] H. Wieneke, M. Haude, M. Knocks, A. Guttersohn, C. von Birgelen, D. Baumgart, and R. Erbel. Evaluation of coronary stents in the animal model: A review. *Mat Wiss Werkstofftech*, 30(12):809–813, 1999.
- [8] F.G.P. Welt and C. Rogers. Inflammation and restenosis in the stent era. *Arterioscler Thromb Vasc Biol*, 22(11):1769–1776, 2002.
- [9] A.K. Mitra and K. Agrawal. In stent restenosis: Bane of the stent era. *J Clin Pathol*, 59(3):232–239, 2006.
- [10] M. Joner, A.V. Finn, A. Farb, E.K. Mont, F.D. Kolodgie, E. Ladich, R. Kutys, K. Skorija, H.K. Gold, and R. Virmani. Pathology of drug-eluting stents in humans: Delayed healing and late thrombotic risk. *J Am Coll Cardiol*, 48(1):193–202, 2006.
- [11] C. Kaiser, S. Galatius, P. Erne, F. Eberli, H. Alber, H. Rickli, G. Pedrazzini, B. Hornig, O. Bertel, P. Bonetti, S. de Servi, H. Brunner-La Rocca, I. Ricard, and M. Pfisterer. Drug-eluting versus bare-metal stents in large coronary arteries. *N Engl J Med*, 363(24):2310–2319, 2010.
- [12] M. Sabate, A. Cequier, A. Iñiguez, A. Serra, R. Hernandez-Antolin, V. Mainar, M. Valgimigli, M. Tsepili, P. den Heijer, A. Bethencourt, N. Vazquez, J.A. Gómez-Hospital, J.A. Baz, V. Martin-Yuste, R. van Geuns, F. Alfonso, P. Bordes, M. Tebaldi, M. Masotti, A. Silvestro, B. Backx, S. Brugaletta, G.A. van Es, and P.W. Serruys. Everolimus-eluting stent versus bare-metal stent in ST-segment elevation myocardial infarction (EXAMINATION): 1 year results of a randomised controlled trial. *Lancet*, 380(9852):1482–1490, 2012.
- [13] V.W. Lee, F.W. Cheng, A.Y. Choi, S.T. Fong, C.M. Yu, and B.P. Yan. Clinical, humanistic, and economic outcomes between drug-eluting stent (DES) and bare metal stent (BMS): 18-month follow-up study. *J Med Econ*, 20(3):239–245, 2017.
- [14] P. Kübler and K. Reczuch. Optimal stent treatment of cardiogenic shock complicating acute myocardial infarction: Bare-metal or drug-eluting stent? *Heart*, 103(15):1146–1147, 2017.

- [15] K.N. Dubé, P.R. Riley, and N. Smart. Coronary vessel development and insight towards neovascular therapy. *Int J Exp Pathol*, 90(3):262–283, 2009.
- [16] R. Madonna, M. Massaro, E. Scoditti, I. Pescetelli, and R. de Caterina. The epicardial adipose tissue and the coronary arteries: Dangerous liaisons. *Cardiovasc Res*, 115(6):1013–1025, 2019.
- [17] J.T. Dodge, B.G. Brown, E.L. Bolson, and H.T. Dodge. Lumen diameter of normal human coronary arteries. Influence of age, sex, anatomic variation, and left ventricular hypertrophy or dilation. *Circulation*, 86(1):232–246, 1992.
- [18] Z. Abedin and J. Goldberg. Origin and length of left main coronary artery: Its relation to height, weight, sex, age, pattern of coronary distribution, and presence or absence of coronary artery disease. *Catheter Cardiovasc Interv*, 4(3):335–340, 1978.
- [19] A.D. Villa, E. Sammut, A. Nair, R. Rajani, R. Bonamini, and A. Chiribiri. Coronary artery anomalies overview: The normal and the abnormal. *World J Radiol*, 8(6):537–555, 2016.
- [20] B.F. Waller, C.M. Orr, J.D. Slack, C.A. Pinkerton, J. van Tassel, and T. Peters. Anatomy, histology, and pathology of coronary arteries: A review relevant to new interventional and imaging techniques—part I. *Clin Cardiol*, 15(6):451–457, 1992.
- [21] P.S. Douglas, J. Fiolkoski, B. Berko, and N. Reichek. Echocardiographic visualization of coronary artery anatomy in the adult. *J Am Coll Cardiol*, 11(3):565–571, 1988.
- [22] J. Namgung and J.A. Kim. The prevalence of coronary anomalies in a single center of Korea: origination, course, and termination anomalies of aberrant coronary arteries detected by ECG-gated cardiac MDCT. *BMC Cardiovasc Disord*, 14:48, 2014.
- [23] O. Soran, G. Pamir, C. Erol, C. Kocakavak, and I. Sabah. The incidence and significance of myocardial bridge in a prospectively defined population of patients undergoing coronary angiography for chest pain. *Tokai J Exp Clin Med*, 25(2):57–60, 2000.
- [24] J.E. Shriki, J.S. Shinbane, M.A. Rashid, A. Hindoyan, J.G. Withey, A. DeFrance, M. Cunningham, G.R. Oliveira, B.H. Warren, and A. Wilcox. Identifying, characterizing, and classifying congenital anomalies of the coronary arteries. *Radiographics*, 32(2):453–468, 2012.
- [25] A.C. van der Wal. Coronary artery pathology. *Heart*, 93(11):1484–1489, 2007.
- [26] J. Koerselman, Y. van der Graaf, P.P.Th. de Jaegere, and D.E. Grobbee. Coronary collaterals: An important and underexposed aspect of coronary artery disease. *Circulation*, 107(19):2507–2511, 2003.
- [27] C. Seiler. The human coronary collateral circulation. *Heart*, 89(11):1352–1357, 2003.
- [28] M. Félétou. *The endothelium, part I: multiple functions of the endothelial cells – focus on endothelium-derived vasoactive mediators*, volume 3. Morgan & Claypool Life Sciences, San Rafael (CA), USA, 2011.
- [29] W.P. Arnold, C.K. Mittal, S. Katsuki, and F. Murad. Nitric oxide activates guanylate cyclase and increases guanosine 3':5'-cyclic monophosphate levels in various tissue preparations. *PNAS*, 74(8):3203–3207, 1977.
- [30] R.K. Kharbanda and J.E. Deanfield. Functions of the healthy endothelium. *Coron Artery Dis*, 12(6):485–491, 2001.
- [31] A. Pothula, V.L. Serebruany, P. Gurbel, M.E. McKenzie, and D. Atar. Pathophysiology and therapeutic modification of thrombin generation in patients with coronary artery disease. *Eur J Pharmacol*, 402(1-2):1–10, 2000.
- [32] W.C. Aird. Phenotypic heterogeneity of the endothelium: I. Structure, function, and mechanisms. *Circulation research*, 100(2):158–173, 2007.

- [33] W.C. Aird. Phenotypic heterogeneity of the endothelium: II. Representative vascular beds. *Circ Res*, 100(2):174–190, 2007.
- [34] M.M. Thompson and R. Fitridge, editors. *Mechanisms of vascular disease: A reference book for vascular specialists*. Barr Smith Press, Adelaide, 2011.
- [35] N. Zhou, S. Stoll, C. Leimena, and H. Qiu. Vascular smooth muscle cell. In K. Sakuma, editor, *Muscle cell and tissue - current status of research field*. InTechOpen, 2018.
- [36] M.R. Roach and A.C. Burton. The reason for the shape of the distensibility curves of arteries. *Can J Biochem Physiol*, 35(8):681–690, 1957.
- [37] H. Wolinsky and S. Glagov. Structural basis for the static mechanical properties of the aortic media. *Circ Res*, 14:400–413, 1964.
- [38] T. Matsumoto and K. Nagayama. Tensile properties of vascular smooth muscle cells: Bridging vascular and cellular biomechanics. *J Biomech*, 45(5):745–755, 2012.
- [39] P. Kochová, J. Kuncová, J. Svíglerová, R. Cimrman, M. Miklíková, V. Liška, and Z. Tonar. The contribution of vascular smooth muscle, elastin and collagen on the passive mechanics of porcine carotid arteries. *Physiological measurement*, 33(8):1335–1351, 2012.
- [40] X. Lu and G.S. Kassab. Vasoactivity of blood vessels using a novel isovolumic myograph. *Ann Biomed Eng*, 35(3):356–366, 2007.
- [41] Y. Huo, Y. Cheng, X. Zhao, X. Lu, and G.S. Kassab. Biaxial vasoactivity of porcine coronary artery. *Am J Physiol Heart Circ Physiol*, 302(10):H2058–63, 2012.
- [42] L. Bacakova, M. Travnickova, E. Filova, R. Matějka, J. Stepanovska, J. Musilkova, J. Zarubova, and M. Molitor. The role of vascular smooth muscle cells in the physiology and pathophysiology of blood vessels. In K. Sakuma, editor, *Muscle cell and tissue - current status of research field*. InTechOpen, 2018.
- [43] J.M. Sorrell and A.I. Caplan. Chapter 4 fibroblasts—A diverse population at the center of It all. In K. Jeon, editor, *International Review Of Cell and Molecular Biology*, volume 276 of *International Review of Cell and Molecular Biology*, pages 161–214. Elsevier, s.l., 2009.
- [44] J. Folkman and A. Moscona. Role of cell shape in growth control. *Nature*, 273(5661):345–349, 1978.
- [45] X. Liao, Y. Shen, R. Zhang, K. Sugi, N.T. Vasudevan, M.A. Alaiti, D.R. Sweet, L. Zhou, Y. Qing, S.L. Gerson, C. Fu, A. Wynshaw-Boris, R. Hu, M.A. Schwartz, H. Fujioka, B. Richardson, M.J. Cameron, H. Hayashi, J.S. Stamler, and M.K. Jain. Distinct roles of resident and nonresident macrophages in nonischemic cardiomyopathy. *Proc Natl Acad Sci U S A*, 115(20):E4661–E4669, 2018.
- [46] T.A. Wynn and K.M. Vannella. Macrophages in tissue repair, regeneration, and fibrosis. *Immunity*, 44(3):450–462, 2016.
- [47] J. Xu and G.-P. Shi. Vascular wall extracellular matrix proteins and vascular diseases. *Biochim Biophys Acta*, 1842(11):2106–2119, 2014.
- [48] J.D. Humphrey, J.F. Eberth, W.W. Dye, and R.L. Gleason. Fundamental role of axial stress in compensatory adaptations by arteries. *J Biomech*, 42(1):1–8, 2009.
- [49] M.K. O’Connell, S. Murthy, S. Phan, C. Xu, J. Buchanan, R. Spilker, R.L. Dalman, C.K. Zarins, W. Denk, and C.A. Taylor. The three-dimensional micro- and nanostructure of the aortic medial lamellar unit measured using 3D confocal and electron microscopy imaging. *Matrix Biol*, 27(3):171–181, 2008.
- [50] J. Myllyharju and K.I. Kivirikko. Collagens and collagen-related diseases. *Ann Med*, 33(1):7–21, 2001.

- [51] K.I. Kivirikko. Collagens and their abnormalities in a wide spectrum of diseases. *Annals of medicine*, 25(2):113–126, 1993.
- [52] S. Ricard-Blum. The collagen family. *Cold Spring Harb Perspect Biol*, 3(1):a004978, 2011.
- [53] J.-Y. Exposito, C. Cluzel, C. Lethias, and U. Valcourt. The fibrillar collagen family. *Int J Mol Sci*, 11(2):407–426, 2010.
- [54] A. Zoumi, X. Lu, G.S. Kassab, and B.J. Tromberg. Imaging coronary artery microstructure using second-harmonic and two-photon fluorescence microscopy. *Biophys J*, 87(4):2778–2786, 2004.
- [55] J. Díez. Arterial stiffness and extracellular matrix. *Adv Cardiol*, 44:76–95, 2007.
- [56] M. Yamamoto, K. Yamamoto, and T. Noumura. Type I collagen promotes modulation of cultured rabbit arterial smooth muscle cells from a contractile to a synthetic phenotype. *Exp Cell Res*, 204(1):121–129, 1993.
- [57] M. Hirose, H. Kosugi, K. Nakazato, and T. Hayashi. Restoration to a quiescent and contractile phenotype from a proliferative phenotype of myofibroblast-like human aortic smooth muscle cells by culture on type IV collagen gels. *J Biochem*, 125(6):991–1000, 1999.
- [58] J.A. Rhodin. Fine structure of vascular walls in mammals with special reference to smooth muscle component. *Physiol Rev Suppl*, 5:48–87, 1962.
- [59] G.A. Holzapfel, G. Sommer, C.T. Gasser, and P. Regitnig. Determination of layer-specific mechanical properties of human coronary arteries with non-atherosclerotic intimal thickening, and related constitutive modeling. *Am J Physiol Heart Circ Physiol*, 289(5):H2048–2058, 2005.
- [60] G.A. Holzapfel, T.C. Gasser, and R.W. Ogden. A new constitutive framework for arterial wall mechanics and a comparative study of material models. *J. Elast*, 61(1/3):1–48, 2000.
- [61] H. Chen and G.S. Kassab. Microstructure-based biomechanics of coronary arteries in health and disease. *J Biomech*, 49(12):2548–2559, 2016.
- [62] M.A. Farcas, L. Rouleau, R. Fraser, and R.L. Leask. The development of 3-D, in vitro, endothelial culture models for the study of coronary artery disease. *Biomed Eng Online*, 8(1):30, 2009.
- [63] K.S. Moulton, B.R. Olsen, S. Sonn, N. Fukai, D. Zurakowski, and X. Zeng. Loss of collagen XVIII enhances neovascularization and vascular permeability in atherosclerosis. *Circulation*, 110(10):1330–1336, 2004.
- [64] R. Hallmann, N. Horn, M. Selg, O. Wendler, F. Pausch, and L.M. Sorokin. Expression and function of laminins in the embryonic and mature vasculature. *Physiol Rev*, 85(3):979–1000, 2005.
- [65] P.D. Yurchenco. Basement membranes: Cell scaffoldings and signaling platforms. *Cold Spring Harb Perspect Biol*, 3(2):a004911, 2011.
- [66] H.J. Carpenter, A. Gholipour, M.H. Ghayesh, A.C. Zander, and P.J. Psaltis. A review on the biomechanics of coronary arteries. *Int J Eng Sci*, 147:103201, 2020.
- [67] G. Wick, R.W. Glanville, and R. Timpl. Characterization of antibodies to basement membrane (type IV) collagen in immunohistological studies. *Immunobiology*, 156(4-5):372–381, 1980.
- [68] S.M. Schwartz and E.P. Benditt. Studies on aortic intima. I. Structure and permeability of rat thoracic aortic intima. *Am J Pathol*, 66(2):241–264, 1972.
- [69] J.A. Rhodin. Architecture of the vessel wall. In R. Terjung, editor, *Comprehensive Physiology*, pages 1–31. Wiley, Hoboken (NJ), USA, 2011.
- [70] M.H. Ross and W. Pawlina. *Histology: A text and atlas; with correlated cell and molecular biology*. Wolters Kluwer/Lippincott Williams & Wilkins Health, Philadelphia (PA), USA, 6 edition, 2011.

- [71] B. Martínez-González, M.dC. Theriot-Girón, N. López-Serna, R. Morales-Avalos, A. Quiroga-Garza, C.G. Reyes-Hernández, A. Villanueva-Olivo, J.I. Leyva-Villegas, A. Soto-Domínguez, D. de La Fuente-Villarreal, R.E. Elizondo-Omaña, and S. Guzmán-López. Morphological analysis of major segments of coronary artery occlusion: Importance in myocardial revascularization surgery. *Int J Morphol*, 33(4):1205–1212, 2015.
- [72] H. Chen, M.N. Slipchenko, Y. Liu, X. Zhao, J.-X. Cheng, Y. Lanir, and G.S. Kassab. Biaxial deformation of collagen and elastin fibers in coronary adventitia. *J Appl Physiol*, 115(11):1683–1693, 2013.
- [73] J.E. Wagenseil and R.P. Mecham. Vascular extracellular matrix and arterial mechanics. *Physiol Rev*, 89(3):957–989, 2009.
- [74] J.M. Clark and S. Glagov. Transmural organization of the arterial media. The lamellar unit revisited. *Arteriosclerosis*, 5(1):19–34, 1985.
- [75] H. Chen, Y. Liu, M.N. Slipchenko, X. Zhao, J.-X. Cheng, and G.S. Kassab. The layered structure of coronary adventitia under mechanical load. *Biophys J*, 101(11):2555–2562, 2011.
- [76] C. Farquharson and S.P. Robins. Immunolocalization of collagen types I and III in the arterial wall of the rat. *Histochem J*, 21(3):172–178, 1989.
- [77] E.C. Davis. Smooth muscle cell to elastic lamina connections in developing mouse aorta. Role in aortic medial organization. *Lab Invest*, 68(1):89–99, 1993.
- [78] C. Baldock, A.F. Oberhauser, L. Ma, D. Lammie, V. Siegler, S.M. Mithieux, Y. Tu, J.Y.H. Chow, F. Suleman, M. Malfois, S. Rogers, L. Guo, T.C. Irving, T.J. Wess, and A.S. Weiss. Shape of tropoelastin, the highly extensible protein that controls human tissue elasticity. *PNAS*, 108(11):4322–4327, 2011.
- [79] H. Wolinsky and S. Glagov. A lamellar unit of aortic medial structure and function in mammals. *Circ Res*, 20(1):99–111, 1967.
- [80] M. Cebova and F. Kristek. Age-dependent ultrastructural changes of coronary artery in spontaneously hypertensive rats. *Gen Physiol Biophys*, 30(4):364–372, 2011.
- [81] M. Garcia and G.S. Kassab. Right coronary artery becomes stiffer with increase in elastin and collagen in right ventricular hypertrophy. *J Appl Physiol*, 106(4):1338–1346, 2009.
- [82] A. Deussen, V. Ohanyan, A. Jannasch, L. Yin, and W. Chilian. Mechanisms of metabolic coronary flow regulation. *J Mol Cell Cardiol*, 52(4):794–801, 2012.
- [83] J.E. Hall. *Guyton and hall textbook of medical physiology: Enhanced e-book*. Guyton Physiology. Elsevier, London, UK, 12 edition, 2010.
- [84] J. Spaan, C. Kolyva, J. van den Wijngaard, R. ter Wee, P. van Horssen, J. Piek, and M. Siebes. Coronary structure and perfusion in health and disease. *Philos Trans A Math Phys Eng Sci*, 366(1878):3137–3153, 2008.
- [85] Y. Huo and G.S. Kassab. Pulsatile blood flow in the entire coronary arterial tree: Theory and experiment. *Am J Physiol Heart Circ Physiol*, 291(3):H1074–87, 2006.
- [86] A.G. Goodwill, G.M. Dick, A.M. Kiel, and J.D. Tune. Regulation of coronary blood flow. *Compr Physiol*, 7(2):321–382, 2017.
- [87] A. Kamiya and T. Togawa. Adaptive regulation of wall shear stress to flow change in the canine carotid artery. *Am J Physiol*, 239(1):H14–21, 1980.
- [88] B.L. Langille, M.P. Bendeck, and F.W. Keeley. Adaptations of carotid arteries of young and mature rabbits to reduced carotid blood flow. *Am J Physiol*, 256(4 Pt 2):H931–9, 1989.

- [89] R.D. Rudic, E.G. Shesely, N. Maeda, O. Smithies, S.S. Segal, and W.C. Sessa. Direct evidence for the importance of endothelium-derived nitric oxide in vascular remodeling. *J Clin Invest*, 101(4):731–736, 1998.
- [90] E. Sho, H. Nanjo, M. Sho, M. Kobayashi, M. Komatsu, K. Kawamura, C. Xu, C.K. Zarins, and H. Masuda. Arterial enlargement, tortuosity, and intimal thickening in response to sequential exposure to high and low wall shear stress. *J Vasc Surg*, 39(3):601–612, 2004.
- [91] G-X Wang, S-X Cai, P-Q Wang, K-Q Ouyang, Y-L Wang, and S-R Xu. Shear-induced changes in endothelin-1 secretion of microvascular endothelial cells. *Microvasc Res*, 63(2):209–217, 2002.
- [92] H. Chen, T. Luo, X. Zhao, X. Lu, Y. Huo, and G.S. Kassab. Microstructural constitutive model of active coronary media. *Biomaterials*, 34(31):7575–7583, 2013.
- [93] P. van Loon. Length-force and volume-pressure relationships of arteries. *Biorheology*, 14(4):181–201, 1977.
- [94] H.W. Weizsäcker, H. Lambert, and K. Pascale. Analysis of the passive mechanical properties of rat carotid arteries. *J Biomech*, 16(9):703–715, 1983.
- [95] L.J. Brossollet and R.P. Vito. An alternate formulation of blood vessel mechanics and the meaning of the in vivo property. *J Biomech*, 28(6):679–687, 1995.
- [96] C.A.J. Schulze-Bauer, C. Mörth, and G.A. Holzapfel. Passive biaxial mechanical response of aged human iliac arteries. *J Biomech Eng*, 125(3):395–406, 2003.
- [97] G. Sommer, C. Benedikt, J.A. Niestrawska, G. Hohenberger, C. Viertler, P. Regitnig, T.U. Cohnert, and G.A. Holzapfel. Mechanical response of human subclavian and iliac arteries to extension, inflation and torsion. *Acta Biomater*, 75:235–252, 2018.
- [98] P. Fridez, M. Zulliger, F. Bobard, G. Montorzi, H. Miyazaki, K. Hayashi, and N. Stergiopoulos. Geometrical, functional, and histomorphometric adaptation of rat carotid artery in induced hypertension. *J Biomech*, 36(5):671–680, 2003.
- [99] W.L. Hammer. *Functional soft tissue examination and treatment by manual methods: The extremities*. Aspen Publishers, Gaithersburg (MD), USA, 1991.
- [100] J.-L. Martiel, G. Finet, G.A. Holzapfel, M. Stuber, T. Matsumoto, R.I. Pettigrew, and J. Ohayon. Importance of residual stress and basal tone in healthy and pathological human coronary arteries. In J. Ohayon, G. Finet, and R. Pettigrew, editors, *Biomechanics of coronary atherosclerotic plaque*, Biomechanics of living organs, pages 443–473. Academic Press, Amsterdam, NLD, 2020.
- [101] P.B. Dobrin, T.H. Schwarcz, and R. Mrkvicka. Longitudinal retractive force in pressurized dog and human arteries. *J Surg Res*, 48(2):116–120, 1990.
- [102] P.J. Zeller and T.C. Skalak. Contribution of individual structural components in determining the zero-stress state in small arteries. *J Vasc Res*, 35(1):8–17, 1998.
- [103] Y. Liu, W. Zhang, C. Wang, and G.S. Kassab. A linearized and incompressible constitutive model for arteries. *J Theor Biol*, 286(1):85–91, 2011.
- [104] R. Wang, J. Raykin, L.P. Brewster, and R.L. Gleason. A novel approach to assess the in situ versus ex vivo mechanical behaviors of the coronary artery. *J Biomech Eng*, 139(1):0110101–0110107, 2017.
- [105] T. E. Carew, R. N. Vaishnav, and D. J. Patel. Compressibility of the arterial wall. *Circ Res*, 23(1):61–68, 1968.
- [106] C. Lally, A.J. Reid, and P.J. Prendergast. Elastic behavior of porcine coronary artery tissue under uniaxial and equibiaxial tension. *Ann Biomed Eng*, 32(10):1355–1364, 2004.
- [107] X. Lu, A. Pandit, and G.S. Kassab. Biaxial incremental homeostatic elastic moduli of coronary artery:

- Two-layer model. *Am J Physiol Heart Circ Physiol*, 287(4):H1663–9, 2004.
- [108] A. Pandit, X. Lu, C. Wang, and G.S. Kassab. Biaxial elastic material properties of porcine coronary media and adventitia. *Am J Physiol Heart Circ Physiol*, 288(6):H2581–7, 2005.
- [109] Y. Huo, X. Zhao, Y. Cheng, X. Lu, and G.S. Kassab. Two-layer model of coronary artery vasoactivity. *J Appl Physiol*, 114(10):1451–1459, 2013.
- [110] A. Karimi, M. Navidbakhsh, A. Shojaei, and S. Faghihi. Measurement of the uniaxial mechanical properties of healthy and atherosclerotic human coronary arteries. *Mater Sci Eng C Mater Biol Appl*, 33(5):2550–2554, 2013.
- [111] S. Glagov, R. Vito, D.P. Giddens, and C.K. Zarins. Micro-architecture and composition of artery walls: Relationship to location, diameter and the distribution of mechanical stress. *J Hypertens Suppl*, 10(6):S101–4, 1992.
- [112] P.D. Richardson and S.M. Keeny, editors. *Anisotropy of human coronary artery intima: Proceedings of the Fifteenth Annual Northeast Bioengineering Conference*. IEEE, Boston (MA), USA, 1989.
- [113] J.D. Ferry. *Viscoelastic properties of polymers*. John Wiley & Sons, New York and Chichester and Brisbane and Toronto and Singapore, 3 edition, 1980.
- [114] B.S. Gow and M.G. Taylor. Measurement of viscoelastic properties of arteries in the living dog. *Circ Res*, 23(1):111–122, 1968.
- [115] G.A. Holzapfel and T.C. Gasser. A viscoelastic model for fiber-reinforced composites at finite strains: Continuum basis, computational aspects and applications. *Comput Method Appl M*, 190(34):4379–4403, 2001.
- [116] G.A. Holzapfel, C.T. Gasser, and M. Stadler. A structural model for the viscoelastic behavior of arterial walls: Continuum formulation and finite element analysis. *Eur J Mech A Solids*, 21(3):41–463, 2002.
- [117] H.E. Burton, J.M. Freij, and D.M. Espino. Dynamic viscoelasticity and surface properties of porcine left anterior descending coronary arteries. *Cardiovasc Eng Techn*, 8(1):41–56, 2017.
- [118] D.W.L. Hukins, J.C. Leahy, and K.J. Mathias. Biomaterials: Defining the mechanical properties of natural tissues and selection of replacement materials. *J Mater Chem*, 9(3):629–636, 1999.
- [119] S. Kaptoge, L. Pennells, D. de Bacquer, M.T. Cooney, M. Kavousi, G. Stevens, L.M. Riley, S. Savin, T. Khan, S. Altay, P. Amouyel, G. Assmann, S. Bell, Y. Ben-Shlomo, L. Berkman, J.W. Beulens, C. Björkelund, M. Blaha, D.G. Blazer, T. Bolton, R. Bonita Beaglehole, H. Brenner, E.J. Brunner, E. Casiglia, P. Chamnan, Y.-H. Choi, R. Chowdry, S. Coady, C.J. Crespo, M. Cushman, G.R. Dagenais, R.B. D’Agostino Sr, M. Daimon, K.W. Davidson, G. Engström, I. Ford, J. Gallacher, R.T. Gansevoort, T.A. Gaziano, S. Giampaoli, G. Grandits, S. Grimsgaard, D.E. Grobbee, V. Gudnason, Q. Guo, H. Tolonen, S. Humphries, H. Iso, J.W. Jukema, J. Kauhanen, A.P. Kengne, D. Khalili, W. Koenig, D. Kromhout, H. Krumholz, T.H. Lam, G. Laughlin, A. Marín Ibañez, T.W. Meade, K.G.M. Moons, P.J. Nietert, T. Ninomiya, B.G. Nordestgaard, C. O’Donnell, L. Palmieri, A. Patel, P. Perel, J.F. Price, R. Providencia, P.M. Ridker, B. Rodriguez, A. Rosengren, R. Roussel, M. Sakurai, V. Salomaa, S. Sato, B. Schöttker, N. Shara, J.E. Shaw, H. Shin, L.A. Simons, E. Sofianopoulou, J. Sundström, H. Völzke, R.B. Wallace, N.J. Wareham, P. Willeit, D. Wood, A. Wood, D. Zhao, M. Woodward, G. Danaei, G. Roth, S. Mendis, O. Onuma, C. Varghese, M. Ezzati, I. Graham, R. Jackson, J. Danesh, and E. Di Angelantonio. World Health Organization cardiovascular disease risk charts: Revised models to estimate risk in 21 global regions. *Lancet*, 7(10):e1332–e1345, 2019.
- [120] E.J. Benjamin, P. Muntner, A. Alonso, M.S. Bittencourt, C.W. Callaway, A.P. Carson, A.M. Chamberlain, A.R. Chang, S. Cheng, S.R. Das, F.N. Delling, L. Djousse, M.S.V. Elkind, J.F. Ferguson, M. Fornage, L.C. Jordan, S.S. Khan, B.M. Kissela, K.L. Knutson, T.W. Kwan, D.T. Lackland, T.T. Lewis, J.H. Lichtman, C.T. Longenecker, M.S. Loop, P.L. Lutsey, S.S. Martin, K. Matsushita, A.E. Moran,

- M.E. Mussolino, M. O'Flaherty, A. Pandey, A.M. Perak, W.D. Rosamond, G.A. Roth, U.K.A. Sampson, G.M. Satou, E.B. Schroeder, S.H. Shah, N.L. Spartano, A. Stokes, D.L. Tirschwell, C.W. Tsao, M.P. Turakhia, L.B. VanWagner, J.T. Wilkins, S.S. Wong, and S.S. Virani. Heart disease and stroke statistics-2019 update: A report from the American Heart Association. *Circulation*, 139(10):e56–e528, 2019.
- [121] M.M. Álvarez-Álvarez, D. Zanetti, R. Carreras-Torres, P. Moral, and G. Athanasiadis. A survey of sub-saharan gene flow into the mediterranean at risk loci for coronary artery disease. *Eur J Hum Genet*, 25(4):472–476, 2017.
- [122] M.W. King, T. Bambharoliya, and H. Ramakrishna. *Coronary artery disease and the evolution of angioplasty devices*. SpringerBriefs in Materials. Springer, Cham, CHE, 1 edition, 2020.
- [123] A.K. Malakar, D. Choudhury, B. Halder, P. Paul, A. Uddin, and S. Chakraborty. A review on coronary artery disease, its risk factors, and therapeutics. *J Cell Physiol*, 234(10):16812–16823, 2019.
- [124] D.L. Fry. Mass transport, atherogenesis, and risk. *Arteriosclerosis*, 7(1):88–100, 1987.
- [125] S. Mundi, M. Massaro, E. Scoditti, M.A. Carluccio, V.W.M. van Hinsbergh, M.L. Iruela-Arispe, and R. de Caterina. Endothelial permeability, LDL deposition, and cardiovascular risk factors-a review. *Cardiovasc Res*, 114(1):35–52, 2018.
- [126] C. R. Minick, M. G. Stemerman, and W. Insull. Effect of regenerated endothelium on lipid accumulation in the arterial wall. *Proc Natl Acad Sci U S A*, 74(4):1724–1728, 1977.
- [127] C.R. Minick, M.B. Stemerman, and W. Insull. Role of endothelium and hypercholesterolemia in intimal thickening and lipid accumulation. *Am J Physiol*, 95(1):131–158, 1979.
- [128] H. Vink and B. R. Duling. Capillary endothelial surface layer selectively reduces plasma solute distribution volume. *Am J Physiol Heart Circ Physiol*, 278(1):H285–9, 2000.
- [129] E.V. Orlova, M.B. Sherman, W. Chiu, H. Mowri, L.C. Smith, and A.M. Gotto. Three-dimensional structure of low density lipoproteins by electron cryomicroscopy. *Proc Natl Acad Sci U S A*, 96(15):8420–8425, 1999.
- [130] S. Devaraj, J.-M. Yun, G. Adamson, J. Galvez, and I. Jialal. C-reactive protein impairs the endothelial glycocalyx resulting in endothelial dysfunction. *Cardiovasc Res*, 84(3):479–484, 2009.
- [131] S. Grundmann, S.H. Schirmer, L.H.P. Hekking, J.A. Post, M.G. Ionita, D. de Groot, N. van Royen, B. van den Berg, H. Vink, M. Moser, C. Bode, D. de Kleijn, G. Pasterkamp, J.J. Piek, and I.E. Hoefer. Endothelial glycocalyx dimensions are reduced in growing collateral arteries and modulate leucocyte adhesion in arteriogenesis. *J Cell Mol Med*, 13(9B):3463–3474, 2009.
- [132] F. Schierke, M.J. Wyrwoll, M. Wisdorf, L. Niedzielski, M. Maase, T. Ruck, S.G. Meuth, and K. Kusche-Vihrog. Nanomechanics of the endothelial glycocalyx contribute to Na⁺-induced vascular inflammation. *Sci Rep*, 7:46476, 2017.
- [133] J.C. Lewis, R.G. Taylor, N.D. Jones, R.W. St Clair, and J.F. Cornhill. Endothelial surface characteristics in pigeon coronary artery atherosclerosis. I. Cellular alterations during the initial stages of dietary cholesterol challenge. *Lab Invest*, 46(2):123–138, 1982.
- [134] B.M. van den Berg, J.A.E. Spaan, T.M. Rolf, and H. Vink. Atherogenic region and diet diminish glycocalyx dimension and increase intima-to-media ratios at murine carotid artery bifurcation. *Am J Physiol Heart Circ Physiol*, 290(2):H915–20, 2006.
- [135] L.M. Cancel, E.E. Ebong, S. Mensah, C. Hirschberg, and J.M. Tarbell. Endothelial glycocalyx, apoptosis and inflammation in an atherosclerotic mouse model. *Atherosclerosis*, 252:136–146, 2016.
- [136] R. Keller, B.M. Pratt, H. Furthmayr, and J.A. Madri. Aortic endothelial cell proteoglycan sulfate. II. Modulation by extracellular matrix. *Am J Physiol*, 128(2):299–306, 1987.

- [137] H. Vink, A.A. Constantinescu, and J.A. Spaan. Oxidized lipoproteins degrade the endothelial surface layer: Implications for platelet-endothelial cell adhesion. *Circulation*, 101(13):1500–1502, 2000.
- [138] S. Cooper, K. McDonald, D. Burkat, and R.L. Leask. Stenosis hemodynamics disrupt the endothelial cell glycocalyx by MMP activity creating a proinflammatory environment. *Ann Biomed Eng*, 45(9):2234–2243, 2017.
- [139] R.A. Bradshaw and P.D. Stahl. *Encyclopedia of cell biology*. Elsevier, Amsterdam and Boston and Heidelberg and London and New York and Oxford, 2016.
- [140] E. Vasile, M. Simionescu, and N. Simionescu. Visualization of the binding, endocytosis, and transcytosis of low-density lipoprotein in the arterial endothelium in situ. *J Cell Biol*, 96(6):1677–1689, 1983.
- [141] J.L. Goldstein and M.S. Brown. The LDL receptor. *Arterioscler Thromb Vasc Biol*, 29(4):431–438, 2009.
- [142] S.A. Predescu, D.N. Predescu, and A.B. Malik. Molecular determinants of endothelial transcytosis and their role in endothelial permeability. *Am J Physiol Lung Cell Mol Physiol*, 293(4):L823–42, 2007.
- [143] A. Magalhaes, I. Matias, I. Palmela, M.A. Brito, and S. Dias. LDL-cholesterol increases the transcytosis of molecules through endothelial monolayers. *PLoS one*, 11(10):e0163988, 2016.
- [144] M.G. Lampugnani. Endothelial cell-to-cell junctions: Adhesion and signaling in physiology and pathology. *Cold Spring Harb Perspect Med*, 2(10):a006528, 2012.
- [145] B. Alberts, A. Johnson, J. Lewis, D. Morgan, M. Raff, K. Roberts, and P. Walter. *Molecular biology of the cell*. Garland Science, New York (NY), USA, 6 edition, 2015.
- [146] S. Morel, L. Burnier, and B.R. Kwak. Connexins participate in the initiation and progression of atherosclerosis. *Semin Immunopathol*, 31(1):49–61, 2009.
- [147] L. Eiselein, D.W. Wilson, M.W. Lamé, and J.C. Rutledge. Lipolysis products from triglyceride-rich lipoproteins increase endothelial permeability, perturb zonula occludens-1 and F-actin, and induce apoptosis. *Am J Physiol Heart Circ Physiol*, 292(6):H2745–53, 2007.
- [148] E. Dejana, F. Orsenigo, C. Molendini, P. Baluk, and D.M. McDonald. Organization and signaling of endothelial cell-to-cell junctions in various regions of the blood and lymphatic vascular trees. *Cell Tissue Res*, 335(1):17–25, 2009.
- [149] H.V. van Rijen, M.J. van Kempen, S. Postma, and H.J. Jongsma. Tumour necrosis factor alpha alters the expression of connexin43, connexin40, and connexin37 in human umbilical vein endothelial cells. *Cytokine*, 10(4):258–264, 1998.
- [150] B.R. Kwak, F. Mulhaupt, N. Veillard, D.B. Gros, and F. Mach. Altered pattern of vascular connexin expression in atherosclerotic plaques. *Arterioscler Thromb Vasc Biol*, 22(2):225–230, 2002.
- [151] H.-I. Yeh, C.-S. Lu, Y.-J. Wu, C.-C. Chen, R.-C. Hong, Y.-S. Ko, M.-S. Shiao, N.J. Severs, and C.-H. Tsai. Reduced expression of endothelial connexin37 and connexin40 in hyperlipidemic mice: Recovery of connexin37 after 7-day simvastatin treatment. *Arterioscler Thromb Vasc Biol*, 23(8):1391–1397, 2003.
- [152] J. Zou, X.-Y. Yue, S.-C. Zheng, G. Zhang, H. Chang, Y.-C. Liao, Y. Zhang, M.-Q. Xue, and Z. Qi. Cholesterol modulates function of connexin 43 gap junction channel via PKC pathway in H9c2 cells. *Biochim Biophys Acta*, 1838(8):2019–2025, 2014.
- [153] L.T. Welson. *Triglycerides and cholesterol research*. Nova Biomedical Books, New York (NY), USA, 2006.

- [154] C. Weber and H. Noels. Atherosclerosis: Current pathogenesis and therapeutic options. *Nat Med*, 17(11):1410–1422, 2011.
- [155] K. Sakakura, M. Nakano, F. Otsuka, E. Ladich, F.D. Kolodgie, and R. Virmani. Pathophysiology of atherosclerosis plaque progression. *Heart Lung Circ*, 22(6):399–411, 2013.
- [156] F.K. Swirski, P. Libby, E. Aikawa, P. Alcaide, F.W. Lusinskas, R. Weissleder, and M.J. Pittet. Ly-6Chi monocytes dominate hypercholesterolemia-associated monocytosis and give rise to macrophages in atheromata. *J Clin Invest*, 117(1):195–205, 2007.
- [157] J.L. Johnson and A.C. Newby. Macrophage heterogeneity in atherosclerotic plaques. *Curr Opin Lipidol*, 20(5):370–378, 2009.
- [158] I.A. Zani, S.L. Stephen, N.A. Mughal, D. Russell, S. Homer-Vanniasinkam, S.B. Wheatcroft, and S. Ponnambalam. Scavenger receptor structure and function in health and disease. *Cells*, 4(2):178–201, 2015.
- [159] K.E. Paulson, S.-N. Zhu, M. Chen, S. Nurmohamed, J. Jongstra-Bilen, and M.I. Cybulsky. Resident intimal dendritic cells accumulate lipid and contribute to the initiation of atherosclerosis. *Circ Res*, 106(2):383–390, 2010.
- [160] D.A. Chistiakov, A.A. Melnichenko, V.A. Myasoedova, A.V. Grechko, and A.N. Orekhov. Mechanisms of foam cell formation in atherosclerosis. *J Mol Med (Berl)*, 95(11):1153–1165, 2017.
- [161] F.D. Kolodgie, A.P. Burke, A. Farb, H.K. Gold, J. Yuan, J. Narula, A.V. Finn, and R. Virmani. The thin-cap fibroatheroma: A type of vulnerable plaque: The major precursor lesion to acute coronary syndromes. *Curr Opin Cardiol*, 16(5):285–292, 2001.
- [162] M. Tennant and J.K. McGeachie. Platelet-derived growth factor and its role in atherogenesis: A brief review. *Aust N Z J Surg*, 61(7):482–488, 1991.
- [163] L. Hegyi, J.N. Skepper, N.R. Cary, and M.J. Mitchinson. Foam cell apoptosis and the development of the lipid core of human atherosclerosis. *J Pathol*, 180(4):423–429, 1996.
- [164] P. Libby, P.M. Ridker, and G.K. Hansson. Progress and challenges in translating the biology of atherosclerosis. *Nature*, 473(7347):317–325, 2011.
- [165] A. Kelly-Arnold, N. Maldonado, D. Laudier, E. Aikawa, L. Cardoso, and S. Weinbaum. Revised microcalcification hypothesis for fibrous cap rupture in human coronary arteries. *Proc Natl Acad Sci U S A*, 110(26):10741–10746, 2013.
- [166] A.N. Kapustin and C.M. Shanahan. Calcium regulation of vascular smooth muscle cell-derived matrix vesicles. *Trends Cardiovas Med*, 22(5):133–137, 2012.
- [167] F. Otsuka, K. Sakakura, K. Yahagi, M. Joner, and R. Virmani. Has our understanding of calcification in human coronary atherosclerosis progressed? *Arterioscler Thromb Vasc Biol*, 34(4):724–736, 2014.
- [168] S. Ehara, Y. Kobayashi, M. Yoshiyama, K. Shimada, Y. Shimada, D. Fukuda, Y. Nakamura, H. Yamashita, H. Yamagishi, K. Takeuchi, T. Naruko, K. Haze, A.E. Becker, J. Yoshikawa, and M. Ueda. Spotty calcification typifies the culprit plaque in patients with acute myocardial infarction: An intravascular ultrasound study. *Circulation*, 110(22):3424–3429, 2004.
- [169] S. Motoyama, T. Kondo, M. Sarai, A. Sugiura, H. Harigaya, T. Sato, K. Inoue, M. Okumura, J. Ishii, H. Anno, R. Virmani, Y. Ozaki, H. Hishida, and J. Narula. Multislice computed tomographic characteristics of coronary lesions in acute coronary syndromes. *J Am Coll Cardiol*, 50(4):319–326, 2007.
- [170] Z.-Y. Li, S. Howarth, T. Tang, M. Graves, J. U-King-Im, and J.H. Gillard. Does calcium deposition play a role in the stability of atheroma? Location may be the key. *Cerebrovasc Dis*, 24(5):452–459, 2007.

- [171] T. Hoshino, L.A. Chow, J.J. Hsu, A.A. Perlowski, M. Abedin, J. Tobis, Y. Tintut, A.K. Mal, W.S. Klug, and L.L. Demer. Mechanical stress analysis of a rigid inclusion in distensible material: A model of atherosclerotic calcification and plaque vulnerability. *Am J Physiol Heart Circ Physiol*, 297(2):H802–10, 2009.
- [172] T. Zhongzhao, H. Jing, U. Sadat, J.R. Mercer, W. Xiaoyan, N.S. Bahaei, O.M. Thomas, and J.H. Gillard. How does juxtaluminal calcium affect critical mechanical conditions in carotid atherosclerotic plaque? An exploratory study. *IEEE Trans Biomed Eng*, 61(1):35–40, 2014.
- [173] A. Shioi and Y. Ikari. Plaque calcification during atherosclerosis progression and regression. *J Atheroscler Thromb*, 25(4):294–303, 2018.
- [174] X. Shi, J. Gao, Q. Lv, H. Cai, F. Wang, R. Ye, and X. Liu. Calcification in atherosclerotic plaque vulnerability: Friend or foe? *Front Physiol*, 11:56, 2020.
- [175] H.C. Stary, D.H. Blankenhorn, A.B. Chandler, S. Glagov, W. Insull, M. Richardson, M.E. Rosenfeld, S.A. Schaffer, C.J. Schwartz, and W.D. Wagner. A definition of the intima of human arteries and of its atherosclerosis-prone regions. A report from the Committee on Vascular Lesions of the Council on Arteriosclerosis, American Heart Association. *Circulation*, 85(1):391–405, 1992.
- [176] H.C. Stary, A.B. Chandler, S. Glagov, J.R. Guyton, W. Insull, M.E. Rosenfeld, S.A. Schaffer, C.J. Schwartz, W.D. Wagner, and R.W. Wissler. A definition of initial, fatty streak, and intermediate lesions of atherosclerosis. A report from the Committee on Vascular Lesions of the Council on Arteriosclerosis, American Heart Association. *Circulation*, 89(5):2462–2478, 1994.
- [177] H.C. Stary, A.B. Chandler, R.E. Dinsmore, V. Fuster, S. Glagov, W. Insull, M.E. Rosenfeld, C.J. Schwartz, W.D. Wagner, and R.W. Wissler. A definition of advanced types of atherosclerotic lesions and a histological classification of atherosclerosis. A report from the Committee on Vascular Lesions of the Council on Arteriosclerosis, American Heart Association. *Circulation*, 92(5):1355–1374, 1995.
- [178] R. Virmani, F.D. Kolodgie, A.P. Burke, A. Farb, and S.M. Schwartz. Lessons from sudden coronary death: A comprehensive morphological classification scheme for atherosclerotic lesions. *Arterioscler Thromb Vasc Biol*, 20(5):1262–1275, 2000.
- [179] T. Yonetsu and I.K. Jang. Advances in intravascular imaging: New insights into the vulnerable plaque from imaging studies. *Korean Circ J*, 48(1):1–15, 2018.
- [180] H.C. Stary. Natural history and histological classification of atherosclerotic lesions: An update. *Arterioscler Thromb Vasc Biol*, 20(5):1177–1178, 2000.
- [181] H.C. Stary. *Atlas of atherosclerosis: Progression and regression*. The encyclopedia of visual medicine series. Parthenon Publ. Group, Boca Raton (FL), USA, 2 edition, 2003.
- [182] A.C. Akyildiz, L. Speelman, and F. Gijssen. Mechanical properties of human atherosclerotic intima tissue. *J Biomech*, 47(4):773–783, 2014.
- [183] T.A. Rousan and U. Thadani. Stable angina medical therapy management guidelines: A critical review of guidelines from the European Society of Cardiology and National Institute for Health and Care Excellence. *Eur Cardiol*, 14(1):18–22, 2019.
- [184] J. Abrams and U. Thadani. Therapy of stable angina pectoris: The uncomplicated patient. *Circulation*, 112(15):e255–9, 2005.
- [185] U. Thadani. Current medical management of chronic stable angina. *J Cardiovasc Pharm T*, 9 Suppl 1:S11–29; quiz S98–9, 2004.
- [186] S. Glagov and C.K. Zarins. Is intimal hyperplasia an adaptive response or a pathologic process?—observations on the nature of nonatherosclerotic intimal thickening. *J Vasc Surg*, 10(5):571–573, 1989.

- [187] P. Richardson. Influence of plaque configuration and stress distribution on fissuring of coronary atherosclerotic plaques. *Lancet*, 2(8669):941–944, 1989.
- [188] S.D. Gertz and W.C. Roberts. Hemodynamic shear force in rupture of coronary arterial atherosclerotic plaques. *Am J Cardiol*, 66(19):1368–1372, 1990.
- [189] P. Libby. Current concepts of the pathogenesis of the acute coronary syndromes. *Circulation*, 104(3):365–372, 2001.
- [190] Y. Liang, H. Zhu, T. Gehrig, and M.H. Friedman. Measurement of the transverse strain tensor in the coronary arterial wall from clinical intravascular ultrasound images. *J Biomech*, 41(14):2906–2911, 2008.
- [191] L. Badimon and G. Vilahur. Platelets, arterial thrombosis and cerebral ischemia. *Cerebrovasc Dis*, 24(Suppl 1):30–39, 2007.
- [192] L. Badimon and G. Vilahur. Coronary atherothrombotic disease: Progress in antiplatelet therapy. *Rev Esp Cardiol*, 61(5):501–513, 2008.
- [193] L. Badimón, G. Vilahur, and T. Padró. Lipoproteins, platelets, and atherothrombosis. *Rev Esp Cardiol*, 62(10):1161–1178, 2009.
- [194] L. Badimon, R.F. Storey, and G. Vilahur. Update on lipids, inflammation and atherothrombosis. *Thromb Haemost*, 105(Suppl 1):S34–42, 2011.
- [195] N.G. Frangogiannis. Pathophysiology of myocardial infarction. *Compr Physiol*, 5(4):1841–1875, 2015.
- [196] T. Shoji, K. Maekawa, M. Emoto, S. Okuno, T. Yamakawa, E. Ishimura, M. Inaba, and Y. Nishizawa. Arterial stiffness predicts cardiovascular death independent of arterial thickness in a cohort of hemodialysis patients. *Atherosclerosis*, 210(1):145–149, 2010.
- [197] C. Velican and D. Velican. Study of coronary intimal thickening. *Atherosclerosis*, 56(3):331–344, 1985.
- [198] D. Velican and C. Velican. Comparative study on age-related changes and atherosclerotic involvement of the coronary arteries of male and female subjects up to 40 years of age. *Atherosclerosis*, 38(1-2):39–50, 1981.
- [199] C. Velican and D. Velican. Differences in the pattern of atherosclerotic involvement between non-branched regions and adjacent branching points of human coronary arteries. *Atherosclerosis*, 54(3):333–342, 1985.
- [200] I. Ozolanta, G. Tetere, B. Purinya, and V. Kasyanov. Changes in the mechanical properties, biochemical contents and wall structure of the human coronary arteries with age and sex. *Med Eng Phys*, 20(7):523–533, 1998.
- [201] M.A. Jankowska, M. Bartkowiak-Jowska, and R. Bedzinski. Experimental and constitutive modeling approaches for a study of biomechanical properties of human coronary arteries. *J Mech Behav Biomed Mater*, 50:1–12, 2015.
- [202] G. Mintz. American College of Cardiology clinical expert consensus document on standards for acquisition, measurement and reporting of intravascular ultrasound studies (IVUS). A report of the American College of Cardiology task force on clinical expert consensus documents developed in collaboration with the European Society of Cardiology endorsed by the Society of Cardiac Angiography and Interventions. *Eur J Echocardiogr*, 2(4):299–313, 2001.
- [203] J. Ophir, I. Céspedes, H. Ponnekanti, Y. Yazdi, and X. Li. Elastography: A quantitative method for imaging the elasticity of biological tissues. *Ultrason Imaging*, 13(2):111–134, 1991.

- [204] C.L. de Korte, G. Pasterkamp, A.F. van der Steen, H.A. Woutman, and N. Bom. Characterization of plaque components with intravascular ultrasound elastography in human femoral and coronary arteries in vitro. *Circulation*, 102(6):617–623, 2000.
- [205] C.L. de Korte, S.G. Carlier, F. Mastik, M.M. Doyley, A.F.W. van der Steen, P.W. Serruys, and N. Bom. Morphological and mechanical information of coronary arteries obtained with intravascular elastography; feasibility study in vivo. *Eur Heart J*, 23(5):405–413, 2002.
- [206] Z. Keshavarz-Motamed, Y. Saijo, Y. Majdouline, L. Riou, J. Ohayon, and G. Cloutier. Coronary artery atherectomy reduces plaque shear strains: An endovascular elastography imaging study. *Atherosclerosis*, 235(1):140–149, 2014.
- [207] G.A. Diamond and J.S. Forrester. Analysis of probability as an aid in the clinical diagnosis of coronary-artery disease. *N Engl J Med*, 300(24):1350–1358, 1979.
- [208] L. Goldman, E.F. Cook, P.A. Johnson, D.A. Brand, G.W. Rouan, and T.H. Lee. Prediction of the need for intensive care in patients who come to emergency departments with acute chest pain. *N Engl J Med*, 334(23):1498–1504, 1996.
- [209] A.P. Morise, W.J. Haddad, and D. Beckner. Development and validation of a clinical score to estimate the probability of coronary artery disease in men and women presenting with suspected coronary disease. *Am J Med*, 102(4):350–356, 1997.
- [210] E.M. Antman, M. Cohen, P.J. Bernink, C.H. McCabe, T. Horacek, G. Papuchis, B. Mautner, R. Corbalan, D. Radley, and E. Braunwald. The TIMI risk score for unstable angina/non-ST elevation MI: A method for prognostication and therapeutic decision making. *JAMA*, 284(7):835–842, 2000.
- [211] S.D. Fihn, J.M. Gardin, J. Abrams, K. Berra, J.C. Blankenship, A.P. Dallas, P.S. Douglas, J.M. Foody, T.C. Gerber, A.L. Hinderliter, S.B. King, P.D. Kligfield, H.M. Krumholz, R.Y.K. Kwong, M.J. Lim, J.A. Linderbaum, M.J. Mack, M.A. Munger, R.L. Prager, J.F. Sabik, L.J. Shaw, J.D. Sikkema, C.R. Smith, S.C. Smith, J.A. Spertus, and S.V. Williams. 2012 ACCF/AHA/ACP/AATS/PCNA/SCAI/STS guideline for the diagnosis and management of patients with stable ischemic heart disease: A report of the American College of Cardiology Foundation/American Heart Association task force on practice guidelines, and the American College of Physicians, American Association for Thoracic Surgery, Preventive Cardiovascular Nurses Association, Society for Cardiovascular Angiography and Interventions, and Society of Thoracic Surgeons. *Circulation*, 60(24):e44–e164, 2012.
- [212] A.C. Skelly, R. Hashimoto, D.I. Buckley, E.D. Brodt, N. Noelck, A.M. Totten, J.R. Lindner, R. Fu, and M. McDonagh. *Noninvasive testing for coronary artery disease*. Agency for Healthcare Research and Quality, Rockville (MD), USA, 2016.
- [213] A.J. Nelson, M. Ardissino, and P.J. Psaltis. Current approach to the diagnosis of atherosclerotic coronary artery disease: More questions than answers. *Ther Adv Chronic Dis*, 10, 2019.
- [214] D.M. Shavelle. Long term medical treatment of stable coronary disease. *Heart*, 93(11):1473–1477, 2007.
- [215] S.D. Cagle and N. Cooperstein. Coronary artery disease: Diagnosis and management. *Prim Care*, 45(1):45–61, 2018.
- [216] E. Barbato, E. Shlofmitz, A. Milkas, R. Shlofmitz, L. Azzalini, and A. Colombo. State of the art: Evolving concepts in the treatment of heavily calcified and undilatable coronary stenoses - from debulking to plaque modification, a 40-year-long journey. *EuroIntervention*, 13(6):696–705, 2017.
- [217] M.N.T. Forero and J. Daemen. The coronary intravascular lithotripsy system. *Interv Cardiol*, 14(3):174–181, 2019.
- [218] S. Windecker, P. Kolh, F. Alfonso, J.-P. Collet, J. Cremer, V. Falk, G. Filippatos, C. Hamm, S.J. Head, P. Jüni, A.P. Kappetein, A. Kastrati, J. Knuuti, U. Landmesser, G. Laufer, F.-J. Neumann,

- D.J. Richter, P. Schauerte, M. Sousa Uva, G.G. Stefanini, D.P. Taggart, L. Torracca, M. Valgimigli, W. Wijns, and A. Witkowski. 2014 ESC/EACTS Guidelines on myocardial revascularization: The task force on myocardial revascularization of the European Society of Cardiology (ESC) and the European Association for Cardio-Thoracic Surgery (EACTS) Developed with the special contribution of the European Association of Percutaneous Cardiovascular Interventions (EAPCI). *Eur Heart J*, 35(37):2541–2619, 2014.
- [219] J. Escaned, C. Collet, N. Ryan, G.L. de Maria, S. Walsh, M. Sabate, J. Davies, M. Lesiak, R. Moreno, I. Cruz-Gonzalez, S.P. Hoole, N. Ej West, J.J. Piek, A. Zaman, F. Fath-Ordoubadi, R.H. Stables, C. Appleby, N. van Mieghem, R.J. van Geuns, N. Uren, J. Zueco, P. Buszman, A. Iñiguez, J. Goicolea, D. Hildick-Smith, A. Ochala, D. Dudek, C. Hanratty, R. Cavalcante, A.P. Kappetein, D.P. Taggart, G.-A. van Es, M.-A. Morel, T. de Vries, Y. Onuma, V. Farooq, P.W. Serruys, and A.P. Banning. Clinical outcomes of state-of-the-art percutaneous coronary revascularization in patients with de novo three vessel disease: 1-year results of the SYNTAX II study. *Eur Heart J*, 38(42):3124–3134, 2017.
- [220] R. Cavalcante, Y. Onuma, Y. Sotomi, C. Collet, B. Thomsen, C. Rogers, Y. Zeng, E. Tenekecioglu, T. Asano, Y. Miyasaki, M. Abdelghani, M. Morel, and P.W. Serruys. Non-invasive Heart Team assessment of multivessel coronary disease with coronary computed tomography angiography based on SYNTAX score II treatment recommendations: Design and rationale of the randomised SYNTAX III Revolution trial. *EuroIntervention*, 12(16):2001–2008, 2017.
- [221] D.G. Katritsis, D.B. Mark, and B.J. Gersh. Revascularization in stable coronary disease: Evidence and uncertainties. *Nat Rev Cardiol*, 15(7):408–419, 2018.
- [222] C. Gao, R. Wang, F. Sharif, K. Takahashi, M. Ono, H. Hara, M. Tomaniak, H. Kawashima, R. Modolo, R.M. van Geuns, D. Capodanno, R.A. Byrne, W. Wijns, Y. Onuma, and P.W. Serruys. The year in review: Coronary interventions. *EuroIntervention*, 15(17):1534–1547, 2020.
- [223] A. Baumbach, C.V. Bourantas, P.W. Serruys, and W. Wijns. The year in cardiology: Coronary interventions. *Eur Heart J*, 41(3):394–405, 2020.
- [224] S.S. Virani, A. Alonso, E.J. Benjamin, M.S. Bittencourt, C.W. Callaway, A.P. Carson, A.M. Chamberlain, A.R. Chang, S. Cheng, F.N. Delling, L. Djousse, M.S.V. Elkind, J.F. Ferguson, M. Fornage, S.S. Khan, B.M. Kissela, K.L. Knutson, T.W. Kwan, D.T. Lackland, T.T. Lewis, J.H. Lichtman, C.T. Longenecker, M.S. Loop, P.L. Lutsey, S.S. Martin, K. Matsushita, A.E. Moran, M.E. Mussolino, A.M. Perak, W.D. Rosamond, G.A. Roth, U.K.A. Sampson, G.M. Satou, E.B. Schroeder, S.H. Shah, C.M. Shay, N.L. Spartano, A. Stokes, D.L. Tirschwell, L.B. VanWagner, and C.W. Tsao. Heart disease and stroke statistics-2020 update: a report from the American Heart Association. *Circulation*, 141(9):e139–e596, 2020.
- [225] A. Timmis, N. Townsend, C. Gale, R. Grobbee, N. Maniadakis, M. Flather, E. Wilkins, L. Wright, R. Vos, J. Bax, M. Blum, F. Pinto, and P. Vardas. European Society of Cardiology: Cardiovascular Disease Statistics 2017. *Eur Heart J*, 39(7):508–579, 2018.
- [226] A. Timmis, N. Townsend, C.P. Gale, A. Torbica, M. Lettino, S.E. Petersen, E.A. Mossialos, A.P. Maggioni, D. Kazakiewicz, H.T. May, D. de Smedt, M. Flather, L. Zuhlke, J.F. Beltrame, R. Huculeci, L. Tavazzi, G. Hindricks, J. Bax, B. Casadei, S. Achenbach, L. Wright, and P. Vardas. European Society of Cardiology: Cardiovascular Disease Statistics 2019. *Eur Heart J*, 41(1):12–85, 2020.
- [227] A.R. Grüntzig, A. Senning, and W.E. Siegenthaler. Nonoperative dilatation of coronary-artery stenosis: Percutaneous transluminal coronary angioplasty. *N Engl J Med*, 301(2):61–68, 1979.
- [228] U. Sigwart, J. Puel, V. Mirkovitch, F. Joffre, and L. Kappenberger. Intravascular stents to prevent occlusion and restenosis after transluminal angioplasty. *N Engl J Med*, 316(12):701–706, 1987.
- [229] J.C. Palmaz. Balloon-expandable intravascular stent. *Am J Roentgenol*, 150(6):1263–1269, 1988.
- [230] T.J. Watson, P.J.L. Ong, and E. Tchong, editors. *Primary angioplasty: a practical guide*. Springer,

- Singapore, 2018.
- [231] P.H. Hertrich. *Practical radiography: Principles and applications*. Publicis Corp. Publ, Erlangen, GER, 2005.
- [232] C.A. Bellemare and T.G. Poder. Effectiveness of biplane angiography compared to monoplane angiography for vascular neuro-interventions: A systematic review of the literature. *Clin Radiol*, 72(7):612.e1–612.e5, 2017.
- [233] P. Sorajja, M.J. Lim, and M.J. Kern, editors. *Kern's cardiac catheterization handbook*. Elsevier, Philadelphia (PA), USA, 7 edition, 2020.
- [234] P. Udaya Prashant. Current and emerging catheter technologies for percutaneous transluminal coronary angioplasty. *Res Rep Clin Cardiol*, page 213, 2014.
- [235] L.H. Piers, M.A. Vink, and G. Amoroso. Transradial approach in primary percutaneous coronary intervention: Lessons from a High-volume Centre. *Interv Cardiol*, 11(2):88, 2016.
- [236] F.A. Bhat, K.H. Chagal, H. Raina, N.A. Trambo, and H.A. Rather. Transradial versus transfemoral approach for coronary angiography and angioplasty - a prospective, randomized comparison. *BMC Cardiovas Disord.*, 17(1):23, 2017.
- [237] C.W. Lee and S.C. Cho. The transradial approach for coronary intervention: More comfort, better outcome. *Korean Circ J*, 48(8):728–730, 2018.
- [238] T. Ando, S. Aoi, S. Ashraf, P.A. Villablanca, T. Telila, A. Briasoulis, H. Takagi, L. Afonso, and C.L. Grines. Transradial versus transfemoral percutaneous coronary intervention of left main disease: A systematic review and meta-analysis of observational studies. *Catheter Cardiovasc Interv*, 94(2):264–273, 2019.
- [239] P. Lanzer, editor. *Textbook of catheter-based cardiovascular interventions: A knowledge-based approach*. Springer, Cham, CHE, 2 edition, 2018.
- [240] K.A. Ellenbogen, B.L. Wilkoff, G.N. Kay, C.P. Lau, and A. Auricchio, editors. *Clinical cardiac pacing, defibrillation and resynchronization therapy*. Elsevier, s.l., 5 edition, 2017.
- [241] J. Butany, K. Carmichael, S.W. Leong, and M.J. Collins. Coronary artery stents: Identification and evaluation. *J Clin Pathol*, 58(8):795–804, 2005.
- [242] A. Corti, A. de Paolis, J. Tarbell, and L. Cardoso. Stenting-induced vasa vasorum compression and subsequent flow resistance: A finite element study. *Biomech Model Mechanobiol*, 2020.
- [243] I. Karalis, T.A.H.N. Ahmed, and J.W. Jukema. Late acquired stent malapposition: why, when and how to handle? *Heart*, 98(20):1529–1536, 2012.
- [244] N.J. Wimmer, E.A. Secemsky, L. Mauri, M.T. Roe, P. Saha-Chaudhuri, D. Dai, J.M. McCabe, F.S. Resnic, H.S. Gurm, and R.W. Yeh. Effectiveness of arterial closure devices for preventing complications with percutaneous coronary intervention: An instrumental variable analysis. *Circ Cardiovasc Interv*, 9(4):e003464, 2016.
- [245] J. Walter, M. Vogl, M. Holderried, C. Becker, A. Brandes, M.F. Sinner, W. Rogowski, and J. Maschmann. Manual compression versus vascular closing device for closing access puncture site in femoral left-heart catheterization and percutaneous coronary interventions: A retrospective cross-sectional comparison of costs and effects in inpatient care. *Value Health*, 20(6):769–776, 2017.
- [246] V.J. Noori and J. Eldrup-Jørgensen. A systematic review of vascular closure devices for femoral artery puncture sites. *J Vasc Surg*, 68(3):887–899, 2018.
- [247] K. Nakamura, J.H. Keating, and E.R. Edelman. Pathology of endovascular stents. *Interventional Cardiology Clinics*, 5(3):391–403, 2016.

- [248] P. Libby and H. Tanaka. The molecular bases of restenosis. *Prog Cardiovasc Dis*, 40(97–106), 1997.
- [249] H.C. Lowe, S.N. Oesterle, and L.M. Khachigian. Coronary in-stent restenosis: Current status and future strategies. *J Am Coll Cardiol*, 39(2):183–193, 2002.
- [250] H.D. Danenberg, F.G.P. Welt, M. Walker, P. Seifert, G.S. Toegel, and E.R. Edelman. Systemic inflammation induced by lipopolysaccharide increases neointimal formation after balloon and stent injury in rabbits. *Circulation*, 105(24):2917–2922, 2002.
- [251] P. Schoenhagen, K.M. Ziada, D.G. Vince, S.E. Nissen, and E.M. Tuzcu. Arterial remodeling and coronary artery disease: The concept of “dilated” versus “obstructive” coronary atherosclerosis. *J Am Coll Cardiol*, 38(2):297–306, 2001.
- [252] R.F. Fishman, R.E. Kuntz, J.P. Carrozza, M.J. Miller, C.C. Senerchia, S.J. Schnitt, D.J. Diver, R.D. Safian, and D.S. Baim. Long-term results of directional coronary atherectomy: Predictors of restenosis. *J Am Coll Cardiol*, 20(5):1101–1110, 1992.
- [253] C. Le Feuvre, R. Bonan, J. Lespérance, G. Gosselin, M. Joyal, and J. Crépeau. Predictive factors of restenosis after multivessel percutaneous transluminal coronary angioplasty. *Am J Cardiol*, 73(12):840–844, 1994.
- [254] A. Bakhai, J. Booth, N. Delahunty, F. Nugara, T. Clayton, J. McNeill, S.W. Davies, D.C. Cumberland, and R.H. Stables. The SV stent study: A prospective, multicentre, angiographic evaluation of the BiodivYsio phosphorylcholine coated small vessel stent in small coronary vessels. *Int J Cardiol*, 102(1):95–102, 2005.
- [255] P. Agostoni, M. Valgimigli, G.G. L. Biondi-Zoccai, A. Abbate, H.M. Garcia Garcia, M. Anselmi, M. Turri, E.P. McFadden, C. Vassanelli, P.W. Serruys, and A. Colombo. Clinical effectiveness of bare-metal stenting compared with balloon angioplasty in total coronary occlusions: Insights from a systematic overview of randomized trials in light of the drug-eluting stent era. *Am Heart J*, 151(3):682–689, 2006.
- [256] I.-M.o Chung, H.K. Gold, S.M. Schwartz, Y. Ikari, M.A. Reidy, and T.N. Wight. Enhanced extracellular matrix accumulation in restenosis of coronary arteries after stent deployment. *J Am Coll Cardiol*, 40(12):2072–2081, 2002.
- [257] T. Kimura, H. Yokoi, Y. Nakagawa, T. Tamura, S. Kaburagi, Y. Sawada, Y. Sato, N. Hamasaki, and H. Nosaka. Three-year follow-up after implantation of metallic coronary-artery stents. *N Engl J Med*, 334(9):561–566, 1996.
- [258] N. Kuroda, Y. Kobayashi, M. Nameki, N. Kuriyama, T. Kinoshita, T. Okuno, Y. Yamamoto, N. Komiyama, and Y. Masuda. Intimal hyperplasia regression from 6 to 12 months after stenting. *Am J Cardiol*, 89(7):869–872, 2002.
- [259] E.R. Edelman and C. Rogers. Pathobiologic responses to stenting. *Am J Cardiol*, 81(7):4E–6E, 1998.
- [260] A. Farb, G. Sangiorgi, A.J. Carter, V.M. Walley, W.D. Edwards, R.S. Schwartz, and R. Virmani. Pathology of acute and chronic coronary stenting in humans. *Circulation*, 99(1):44–52, 1999.
- [261] M.K. Hong, K.M. Kent, R. Mehran, G.S. Mintz, F.O. Tio, M. Foegh, S.C. Wong, S.S. Cathapermal, and M.B. Leon. Continuous subcutaneous angiopeptin treatment significantly reduces neointimal hyperplasia in a porcine coronary in-stent restenosis model. *Circulation*, 95(2):449–454, 1997.
- [262] F. Bozsak, D. Gonzalez-Rodriguez, Z. Sternberger, P. Belitz, T. Bewley, J.-M. Chomaz, and A.I. Barakat. Optimization of drug delivery by drug-eluting stents. *PloS one*, 10(6):e0130182, 2015.
- [263] R. Wessely, A. Schömig, and A. Kastrati. Sirolimus and paclitaxel on polymer-based drug-eluting stents: Similar but different. *J Am Coll Cardiol*, 47(4):708–714, 2006.
- [264] S.O. Marx, T. Jayaraman, L.O. Go, and A.R. Marks. Rapamycin-FKBP inhibits cell cycle regulators

- of proliferation in vascular smooth muscle cells. *Circ Res*, 76(3):412–417, 1995.
- [265] C. Herdeg, M. Oberhoff, A. Baumbach, A. Blattner, D.I. Axel, S. Schröder, H. Heinle, and K.R. Karsch. Local paclitaxel delivery for the prevention of restenosis: Biological effects and efficacy in vivo. *J Am Coll Cardiol*, 35(7):1969–1976, 2000.
- [266] J.W. Moses, M.B. Leon, J.J. Popma, P.J. Fitzgerald, D.R. Holmes, C. O’Shaughnessy, R.P. Caputo, D.J. Kereiakes, D.O. Williams, P.S. Teirstein, J.L. Jaeger, R.E. Kuntz, and SIRIUS Investigators. Sirolimus-eluting stents versus standard stents in patients with stenosis in a native coronary artery. *N Engl J Med*, 349(14):1315–1323, 2003.
- [267] G.W. Stone, S.G. Ellis, D.A. Cox, J. Hermiller, C. O’Shaughnessy, J.T. Mann, M. Turco, R. Caputo, P. Bergin, J. Greenberg, J.J. Popma, M.E. Russell, and TAXUS-IV Investigators. One-year clinical results with the slow-release, polymer-based, paclitaxel-eluting TAXUS stent: the TAXUS-IV trial. *Circulation*, 109(16):1942–1947, 2004.
- [268] E.P. McFadden, E. Stabile, E. Regar, E. Cheneau, A.T.L. Ong, T. Kinnaird, W.O. Suddath, N.J. Weissman, R. Torguson, K.M. Kent, A.D. Pichard, L.F. Satler, R. Waksman, and P.W. Serruys. Late thrombosis in drug-eluting coronary stents after discontinuation of antiplatelet therapy. *Lancet*, 364(9444):1519–1521, 2004.
- [269] A. Kastrati, J. Mehilli, J. Dirschinger, F. Dotzer, H. Schühlen, F.J. Neumann, M. Fleckenstein, C. Pfafferott, M. Seyfarth, and A. Schömig. Intracoronary stenting and angiographic results: Strut thickness effect on restenosis outcome (ISAR-STEREO) trial. *Circulation*, 103(23):2816–2821, 2001.
- [270] C. Briguori, C. Sarais, P. Pagnotta, F. Liistro, M. Montorfano, A. Chieffo, F. Sgura, N. Corvaja, R. Albiro, G. Stankovic, C. Toutoutzas, E. Bonizzoni, C. Di Mario, and A. Colombo. In-stent restenosis in small coronary arteries. *J Am Coll Cardiol*, 40(3):403–409, 2002.
- [271] B. O’Brien, H. Zafar, A. Ibrahim, J. Zafar, and F. Sharif. Coronary stent materials and coatings: A technology and performance update. *Ann Biomed Eng*, 44(2):523–535, 2016.
- [272] S. Garg and P.W. Serruys. Coronary stents: looking forward. *J Am Coll Cardiol*, 56(10 Suppl):S43–78, 2010.
- [273] T. Tada, R.A. Byrne, I. Simunovic, L.A. King, S. Cassese, M. Joner, M. Fusaro, S. Schneider, S. Schulz, T. T. Ibrahim, I. Ott, S. Massberg, K.-L. Laugwitz, and A. Kastrati. Risk of stent thrombosis among bare-metal stents, first-generation drug-eluting stents, and second-generation drug-eluting stents: Results from a registry of 18,334 patients. *J Am Coll Cardiol*, 6(12):1267–1274, 2013.
- [274] S. Cassese, R.A. Byrne, T. Tada, S. Pinieck, M. Joner, T. Ibrahim, L.A. King, M. Fusaro, K.-L. Laugwitz, and A. Kastrati. Incidence and predictors of restenosis after coronary stenting in 10 004 patients with surveillance angiography. *Heart*, 100(2):153–159, 2014.
- [275] S.-Y. Lee, S.-H. Hur, S.-G. Lee, S.-W. Kim, D.-H. Shin, J.-S. Kim, B.-K. Kim, Y.-G. Ko, D. Choi, Y. Jang, and M.-K. Hong. Optical coherence tomographic observation of in-stent neoatherosclerosis in lesions with more than 50% neointimal area stenosis after second-generation drug-eluting stent implantation. *Circ Cardiovasc Interv*, 8(2):e001878, 2015.
- [276] R. Iijima, T. Araki, Y. Nagashima, K. Yamazaki, M. Utsunomiya, M. Hori, H. Itaya, H. Shinji, M. Shiba, H. Hara, M. Nakamura, and K. Sugi. Incidence and predictors of the late catch-up phenomenon after drug-eluting stent implantation. *Int J Cardiol*, 168(3):2588–2592, 2013.
- [277] R.A. Byrne. Bioresorbable vascular scaffolds—will promise become reality? *N Engl J Med*, 373(20):1969–1971, 2015.
- [278] B.D. Gogas, V. Farooq, Y. Onuma, and P.W. Serruys. The ABSORB bioresorbable vascular scaffold: An evolution or revolution in interventional cardiology? *Hell J Cardiol*, 53(4):301–309, 2012.

- [279] N.T. Kirkland. Magnesium biomaterials: Past, present and future. *Corros Eng Sci Techn*, 47(5):322–328, 2012.
- [280] S.T. Alam, A.Q. Ansari, S. Urooj, and M. Aldobali. A Review based on biodegradable and bioabsorbable stents for coronary artery disease. *Procedia Comput Sci*, 152:354–359, 2019.
- [281] B. Pandya, S. Gaddam, M. Raza, D. Asti, N. Nalluri, T. Vazzana, R. Kandov, and J. Lafferty. Biodegradable polymer stents vs second generation drug eluting stents: A meta-analysis and systematic review of randomized controlled trials. *World J Cardiol*, 8(2):240–246, 2016.
- [282] R.A. Montone, G. Niccoli, F. de Marco, S. Minelli, F. D’Ascenzo, L. Testa, F. Bedogni, and F. Crea. Temporal trends in adverse events after everolimus-eluting bioresorbable vascular scaffold versus everolimus-eluting metallic stent implantation: A meta-analysis of randomized controlled trials. *Circulation*, 135(22):2145–2154, 2017.
- [283] S. Sorrentino, G. Giustino, R. Mehran, A.S. Kini, S.K. Sharma, M. Faggioni, S. Farhan, B. Vogel, C. Indolfi, and G.D. Dangas. Everolimus-eluting bioresorbable scaffolds versus everolimus-eluting metallic stents. *J Am Coll Cardiol*, 69(25):3055–3066, 2017.
- [284] S. Bangalore, B. Toklu, N. Patel, F. Feit, and G.W. Stone. Newer-generation ultrathin strut drug-eluting stents versus older second-generation thicker strut drug-eluting stents for coronary artery disease. *Circulation*, 138(20):2216–2226, 2018.
- [285] R.A. Buiten, E.H. Ploumen, P. Zocca, C.J.M. Doggen, L.C. van der Heijden, M.M. Kok, P.W. Danse, C.E. Schotborgh, M. Scholte, F.H.A.F. de Man, G.C.M. Linssen, and C. von Birgelen. Outcomes in patients treated with thin-strut, very thin-strut, or ultrathin-strut drug-eluting stents in small coronary vessels: A prespecified analysis of the randomized BIO-RESORT trial. *JAMA Cardiol*, 4(7):659–669, 2019.
- [286] R. Piccolo, K.H. Bona, O. Efthimiou, O. Varenne, A. Baldo, P. Urban, C. Kaiser, W. Remkes, L. Räber, A. de Belder, A.W.J. van ’t Hof, G. Stankovic, P.A. Lemos, T. Wilsgaard, J. Reifart, A.E. Rodriguez, E.E. Ribeiro, P.W.J.C. Serruys, A. Abizaid, M. Sabaté, R.A. Byrne, J.M. de La Torre Hernandez, W. Wijns, P. Jüni, S. Windecker, M. Valgimigli, and A.W.J. van’t Hof. Drug-eluting or bare-metal stents for percutaneous coronary intervention: a systematic review and individual patient data meta-analysis of randomised clinical trials. *Lancet*, 393(10190):2503–2510, 2019.
- [287] R.V. Jeger, S. Eccleshall, W.A. Wan Ahmad, J. Ge, T.C. Poerner, E.-S. Shin, F. Alfonso, A. Latib, P.J. Ong, T. Rissanen, J. Saucedo, B. Scheller, and F.X. Kleber. Drug-coated balloons for coronary artery disease: third report of the International DCB Consensus Group. *JACC Cardiovasc Interv*, 13(12):1391–1402, 2020.
- [288] K. Sauerteig and M. Giese. The effect of extrusion and blow molding parameters on angioplastyballoon production. *Med Device Diagn Ind*, pages 46–52, 1998.
- [289] S. Garramone. *Structure-property relationships in angioplasty balloons*. PhD thesis, Worcester Polytechnic Institute, 2001.
- [290] X. Fu, H. He, and W. Wang. Numerical simulation of forming process conditions and wall thickness for balloon. In Y. Huang, H. Wu, L. Honghai, and Z. Yin, editors, *Intelligent robotics and applications*, volume 10464 of *Lecture notes in computer science Lecture notes in artificial intelligence*, pages 808–818. Springer, Cham, 2017.
- [291] D. Stoeckel, C. Bonsignore, and S. Duda. A survey of stent designs. *Minim Invasive Ther Allied Technol*, 11(4):137–147, 2002.
- [292] B. Pamukçu, editor. *Angiography*. InTechOpen, 2019.
- [293] G.A. Holzapfel and T.C. Gasser. Computational stress-deformation analysis of arterial walls including high-pressure response. *Int J Cardiol*, 116(1):78–85, 2007.

- [294] M. de Beule, P. Mortier, S.G. Carlier, B. Verhegghe, R. van Impe, and P. Verdonck. Realistic finite element-based stent design: The impact of balloon folding. *J Biomech*, 41(2):383–389, 2008.
- [295] J. Yang, M.B. Liang, N. Huang, and Y.L. Liu. Studying the non-uniform expansion of a stent influenced by the balloon. *J Med Eng Technol*, 34(5-6):301–305, 2010.
- [296] H.-M. Hsiao, Y.-H. Chiu, K.-H. Lee, and C.-H. Lin. Computational modeling of effects of intravascular stent design on key mechanical and hemodynamic behavior. *Comput Aided Des*, 44(8):757–765, 2012.
- [297] D. Perrin, P. Badel, L. Orgéas, C. Geindreau, A. Dumenil, J.-N. Albertini, and S. Avril. Patient-specific numerical simulation of stent-graft deployment: Validation on three clinical cases. *J Biomech*, 48(10):1868–1875, 2015.
- [298] N. Debusschere, P. Segers, P. Dubrue, B. Verhegghe, and M. de Beule. A finite element strategy to investigate the free expansion behaviour of a biodegradable polymeric stent. *J Biomech*, 48(10):2012–2018, 2015.
- [299] J. Xu, J. Yang, N. Huang, C. Uhl, Y. Zhou, and Y. Liu. Mechanical response of cardiovascular stents under vascular dynamic bending. *Biomed Eng Online*, 15:21, 2016.
- [300] C. Dumoulin and B. Cochelin. Mechanical behaviour modelling of balloon-expandable stents. *J Biomech*, 33(11):1461–1470, 2000.
- [301] L.B. Tan, D.C. Webb, K. Kormi, and S.T.S. Al-Hassani. A method for investigating the mechanical properties of intracoronary stents using finite element numerical simulation. *Int J Cardiol*, 78(1):51–67, 2001.
- [302] F. Migliavacca, L. Petrini, M. Colombo, F. Auricchio, and R. Pietrabissa. Mechanical behavior of coronary stents investigated through the finite element method. *J Biomech*, 35(6):803–811, 2002.
- [303] F. Migliavacca, F. Gervaso, M. Prosi, P. Zunino, S. Minisini, L. Formaggia, and G. Dubini. Expansion and drug elution model of a coronary stent. *Comput Methods Biomech Biomed Engin*, 10(1):63–73, 2007.
- [304] M. Early, C. Lally, P.J. Prendergast, and D.J. Kelly. Stresses in peripheral arteries following stent placement: A finite element analysis. *Comput Methods Biomech Biomed Engin*, 12(1):25–33, 2009.
- [305] H. Zahedmanesh and C. Lally. Determination of the influence of stent strut thickness using the finite element method: Implications for vascular injury and in-stent restenosis. *Med Biol Eng Comput*, 47(4):385–393, 2009.
- [306] G.J. Hall and E.P. Kasper. Comparison of element technologies for modeling stent expansion. *J Biomech Eng*, 128(5):751–756, 2006.
- [307] W.-Q. Wang, D.-K. Liang, D.-Z. Yang, and M. Qi. Analysis of the transient expansion behavior and design optimization of coronary stents by finite element method. *J Biomech*, 39(1):21–32, 2006.
- [308] K. Takashima, T. Kitou, K. Mori, and K. Ikeuchi. Simulation and experimental observation of contact conditions between stents and artery models. *Med Eng Phys*, 29(3):326–335, 2007.
- [309] W. Wu, W.Q. Wang, D.Z. Yang, and M. Qi. Stent expansion in curved vessel and their interactions: A finite element analysis. *J Biomech*, 40(11):2580–2585, 2007.
- [310] F. Ju, Z. Xia, and K. Sasaki. On the finite element modelling of balloon-expandable stents. *J Mech Behav Biomed Mater*, 1(1):86–95, 2008.
- [311] D.E. Kioussis, A. Wulff, and G.A. Holzapfel. Experimental studies and numerical analysis of the inflation and interaction of vascular balloon catheter-stent systems. *Ann Biomed Eng*, 37(2):315–330, 2009.

- [312] D. Laroche, S. Delorme, T. Anderson, and R. DiRaddo. Computer prediction of friction in balloon angioplasty and stent implantation. In M. Harders and G. Székely, editors, *Biomedical Simulation*, pages 1–8. Springer, Zurich, CHE, 2006.
- [313] P. Mortier, G.A. Holzapfel, M. de Beule, D. van Loo, Y. Taeymans, P. Segers, P. Verdonck, and B. Verheghe. A novel simulation strategy for stent insertion and deployment in curved coronary bifurcations: Comparison of three drug-eluting stents. *Ann Biomed Eng*, 38(1):88–99, 2010.
- [314] J. Bukala, P. Kwiatkowski, and J. Malachowski. Numerical analysis of stent expansion process in coronary artery stenosis with the use of non-compliant balloon. *BIOCY*, 36(1):145–156, 2016.
- [315] J. Bukala, P. Kwiatkowski, and J. Malachowski. Numerical analysis of crimping and inflation process of balloon-expandable coronary stent using implicit solution. *Int J Numer Method Biomed Eng*, 33(12):e2890, 2017.
- [316] L. Wiesent, M.A. Geith, and M. Wagner, editors. *Simulation of fluid-structure interaction between injection medium and balloon catheter using ICFD: Proceedings of the 11th European LS-DYNA Conference 2017*. DYNAMore, Salzburg, Austria, 2017.
- [317] G.A. Holzapfel and R.W. Ogden. Biomechanical relevance of the microstructure in artery walls with a focus on passive and active components. *Am J Physiol Heart Circ Physiol*, 315(3):H540–H549, 2018.
- [318] D. Martin and F.J. Boyle. Computational structural modelling of coronary stent deployment: A review. *Comput Methods Biomech Biomed Engin*, 14(4):331–348, 2011.
- [319] Livermore Software Technologie Corporation. LS-DYNAVVolume II: Materials, 2018.
- [320] Dassault Systemes Simulia Corp. ABAQUS 2020X, 2020.
- [321] Y. Lanir. A structural theory for the homogeneous biaxial stress-strain relationships in flat collagenous tissues. *J Biomech*, 12(6):423–436, 1979.
- [322] W.F. Decraemer, M.A. Maes, and V.J. Vanhuyse. An elastic stress-strain relation for soft biological tissues based on a structural model. *J Biomech*, 13(6):463–468, 1980.
- [323] Y. Lanir. Constitutive equations for fibrous connective tissues. *J Biomech*, 16(1):1–12, 1983.
- [324] F.L. Wuyts, V.J. Vanhuyse, G.J. Langewouters, W.F. Decraemer, E.R. Raman, and S. Buyle. Elastic properties of human aortas in relation to age and atherosclerosis: A structural model. *Phys Med Biol*, 40(10):1577–1597, 1995.
- [325] Y. Hollander, D. Durban, X. Lu, G.S. Kassab, and Y. Lanir. Experimentally validated microstructural 3D constitutive model of coronary arterial media. *J Biomech Eng*, 133(3):031007, 2011.
- [326] H. Chen, X. Guo, T. Luo, and G.S. Kassab. A validated 3D microstructure-based constitutive model of coronary artery adventitia. *J Appl Physiol*, 121(1):333–342, 2016.
- [327] M.A. Zulliger, P. Fridez, K. Hayashi, and N. Stergiopoulos. A strain energy function for arteries accounting for wall composition and structure. *J Biomech*, 37(7):989–1000, 2004.
- [328] D. Li and A.M. Robertson. A structural multi-mechanism constitutive equation for cerebral arterial tissue. *J Biomech Eng*, 46(14-15):2920–2928, 2009.
- [329] G.A. Holzapfel, J.A. Niestrawska, R.W. Ogden, A.J. Reinisch, and A.J. Schriefl. Modelling non-symmetric collagen fibre dispersion in arterial walls. *J R Soc Interface*, 12(106):20150188, 2015.
- [330] F. Gervaso, C. Capelli, L. Petrini, S. Lattanzio, L. Di Virgilio, and F. Migliavacca. On the effects of different strategies in modelling balloon-expandable stenting by means of finite element method. *J Biomech*, 41(6):1206–1212, 2008.
- [331] H. Zahedmanesh, D.J. Kelly, and C. Lally. Simulation of a balloon expandable stent in a realistic

- coronary artery – determination of the optimum modelling strategy. *J Biomech*, 43(11):2126–2132, 2010.
- [332] I.M. Ward and J. Sweeney. *Mechanical properties of solid polymers*. Wiley, Chichester, UK, 3 edition, 2013.
- [333] T.C. Gasser and G.A. Holzapfel. Finite element modeling of balloon angioplasty by considering overstretch of remnant non-diseased tissues in lesions. *Comput Mech*, 40(1):47–60, 2007.
- [334] V. Mühlberger, L. Kaltenbach, and H. Ulmer. Cardiac catheterization, coronary angiography (CA) and percutaneous coronary interventions PCI in Austria during the year 2017 (Registry Data including Audit 2018). *J für Kardiologie*, 26:10–26, 2019.
- [335] P.C. Gordon, C.M. Gibson, D.J. Cohen, J.P. Carrozza, R.E. Kuntz, and D.S. Baim. Mechanisms of restenosis and redilation within coronary stents: quantitative angiographic assessment. *J Am Coll Cardiol*, 21(5):1166–1174, 1993.
- [336] J.E. Sousa, M.A. Costa, A.C. Abizaid, B.J. Rensing, A.S. Abizaid, L.F. Tanajura, K. Kozuma, G. van Langenhove, A.G.M.R. Sousa, R. Falotico, J. Jaeger, J.J. Popma, and P.W. Serruys. Sustained suppression of neointimal proliferation by sirolimus-eluting stents: one-year angiographic and intravascular ultrasound follow-up. *Circulation*, 104(17):2007–2011, 2001.
- [337] D.S. Baim, M.J. Levine, M.B. Leon, S. Levine, S.G. Ellis, R.A. Schatz, and The U.S. Palmaz-Schatz Stent Investigators. Management of restenosis within the Palmaz-Schatz coronary stent (the U.S. multicenter experience). *Am J Cardiol*, 71(4):364–366, 1993.
- [338] D.L. Fischman, M.B. Leon, D.S. Baim, R.A. Schatz, M.P. Savage, I. Penn, K. Detre, L. Veltri, D. Ricci, M. Nobuyoshi, M.W. Cleman, R.R. Heuser, D. Almond, P.S. Teirstein, R.D. Fish, A. Colombo, J. Brinker, J. Moses, A. Shalovich, J. Hirshfeld, S. Bailey, S. Ellis, R. Rake, and S. Goldberg for the Stent Restenosis Study Investigators. A randomized comparison of coronary-stent placement and balloon angioplasty in the treatment of coronary artery disease. *N Engl J Med*, 331:496–501, 1994.
- [339] J.E. Sousa, M.A. Costa, A. Abizaid, A.S. Abizaid, F. Feres, I.M.F. Pinto, A.C. Seixas, R. Staico, L.A. Mattos, A.G.M.R. Sousa, R. Falotico, J. Jaeger, J.J. Popma, and P.W. Serruys. Lack of neointimal proliferation after implantation of sirolimus-coated stents in human coronary arteries: A quantitative coronary angiography and three-dimensional intravascular ultrasound study. *Circulation*, 103(2):192–195, 2001.
- [340] M. Degertekin, E. Regar, K. Tanabe, P.C. Smits, W.J. van der Giessen, S.G. Carlier, P. de Feyter, J. Vos, D.P. Foley, J.M. Ligthart, J.J. Popma, and P.W. Serruys. Sirolimus-eluting stent for treatment of complex in-stent restenosis: the first clinical experience. *J Am Coll Cardiol*, 41(2):184–189, 2003.
- [341] G.S. Werner, U. Emig, A. Krack, G. Schwarz, and H.R. Figulla. Sirolimus-eluting stents for the prevention of restenosis in a worst-case scenario of diffuse and recurrent in-stent restenosis. *Catheter Cardiovasc Interv*, 63(3):259–264, 2004.
- [342] A.T. Ong, E.P. McFadden, E. Regar, P.P. de Jaegere, R.T. van Domburg, and P.W. Serruys. Late angiographic stent thrombosis (LAST) events with drug-eluting stents. *J Am Coll Cardiol*, 45(12):2088–2092, 2005.
- [343] G. Nakazawa, A.V. Finn, M. Vorpahl, E.R. Ladich, F.D. Kolodgie, and R. Virmani. Coronary responses and differential mechanisms of late stent thrombosis attributed to first-generation sirolimus- and paclitaxel-eluting stents. *J Am Coll Cardiol*, 57(4):390–398, 2011.
- [344] B.L. van der Hoeven, S.-S. Liem, J. Dijkstra, S.C. Bergheanu, H. Putter, M.L. Antoni, D.E. Atsma, M. Bootsma, K. Zeppenfeld, J.W. Jukema, and M.J. Schalij. Stent malapposition after sirolimus-eluting and bare-metal stent implantation in patients with ST-segment elevation myocardial infarction:

- acute and 9-month intravascular ultrasound results of the MISSION! intervention study. *J Am Coll Cardiol*, 1(2):192–201, 2008.
- [345] I.K. de Scheerder, K.L. Wilczek, E.V. Verbeke, J. Vandorpe, P.N. Lan, E. Schacht, H. de Geest, and J. Piessens. Biocompatibility of polymer-coated oversized metallic stents implanted in normal porcine coronary arteries. *Atherosclerosis*, 114(1):105–114, 1995.
- [346] W.J. van der Giessen, A.M. Lincoff, R.S. Schwartz, H.M. van Beusekom, P.W. Serruys, D.R. Holmes Jr, S.G. Ellis, and E.J. Topol. Marked inflammatory sequelae to implantation of biodegradable and nonbiodegradable polymers in porcine coronary arteries. *Circulation*, 94(7):1690–1697, 1996.
- [347] L.H. Timmins, M.W. Miller, F.J. Clubb Jr, and J.E. Moore Jr. Increased artery wall stress post-stenting leads to greater intimal thickening. *Lab Invest*, 91(6):955–967, 2011.
- [348] T. Schratzenstaller. *Entwicklung eines traumareduzierenden Stent-Delivery-Systems*. PhD thesis, Technische Universität München, Munich, 2006.
- [349] P. Mortier, M. de Beule, D. van Loo, B. Masschaele, P. Verdonck, and B. Verhegghe. Automated generation of a finite element stent model. *Med Biol Eng Comput*, 46(11):1169–1173, 2008.
- [350] W. Wu, D. Gastaldi, K. Yang, L. Tan, L. Petrini, and F. Migliavacca. Finite element analyses for design evaluation of biodegradable magnesium alloy stents in arterial vessels. *Mater Sci Eng B*, 176:1733–1740, 2011.
- [351] J. Li, F. Zheng, X. Qiu, P. Wan, L. Tan, and K. Yang. Finite element analyses for optimization design of biodegradable magnesium alloy stent. *Mater Sci Eng C Mater Biol Appl*, 42:705–714, 2014.
- [352] A. Schiavone, T.-Y. Qiu, and L.-G. Zhao. Crimping and deployment of metallic and polymeric stents – finite element modelling. *Vessel Plus*, 1:12–21, 2017.
- [353] D. Möller, W. Reimers, A. Pyzalla, and A. Fischer. Residual stresses in coronary artery stents. *J Biomed Mater Res*, 58(1):69–74, 2001.
- [354] F. Rondeau, P. Pilet, D. Heymann, D. Crochet, and G. Grimandi. Balloon surface changes after stent deployment: Influence of the crimping technique. *ITBM-RBM*, 23(6):357–362, 2002.
- [355] H.-H. Choi, S.-M. Hwang, Y.H. Kang, J. Kim, and B.S. Kang. Comparison of implicit and explicit finite-element methods for the hydroforming process of an automobile lower arm. *Int J Adv Manuf Technol*, 20:407–413, 2002.
- [356] L. Olovsson, M. Unosson, and K. Simonsson. Selective mass scaling for thin walled structures modeled with tri-linear solid elements. *Comput Mech*, 34:134–136, 2004.
- [357] M.A. Geith, G. Sommer, T. Schratzenstaller, and G.A. Holzapfel. Biomechanical and structural quantification of vascular damage: A unique investigation of stent implantation. *Art Res*, 20:50, 2017.
- [358] M. Wagner. *Lineare und nichtlineare FEM: Eine Einführung mit Anwendungen in der Umformsimulation mit LS-DYNA*. Springer, Wiesbaden, GER, 2017.
- [359] R. Fletcher. *Practical methods of optimization*. John Wiley & Sons, Hoboken (NJ), USA, 2 edition, 2000.
- [360] Livermore Software Technologie Corporation. LS-DYNA Theory manual, 2018.
- [361] Livermore Software Technologie Corporation. LS-DYNA Volume I: Keyword, 2018.
- [362] M.A. Puso and T.A. Laursen. A mortar segment-to-segment contact method for large deformation solid mechanics. *Comput Method Appl M*, 193(6-8):601–629, 2004.
- [363] M.A. Geith, K. Swidergal, B. Hochholdinger, T.G. Schratzenstaller, M. Wagner, and G.A. Holzapfel. On the importance of modeling balloon folding, pleating, and stent crimping: An FE study comparing

- experimental inflation tests. *Int J Numer Method Biomed Eng*, 35(11):e3249, 2019.
- [364] L. Wiesent, U. Schultheiß, C. Schmid, T. Schratzenstaller, and A. Nonn. Experimentally validated simulation of coronary stents considering different dogboning ratios and asymmetric stent positioning. *PLoS one*, 14(10):e0224026, 2019.
- [365] D.R. Holmes, R.G. Miller, R.P. Palmer, and C.W. Bunn. Crossed amorphous and crystalline chain orientation in polythene film. *Nature*, 171(4364):1104–1106, 1953.
- [366] S.L. Aggarwal, G.P. Tilley, and O.J. Sweeting. Orientation in extruded polyethylene films. *J Appl Polym Sci*, 1(1):91–100, 1959.
- [367] S. Rhee and J.L. White. Crystal structure and morphology of biaxially oriented polyamide 12 films. *Journal of Polymer Science Part B: Polymer Physics*, 40(12):1189–1200, 2002.
- [368] M. Ghahremanpour, G. Lorenz, T. Wörsching, M. Bogner, I. Maier, M. Detert, J. Sägebarth, and H. Sandmaier. Polyamide 12: Carbon nanotube composite material under the aspect of future application as balloon catheter material. In G. Schuh, editor, *Future trends in production engineering*, pages 275–286. Springer, Berlin, GER, 2013.
- [369] E. Mabry. Extruded tubing designed for balloon production. *MDDI Tubing*, 2008.
- [370] G.H. Menary and C.G. Armstrong. Experimental study and numerical modelling of injection stretch blow moulding of angioplasty balloons. *Plast Rubber Compos*, 35(8):348–354, 2006.
- [371] G. Sommer, S. Sherifova, P.J. Oberwalder, O.E. Dapunt, P.A. Ursomanno, A. DeAnda, B.E. Griffith, and G.A. Holzapfel. Mechanical strength of aneurysmatic and dissected human thoracic aortas at different shear loading modes. *J Biomech*, 49(12):2374–2382, 2016.
- [372] N.L.A. McFerran, C.G. Armstrong, and T. McNally. Uniaxial tensile viscoelastic and viscoplastic behaviour of nylon 12 at constant strain rate. *Plast Rubber Compos*, 35(8):310–316, 2006.
- [373] J. Richeton, S. Ahzi, K.S. Vecchio, F.C. Jiang, and R.R. Adharapurapu. Influence of temperature and strain rate on the mechanical behavior of three amorphous polymers: Characterization and modeling of the compressive yield stress. *Int J Solids Struct*, 43(7-8):2318–2335, 2006.
- [374] G. Sommer, M. Eder, L. Kovacs, H. Pathak, L. Bonitz, C. Mueller, P. Regitnig, and G.A. Holzapfel. Multiaxial mechanical properties and constitutive modeling of human adipose tissue: A basis for preoperative simulations in plastic and reconstructive surgery. *Acta Biomater*, 9(11):9036–9048, 2013.
- [375] R.S. Rivlin and D.W. Saunders. Large elastic deformations of isotropic materials VII. Experiments on the deformation of rubber. *Phil Trans R Soc Lond A*, 243(865):251–288, 1951.
- [376] G.A. Holzapfel. *Nonlinear solid mechanics. A continuum approach for engineering*. John Wiley & Sons, Chichester, UK, 2000.
- [377] J.D. Humphrey. *Cardiovascular solid mechanics: Cells, tissues, and organs*. Springer, New York (NY), USA, 2002.
- [378] V.K. Rangari, M. Yousuf, S. Jeelani, M.X. Pulikkathara, and V.N. Khabashesku. Alignment of carbon nanotubes and reinforcing effects in nylon-6 polymer composite fibers. *Nanotechnology*, 19(24):245703, 2008.
- [379] V.K. Rangari, M.Y. Shaik, H. Mahfuz, and S. Jeelani. Fabrication and characterization of high strength Nylon-6/Si3N4 polymer nanocomposite fibers. *Mater Sci Eng A*, 500(1-2):92–97, 2009.
- [380] M.A. Davarpanah, S. Bansal, and R. Malhotra. Influence of single point incremental forming on mechanical properties and chain orientation in thermoplastic polymers. *J Manuf Sci Eng*, 139(2):021012, 2017.
- [381] S.M. Walley, J.E. Field, R.H. Pope, and N.A. Safford. The rapid deformation behaviour of various

- polymers. *J. Phys. III France*, 1(12):1889–1925, 1991.
- [382] R.W Meyer and L.A Pruitt. The effect of cyclic true strain on the morphology, structure, and relaxation behavior of ultra high molecular weight polyethylene. *Polymer*, 42(12):5293–5306, 2001.
- [383] G. Coulon, G. Castelein, and C. G’Sell. Scanning force microscopic investigation of plasticity and damage mechanisms in polypropylene spherulites under simple shear. *Polymer*, 40(1):95–110, 1999.
- [384] R.S. Schwartz, D.J. Holder, D.R. Holmes, J.P. Veinot, A.R. Camrud, M.A. Jorgenson, and R.G. Johnson. Neointimal thickening after severe coronary artery injury is limited by a short-term administration of a factor Xa inhibitor. Results in a porcine model. *Circ J*, 93(8):1542–1548, 1996.
- [385] R. He, L. Zhao, V.V. Silberschmidt, and Y. Liu. Mechanistic evaluation of long-term in-stent restenosis based on models of tissue damage and growth. *Biomech Model Mechanobiol*, 2020.
- [386] R.S. Schwartz, W.D. Edwards, K.R. Bailey, A.R. Camrud, M.A. Jorgenson, and D.R. Holmes Jr. Differential neointimal response to coronary artery injury in pigs and dogs. Implications for restenosis models. *Arterioscler Thromb*, 14(3):395–400, 1994.
- [387] V.J. Swier, L. Tang, K.D. Krueger, M.M. Radwan, M.G. Del Core, and D.K. Agrawal. Coronary injury score correlates with proliferating cells and alpha-smooth muscle actin expression in stented porcine coronary arteries. *PLoS one*, 10(9):e0138539, 2015.
- [388] N.A. Scott. Restenosis following implantation of bare metal coronary stents: pathophysiology and pathways involved in the vascular response to injury. *Adv Drug Deliv Rev*, 58(3):358–376, 2006.
- [389] A. Kibos, A. Campeanu, and I. Tintoiu. Pathophysiology of coronary artery in-stent restenosis. *Acute Card Care*, 15(3):111–119, 2009.
- [390] E. Joviliano, C.E. Piccinato, R. Dellalibera-Joviliano, T. Moriya, and P.R.B. Évora. Inflammatory markers and restenosis in peripheral percutaneous angioplasty with intravascular stenting: current concepts. *Ann Vasc Surg*, 25(6):846–855, 2011.
- [391] J.W. Jukema, J.J.W. Verschuren, T.A.N. Ahmed, and P.H.A. Quax. Restenosis after PCI. Part 1: Pathophysiology and risk factors. *Nat Rev Cardiol*, 9(1):53–62, 2011.
- [392] K. Yahagi, F.D. Kolodgie, F. Otsuka, A.V. Finn, H.R. Davis, M. Joner, and R. Virmani. Pathophysiology of native coronary, vein graft, and in-stent atherosclerosis. *Nat Rev Cardiol*, 13(2):79–98, 2016.
- [393] Z. Dai and G. Xu. Restenosis after carotid artery stenting. *Vascular*, 25(6):576–586, 2017.
- [394] A.J. Schriebl, A.J. Reinisch, S. Sankaran, D.M. Pierce, and G.A. Holzapfel. Quantitative assessment of collagen fibre orientations from two-dimensional images of soft biological tissues. *J R Soc Interface*, 9(76):3081–3089, 2012.
- [395] A.J. Schriebl, H. Wolinski, P. Regitnig, S.D. Kohlwein, and G.A. Holzapfel. An automated approach for three-dimensional quantification of fibrillar structures in optically cleared soft biological tissues. *J R Soc Interface*, 10(80):20120760, 2013.
- [396] J.A. Niestrawska, C. Viertler, P. Regitnig, T.U. Cohnert, G. Sommer, and G.A. Holzapfel. Microstructure and mechanics of healthy and aneurysmatic abdominal aortas: Experimental analysis and modelling. *J R Soc Interface*, 13(124):20160620, 2016.
- [397] S. Sherifova, G. Sommer, C. Viertler, P. Regitnig, T. Caranasos, M.A. Smith, B.E. Griffith, R.W. Ogden, and G.A. Holzapfel. Failure properties and microstructure of healthy and aneurysmatic human thoracic aortas subjected to uniaxial extension with a focus on the media. *Acta Biomater*, 99:443–456, 2019.
- [398] G. Katz, B. Harchandani, and B. Shah. Drug-eluting stents: the past, present, and future. *Curr Atheroscler Rep*, 17(3):485, 2015.

- [399] R.T. Venkatasubramanian, E.D. Grassl, V.H. Barocas, D. Lafontaine, and J.C. Bischof. Effects of freezing and cryopreservation on the mechanical properties of arteries. *Ann Biomed Eng*, 34(5):823–832, 2006.
- [400] F. Salvucci, R.L. Armentano, J.M. Atienza, D. Bia, H. Perez, J.G. Barra, D. Craiem, F.J. Rojo, and G.V. Guinea. Arterial complex elastic modulus was preserved after an intercontinental cryoconserved exchange. *Conf Proc IEEE Eng Med Biol Soc*, pages 3598–3601, 2008.
- [401] I. Masson, A. Fialaire-Legendre, C. Godin, P. Boutouyrie, P. Bierling, and M. Zidi. Mechanical properties of arteries cryopreserved at –80 degrees C and –150 degrees C. *Med Eng Phys*, 31(7):825–832, 2009.
- [402] G. Sommer, D.C. Haspinger, M. Andrä, M. Sacherer, C. Viertler, P. Regitnig, and G.A. Holzapfel. Quantification of shear deformations and corresponding stresses in the biaxially tested human myocardium. *Ann Biomed Eng*, 43(10):2334–2348, 2015.
- [403] A. Eilaghi, J.G. Flanagan, G.W. Brodland, and C.R. Ethier. Strain uniformity in biaxial specimens is highly sensitive to attachment details. *J Biomech Eng*, 131(9):0910031–0910037, 2009.
- [404] C. Wang, M. Garcia, Y. Lanir, and G.S. Kassab. Three-dimensional mechanical properties of porcine coronary arteries: a validated two-layer model. *Am J Physiol Heart Circ Physiol*, 291(3):H1200–9, 2006.
- [405] A. Schiavone, L.G. Zhao, and A.A. Abdel-Wahab. Dynamic simulation of stent deployment – effects of design, material and coating. *J Phys Conf Ser*, 451:012032, 2013.